UNIVERSITY OF SOUTHAMPTON

Faculty of Engineering and Physical Sciences
School of Physics and Astronomy

Core-collapse Supernovae in the Dark Energy Survey

DOI: 10.1002/0470841559.ch1

by

Matthew James Peter Grayling
MSci
ORCiD: 0000-0002-6741-983X

A thesis for the degree of
Doctor of Philosophy

February 2023

University of Southampton

Abstract

Faculty of Engineering and Physical Sciences
School of Physics and Astronomy

Doctor of Philosophy

Core-collapse Supernovae in the Dark Energy Survey

by Matthew James Peter Grayling

Core-collapse supernovae – the deaths of massive stars – are among the most complex and diverse astrophysical phenomena, demonstrating a wide range of spectroscopic and photometric properties. These events result from the cessation of fusion in the cores of massive stars causing gravitational collapse, but there is a great deal that remains uncertain about the exact mechanisms involved. Studying the properties of populations of CCSNe can help constrain our knowledge of the physics involved in the explosion.

In this thesis, I examine the properties of high-redshift core-collapse supernova in the Dark Energy Survey (DES) and compare with local samples from the Lick Observatory Supernova Search (LOSS) and Zwicky Transient Facility (ZTF). Comparing type II SNe in DES and ZTF, I see a difference in peak luminosity of 3.0σ significance and between LOSS and ZTF of 2.5σ. This could be caused by redshift evolution, although simpler causes such as differing levels of host galaxy extinction between the samples cannot be ruled out. I also examine host galaxy properties for these samples, finding an offset in host galaxy colour between DES and ZTF; for the same galaxy stellar mass, a DES galaxy is bluer than a ZTF galaxy. I consider a number of simple explanations for this – including galaxy evolution with redshift, selection biases in either the DES or ZTF samples, and systematic differences due to the different photometric bands available – but find that none can easily reconcile the differences in host colour between the two samples and thus its cause remains uncertain.

During my analysis, I identified a very luminous SN IIb, DES14X2fna. This SN had an unusually high luminosity for its class, reaching ~ -19.4 mag in r-band, and also declined rapidly after peak. SNe IIb are thought to be powered by the decay of ^{56}Ni, but the mass of Ni that would be required to power this luminosity is inconsistent with the fast decline observed. This suggests that some other physics is involved. Using semi-analytic model fits, I show that ^{56}Ni decay alone is unable to power this object, but interaction with surrounding circumstellar material (CSM) or the spin-down of a rapidly rotating neutron star formed in the explosion are two possible explanations for this unusual object.

Finally, I explore the use of Generative Adversarial Networks (GANs) to generate synthetic CCSN light curves. GANs are a type of neural network used for data generation; this approach could be used to augment samples used to train photometric classification algorithms, improving their performance. By training on DES-like simulations I find that GANs are able to generate physically realistic light curves for a variety of CCSN types, demonstrating their potential to improve classification techniques going forward.

Contents

List of Figures

List of Tables

Declaration of Authorship

I declare that this thesis and the work presented in it is my own and has been generated by me as the result of my own original research.

I confirm that:

1. This work was done wholly or mainly while in candidature for a research degree at this University;
2. Where any part of this thesis has previously been submitted for a degree or any other qualification at this University or any other institution, this has been clearly stated;
3. Where I have consulted the published work of others, this is always clearly attributed;
4. Where I have quoted from the work of others, the source is always given. With the exception of such quotations, this thesis is entirely my own work;
5. I have acknowledged all main sources of help;
6. Where the thesis is based on work done by myself jointly with others, I have made clear exactly what was done by others and what I have contributed myself;
7. Parts of this work have been published as: Grayling et al. (2021), Grayling et al. (2022)

Signed:..... Date:.....

Acknowledgements

I am incredibly grateful for all the support from my supervisor, Mark Sullivan. Every time I felt unsure of my direction going into a meeting, I left with a clear vision and renewed confidence – I wouldn't have been able to do my PhD without you. Many thanks also go to Claudia, who was an excellent second supervisor even after moving abroad and was always available to provide support and expertise.

To Phil, Chris, Mat and Charlotte, you were also a key part of my PhD and always happy for me to pop next door with questions and provide encouragement when I needed it. Lisa, you were essentially me from the year above and were great to talk to with all things both PhD related and otherwise, thanks for all your help. To the rest of the supernova group – Tomas, Miika, Marcus and Zoe as well as Maria and Lizi from Portsmouth – you all helped to make the group a fun and supportive environment.

To everyone in office 4053 – Ella, Pip, Marta and others already mentioned – thanks for making wasting time being unproductive in the office such a joy. Random office discussions were some of the best times I had. For everyone in the department generally, thanks for the chats, memories and cat pictures. Particular mentions go to Norman and Jakub for all the great DISCnet outings.

To Cassie, you have always been there throughout the highs and the lows of my PhD and put up with me even while I was writing my thesis. I am very grateful for all the support you've given me.

Finally, to my family; Mum, Dad and Laura, you've given me so much throughout my entire life and hopefully you think it's been worth it! Thanks for everything.

Definitions and Abbreviations

AAT	Anglo-Australian Telescope
AD	Anderson-Darling
ANN	Artificial Neural Network
ASAS-SN	All-Sky Automated Survey for Supernovae
ATLAS	Asteroid Terrestrial-impact Last Alert System
CCSNe	Core-collapse Supernovae
CDF	Cumulative Density Function
CGAN	Conditional Generative Adversarial Network
CNN	Convolutional Neural Network
CSM	Circumstellar Material
CSP	Composite Stellar Population
CTIO	Cerro Tololo Inter-American Observatory (CTIO)
DECam	Dark Energy Camera
DES	Dark Energy Survey
DES-SN	Dark Energy Survey Supernova Programme
DESDM	DES Data Management Team
DLR	Directional Light Radius
GAN	Generative Adversarial Network
GP	Gaussian Process
GRB	Gamma Ray Burst
GRU	Gated Recurrent Unit
GTC	Gran Tescopio Canarias
H_0	Hubble constant
IMF	Initial Mass Function
ISM	Interstellar Medium
KS	Kolmogorov-Smirnov
LO	Lick Observatory
LOSS	Lick Observatory Supernova Search
LSST	Legacy Survey of Space and Time at Vera Rubin Observatory
LSTM	Long Short-term Memory
MC	Monte Carlo
MCMC	Markov chain Monte Carlo

NED	NASA Extragalactic Database
NMF	Non-negative Matrix Factorisation
PÉGASE	Programme d'Étude des Galaxies par Synthèse Évolutive
PCA	Principal Component Analysis
PLasTiCC	Photometric LSST Astronomical Time-series Classification Challenge
PSF	Point Spread Function
PSNID	Photometric Supernova IDentification
ReLU	Rectified Linear Unit
RET	Rapidly Evolving Transients
RNN	Recurrent Neural Network
SALT	South African Large Telescope
SDSS	Sloan Digital Sky Survey
SED	Spectral Energy Distribution
SEDM	SEDMachine
SESNe	Stripped-envelope Supernovae
SFR	Star Formation Rate
SHELS	Smithsonian Hectospec Lensing Survey
SLSNe	Superluminous Supernovae
SN(e)	Supernova(e)
SNe Ia	Type Ia Supernovae
SNe Ib	Type Ib Supernovae
SNe Ibn	Type Ibn Supernovae
SNe Ic	Type Ic Supernovae
SNe Ic-BL	Type Ic-BL Supernovae
SNe Icn	Type Icn Supernovae
SNe II	Type II Supernovae
SNe IIb	Type IIb Supernovae
SNe IIn	Type IIn Supernovae
SNID	Supernova Identification
SNPhotCC	Supernova Photometric Classification Challenge
sSFR	Specific Star Formation Rate
SSP	Simple Stellar Population
U-R	Rest-frame U-R colour
VLT	European Southern Observatory Very Large Telescope
WD	White Dwarf
WGAN	Wasserstein Generative Adversarial Network
YSE	Young Supernova Experiment
z	Redshift
ZTF	Zwicky Transient Facility

Chapter 1

Introduction

"Since the beginning of time man has yearned to destroy the sun."
–Charles Montgomery Burns

Supernovae (SNe) are energetic explosions that occur at the end of the life of some stars. These events can be sufficiently luminous to outshine their host galaxies - considering that galaxies consist of hundreds of millions of stars, the fact that the explosion of one individual star can outshine all the others combined helps to put into context just how bright these events can be.

The term *nova* originates from the Danish astronomer Tycho Brahe who observed the supernova SN 1572, derived from a book written to describe his findings titled *De nova stella*, meaning 'Concerning the new star'in Latin. Over time, more and more similar objects were identified, leading Walter Baade and Fritz Zwicky to coin the term *Super-novae* in 1934 to differentiate these very luminous, energetic events from fainter classical novae (Baade & Zwicky, 1934).

SNe are transient in nature; they become extremely bright after explosion then fade over a period of weeks to months. Observations of SNe were very rare historically as they would need to either be close enough to be visible to the naked eye or happen to be captured at a time when they were bright enough to be detectable by telescopes of the day. Zwicky led the first dedicated SN search at the Palomar Observatory in California, regularly observing nearby galaxies to identify changes and capture live SNe. The improvement in technology over the following decades allowed for detection of fainter, more distant SNe and more regular monitoring of target galaxies. In the present, a variety of different surveys regularly revisit the same areas of the sky to monitor transient events; these surveys include the Zwicky Transient Facility (ZTF; Bellm et al., 2019), Young Supernova Experiment (YSE; Jones et al., 2021), the All-Sky Automated Survey for Supernovae (ASAS-SN; Shappee et al., 2014) and the Asteroid Terrestrial-impact Last Alert System (ATLAS; Tonry et al., 2018). The total number of

SNe detected now sits in the thousands and is expected to grow considerably over the coming decade.

SNe are widely studied because of their significance within both astrophysics and cosmology. Their explosive nature means that SNe have a strong effect on their surroundings; the energy produced allows for the formation of heavy elements and enriches the surrounding environment, while the shock wave resulting from a SN can both trigger and suppress star formation. A particular type of SNe known as SNe Ia show limited variability and can be standardised and used for distance estimation. As a result, SNe Ia can be used to probe different cosmological models; this approach was used to discover the accelerating expansion of the universe (Riess et al., 1998; Perlmutter et al., 1999).

1.1 Supernova Classes and Physical Interpretation

The term SN encompasses a variety of different explosions which take place over different time scales, span different luminosities and are powered by different physical processes. As such, they are categorised into sub-categories depending on their observed properties.

The first spectroscopic classification scheme was presented in Minkowski (1941), focusing on a sample of 14 SNe. Objects which showed spectroscopic features corresponding to hydrogen were classified as type II SNe, while those without hydrogen features were labelled as type I SNe. This split based on the presence of hydrogen remains in the modern SN classification scheme, although there are now many further categories within SNe I and II based on the different spectroscopic and photometric properties seen within these broad classes.

In this section I will discuss the different types of SNe; their differing progenitor systems, observational properties and power sources.

1.1.1 Core-collapse Supernovae

Core-collapse supernovae (CCSNe) are the end-of-life of massive stars, upwards of 8 $M_\odot$. For these stars, after the core is depleted of He and subsequently collapses due to a lack of radiation pressure, the temperatures and pressures reached become sufficiently high to allow for fusion of even heavier elements such as carbon. This process continues for increasingly heavy elements until ^{56}Fe is formed in the core, at which point fusion is halted since the binding energy per nucleon decreases for elements heavier than this. The cessation of fusion in the core means that it can no longer be supported by radiation pressure, and the core is instead supported by

electron degeneracy pressure. However, fusion of Si outside the core continues which leads the core to gain mass until eventually electrons degeneracy pressure is no longer able to support the core which now collapses under gravity at supersonic speeds.

As the core contracts, pressure and temperature rapidly increases. This process leads to the dissociation of Fe nuclei into their constituent nucleons through conversion of the kinetic energy of infalling Fe nuclei into heat (Foglizzo, 2017) and photodissociation caused by the production of high energy γ-rays due to the high temperatures in the core (Janka, 2017). Protons in the core then merge with free electrons via the process of electron capture to produce further neutrons. As the core of the star reaches nuclear densities ($\rho \simeq 2.7 \times 10^{14}$ g cm^{-3}), the collapse begins to slow as the neutrons become able to support themselves against gravity due to neutron degeneracy pressure, forming a neutron star. The collapsing core composed of neutrons will slightly overshoot the equilibrium between internal pressure and gravity, leading it to rebound and briefly expand before remaining stable. This expansion triggers a shock at the boundary between the core and the supersonic infalling material which then propagates outwards. However, this shock ultimately stalls within the core as it loses energy to dissociation of Fe as it travels outwards. As a result, this process alone is not enough to trigger the SN.

For a supernova to occur, some mechanism is required to revive this stalled stock. The processes involved during core-collapse lead to the production of a considerable number of neutrinos – some are produced during electron capture, while others are created via neutrino pair-production in the very high temperature core. While the exact details of the mechanisms that trigger the explosion are not fully understood, current consensus is that the shock is revived by neutrinos transferring a fraction of their energy to their surroundings in a process known as delayed neutrino-heating. Roughly 100 ms after the shock stalls, evolving conditions towards the centre of the star increase the efficiency of neutrino-energy deposition. Firstly, the temperature in the region between the neutron star core the shock front decreases as the density drops. The plasma in this region then becomes more radiation dominated, reducing the effect of neutrino cooling. Simultaneously, as the neutron star gains mass and contracts, its temperature increases which in turn increases the energy of the neutrinos it emits and therefore the number that will interact with free nucleons close to the shock front. In this way, the produced neutrinos are able to transfer a fraction of their energy to the shock and trigger a SN explosion (Janka, 2017).

CCSNe are powered at least in part by the radioactive decay of ^{56}Ni which is synthesised in the explosion. ^{56}Ni is a radioactive isotope which decays into ^{56}Co with a half-life of $\sim$ 6 days, which in turn decays into stable ^{56}Fe with a half life of $\sim$ 77 days. Gamma rays and positrons produced in this radioactive decay process interact with surrounding material and are reprocessed into optical and near-infrared photons, leading to the light curves which are observed. In cases of an explosion powered

exclusively by ^{56}Ni decay, the light curve can be treated using the 'Arnett' model (Arnett, 1982). However, despite sharing the same processes of core-collapse and ^{56}Ni power, CCSNe exhibit a wide variety of properties depending on both the nature of the progenitor star and its surroundings.

1.1.1.1 Hydrogen-rich Supernovae

As previously discussed, SNe II are classified based on the presence of hydrogen features in the SN spectra around peak brightness. At the end of its life, the progenitor star consists of shells of increasingly light elements towards the exterior. A progenitor star with an outer envelope of hydrogen will lead to a SN that shows hydrogen features and hence a SN II. An example of a typical SN II spectrum is shown in Figure 1.1.

For these events, the outer hydrogen envelope is ionised by the initial shock and becomes opaque which affects the shape of the observed light curve. As the outer material further from the star cools, it reaches the recombination temperature of hydrogen which leads to the formation of a recombination front separating opaque ionised hydrogen from lower opacity recombined hydrogen - this recombination front moves towards lower radius from the progenitor star as the material continues to cool.

In some cases, the movement of the recombination front towards the star is balanced out by the expansion of the ejecta after the explosion which leads to a surface of constant temperature and radius, causing luminosity to remain roughly constant. These objects show clear plateaus in their light curves and are sometimes referred to as SNe IIP. In other cases, rather than showing a plateau these events follow a linear decline after maximum which has led these objects to be sometimes denoted as SNe IIL. SNe IIL and IIP are sometimes kept as separate classes, though Anderson et al. (2014) demonstrated a continuum in photometric properties from fainter, slow declining to brighter, fast declining objects and concluded that the mass of the hydrogen envelope at the time of explosion is responsible for this diversity. Similar results were also found in Valenti et al. (2016), Galbany et al. (2016) and Gutiérrez et al. (2017b). In this thesis, I will refer to SNe II rather than separating SNe IIP and IIL.

1.1.1.2 Stripped Envelope Supernovae

Stripped envelope supernovae (SESNe) comprise a number of different subclasses which show different spectroscopic features but share one common characteristic; their progenitor stars have had their outer envelopes of lighter elements at least partially stripped away. Without the presence of a thick hydrogen envelope which becomes ionised by the explosion like SNe II, SESNe are powered by the decay chain

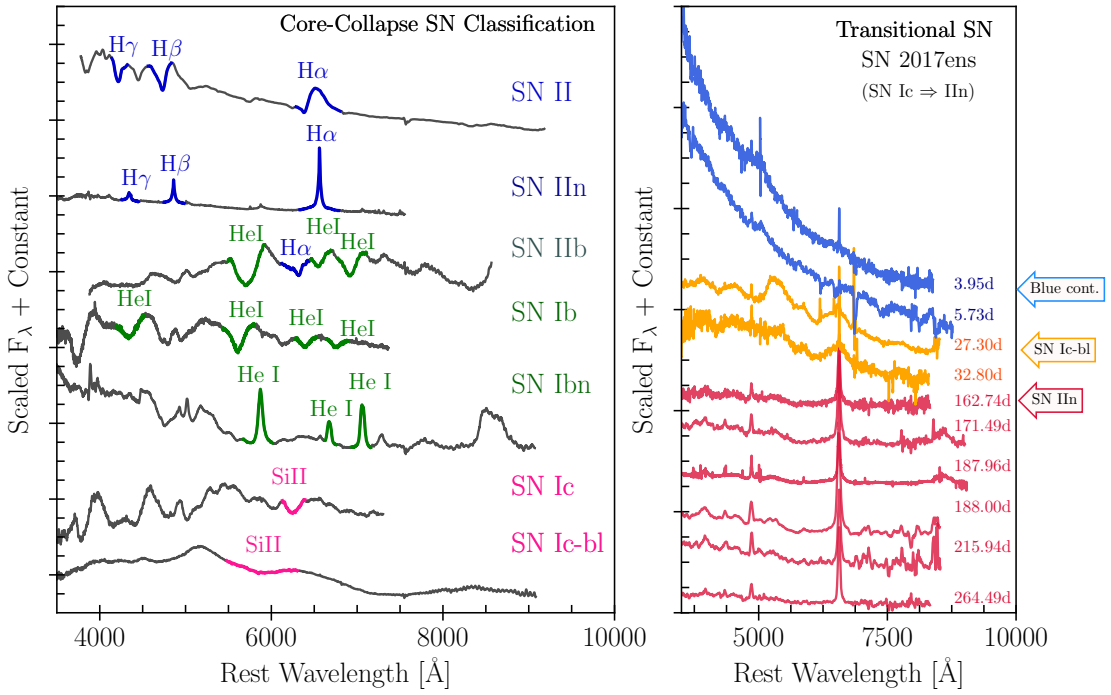

FIGURE 1.1: **Left:** Examples of spectra for a variety of different CCSN types. **Right:** The spectral time series of SN 2017ens, showing its features transitioning from a blue continuum to a SN Ic-BL and then a SN IIn; Figure 1 from Modjaz et al. (2019).

of ^{56}Ni as outlined in Section 1.1.1 and typically display bell-shaped light curves around peak (Taddia et al., 2018). The various subclasses are classified based on the presence of different spectroscopic features. For a SN Ib, the progenitor star has had its outer envelope of hydrogen stripped meaning that helium features are seen in its spectra rather than the hydrogen features associated with SNe II. For SNe Ic, the helium envelope has also been stripped meaning that neither hydrogen nor helium features are seen. SNe IIb are an intermediate class of SESNe, displaying hydrogen lines at early times similar to SNe II before the appearance of helium lines as seen in SNe Ib (Filippenko, 1997; Gal-Yam, 2017; Modjaz et al., 2019). The commonly-accepted physical explanation for SNe IIb is that their progenitors have had their outer hydrogen envelope partially, but not fully, stripped away. As the spectroscopic properties of a stripped-envelope SN differ primarily due to the degree of stripping of the progenitor star, it is an open question as to whether SNe IIb, Ib and Ic are distinct classes or part of a continuum (Modjaz et al., 2019). The left panel of Figure 1.1 includes typical spectra for these classes.

The exact mechanism driving the envelope stripping of these SNe is unclear, but proposed solutions include stellar winds (e.g. Woosley et al., 1993) and interaction with a binary companion (e.g. Nomoto et al., 1995) in the case of a binary progenitor system. Stellar winds require massive progenitors of $\gtrsim$ 25–30 $M_\odot$ in order to remove at least the majority of the hydrogen envelope (Eldridge & Tout, 2004). Pre-explosion and late-time images of the SN environment of the well-studied SN IIb SN 1993J

(Aldering et al., 1994; Fox et al., 2014) indicate the presence of a binary system, with evidence of a binary companion also found in SN 2001ig (Ryder et al., 2018) and SN 2011dh (Folatelli et al., 2014). However, deep imaging studies of the SN IIb remnant Cassiopeia A have not indicated a binary companion (Kochanek, 2018; Kerzendorf et al., 2019), suggesting that both of these progenitor scenarios may occur.

Some SNe IIb (e.g. 1993J, Richmond et al. 1994; 2016gkg, Arcavi et al. 2017b; Bersten et al. 2018) exhibit an initial peak in their light curves which has been attributed to post-shock-breakout cooling in the case of a progenitor with a compact core surrounded by extended, low-mass material (Bersten et al., 2012; Nakar & Piro, 2014). This typically occurs over a short period of a few days, and is not observed in all SNe IIb (e.g. SN 2008ax; Pastorello et al., 2008), potentially because the SN is not discovered until after this phase. This pre-max bump can help infer properties of the progenitor including radius and binarity using hydrodynamic simulations (e.g. Bersten et al., 2012; Piro, 2015; Sapir & Waxman, 2017).

As SESNe are powered by the decay chain of ^{56}Ni to ^{56}Co and ^{56}Fe, they have relatively fixed behaviour at late times. At these epochs, when it can be assumed that all ^{56}Ni has already decayed into ^{56}Co, the decline rate of SNe is limited by the decay timescales of ^{56}Co. Under the assumption that γ-rays produced in this decay process are fully trapped and all deposit their energy, the luminosity of SNe will decline at a rate of 0.98 mag (100d)$^{-1}$ (Woosley et al., 1989). A decline rate faster than this indicates that γ-rays produced are not fully trapped and therefore some of their energy is not observed in the optical light curve. A decline rate slower than this indicates that an additional source of luminosity is present.

1.1.1.3 'Broad-line' Supernovae

SNe Ic with broad spectral lines (SNe Ic-BL) are a subset of SNe Ic which show very broad spectral features, indicating fast expansion velocities of up to 20,000 km s^{-1} (Modjaz et al., 2016) and kinetic energies an order of magnitude greater than typical for CCSNe (e.g. Lyman et al., 2016; Prentice et al., 2016). These events are often associated with gamma-ray bursts (GRBs), and of GRB events with an associated SN the vast majority are SNe Ic-BL (Ho et al., 2020). A typical SN Ic-BL spectrum is shown in the left panel of Figure 1.1.

Despite being SESNe, these objects are not fit well by the Arnett model of ^{56}Ni decay which cannot reproduce both the luminous peaks and the late-time light curves of these objects. These objects have traditionally been fit with a two-component model, with the light curve peak and broad spectral features powered by a fast-moving component and the exponential decline powered by a slower-moving dense component (Maeda et al., 2003). However, another possibility which has been

considered more recently is the idea that the spin-down of a rapidly rotating neutron star (magnetar) formed by the collapsing core injects additional energy into the system beyond ^{56}Ni decay. Wang et al. (2017) shows that a combination of a magnetar with ^{56}Ni decay successfully fits the light curves of the SNe Ic-BL SN 1998bw and SN 2002ap, with the magnetar able to explain the deviation of the late-time light curve from the intermediate exponential decline.

1.1.1.4 'Narrow line' Supernovae

For some SNe, the progenitor star is surrounded by a dense circumstellar medium (CSM). When these objects explode, the fast-moving expanding ejecta will collide with the CSM leading to the formation of a shock. This has two main effects on the properties of the SN. The first is that this interaction leads to the presence of narrow emission lines in spectra of the SN. SNe with clear narrow features indicating CSM interaction are typically denoted by 'n' - for example, a SN II which shows narrow features is known as a SN IIn (Schlegel, 1990), while SNe Ib and Ic which show narrow features are respectively known as SNe Ibn (Pastorello et al., 2007) and SNe Icn (Gal-Yam et al., 2021; Perley et al., 2022). Typical spectra of SNe IIn and Ibn are shown in the left panel of 1.1. The second effect is that interaction with CSM provides a significant additional engine to power the light curve of these SNe. When the expanding ejecta collides with the CSM, the kinetic energy of the ejecta is converted into heat, with the heated material then radiating this energy away contributing to the overall luminosity of the SN. The radiative shock that is formed where the ejecta collides with the CSM is very efficient at converting the kinetic energy of the ejecta into emission of electromagnetic radiation at visible wavelengths (Smith, 2017).

While CSM interaction is typically associated with narrow emission lines, it should be noted that it has also been invoked as a power source for some SNe which do not show these narrow features. For example, PTF11iqb showed narrow features at early times which later faded as the SN began to resemble a more typical SN II, with a proposed explanation being a highly asymmetric CSM distribution (Smith et al., 2015). Reynolds et al. (2020) proposed that CSM interaction powered in part the light curve of SN 2016gsd with the absence of narrow emission features for this object resulting from a CSM concentrated close to the progenitor star with low density outside the region swept up by the SN ejecta.

1.1.2 Thermonuclear Supernovae

Thermonuclear SNe are the second main class of SNe, separate from CCSNe, which originate from white dwarf (WD) progenitor stars in binary systems. The most common type of thermonuclear SN is a SN Ia, which are spectroscopically similar to

SNe Ib and Ic in that they lack hydrogen features but can be differentiated by the presence of silicon features that SNe Ib lack and which are very weak in SNe Ic. Other types of transient such as calcium-rich transients are also thought to be thermonuclear SNe (e.g. Kasliwal et al., 2012; García-Berro et al., 2017), but here I will focus solely on SNe Ia as these are the most common and widely-used member of this class.

In a simple picture of a SN Ia, the progenitor star is a carbon-oxygen WD located in a binary system which accretes material from its companion. As the WD gains mass, it approaches the Chandrasekhar mass ($1.4M_{\odot}$; Chandrasekhar, 1931), the point at which point electron degeneracy pressure is no longer able to balance gravity and the WD will collapse. At $\sim 1.37M_{\odot}$, carbon in the WD will begin to fuse which increases the temperature and oxygen also begins to fuse. This leads to fusion of increasingly heavy elements and a runaway thermonuclear reaction which unbinds the white dwarf and powers the SN. This process leads to the synthesis of ^{56}Ni which follows the same decay chain as outlined in Section 1.1.1, and overall SNe Ia display similar light curve shapes to SESNe due to their shared power source. However, SNe Ia are typically much brighter than SESNe as the mass of ^{56}Ni produced is significantly greater; SESNe have ^{56}Ni masses up to $\sim 0.2\mathrm{M}_{\odot}$ (Meza & Anderson, 2020) while SNe Ia can exceed this by a factor of $2-3$ (Childress et al., 2015).

While it is generally accepted that SN Ia originate from binary systems, the exact nature of these systems remains uncertain. In one picture known as the single-degenerate scenario, the binary companion of the WD is either a red giant or main sequence star from which the WD accretes mass (Whelan & Iben, 1973). In another, the binary system consists of two WDs which allows for a wider set of possible triggers of the explosion. It could be the case that, as in the picture outlined above, one WD accretes mass from the other and approaches the Chandrasekhar mass. However, it could also be the case that the two WDs infall in a spiral and ultimately collide and merge also triggering the thermonuclear runaway (Iben & Tutukov, 1984). A third option is the 'double-detonation' scenario where a shock wave caused by helium fusion on the surface of one of the WDs triggers carbon burning in its core (Woosley & Weaver, 1994). There is ongoing debate over which of these models is the true progenitor system of SNe Ia and whether multiple different scenarios could occur.

1.1.3 Superluminous Supernovae

Superluminous supernovae (SLSNe) are an additional class of SNe discovered more recently than either core-collapse or thermonuclear SNe. These objects are not discussed in detail as they are not the subject of this analysis, however I will briefly summarise their properties here for completeness; for recent reviews, see e.g. Gal-Yam (2019), Inserra (2019) and Nicholl (2021). As the name suggests, these objects were first identified as their peak absolute magnitudes were far in excess of traditional SNe,

reaching absolute magnitudes of ~ -21−−22 in comparison to the typical range from $\sim -15 - -20$ covering CCSNe and SNe Ia. The significance of this is that the typical power source of SNe, ^{56}Ni decay, does not provide enough luminosity to power the light curves of these objects. One proposed power source for SLSNe is interaction with surrounding CSM as described in Section 1.1.1.4. Another idea is that these objects are powered by energy released by the spin-down of a rapidly rotating magnetar formed by the collapse of the core of the progenitor star as discussed in Section 1.1.1.3.

SLSNe, like CCSNe, can be divided into two separate subtypes based on the presence or absence of hydrogen in the SN spectra. SLSNe-I are hydrogen-poor – the light curves of these objects resemble SNe Ic but brighter and with a much longer duration. Similarly to SESNe, it may be that SLSNe-I are also have progenitor stars which have had their outer hydrogen envelope stripped. SLSNe-II are hydrogen rich and appear similar to SNe IIL and SNe IIn except with a higher brightness and longer duration, although only a few members of this class have been observed.

1.2 Significance of Supernovae

As mentioned at the beginning of this chapter, SNe are of great significance within astrophysics and cosmology. In this section I will outline the key motivations behind the study of SNe.

1.2.1 SNe Ia

While SNe Ia are not the main focus of this thesis, they are the most widely studied class of SN and as such, I will begin by briefly exploring the reasons for this. In the simple picture outlined in Section 1.1.2, SNe Ia result from WD progenitors which approach the Chandrasekhar mass and subsequently explode which would mean that these objects all explode with the same energy and are therefore 'standard candles' with a fixed intrinsic luminosity. In reality, SNe Ia are more complex than this and show diversity in their peak luminosities. Nevertheless, observations of SNe Ia in the 1970s revealed a relation between the peak luminosity and decline rate of SNe Ia (Rust, 1974; Pskovskii, 1977) – these were subsequently formalised into the 'Phillips relation' (Phillips, 1993) which linked the peak *B*-band absolute magnitude of SNe Ia to the decline in mags in the 15 days after peak. By applying corrections to their observed light curves, SNe Ia can be 'standardised' which allows them to be used as distance indicators and used in cosmological analysis (e.g. Riess et al., 1998; Perlmutter et al., 1999). Modern cosmological studies (e.g. Abbott et al., 2019; Riess et al., 2022) correct the light curves of SNe Ia based on both their decline timescales and colour at peak.

The role SNe Ia play in cosmological analysis is a major motivation for the study of these objects. Beyond cosmology, however, there are also many open questions relating to the astrophysics of these objects. The nature of their progenitor systems remain open for debate, along with the mechanism that triggers the thermonuclear runaway which causes the SN. SNe Ia, as well as CCSNe, also have a strong influence on their surroundings – this is discussed in the next section.

1.2.2 Core-collapse Supernovae

I will now discuss the significance of CCSNe, the main focus of this thesis, which are of great importance in an astrophysical context. These energetic events provide an ideal opportunity to study extreme physics, including fluid dynamics and shock physics as well as neutrino physics, and there is significant ongoing work to simulate the explosion mechanism of these events in order to better understand the processes involved. Beyond the physics of the explosion mechanism itself, CCSNe play a key role in the evolution of the universe. The extreme energies released during CCSNe and SNe Ia allow for the synthesis of heavier elements beyond iron, meaning that these events have a large impact on the elemental abundance of the universe (Burbidge et al., 1957). CCSNe also have a strong impact on the galaxies in which they explode in a variety of ways. The energy and momentum released in SNe can lead to outflows and gas loss from a galaxy, reducing the material available for star formation (Larson, 1974), and also lead to turbulence in the interstellar medium (ISM) which can in turn inhibit star formation (Joung & Mac Low, 2006). However, the shock waves driven by these events can also trigger star formation (e.g. Li et al., 2014). In addition, the neutrinos produced in CCSNe make up a substantial proportion of the relic cosmic neutrino background (Mathews et al., 2020).

Despite their significance, however, many gaps remain in our knowledge of CCSNe. As outlined in Section 1.1.1, these objects exhibit very diverse properties with a variety of mechanisms driving the different subtypes that are not fully understood. Simulations of the core-collapse procedure itself have improved considerably over time to the point where the neutrino mechanisms used in 3d simulations lead to explosions with the correct rough properties, however further work is required to ensure that outputs such as explosion energy, neutron star mass and nucleosynthesis match observations (Burrows & Vartanyan, 2021). As discussed in Section 1.1.1.2, it is still an open question whether the variety of classes of SESNe are distinct or form a continuum, with further work required to confirm this. The right panel of 1.1 shows spectroscopy of the transitional object SN 2017ens which first resembled a SN Ic-BL before later showing features typical for a SN IIn, demonstrating that some objects do not fit neatly into the current classification scheme. In addition, as the number of observed SNe increases so too does the number of SNe which display unusual

properties that challenge our understanding of their class. For example, iPTF14hls spectroscopically resembled a SN II but remained bright for in excess of 600 days and displayed five peaks (Arcavi et al., 2017a). OGLE-2014-SN-073 was a SN II which possessed a very broad light curve with high ejecta velocities. Recently, the SNe IIb ASASSN-18am and DES14X2fna (Grayling et al., 2021; Bose et al., 2020) have been identified as far more luminous than typical objects of their class. Continual study of the properties of CCSNe is necessary in order to further refine our understanding of the physics involved in the explosion as well as the effect that these extreme events have on their surroundings.

In addition to the astrophysics involved, better understanding of CCSNe will also assist in cosmological analysis. While SN cosmology typically focuses on SNe Ia, the steps involved in standardising these objects are all based on empirical relations. Previous studies have focused on finding similar relations to allow CCSNe to be used for cosmological analysis. de Jaeger et al. (2020a) demonstrates a method of standardising SNe II using corrections based on the velocity of the Hβ line and the colour of the SN at peak – this method was then applied to measure the value of the Hubble constant H_0 in de Jaeger et al. (2020b) and further refined in de Jaeger et al. (2022) to obtain an estimate with a statistical uncertainty of less than 5 per cent. Developing our understanding of CCSNe will help to assist this process by allowing for more refined standardisation.

1.3 Studying Core-collapse Supernova Population Demographics

Having discussed the importance of CCSNe in Section 1.2.2, I will now outline how the population of these objects can be studied.

1.3.1 Luminosity Functions

The most straightforward population diagnostic which can be used to investigate CCSNe is the luminosity function, the distribution of peak luminosities observed across the SN population. Figure 1.2 shows an example of a luminosity functions for SNe II from Li et al. (2011, hereafter L11), on this occasion split by the morphology of the host galaxy. Accurate knowledge of the luminosity is important for two key reasons:

- The luminosity function can be used to help constrain CCSN explosion physics. As discussed in Section 1.1.1, there are a wide variety of different mechanisms which contribute to the light curve of a CCSN and many aspects of the

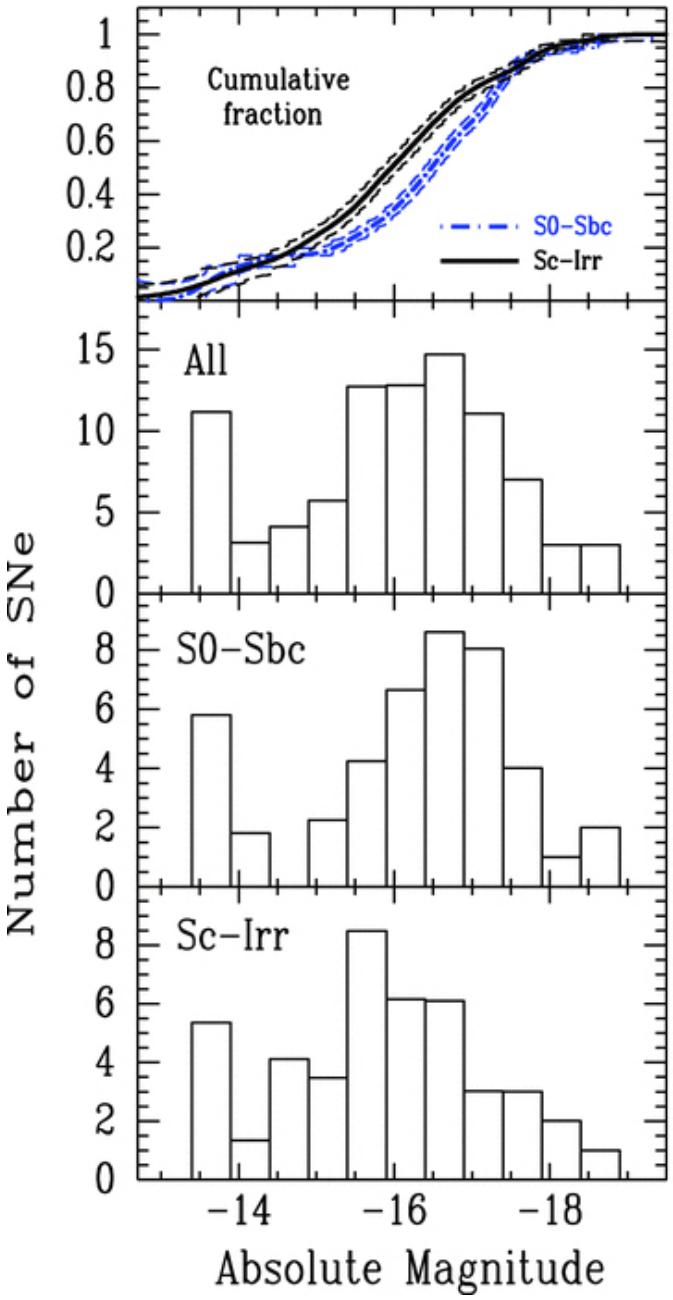

FIGURE 1.2: An example of a SN luminosity function, in this case looking at SNe II in host galaxies with different morphologies; Figure 7 from Li et al. (2011).

underlying physics are not fully understood. Any proposed models for the explosion physics must be able to reproduce the full range of SN luminosities seen in nature making good knowledge of this luminosity distribution vital.

- A common technique applied in the field of SNe is to simulate full sky surveys. These simulations involve creating a synthetic sample of SNe and replicating the observing conditions of a given survey to see what that survey would observe based on this synthetic SN population. Simulations of this nature are used for a number of applications, for example calculating SN rates (e.g. Bazin et al., 2009; Graur et al., 2017a; Frohmaier et al., 2021), optimising observing strategies and preparing for upcoming surveys (e.g. Jones et al., 2017; Villar et al., 2018) and modelling the contamination of CCSNe in cosmological samples of SNe Ia (e.g. Vincenzi et al., 2019, 2021). Reliable luminosity functions are of great importance in ensuring that the synthetic SN population is representative of the true population in order for these methods to be reliable.

Several studies have examined CCSN luminosity functions. L11 produced luminosity functions for all SNe in the Lick Observatory Supernova Search (LOSS; Li, 2000), including 105 CCSNe – these luminosity functions have been used for simulations in other works such as Vincenzi et al. (2021). However, this sample is very local with a maximum redshift of ~ 0.014. It is possible that redshift evolution in the underlying stellar population and progenitor stars in turn leads to an evolution with redshift of the luminosity function. If this were the case, simulating SN populations at higher redshifts based on local luminosity functions would introduce bias into the analysis – this possibility is considered in Vincenzi et al. (2021). Richardson et al. (2014) presented luminosity functions based on data from the Asiago Supernova Catalogue (Barbon et al., 1989) supplemented by further SNe from other studies and contains CCSNe up to a maximum redshift of $\sim 0.2 - 0.3$. However, this sample includes bias corrections which assume that the luminosity function does not evolve with redshift meaning that it may also not be suitable at higher redshift.

1.3.2 Supernova Host Galaxies

CCSNe can also be investigated by studying the properties of the host galaxies in which they explode, which can help inform about the nature of their progenitor systems. As a very simple example, CCSNe result from massive progenitor stars which means that they are found in star-forming galaxies but not quiescent galaxies, which lack these massive stars.

In general, CCSNe are found across a wide variety of star-forming host environments (e.g. Anderson et al., 2010; Graur et al., 2017b) but some types of SNe have been observed to occur preferentially in specific types of environment. The most luminous

transients, including SLSNe but also SNe Ic-BL, are typically found in low mass, low metallicity and/or strongly star-forming environments (e.g. Angus et al., 2016; Perley et al., 2016; Modjaz et al., 2020). Previous work analysing the local environment around the SN position has also found that SNe Ib/c more closely trace underlying star formation in their host galaxies than SNe II (e.g. Anderson & James, 2009; Galbany et al., 2018), suggesting that they are more associated with star formation. As discussed in Section 1.1.1.2, it remains an open question whether the various classes of SESNe form a continuum or are distinct. Galbany et al. (2018) finds that SNe IIb have unusual host properties compared with other core-collapse SN hosts, having particularly low metallicity and star formation rate (SFR). However, Schulze et al. (2021) finds that the host properties of SNe IIb are consistent with those of SNe II.

It is widely established that the properties of galaxies evolve with redshift. The overall star formation in the universe is decreasing over time, which means that star formation rate increases at higher redshifts (e.g. Lilly et al., 1996). Galaxy metallicity also evolves with redshift due to enrichment from events such as SNe (e.g. Zahid et al., 2012). As a result, the host galaxy properties of CCSNe are also expected to evolve with redshift which may in turn have an effect on the properties of the CCSN population.

1.4 Photometric Classification of Supernovae

The future of transient science is promising with the advent of new large-scale time domain surveys, most notably the Legacy Survey of Space and Time at the Vera Rubin Observatory (LSST). This survey will image the entire southern sky every 5 nights in *ugrizY* bands and is expected to discover upwards of 10 million SNe (LSST Science Collaboration et al., 2009). While this is exciting in terms of the science questions that can be tackled with this quantity of objects, the vast size of the data-set also presents a number of challenges. The number of SNe that LSST will observe is far in excess of the number that will feasibly be able to receive follow-up spectroscopy. As a result, classification based only on photometry and not spectroscopy will become increasingly vital going forward.

Photometric classification of SNe is an area that has seen significant development over the last decade, particularly with the rise in use of machine learning techniques more generally. The Supernova Photometric Classification Challenge (SNPhotCC; Kessler et al., 2010a,b) was a public challenge which focused on the photometric classification of a variety of SN classes in advance of the Dark Energy Survey (DES), based on a dataset derived from simulations of DES-like observations using the simulation code SNANA (Kessler et al., 2009). A number of different methods were used to approach this including comparing the photometry to light curve templates (Sako et al., 2011),

parametric light curve fits (Karpenka et al., 2013) and semi-supervised learning (Richards et al., 2012).

Since SNPhotCC in 2010, development of these techniques has continued. Preparation for LSST led to another challenge, the Photometric LSST Astronomical Time-series Classification Challenge (PLasTiCC; Hložek et al., 2020), hosted on the Kaggle data science platform in 2018. This challenge involved classifying a three-year simulation of LSST observations, containing approximately 3.5 million transient objects, based on a training set of approximately 8000 labelled objects designed to represent the expected subset of the full sample with spectroscopic classifications which would be obtained in practice. The most successful method in this challenge utilised boosted decision trees (Boone, 2019), composed of an ensemble of separate decision trees (Friedman, 2001). A number of other approaches used neural networks, a form of model composed of interconnected nodes inspired by neurons in the brain (Fitch, 1944). Since the challenge was run, work has continued on developing neural network-based photometric classifiers. Muthukrishna et al. (2019) presented a classifier for transient light curves based on recurrent neural networks (RNNs), a form of neural network designed for sequence classification, and Möller & de Boissière (2019) focused on photometric classification of SNe using RNNs and also Bayesian RNNs, which are better equipped to handle uncertainties. Pasquet et al. (2019) instead used a model based on an alternative neural network architecture known as Convolutional Neural Networks (CNNs). Boone (2021) presented a model designed to create a lower dimensional representation of SN light curves in the rest-frame, which can also be used for photometric classification.

Overall, new photometric classifiers continue to improve in performance. However, much of this work focuses on photometric classification of SNe Ia due to their use in cosmological analysis. Both Muthukrishna et al. (2019) and Boone (2021) perform significantly better on SNe Ia than on CCSNe, and Pasquet et al. (2019) focuses only on the classification of SNe Ia. Although Möller & de Boissière (2019) in fact performs better on CCSNe than SNe Ia when differentiating seven different classes, it still has difficulty in classifying SNe IIP. A key factor which affects the performance of photometric classifiers is the quality of the data-set used to train them. Typically, spectroscopically confirmed SN samples contain more SNe Ia than CCSNe. This is partly because potential SNe Ia are prioritised in follow-up for inclusion in cosmological samples, and party because SNe Ia are on average more luminous than CCSNe which means they are easier to obtain spectra for. In the future, larger samples of CCSN light curves will be required for better training of photometric classifiers to identify them.

1.5 Thesis Outline

In this thesis, I leverage the deep, high quality photometry provided by the Dark Energy Survey Supernova Programme to study the population of CCSNe. The sample of CCSNe provided by DES allows for the construction of a comparatively high-redshift luminosity function for these objects which can be used in simulations going forward, and also allows for the properties of more distant CCSN hosts to be compared to those in more local surveys. I also focus on techniques to improve the performance of photometric classifiers, which will be of great significance for future study of CCSNe.

In Chapter 2, I focus on the key data-sets and methods used in this thesis. I introduce the Dark Energy Survey and the DES-SN survey within it, alongside the OzDES programme for obtaining spectroscopic redshifts of SN host galaxies. I detail the samples of CCSNe and host galaxies from DES-SN and comparison samples from LOSS and ZTF, and describe the steps involved in calculating both SN and galaxy properties.

In Chapter 3, I present the luminosity functions of the CCSN populations in DES, LOSS and ZTF and investigate the possibility that the CCSN luminosity function evolves with redshift by considering what might explain any differences between these samples. I also study the host galaxy properties of these SN samples, comparing their stellar masses and rest-frame colours and investigating differences seen in their colour distributions. I also investigate if there are any relations between SN properties and the properties of its respective host galaxy.

In Chapter 4, I investigate in detail the properties of the unusual SN IIb DES14X2fna which was identified as part of the DES CCSN sample. This object displays a bright peak absolute magnitude and fast decline after peak which is uncharacteristic for a member of its class. I compare this object with other SNe IIb and perform semi-analytic model fits in order to investigate the power source of this object. I also consider the extent to which these objects could act as contaminants of photometric samples of SNe Ia for cosmology.

Chapter 5 switches focus to a related piece of work investigating the possibility of generating synthetic SN light curves using Generative Adversarial Networks (GANs) in order to augment data sets used to train photometric classifiers. I introduce the variety of machine learning techniques currently used within the study of SNe and describe the model I have trained in order to generate light curves.

In Chapter 6, I present the results of the synthetic light curve generation. I compare the physical properties of the generated light curves to those of the samples the models are trained on and consider whether this technique can be used to improve the performance of photometric classifiers.

Finally, in Chapter 7 I summarise the main findings of this work and consider these results within the context of the future of the field.

Chapter 2

Data and Methods

In this chapter I describe the samples and methods that were used for this analysis. I introduce the Dark Energy Survey and the SN programme within it, before detailing the steps involved in calculating the properties of SNe and their respective host galaxies.

2.1 The Dark Energy Survey

In the late 20th century, the discovery of increasing numbers of SNe began to allow for cosmological analysis of type Ia SN samples (Riess et al., 1998; Perlmutter et al., 1999), as discussed in Section 1.2.1. This led to the discovery of the accelerating universe - rather than an expansion that is slowed by gravitational attraction, these studies found that the expansion of the universe was accelerating. No known physical mechanism can explain this and the cause of the acceleration was denoted as 'dark energy' due to its mysterious nature. Understanding the nature of dark energy is one of the biggest open questions in Physics, and was the basis for the Dark Energy Survey (DES).

DES was a six-year optical survey covering $\sim$5100 deg^2 of the southern sky with the aim of constraining cosmological parameters through the study of multiple probes. These included weak gravitational lensing, galaxy clusters, large scale structure and - of relevance here - SNe Ia. DES used the Dark Energy Camera (Flaugher et al., 2015, DECam), a specially designed instrument with a 3 deg^2 field of view and a resolution of 0.263$''$ per pixel which was mounted at the 4 m Blanco Telescope at the Cerro Tololo Inter-American Observatory (CTIO).

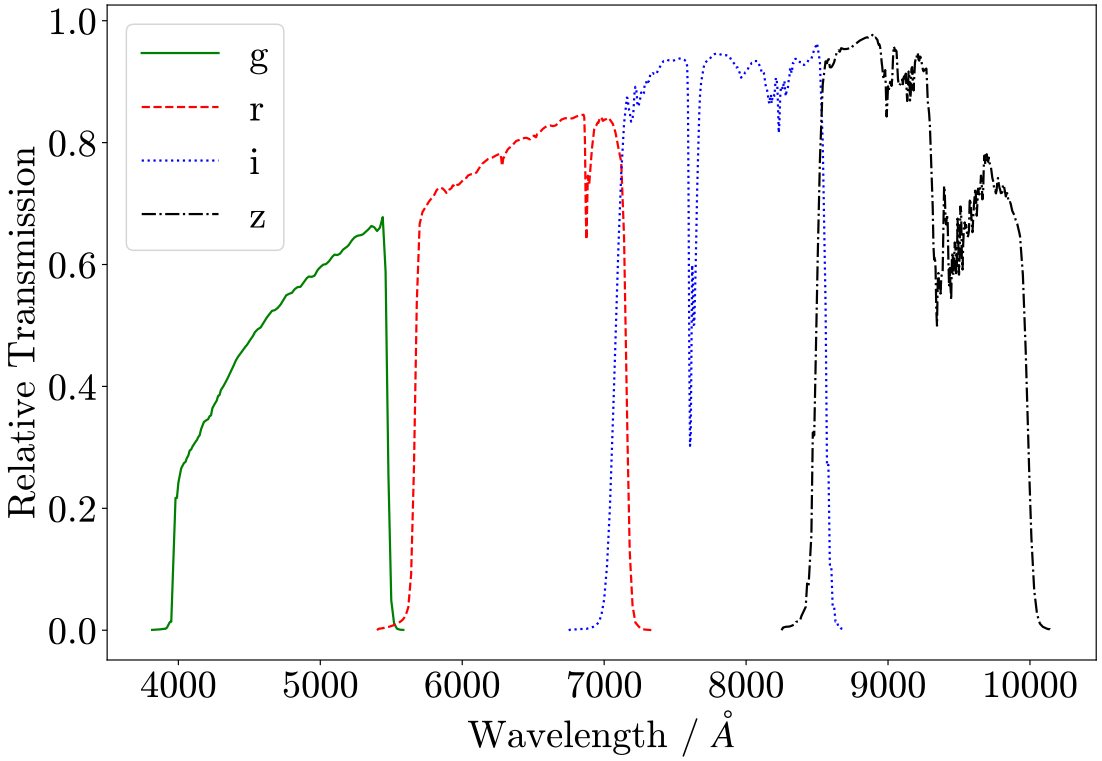

FIGURE 2.1: Filter responses for DES *griz* filters.

2.1.1 DES-SN Programme

One component of DES was the DES SN programme (DES-SN Bernstein et al., 2012). This was a time-domain survey which observed annually for ∼5.5 month observing seasons over five years. DES-SN observed with a mean cadence (interval between observations of the same area of sky) of ≃7 days in *griz* photometric bands – the filter responses of the bands in DES are shown in Figure 2.1. This survey observed 27 deg^2 on the sky over ten different fields, each of which corresponded to a single pointing of DECam. Of these ten fields, eight were 'shallow' (an average single-epoch depth of 23.5 mag) and two were deep (an average single-epoch depth of 24.5 mag).

While DES-SN was designed to detect and measure SNe Ia for cosmological analysis, in practice identified transients encompass a variety of classes including SNe Ia (e.g. Brout et al., 2019a; Brout et al., 2019b), CCSNe (e.g. Gutiérrez et al., 2020; de Jaeger et al., 2020a; Wiseman et al., 2020a), superluminous SNe (e.g. Papadopoulos et al., 2015; Smith et al., 2016; Angus et al., 2019) and rapidly-evolving transients (RETs; e.g. Pursiainen et al., 2018; Wiseman et al., 2020b). Compared with most other previous and ongoing time-domain surveys such as LOSS and ZTF, DES-SN covers a smaller area on the sky but is able to image to a greater depth. This provides two main benefits in terms of the CCSN population: the DES CCSN sample is at higher redshift, allowing for the study of potential redshift evolution of CCSN, and is less affected by Malmquist bias.

After DES exposures are captured but before scientific analysis, they are processed by the DES Data Management team (DESDM; Morganson et al., 2018) - this includes masking known bad pixels, flat fielding, bias subtraction and correction for instrument crosstalk. Any cosmic rays and satellites visible in the image are also masked along with the 'bleed trails' from saturated stars. After processing, these images are fed to the DES-SN Difference Imaging Pipeline (Kessler et al., 2015, DIFFIMG) to identify transient events. DIFFIMG produces a 'difference image' to identify potential candidates by comparing reference images to coadded images in a given band - possible new sources will appear in the difference image, while static sources will be unchanged between new and reference images and therefore will not appear in the difference image.

While this process will identify new transients, many of these candidates are artefacts. A number of quality cuts are applied: objects must have a signal-to-noise greater than 3.5, a point spread function (PSF) consistent with a point source and must be brighter than 30 mag (Kessler et al., 2015). However, even after this numerous false objects pass the cuts - in total, $\sim$ 1.6 million candidate transients passed the pipeline in each season of DES-SN. Traditionally, these candidate objects would be visually inspected individually in order to verify whether they were real transient objects. However, the large number of objects from DES-SN make this impractical and this approach also has the effect of introducing possible human bias on the selection which is difficult to quantify. To avoid these limitations, DES-SN utilised a supervised machine learning classifier (AUTOSCAN; Goldstein et al., 2015) to classify each object as real or fake, which is used to remove a significant fraction of artefacts.

2.1.2 Spectroscopic Follow-up of SNe

Alongside the DES photometric survey, a number of SNe were targeted for spectroscopic followup in order to obtain classifications and allow detailed analysis of their properties. A full summary of the DES-SN Spectroscopy Program is presented in Smith et al. (2020a); the telescopes used for this programme include the Anglo-Australian Telescope (AAT), Gemini, Gran Tescopio Canarias (GTC), Keck, Magellan, MMT, the South African Large Telescope (SALT) and the European Southern Observatory Very Large Telescope (VLT).

Observing time was only available to measure SN spectroscopy for a fraction of the total DES sample. While the survey was ongoing, the photometric classifier Photometric Supernova IDentification (PSNID Sako et al., 2011) was used to give a provisional SN classification; PSNID works by comparing light curves to templates of different SN types to give a probability of belonging to each class, which allows SNe to be targeted for follow-up with a prior indication of their nature. The predicted classes from PSNID were updated after each new epoch of observations. For SNe

which were not targeted for spectroscopic observations, the PSNID output to the full observed light curves can be used to estimate their class.

2.1.3 Host Galaxy Analysis

Alongside the observations of the SNe themselves, DES-SN also involved observations of their host galaxies. A significant reason for this is that host galaxy spectroscopy can be used to measure redshift, even in the absence of spectroscopy of the SN itself. For the context of this thesis, this is of great importance as a redshift allows for distance estimation meaning that the intrinsic luminosity of each SN can be determined. The majority of host galaxy redshifts for DES-SN were measured by the OzDES programme (Yuan et al., 2015; Childress et al., 2017; Lidman et al., 2020) using the AAT. A small fraction of SNe also have host redshifts from other sources including SDSS and external catalogues as summarised in Vincenzi et al. (2021).

In DES-SN, SNe are matched to host galaxies using the directional light radius method (DLR; Sullivan et al., 2006). This method normalises the separation between the SN and the centre of surrounding galaxies by the size of the galaxy along the line between them; the galaxy with the lowest DLR is assigned as the host. The host matching is done based on coadded photometry created by Dr Phil Wiseman, a colleague at Southampton and in DES. This work is presented in detail in Wiseman et al. (2020a), but I will briefly outline it here.

Over the five observing seasons of DES-SN, hundreds of exposures were taken of each of the ten fields. The motivation behind the creation of these coadded images was to combine these exposures to create very deep images of the galaxies in these fields, allowing for precise photometry and observation of faint host galaxies. As part of this process, it is essential to ensure that exposures which are contaminated by light from the SN are excluded to ensure that the images include only galaxy light. As a result, five separate 4-season coadds are created for each filter and SN field which each exclude exposures taken from one of the observing seasons; for a SN which exploded in the second observing season, for example, the coadded host photometry would only include exposures from the first, third, fourth and fifth observing seasons to avoid this contamination. To produce these coadds, a number of quality cuts are applied to each exposure based on instrument noise, atmospheric conditions, the size of the PSF and sky brightness. Exposures which pass these cuts are processed with the DES Image Processing Pipeline (Morganson et al., 2018) and then combined using SWARP (Bertin, 2010). Overall, the deep coadded photometry results in images with typical limiting magnitudes of $\sim$26 mag, reaching $\sim$27 mag in g-band.

TABLE 2.1: Sample sizes for luminosity functions after applying selection criteria.

Survey	Total Sample Size		Sample After Quality Cuts		Sample After Redshift and Magnitude Cuts	
	SNe II	SNe Ibc	SNe II	SNe Ibc	SNe II	SNe Ibc
DES (spectroscopically confirmed CCSNe)	52	18	33	13	31	11
DES (photometric CCSNe with host spec-z)	–	–	56	42	38	39
LOSS	69	36	–	–	37	21
ZTF	349	162	214	105	174	89

2.2 Core-collapse SN Samples

I will now detail the different samples of CCSNe which have been used for this analysis. As discussed in Section 1.1.1, CCSNe comprise a myriad of different subclasses. Throughout this analysis, I will treat CCSNe as two general classes rather than subdividing further. This is to ensure sufficient numbers of SNe in each class, and to acknowledge the uncertainties in the photometric SN classification that are used in the DES-SN sample. I refer to type II SNe to include all hydrogen-rich SNe and type Ibc SNe to include all hydrogen-poor/stripped-envelope SNe. Although SNe IIb, such as the very luminous SN IIb DES14X2fna in the DES-SN sample (discussed in Chapter 4), do show hydrogen features at early times, they also have a partially stripped outer hydrogen envelope and are included with SNe Ibc for this analysis. Table 2.1 contains summary information for each sample.

2.2.1 DES

I begin with the CCSN sample in DES, the main focus of this work. As the goal is to produce luminosity functions for these objects, only SNe which have well-constrained peak luminosities from their light curves and spectroscopic host redshifts are included in the final sample. The sample of observed CCSNe from DES-SN can be split into three general categories based on the available data: those with a spectroscopic classification based on observed spectra of the SN explosion itself, those with only photometric observations but which have a spectroscopic redshift of the host galaxy, and those with photometric observations and only photometric redshift information for the host galaxy. I will now discuss each of these samples in turn.

2.2.1.1 Spectroscopically-confirmed CCSNe

The DES-SN CCSN sample has 70 spectroscopically-confirmed CCSNe between redshifts $0.045 < z < 0.33$. However, not all of these will be suitable for inclusion in a luminosity function. The following selection criteria are applied to ensure that the light curve can be analysed to measure the peak SN brightnesses required for the luminosity function:

- Each SN must have photometric coverage before and after the observed maximum luminosity to ensure an accurate interpolation of the peak luminosity.
- Each object must have a well-constrained explosion epoch inferred either from the date of last non-detection of the SN, or from spectral template matching using the Supernova Identification code (SNID; Blondin & Tonry, 2007) following the prescriptions of Gutiérrez et al. (2017a). An explosion epoch is required to select an appropriate model spectral energy distribution (SED) at each epoch for the K-correction of observed photometry to the rest-frame, as the SED models used are defined with respect to explosion (see Section 2.3.2 for discussion of this). For objects with pre-explosion non-detections, an explosion epoch halfway between the last non-detection and the first detection is assumed.
- Each object must have at least 9 detections which pass AUTOSCAN. A limit of 9 is selected to maximise both the sample size and photometric coverage, as overall this cut eliminates only 4 objects with the next object only having 6 detections.

This selection leaves 46 spectroscopically-confirmed CCSNe in DES. Of these, 33 are spectroscopically hydrogen-rich (type II) and 13 hydrogen-poor/stripped-envelope (type Ibc).

2.2.1.2 Photometric CCSNe with Host Spectroscopic Redshift

A much larger number of transients observed by DES-SN have no spectroscopic confirmation. I next consider the sample of CCSNe in DES which fall into this category which also have a spectroscopic measurement of the SN host galaxy redshift, allowing for distance estimation and inclusion in a luminosity function. To identify this sample, I first apply a number of cuts to the full sample of DES transient candidates to select object that:

- were detected in less than 40 epochs, to remove some obvious AGN.
- were detected in at least 9 epochs which pass AUTOSCAN to ensure good photometric coverage, matching the cut applied to spectroscopically confirmed sample in Section 2.2.1.1.
- have an assigned host galaxy with a spectroscopic redshift less than 0.3 (as an initial redshift cut).
- were single season transients.

which gave a total of 1609 transients. In the absence of spectroscopic confirmation, care must be taken to ensure that object which are not CCSNe are removed from to

analysis to ensure the sample is pure. The following steps are taken to produce the final sample:

- All spectroscopically-confirmed objects are removed from the sample, including CCSNe to avoid duplicates with the sample outlined in Section 2.2.1.1 and other objects that are not CCSNe (e.g. SNe Ia, AGN).
- Remaining AGN are removed from the sample using the classifier discussed in Section 2.2.3 of Wiseman et al. (2020b). This classifier uses a convolutional neural network (CNN) architecture to label input light curves as belonging to either SNe or AGN.
- SNe Ia are removed from the sample using the photometric SN classifier SuperNNova (Möller & de Boissière, 2019), using the trained model discussed in Vincenzi et al. (2022) which has a high degree of accuracy upward of 98 per cent. This model is a binary classifier, returning a probability that a given input light curve is a SN Ia (P_{Ia}). I have followed Wiseman et al. (2021), Möller et al. (2022) and Vincenzi et al. (2022) in treating all objects with P_{Ia} greater than 0.5 as SNe Ia, hence removing them from the sample. It should be noted that in most cases, P_{Ia} is close to 0 or 1 meaning that the results are not sensitive to this threshold.
- For remaining objects, the same quality cuts are applied in terms of requiring coverage pre- and post-peak and a well-constrained explosion date as in Section 2.2.1.1.
- Each of the remaining light curves are visually inspected to ensure they are consistent with CCSNe.
- The remaining objects are classified as SNe II and SNe Ibc using the light curve template fitter pSNid (Sako et al., 2011). As mentioned, the trained SuperNNova model presented in Vincenzi et al. (2022) is highly accurate and is treated in this analysis as reliably removing SNe Ia. There are a few objects which are not considered SNe Ia by this model but are classified as SNe Ia by pSNid. These objects are excluded from the analysis as their true class, either SNe II or Ibc, is uncertain. In addition, some objects are consistent with both SNe II and Ibc and also have an uncertain class so are excluded. In total, 8 SNe are excluded on this basis.

Applying all of these steps, the final sample consists of 98 photometrically-confirmed CCSNe from DES, of which 56 are SNe II and 42 SNe Ibc; combined with spectroscopically-confirmed objects, the total DES CCSN sample with spectroscopic redshifts has 89 SNe II and 55 SNe Ibc. The requirement for constraint of peak

luminosity means that the quality cuts applied are relatively strict, making this sample smaller than might be used for other purposes such as rate calculations.

To assess the suitability of pSNid for these purposes, its performance was evaluated for the full sample of 70 spectroscopically-confirmed SNe in DES; an estimated pSNid class was obtained for 69 of these. For SNe II, there are 8 misclassifications out of 51 - 6 are classified as SNe Ia and 2 as SNe Ibc by pSNid. For SNe Ibc, there are 2 misclassifications out of 18 objects, with one misclassified as a SN Ia and one as a SN II. This gives accuracy for these classes of 84 and 89 per cent respectively and an overall accuracy of 86 per cent.

2.2.1.3 Photometric CCSNe with Host Photometric Redshift

Beyond the sample of CCSNe with spectroscopic host redshifts, there are a number of CCSNe in DES with no spectroscopic information, for example because the host was too faint to take a reliable spectrum. While these objects cannot be included in luminosity functions, it is important to understand any selection effects that arise from excluding these objects from the sample.

Photometric redshifts have been produced for three of the ten DES-SN fields from coadded photometry as outlined in Hartley et al. (2022), based on the photometric redshift fitting code EAzY (Brammer et al., 2008). To produce a sample of DES CCSNe without spectroscopic host redshifts, I repeat the selection process outlined in Section 2.2.1.2 except this time including only SNe which do not have spectroscopic host redshifts. As the photometric redshifts have large uncertainties, the number of objects in this sample which overlap with the rest of the sample in redshift is uncertain.

For this sample, the data includes the 0.5th, 2.5th, 16th, 84th, 97.5th and 99.5th percentiles of the photometric redshift distribution; the maximum possible sample size is based on the whether the 0.5th percentile overlaps with the redshift range of the rest of the sample. For a redshift cut at 0.25 (the final redshift cut applied for this work, see Section 2.3.4), the sample contains a maximum of 25 CCSNe. Studying the cumulative distributions of these values shows the distribution to be approximately Gaussian. Figure 2.2 shows the percentiles mentioned above, along with a generalised error function that has been fitted to estimate the mean and standard deviation of these distributions, for four example host galaxies within the sample. As these fits align well with the data, I opt to model these photometric redshift distributions as Gaussian distributions with the mean and standard deviation estimated from the fitting process.

Using a Monte Carlo process, the likely sample size is estimated by drawing randomised redshifts from these distributions for each SN in the sample 10,000 times. Overall, this sample typically varies between 3 and 8. Extrapolating this to cover all ten of the DES fields, this indicates that there are expected to be between 10–27 CCSNe

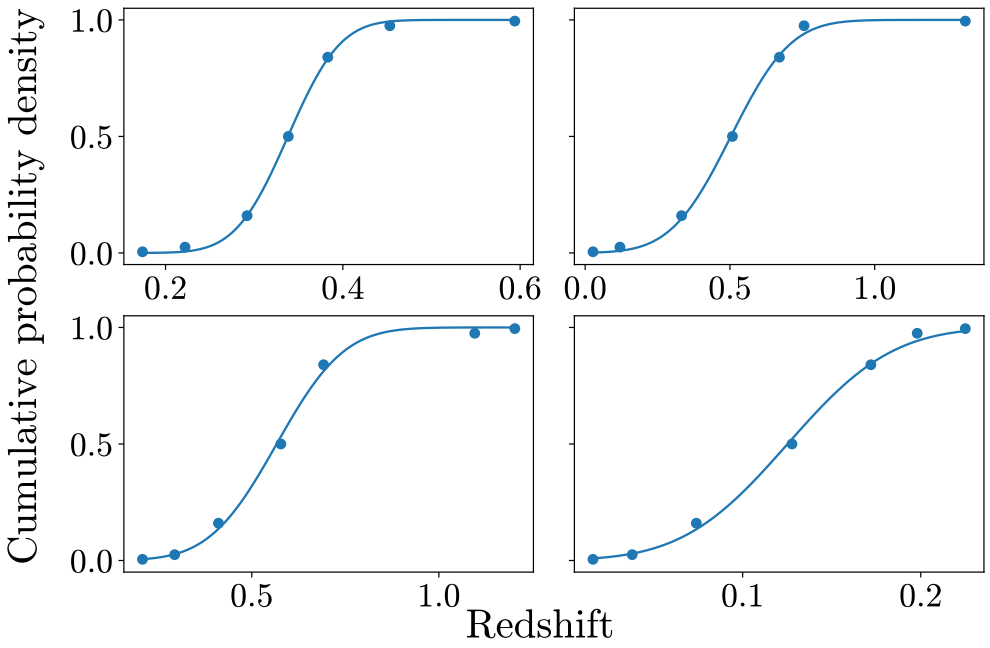

FIGURE 2.2: Four examples of photometric redshift distributions for SN host galaxies in DES. Data points represent the 0.5th, 2.5th, 16th, 84th, 97.5th and 99.5th percentiles of the distributions, while the line shows a generalised error function that has been fit to these distributions in order to estimate their mean and standard deviation.

without host spectroscopic redshifts which suggests that spectroscopic host redshifts are obtained for $\sim 75-90$ per cent of CCSNe observed by DES. This sample of SNe with photometric redshifts is used only for selection efficiency checks.

2.2.2 Comparison Samples

As discussed in Section 1.3, the deep nature of DES allows for a comparison with other, more local luminosity functions to examine whether there is any evolution in the CCSN population with redshift.

Of the previously published work looking at peak luminosities of CCSNe, I have elected to compare only with the sample from L11 and not from Richardson et al. (2014). This is because the sample presented in the latter work is from a wide variety of different instruments and surveys which makes it very difficult to correct for Malmquist bias based on the limiting magnitude of each survey as I have done here (see Section 2.3.5). I also do not include the sample of SNe Ibc from Drout et al. (2011) as these objects are all brighter than -17.5, suggesting that this sample only includes the most intrinsically luminous events making it unsuitable for a comparison. Finally, the CCCP samples of SNe II and IIn presented in Arcavi et al. (2012) and Kiewe et al. (2012) have not been included due to the small sample size – combined, these samples

include only 12 CCSNe with estimates of peak absolute magnitudes, with a further 9 having only absolute magnitudes of the plateau phase of a SN II rather than peak and 5 have only lower limits for the peak.

To allow for further comparison with other samples, I have also examined a sample from the Zwicky Transient Facility (ZTF). I will now discuss each of the samples from LOSS and ZTF.

2.2.2.1 LOSS

LOSS was a local, galaxy-targeted SN survey which ran from 1998 to 2008. The LOSS sample comprises a total of 929 SNe, of which 917 are spectroscopically classified (Leaman et al., 2011). L11 presents luminosity function of different SN subtypes in LOSS; I have re-categorised these into the broader labels of SNe II and SNe Ibc. Note that L11 includes SNe IIb with SNe II rather than SNe Ibc, hence the LOSS luminosity functions presented here will differ slightly from L11. With this classification scheme the LOSS sample contains 105 CCSNe: 69 SNe II and 36 SNe Ibc. It should be noted that Shivvers et al. (2017) revisits the classification of the LOSS sample, with some object classes modified from L11. However, as I am using broad labels of SNe II and Ibc, in all cases the new class falls into the same category as the original. In Shivvers et al. (2017), there are a small number of SNe which show hydrogen lines with only a single spectrum which are presented as having an uncertain class of either SN II or SN IIb. I have classed these objects as SNe II as robust classification of a SN IIb requires multiple spectra showing the transition from hydrogen to helium.

Note that for this analysis I correct the LOSS absolute magnitudes presented in L11 from $H_0 = 73$ km s^{-1} Mpc^{-1} to $H_0 = 70$ km s^{-1} Mpc^{-1} and also convert from Vega to AB magnitudes using conversions from Blanton & Roweis (2007).

2.2.2.2 ZTF

The Zwicky Transient Facility (ZTF) is an ongoing automated, rolling SN search. Perley et al. (2020) presents a public catalogue of transients from the ZTF Bright Transient Survey with spectroscopic classifications. Excluding SNe Ia and super-luminous SNe, this sample consists of 511 CCSNe. For all of these objects, I gather publicly-available g and r-band photometry from the Lasair[1] transient broker (Smith et al., 2019). The final sample is selected by applying the same cuts as for the DES sample, only including objects with photometric coverage both pre- and post-peak in both bands and with a well-constrained explosion date. This leaves a

[1] Available at `https://lasair.roe.ac.uk/`

sample of 319 CCSNe from ZTF: 214 SNe II and 105 SNe Ibc, applying the broad classifications described earlier.

2.3 Calculating Luminosity Functions

I have now described the samples used throughout this thesis. I will next describe how the luminosity functions were constructed for the DES and ZTF samples; for LOSS, I have used the published luminosity functions from L11.

2.3.1 Gaussian Processes

I will begin by introducing Gaussian Process (GP) regression, a technique I make extensive use of throughout this work in order to interpolate observed light curves and calculate the peak absolute magnitudes of SNe.

GPs are a data-driven, non-parametric approach to fitting observations. Rather than trying to fit a specific functional form to data, GPs instead consider the distribution of possible functions which could match the data – this distribution of functions is treated as a normal distribution, and any finite subset of the full distribution can be described as a multivariate Gaussian. GPs consist of two separate components, a mean function $\mu(x)$ and an additional function known as a 'kernel' $k(x, x')$ with an overall function given by

$$f(x) = GP(\mu(x), k(x, x')). \tag{2.1}$$

Each point in the reconstructed function $f(x)$ is treated as a normal distribution and the relation between neighbouring points is described by the kernel. The principle behind GPs is that the exact functional form of $f(x)$ is unknown but must lie within the full distribution of possible function. The mean function $\mu(x)$ therefore represents the mean value from which the distribution of possible different functions is drawn from. The kernel $k(x, x')$, meanwhile, describes the covariance between neighbouring data points x and x'. For a given kernel, GP interpolation can be used to estimate a continuous function $f(x)$, with an associated uncertainty, from which the observed data is sampled.

For this work I follow Angus et al. (2016) in using a Matern 3/2 kernel when using GPs to interpolate DES light curves; this kernel has the form

$$k(r) = \sigma^2 \Big(1 + \frac{\sqrt{3}r}{l}\Big) \exp\Big(\frac{-\sqrt{3}r}{l}\Big) \tag{2.2}$$

where σ is the uncertainty of a given observation, r is the separation between observations and l is the characteristic length scale over which the data varies.

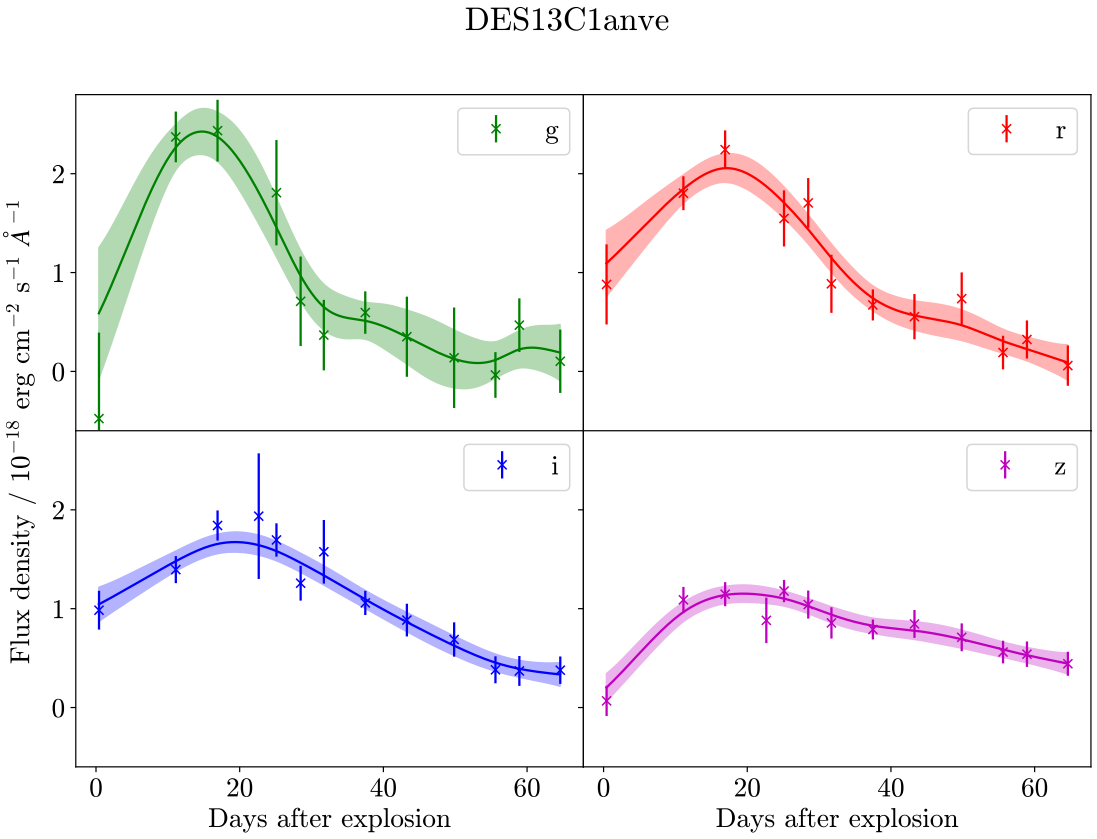

FIGURE 2.3: An example of GP interpolation applied to the observed *griz* photometry of DES13C1anve, corrected for Milky Way extinction.

With this kernel, the interpolated light curve is dependent on the value of the hyperparameter l; a large value of l will give a smoother interpolation but may fail to capture the shorter term changes in the light curve, while a small value of l will capture these shorter term changes but may introduce additional unphysical variations in the interpolation. When using GP interpolation, I optimise the value of l by finding the value which maximises the log-likelihood of the interpolated light curve compared to the observed data. This is done independently for each of *griz* bands for each SN in the sample.

DES-SN provides photometry for SNe in DES for five different observing seasons. In theory, it is possible to use GP interpolation to cover all available data including negative flux values which arise from difference imaging. However, I have found that including non-detections as part of the GP interpolation leads to unphysical undulations in the early light curve. As a result, for this work I have included only observations after explosion and from the first observing season featuring the SN – the GP interpolation is only applied during the SN explosion. Fig. 2.3 shows an example of a GP interpolation to the observed *griz* photometry of DES13C1anve, corrected for Milky Way extinction.

2.3.2 Photometry, Synthetic Magnitudes and K-correction

I will now describe the related processes of calculating synthetic magnitudes and K-correction, which are also used in calculating the luminosity functions. The intensity of the electromagnetic radiation emitted by a source can be described by its SED, which is defined as the energy emitted per unit area, time and wavelength or frequency and is commonly referred to as the flux density. In the frame of the source, the emitted SED in wavelength space is described by $f_\lambda(\lambda_e)$ where λ_e is the rest-frame wavelength. In the frame of an observer, this SED is reduced in intensity as the emitted radiation is distributed over a much larger area but in addition, redshifting effects due to the expansion of the universe mean that the observer will sample this SED at a different wavelength $\lambda_o = (1+z)\lambda_e$ where z is the redshift of the source; the observed SED is described by $g_\lambda(\lambda_o)$. When this SED is sampled in the observer frame using a broad-band filter with a response given by $R(\lambda)$, the flux density measured is given by:

$$F_\lambda = \frac{\int \lambda_o f_\lambda(\lambda_o) R(\lambda_o) d\lambda_o}{\int \lambda_o R(\lambda_o) d\lambda_o}. \tag{2.3}$$

Typically, flux densities are converted to magnitudes which normalise the observed flux density to some reference source $z(\lambda)$. The magnitude is then given by:

$$m = -2.5 \log \left(\frac{\int \lambda_o f_\lambda(\lambda_o) R(\lambda_o) d\lambda_o}{\int \lambda_o z_\lambda(\lambda_o) R(\lambda_o) d\lambda_o} \right). \tag{2.4}$$

A number of different reference sources can be used for $z_\lambda(\lambda)$. For this work I use the AB magnitude system where the reference source is a theoretical source with a constant flux density in frequency space of $z_\nu = 3631$ Jy; in wavelength space, this corresponds to a flux density of $z_\lambda = c\lambda^{-2} \times 3631$ Jy.

Given a model SED, these equations can be used to calculate the observed broad-band photometry corresponding to that SED. As mentioned, redshifting due to the expansion of the universe means that the wavelength observed when studying a source is not the same as the emitted wavelength. This means that observer-frame photometry in broad-band filters from sources at different redshifts is not directly comparable since these observations correspond to different wavelength. However, given a model SED of the radiation emitted by each source in the rest-frame ($L_\lambda(\lambda_e)$ it is possible to use these techniques to calculate the correction that needs to be applied to observer-frame photometry to correct it into the rest frame. This correction is known as the K-correction and is given by the following expression:

$$K_{QR} = -2.5 \log \left(\frac{1}{1+z} \frac{\int \lambda_o L_\lambda(\frac{\lambda_o}{1+z}) R(\lambda_o) d\lambda_o \int \lambda_e g_\lambda^Q(\lambda_e) Q(\lambda_e) d\lambda_e}{\int \lambda_o g_\lambda^R(\lambda_o) R(\lambda_o) d\lambda_o \int \lambda_e L_\lambda(\lambda_e) Q(\lambda_e) d\lambda_e} \right) \tag{2.5}$$

where Q and R denote the rest and observer-frame filters respectively, K_{QR} is the correction in mags to convert from one band to the other and g_λ^R and g_λ^Q refer to the reference SEDs used for each band. The factor of $\frac{1}{1+z}$ comes about because redshifting of emitted photons also means that they are observed with a different energy in the observer frame compared to the rest frame. Throughout this analysis I use the K-correction to correct from observed photometry in *griz* bands for DES and *gr* bands for ZTF into rest-frame Bessell filters.

2.3.3 Calculating Peak Absolute Magnitudes

Having described the process of GP interpolation and K-correction, I will now detail the steps involved in calculating the peak absolute magnitudes of the SNe in these samples. This procedure is described as follows:

1. First, the observed photometry is corrected for Milky Way extinction using the dust maps presented in Schlegel et al. (1998) and re-calibrated in Schlafly & Finkbeiner (2011), assuming $R_V = 3.1$.

2. This photometry is interpolated in flux space using GPs to obtain observations at the same time in all photometric bands (*griz* in the case of DES, *gr* for ZTF) following the process outlined in Section 2.3.1. While in most cases observations in different bands are measured at very similar times, in some cases a given band is missing an observation at a given epoch. Simultaneous observations across all bands are necessary for the next step of the process.

3. The next step is to K-correct this interpolated photometry to the rest-frame. This was done using SED models for SNe II from Dessart et al. (2013)[2] and for SNe Ibc from Levan et al. (2005)[3]. These give time series of SED models with phases defined with respect to explosion. At each epoch of the interpolated light curve, I linearly interpolate the SED time series to obtain the corresponding model SED at that epoch. This model SED is then calibrated to match the colour of the photometry at that epoch, and this final spectrum is used to K-correct the photometry in each band to the rest-frame.

4. The K-corrected rest-frame photometry is interpolated using GPs to estimate the peak flux of each object along with its associated uncertainty. This peak flux is then converted to an apparent magnitude, and subsequently an absolute

[2] Available at `https://www-n.oca.eu/supernova/home.html`
[3] Available at `https://c3.lbl.gov/nugent/nugent_templates.html`

magnitude based on the distance modulus to the measured spectroscopic of the SN in the assumed cosmology for this work.

These steps were used to calculate the peak absolute magnitude in rest-frame *R*-band for each SN in the DES and ZTF samples. For this work, I have used general SNe Ibc SED models rather than separate SED templates for different classes of SESNe. This was necessary given that the photometric classification techniques I have used are unable to differentiate SN classes further than this, however this will introduce some additional uncertainty into the analysis. Nevertheless, the calibration of the SED models to match the colour of the observed photometry will mitigate for this and overall this effect will be small.

2.3.4 Redshift and Absolute Magnitude Cuts

After calculating the peak absolute magnitudes for DES and ZTF, I also make a number of additional selection cuts. The absolute magnitude limit of these combined samples is set by DES as it is the highest redshift survey and thus shallowest in terms of absolute magnitude: objects with a peak absolute magnitude fainter than -16 mag in *R*-band have been excluded since DES is not sensitive to these objects. SNe brighter than -19.5 mag are also excluded to ensure a like-for-like comparison between the samples as these are only present in ZTF.

In addition to this, I make a redshift selection for DES of $z < 0.25$ to obtain a volume-limited sample above this absolute magnitude limit, and similarly use a redshift selection for the ZTF sample of $z < 0.06$. This minimises the overlap in redshift between the DES and ZTF samples. This leaves 69 SNe II and 58 SNe Ibc in DES, 37 SNe II and 21 SNe Ibc in LOSS, and 177 SNe II and 89 SNe Ibc in ZTF, as detailed in Table 2.1.

The final samples are shown in Fig. 2.4, including those objects removed by the selection on absolute magnitude. This plot demonstrates that Malmquist bias (i.e. bias towards more luminous objects at higher redshifts; Malmquist, 1922) is seen in these samples. The ZTF sample in particular shows a strong trend towards more luminous SNe at higher redshift - the redshift cut at 0.25 and greater depth of DES means that it is less affected by this, while the local nature of LOSS means that this sample has good completeness over the absolute magnitude range focused on here.

2.3.5 Correcting for Malmquist Bias

When considering luminosity functions, it is important to take into account the effect that Malmquist bias will have on the sample; at higher redshifts, a magnitude limited

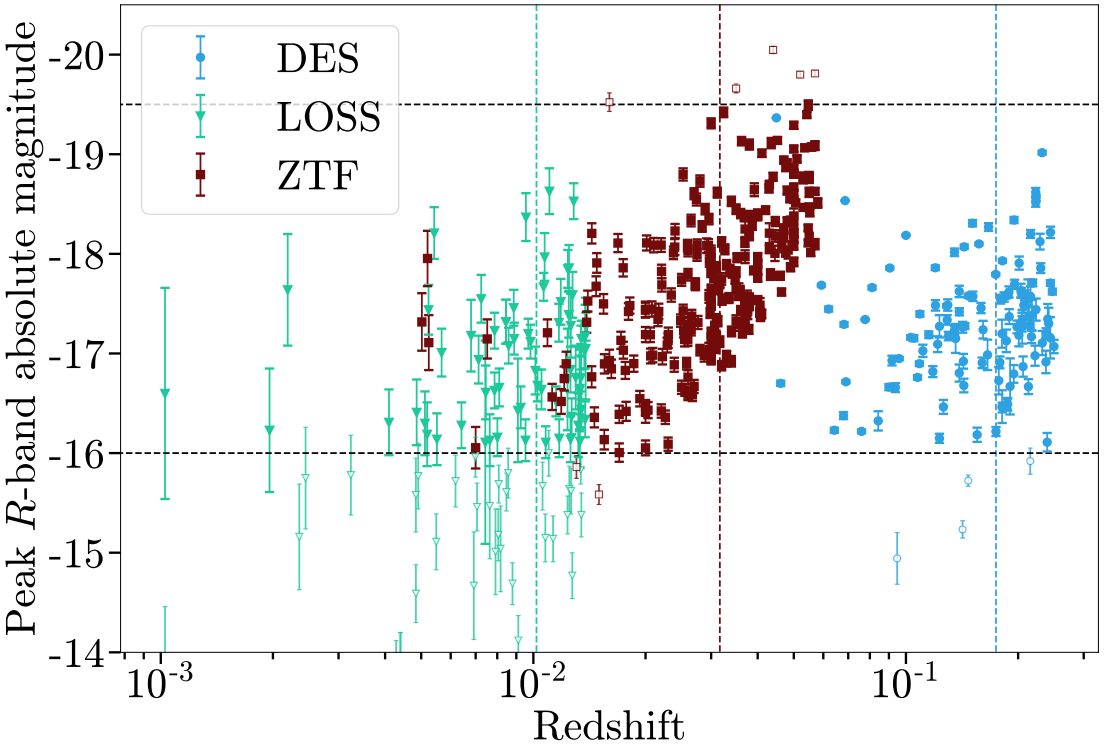

FIGURE 2.4: Peak rest-frame CCSN R-band absolute magnitude, corrected for Milky Way extinction, plotted against redshift for the DES, LOSS and ZTF CCSN samples. Vertical dashed lines indicate the median redshift of each SN sample, while horizontal dashed lines represent the bounds of the absolute magnitude selection cut applied. Closed circles denote SNe included in the final samples and open circles are SNe excluded by the cut.

sample will become biased towards more intrinsically luminous objects since fainter objects will drop below the detection limit of the instrument which observed the sample. This effect must be mitigated for in a luminosity function.

One approach is to take a low redshift cut to restrict the sample to only the region over which it is complete where Malmquist bias does not have an effect. However, this is not desirable as it involves discarding a large proportion of the sample at the brighter end of the luminosity function. In this work, I mitigate for the effect of Malmquist bias using a simple $V_{\rm max}$ correction (Schmidt, 1968; Felten, 1976). This weights fainter objects, which would not be detected over the full survey volume, higher in the luminosity function calculation while preserving the full population of brighter objects. For a volume-limited sample with an upper redshift limit $z_{\rm survey}$, each SN has an upper redshift limit $z_{\rm max}$, beyond which the object would fall below the detection limit of the survey. The weight w each object in the luminosity function is calculated as

$$w = \begin{cases} \left(\frac{d_c(z_{\rm survey})}{d_c(z_{\rm max})}\right)^3 & \text{if } z_{\rm max} < z_{\rm survey} \\ 1 & \text{otherwise} \end{cases} \tag{2.6}$$

where d_c is the comoving distance. Thus, an intrinsically luminous SN that could have been detected over the full survey volume is given a weight of 1, while a fainter SN is assigned an increased weight.

This approach makes the assumption that each survey has a single magnitude limit above which it is complete whereas in reality completeness in SN surveys is more complex than a simple cut-off, and thus this assumption introduces some uncertainty in the analysis. For the DES sample, the magnitude limits used are $m = 23.5$ and $m = 24.5$ for the shallow and deep fields respectively (Kessler et al., 2015). For the ZTF sample, (Perley et al., 2020) quotes the 97, 93 and 75 per cent spectroscopic completeness limits of 18, 18.5 and 19 mag respectively. I elect to use the 75 per cent completeness limit of 19 mag as the magnitude limit in this analysis. These choices for DES and ZTF, and the impact they have on the results, are discussed further in Section 3.1.2. Finally, for the LOSS sample I do consider making a $V_{\rm max}$ correction but find that the sample is complete in the absolute magnitude range that is used for this analysis meaning that this correction is not needed.

2.4 Calculating Host Galaxy Properties

In addition to studying the luminosity functions of CCSNe, in this work I also analyse the population demographics of their host galaxies. In this section I will describe how the host galaxy properties are calculated for each of the DES, LOSS and ZTF samples.

2.4.1 SED Fitting

I will begin by outlining the method used to estimate host galaxy properties in this work; this involved fitting the SED of these galaxies using photometric observations. The SED fits in this work were run by my supervisor, Prof Mark Sullivan, based on the fitting code outlined in Sullivan et al. (2006); Sullivan et al. (2010).

The SED of a galaxy describes the energy emitted by a galaxy as a function of wavelength and is affected by a number of different galaxy properties including its star formation history, gas context and stellar population properties including mass, metallicity and age. The principle behind SED fitting is that these properties can be estimated by finding the set of values which produces a galaxy SED that best matches observed photometry. This can be broken down into a two-step process; creating template galaxy SEDs for different galaxy properties, and then fitting these templates to observed galaxy photometry in order to find the best fitting templates. Template SEDs are created using the following process:

- First, an initial mass function (IMF) is assumed; this is the initial mass distribution of stars immediately after star formation. The SED fits used in this work assume an IMF following Chabrier (2003).
- A star formation history is also assumed, which describes how the star formation rate of the galaxy varies with time. This work assumes an exponential star formation history with SFR(t)$\propto \exp(-t/\tau)$ where t is the galaxy age and τ is the e-folding time.
- By using simulated SEDs of stars of the same age, the IMF can be used to create a model SED for a population of single-age stars known as a simple stellar population (SSP). This work uses SSP models from PÉGASE.2 (Fioc & Rocca-Volmerange, 1997, 2019).
- Combinations of SSP models are convolved with the star formation history to create model SEDs for the entire stellar population of a galaxy; this is known as a composite stellar population (CSP).
- Dust extinction is then applied using a foreground dust screen with $E(B-V)$ values from 0 to 0.30 in steps of 0.05.
- Through different combinations of values for parameters such as t, τ and $E(B-V)$ a large number of different SED templates are created for galaxies of different properties.

Each template SED is then integrated over the filter responses of the observed photometric bands, which allows the templates to be compared with observed photometry of the galaxy. χ^2 minimisation is applied to find the template which best matches observations and therefore determine the properties of the galaxy.

This method can be used to calculate a number of galaxy properties, including stellar mass and star formation rate (SFR). Stellar masses calculated using SED fits are commonly used in SN studies (e.g. Sullivan et al., 2010; Galbany et al., 2018; Wiseman et al., 2020a), however SFRs calculated using this approach are less reliable (Sullivan et al., 2010). Rest-frame galaxy colours can also be calculated from the best-fit template SED and are much better constrained using this method than SFR. Colour can be used to give an indication of the properties of the galaxy; rest-frame $U-R$ colour correlates with morphology and traces star formation (Lintott et al., 2008; Trayford et al., 2016). As a result, for this work I opt to use $U-R$ colour as a proxy for star formation rather than using SFR values directly.

2.4.2 Host Galaxy Samples

I will now introduce the host galaxy samples used for each of DES, LOSS and ZTF.

2.4.2.1 DES

As discussed in Section 2.1.3, DES SNe are matched to their respective host galaxies using the DLR method, based on the coadded photometry presented in Wiseman et al. (2020a). This work provides *griz* photometry for all the host galaxies in the DES sample. I correct this host photometry for Milky Way extinction similarly to the SN photometry, using the dust maps presented in Schlegel et al. (1998) and re-calibrated in Schlafly & Finkbeiner (2011) assuming $R_V = 3.1$. Having obtained host galaxy photometry for the DES CCSN sample, host properties were estimated using the SED fitting procedure outlined in Section 2.4.1.

2.4.2.2 LOSS

L11 presents host galaxy masses using K and B-band mass-to-luminosity ratios, and Graur et al. (2017a) presents stellar mass and SFR values for LOSS hosts from Sloan Digital Sky Survey (SDSS, Blanton et al., 2017) spectroscopy. In addition, the majority of LOSS hosts have stellar mass and SFRs calculated in the literature using a variety of different methods, including using near-infrared and far-ultraviolet flux (Leroy et al., 2019; Karachentseva et al., 2020). However, to ensure consistency between the host properties calculated across different samples I opt to recalculate host properties for the LOSS sample using the same SED fitting procedure as outlined in Section 2.4.1.

Each SN in LOSS is already matched to a host galaxy in Table 4 of Leaman et al. (2011); in order to obtain photometry of these hosts for the SED fitting process, I match them to corresponding SDSS galaxies. Out of 58 CCSNe in the LOSS sample, 30 fall in the SDSS footprint and we are able to match to an SDSS host for 26 of these. The SDSS galaxy catalogues provide *ugriz* photometry for all of these hosts which were used for the same SED fitting process as for DES.

To assess the quality of the host properties derived from these SED fits, I compare the valued obtained with previous work. Fig. 2.5 shows stellar mass and SFR values from these SED fits compared with stellar masses derived from B and K-band mass-to-luminosity ratios presented in L11 and stellar masses and SFRs presented in Leroy et al. (2019) and Karachentseva et al. (2020). Overall, the stellar masses from SED fits are consistent with those from other techniques but there is significant scatter in the SFR values from SED fits compared with literature. This provides further justification for the decision outlined in Section 2.4.2.1 to focus on rest-frame colour as a proxy for star formation.

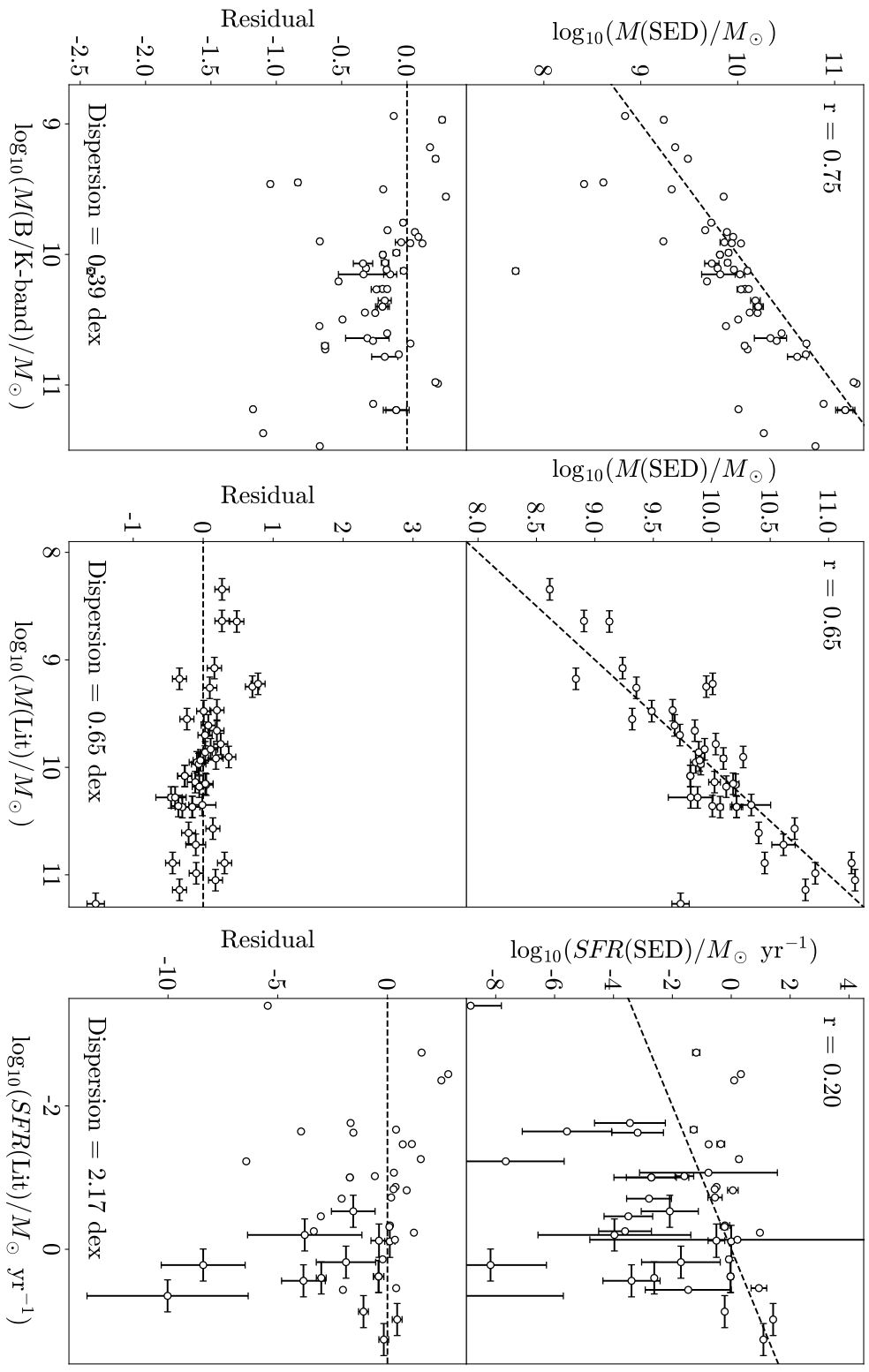

FIGURE 2.5: **Upper panels:** Host galaxy stellar masses and SFRs for LOSS from SED fits to SDSS *ugriz* photometry compared with stellar masses derived from the *K*-band mass-to-luminosity ratio presented in L11 and with stellar masses and SFRs presented in Leroy et al. (2019) and Karachentseva et al. (2020). Correlation coefficients are shown, and the dashed line shows a perfect agreement. **Lower panels:** Residuals from the perfect agreement in the upper panels.

2.4.2.3 ZTF

Host properties are also calculated for the ZTF sample. Unlike for LOSS, CCSNe in the ZTF sample are not already matched to their respective host galaxy. The SDSS galaxy catalogue does not contain ellipse parameters corresponding to the photometry of the host meaning that it is not possible to use the DLR method for these objects. Instead, ZTF SNe are matched to the closest SDSS galaxy using a broad search radius of 50″[4] radius around the SN position, matching to the closest galaxy and then visually confirming the matches. Out of the 263 CCSNe in the ZTF sample, 212 objects lie within the SDSS footprint and 203 of these are matched to an SDSS host galaxy. Using the *ugriz* photometry from SDSS, the same SED fitting process as used for the DES and LOSS samples is used to estimate host galaxy properties for the ZTF sample.

2.5 Summary

In this chapter I have detailed the samples and methods which will be the main focus of this thesis. I have introduced DES, DES-SN and the spectroscopic follow-up programme OzDES, and outlined the different samples of CCSNe available from DES-SN based on the variety of data types available. I have also introduced comparison samples of CCSNe from LOSS and ZTF which will be included in the analysis. Having introduced the samples, I described the quality cuts and steps involved in calculating luminosity functions for SNe within DES-SN and ZTF, as well as detailing how host galaxy properties were calculated for each of the three samples.

In the next chapter, I present the first piece of scientific analysis; presentation of the DES luminosity functions and comparisons with those from LOSS and ZTF.

[4]This was set to a large value to ensure that large, local galaxies were matched correctly

Chapter 3

Core-collapse Luminosity Functions and Host Galaxy Demographics

As discussed in Chapter 1, the deep photometry acquired by DES-SN provides a perfect sample of objects with which to derive luminosity functions of CCSNe at higher redshifts than previous work - these can help to constrain the physics of the explosion mechanism and be used in future simulations. In addition, SNe can also be probed by studying the properties of the environment in which they exploded: their host galaxy. Chapter 2 gives a detailed overview of the steps involved in calculating a luminosity function from observed photometry and using SED fits to calculate host galaxy properties. In this chapter, I present the luminosity functions for the DES, LOSS and ZTF samples. I also examine the host galaxy demographics of SNe in these samples and study any relations between SN and host properties.

3.1 Comparison of Luminosity Functions

I will begin by presenting the DES luminosity functions and comparing them with LOSS and ZTF, as well as justifying the assumptions made in correcting for Malmquist bias as outlined in Section 2.3.5.

3.1.1 CCSN luminosity functions

The left two panels of Figure 3.1 shows the SN II luminosity functions for each of the DES, LOSS and ZTF samples. Histogram uncertainties in the upper panel are derived from Poisson distribution confidence limits presented in Gehrels (1986), while the cumulative density function (CDF) uncertainties in the lower panel are estimated from a Monte Carlo (MC) approach described as follows:

TABLE 3.1: Two-sample KS tests between the SN II and SN Ibc luminosity functions.

Survey 1	Survey 2	KS test significance	
		SNe II	SNe Ibc
DES	LOSS	3.0σ	1.9σ
DES	ZTF	1.8σ	1.1σ
LOSS	ZTF	2.5σ	1.8σ

- The measured values of peak absolute magnitude and their uncertainties are used as the mean and standard deviations of a Gaussian distribution.
- 1000 randomised CDFs are generated using the Gaussian distribution of each data point.
- The mean and standard deviation of the CDFs at each value are calculated – these are the values and uncertainties plotted.

Uncertainties here will depend on both the uncertainty of the luminosity of each SN and also on the sample size, as for a smaller sample changing an individual measurement will have a larger effect on the CDF. As can be seen, LOSS overall has a larger uncertainty in the CDF than DES in this figure. This is because DES photometry has lower uncertainties than LOSS photometry, meaning that the Gaussian distributions of each point are narrower.

In order to investigate any differences present between the luminosity functions of the different samples, I perform two-sample Kolmogorov–Smirnov (KS) tests between the different samples. The weighting provided by the $V_{\max}$ correction has been incorporated into these tests by modifying the cumulative distributions of the different luminosity functions so that they are given by:

$$C(M_n) = \frac{\sum_{i=1}^{n} w_i}{\sum_{i=1}^{N} w_i}, \tag{3.1}$$

where $C(M_n)$ is the cumulative density up to absolute magnitude M, n and i represent index positions in the sorted distribution of M values and N is the total number of objects. The results of these weighted two-sample KS tests are shown in Table 3.1, with the p-values converted to a significance in σ. Overall, the DES sample appears brighter than LOSS and differs at a significance level of 3.0σ. DES also appears brighter than ZTF, although only differs at a significance level of 1.8σ. The ZTF sample is also brighter than LOSS, with the difference between them significant at 2.5σ.

The right two panels of Figure 3.1 shows the luminosity function of SNe Ibc in DES, ZTF and LOSS. The LOSS and ZTF samples are consistent with each other. DES appears slightly more luminous than both although not at high significance (1.9σ and 1.1σ).

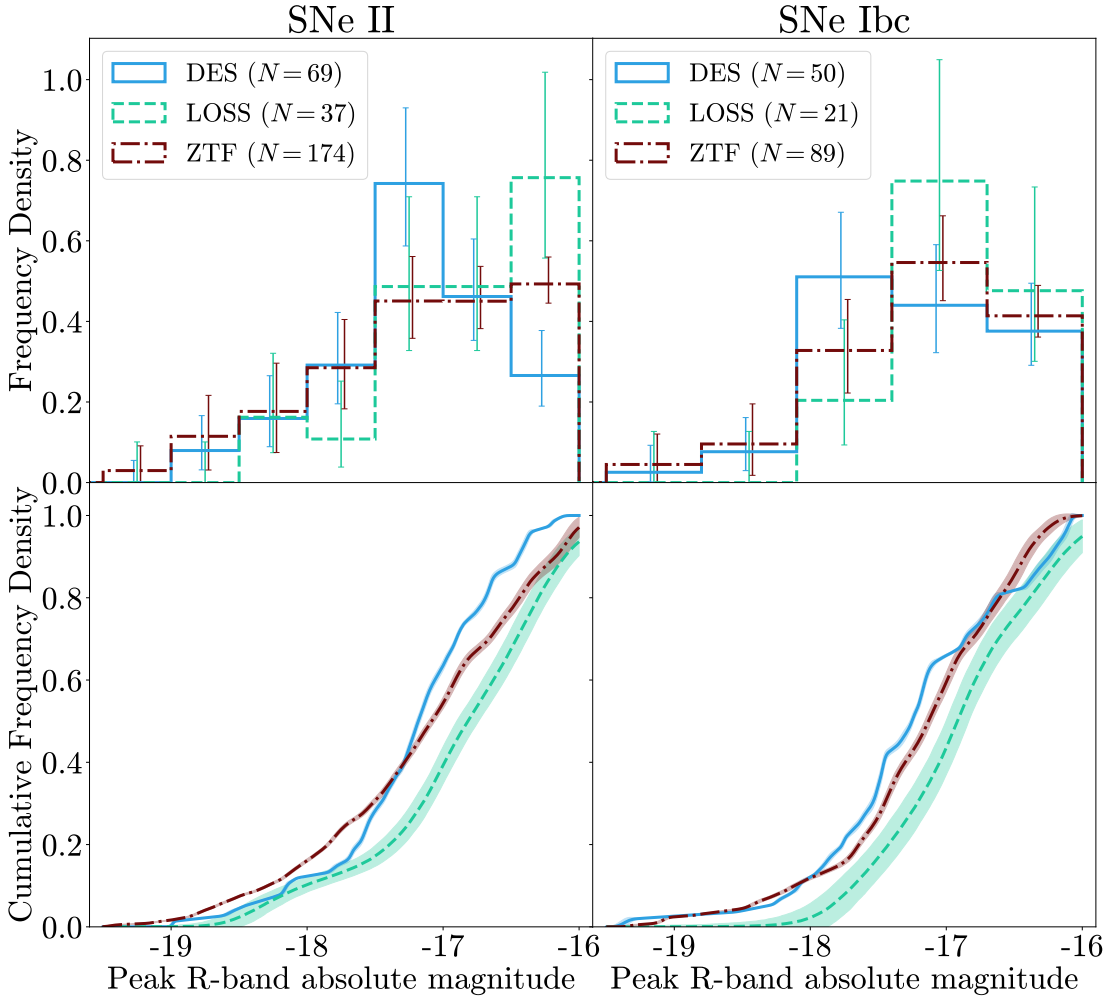

FIGURE 3.1: SNe II and Ibc *R*-band luminosity functions for the DES, LOSS and ZTF samples. Each event has been weighted by equation 2.6 (V_{max} correction). Histogram uncertainties are from the Poisson distribution confidence limits of Gehrels (1986), while CDF uncertainties are derived from a Monte Carlo approach based on the measurement uncertainty of each value.

3.1.2 Assessing Vmax Correction

As discussed in Section 2.3.5, I correct for the effect of Malmquist bias on the luminosity function using a V_{max} correction. This correction involves the assumption that each survey has a single apparent magnitude which defines the completeness limit, which is not the case in reality. LOSS is complete over the magnitude range studied here meaning that this correction does not have an effect. For DES, this limit was set to 23.5 mag for shallow fields and 24.5 mag for deep fields. For ZTF, this limit was set to 19 mag. I will now justify these choices and examine what impact they have on the results.

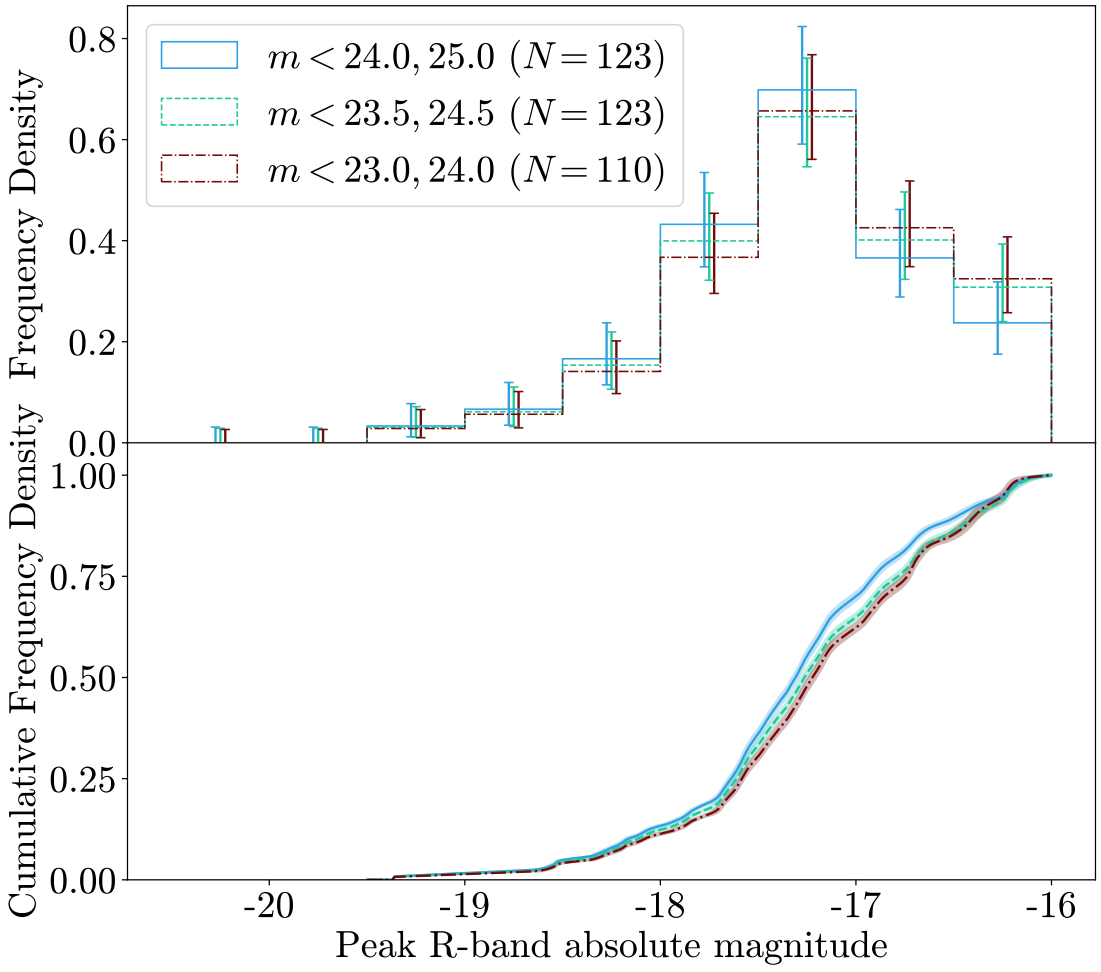

FIGURE 3.2: Luminosity functions for the DES CCSN sample with different magnitude limits for the V_{max} corrections.

3.1.2.1 DES Completeness Limit

The DES completeness limits of 23.5 mag and 24.5 mag for shallow and deep fields respectively are based on analysis presented in Kessler et al. (2015). Figure 3.2 shows the luminosity functions for all CCSNe in DES for these limits as well as for limits varied by ± 0.5 mag and the sample size obtained for each of these completeness limits. The luminosity function obtained by the original limits of 23.5/24.5 mag agree closely with lower limits of 23.0/24.0 mag, although a few objects are cut by this limit suggesting that it is too low. With higher limits of 24.0/25.0 mag, the luminosity function again remains very similar although shows an offset in the CDF. However, given that this higher limit does not lead to the inclusion of more objects in the sample, this completeness limit is too high and leads to an incorrect V_{max} correction. The limits of 23.5/24.5 mag best represent the DES sample.

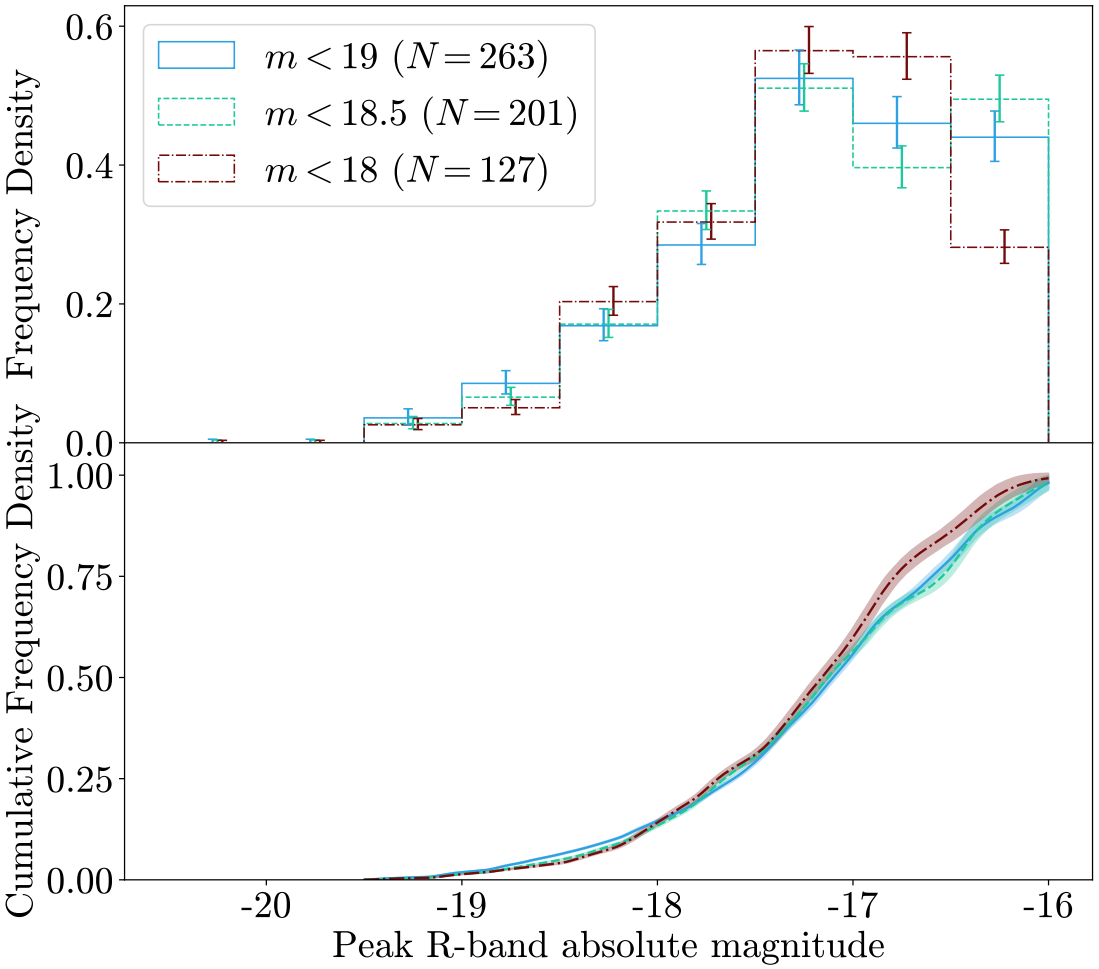

FIGURE 3.3: Luminosity functions for the ZTF CCSN sample with different magnitude limits for the V_{max} corrections.

3.1.2.2 ZTF Completeness Limit

Perley et al. (2020) quotes 97, 93 and 75 per cent spectroscopic completeness limits for the ZTF sample of 18, 18.5 and 19 mag. In order to explore which of these is most appropriate for a V_{max} correction, I derive luminosity functions for all CCSNe in the ZTF sample using each limit - these are shown in Figure 3.3. Above -17 mag, all three appear consistent with each other, however these luminosity functions diverge between -16 and -17. A completeness limit of 18 mag omits some SNe in this region and appears to bias the sample in favour of brighter objects, meaning that this is not a suitable limit for the V_{max} correction. The luminosity functions obtained for limits of 18.5 and 19 mag appear, however, consistent with each other. A limit of 18.5 mag gives a total sample size of 209 SNe, while a limit of 19 mag gives a sample size of 271 SNe. As a result, I use 19 mag as the completeness limit of ZTF since this maximises the sample size while having little impact on the luminosity function.

3.1.3 Parameterised Luminosity Functions

I have now presented and compared luminosity functions from the DES, LOSS and ZTF samples. However, in order for these to be easily used in simulations I fit a number of different distributions to the histograms presented in Section 3.1.1. I do this for the newly derived DES and ZTF luminosity functions; LOSS luminosity functions are already presented in L11. I consider both Gaussian and Lorentzian fits to the luminosity functions. Skewed Gaussian distributions were also considered but the skewness parameter γ could not be constrained with the available data.

3.1.3.1 DES

Figure 3.4 presents fits to the luminosity functions of SNe II and SNe Ibc in DES. This fit requires binning of the luminosity function - these fits are based on the bin edges presented in Figure 3.1, from -19.5 to -16 in steps of 0.5 for SNe II and 0.7 for SNe Ibc.

To assess the quality of each fit, I calculate reduced χ^2 values. These are calculated assuming a $\sqrt{N}$ uncertainty in the histogram, rather than the uncertainties based on Gehrels (1986) presented in Figure 3.1, in order to provide symmetric uncertainties for the fitting process. For SNe II, a Gaussian distribution provides a reasonable fit, with a reduced χ^2 of 1.44, although is too broad around the peak and underestimates the number of brighter SNe. A Lorentzian distribution better fits the sharp peak and brighter tail of the luminosity function, with a reduced χ^2 of 0.41. For SNe Ibc in DES, both distributions provide similar fits although the Gaussian has a lower reduced χ^2 of 1.59 compared to 2.88 for the Lorentzian.

The parameter values for these fits are shown in Table 3.2. The exact parameter values for the distributions are sensitive to the binning of the histogram. The values shown in this table are based on the bin edges presented in Figure 3.1, from -19.5 to -16 in steps of 0.5 for SNe II and 0.7 for SNe Ibc. For these fits, the mean of the absolute magnitudes in each bin is used for the x-coordinates. This table includes the uncertainty in each parameter when fitting to distributions with these bins (fit error). To take into account how varying the binning will affect the parameter values, I also present a binning error; this is defined as the standard deviation of the parameter values measured when considering all possible bin widths from 0.10 to 1.0 in steps of 0.01.

3.1.3.2 ZTF

Figure 3.5 presents fits to the luminosity functions of SNe II and SNe Ibc in ZTF. As in Section 3.1.3.1, these fits are based on the bin edges presented in Figure 3.1.

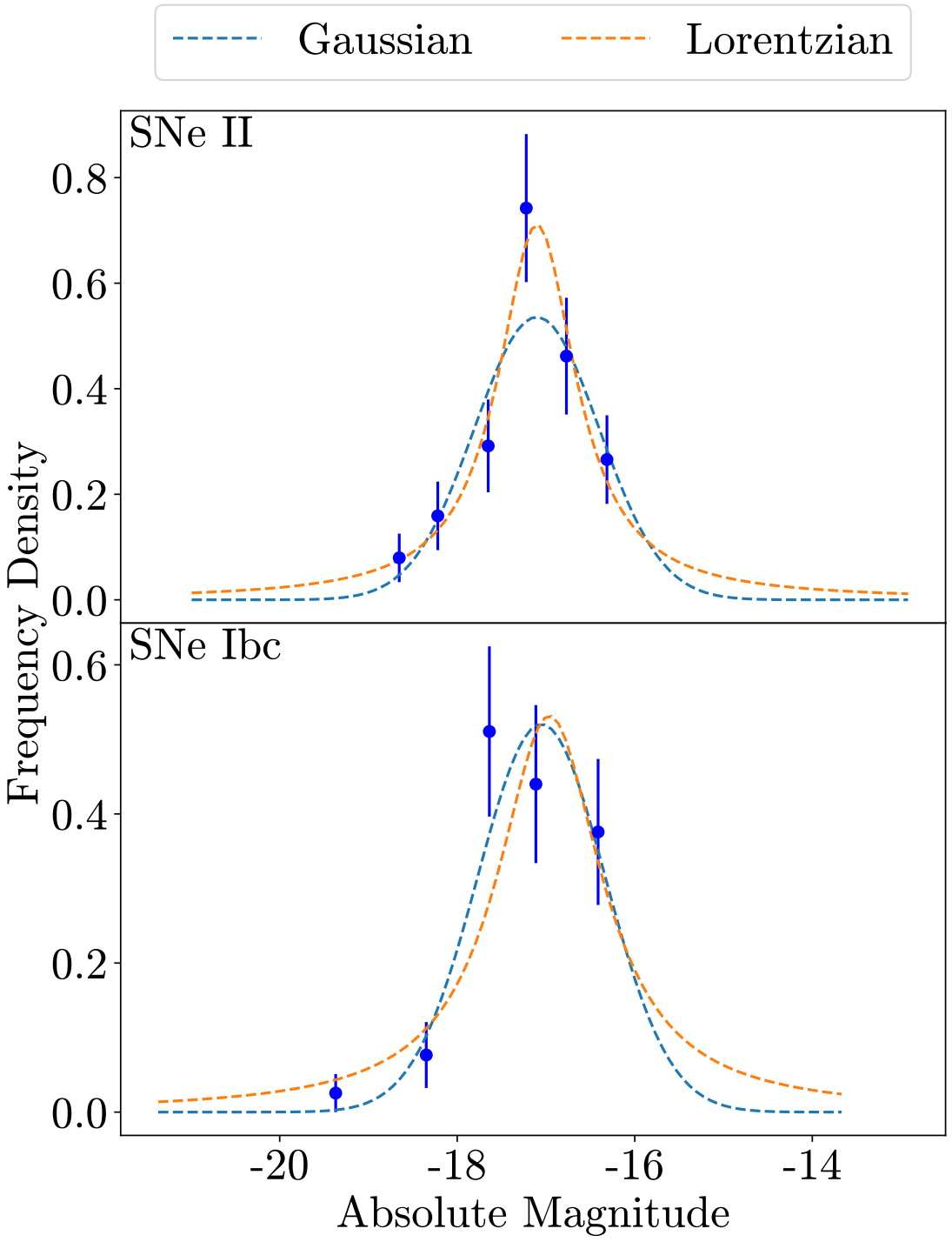

FIGURE 3.4: Gaussian and Lorentzian distribution fits to the DES luminosity functions.

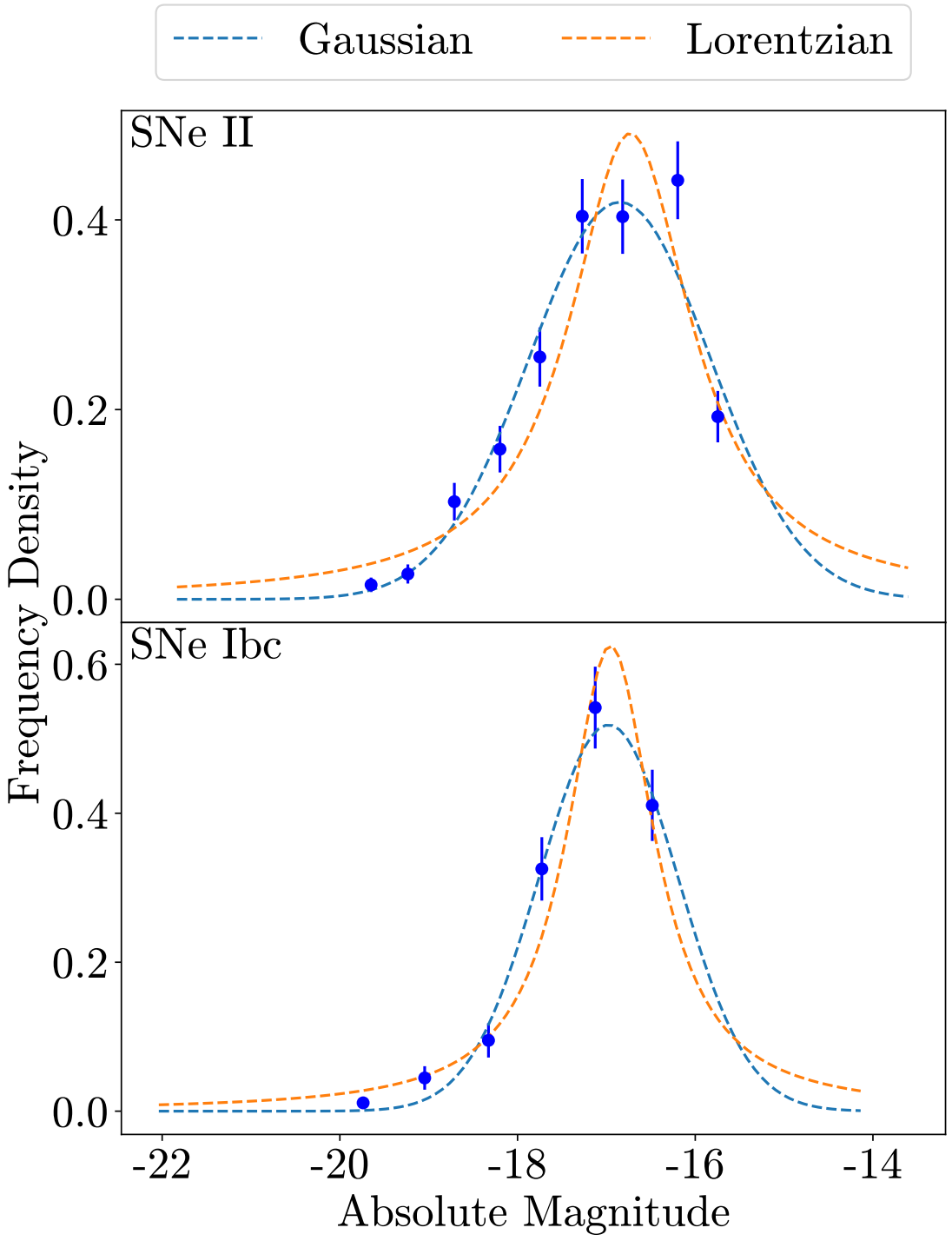

FIGURE 3.5: Gaussian and Lorentzian distribution fits to the ZTF luminosity functions.

TABLE 3.2: Reduced χ^2 values and parameter values for different model fits to the DES and ZTF luminosity functions, including mean μ and width σ. The fit error represents the uncertainty in the fit to the distributions using the binning detailed in Section 3.1.3. The binning error represents the uncertainty in the parameter values based on the binning of the data and is defined as the standard deviation of the parameter values measured when considering all possible bin widths from 0.10 to 1.0 in steps of 0.01.

Survey	SN Type	Model Type	Reduced χ^2	Parameter	Value	Fit Error	Binning Error
DES	II	Gaussian	1.44	μ	-17.10	0.13	0.07
				σ	0.70	0.13	0.06
		Lorentzian	0.41	μ	-17.10	0.05	0.05
				σ	0.53	0.08	0.11
DES	Ibc	Gaussian	1.59	μ	-17.05	0.19	0.18
				σ	0.72	0.16	0.28
		Lorentzian	2.88	μ	-16.96	0.25	0.18
				σ	0.72	0.29	0.38
ZTF*	II	Gaussian	1.98	μ	-16.85	0.09	0.15
				σ	1.02	0.07	0.11
		Lorentzian	5.53	μ	-16.73	0.13	0.12
				σ	0.84	0.15	0.14
ZTF	Ibc	Gaussian	2.11	μ	-16.98	0.14	0.12
				σ	0.78	0.11	0.10
		Lorentzian	3.22	μ	-16.95	0.10	0.10
				σ	0.60	0.11	0.11

*Please note, for SNe II in ZTF two extra objects with a peak R-band absolute magnitude below -16 were included in order to constrain the peak of the distribution.

These fits are only possible where the distributions peak above -16 and begin to decline again as otherwise the location of the peak of the luminosity function cannot be constrained. For SNe II in ZTF, the distribution does not obviously begin to decline above -16 which makes this difficult. As a result, for this fit I include two extra SNe which have a peak R-band magnitude below -16 which allows the peak of the distribution to be constrained. This fit is included for completeness, but I emphasise that the results for SNe II in ZTF should be considered with the strong caveat that these two extra objects have significant weight in determining the location of the peak of the distribution.

For SNe II in ZTF a Gaussian better represents the luminosity function with a reduced χ^2 of 1.98 - a Lorentzian overestimates the number of brighter SNe and has a reduced χ^2 of 5.53. As for SNe Ibc, a Gaussian has a lower reduced χ^2 of 2.11 compared to 3.22 for a Lorentzian, and better represents the luminosity function around peak although again underestimates the number of SNe in the brighter tail. The parameter values for these fits are also shown in Table 3.2, with the same method to incorporate binning errors as for DES.

3.2 Host Galaxy Demographics

I next consider the host galaxy properties from each of the three samples. When considering any differences between the samples I perform both two-sample KS and Anderson-Darling (AD) tests to assess their significance. The KS test is more sensitive to differences in the centre of two distributions while the AD test is more sensitive to differences in the tails (Mohd Razali & Yap, 2011). I elect to use both tests to examine both centres and tails. Note that the AD test was not used in Section 3.1 as the $V_{\rm max}$ weighting could not be incorporated. The results of both KS and AD tests are shown in Table 3.3.

3.2.1 Host Galaxy Stellar Mass

Figure 3.6 shows the distribution of host galaxy stellar masses across the three samples for SNe II and SNe Ibc. DES and ZTF appear consistent with each other, but show discrepancies with LOSS. This difference is expected: LOSS is a galaxy targeted SN survey that monitored massive, luminous galaxies so low mass galaxies will be underrepresented in the LOSS sample. The results of the two-sample KS and AD tests presented in Table 3.3 supports these interpretations.

3.2.2 Host Galaxy Rest-frame Colours

Figure 3.7 shows the distribution of rest-frame $U-R$ colours for the host galaxies in the three samples. For SNe II, differences can be seen between the three samples: the high-redshift DES sample has the bluest host galaxies, followed by the lower-redshift ZTF sample and then the local LOSS sample. Two-sample KS and AD tests show that the differences between the samples have significances in excess of 3σ respectively. Depending on the redshift, observer-frame filters will cover different wavelength ranges in the rest-frame; for the redshift range considered here, DES *griz* filters do not cover rest-frame *U*-band meaning some extrapolation is required to calculate $U-R$. However, similar results are seen when using rest-frame $B-V$ which is covered by *griz*. For SNe Ibc, the distributions visually suggest a similar finding however the offset between DES and ZTF is reduced and significance levels are below 2σ for $U-R$ and below 2.3σ for $B-V$.

Figure 3.8 shows host galaxy stellar mass plotted against host galaxy rest-frame $U-R$ colour for each of the three samples, with the thicker symbols showing the mean and standard error for each property across galaxies in bins of $8.25 < \log(M/M_{\odot}) < 9.25$, $9.25 < \log(M/M_{\odot}) < 10.25$ and $10.25 < \log(M/M_{\odot}) < 11.25$ for each sample. DES, ZTF and LOSS show strong correlations between host stellar mass and host $U-R$

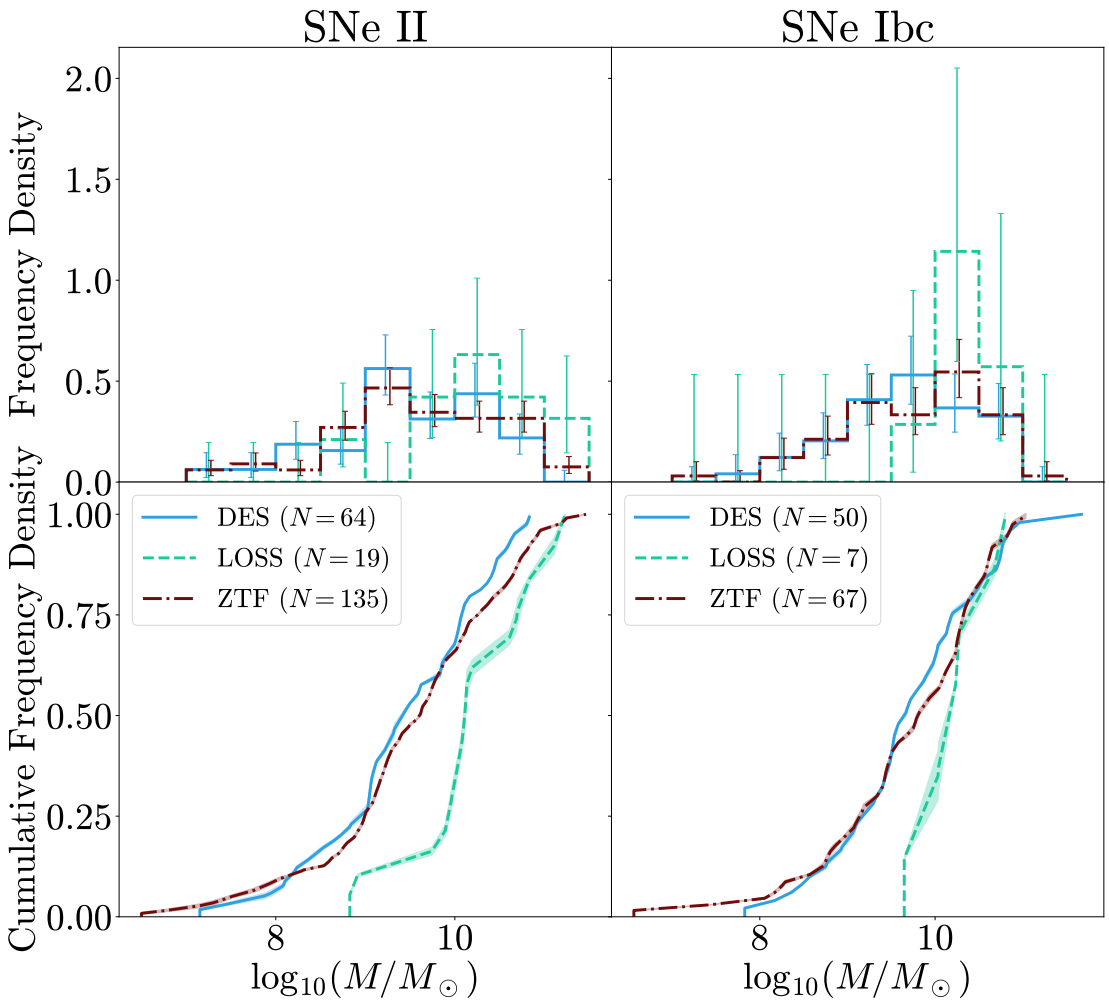

FIGURE 3.6: Host galaxy stellar mass distributions and cumulative distributions for SNe II and SNe Ibc for the DES, LOSS and ZTF samples. Histogram uncertainties here (and throughout this Chapter) are estimated from the Poisson distribution, while CDF uncertainties are estimated from the Monte Carlo approach described in Section 3.1.1.

colour. This plot also shows that the difference in rest-frame $U - R$ colour between DES and ZTF is observed across the range of host galaxy masses in the DES sample, i.e. at fixed stellar mass the DES host galaxy sample is bluer, with this difference more pronounced for SNe II.

3.2.3 Relations Between SN and Host Properties

I next consider the relations between the properties of the SNe and the properties of the host galaxies for the three samples.

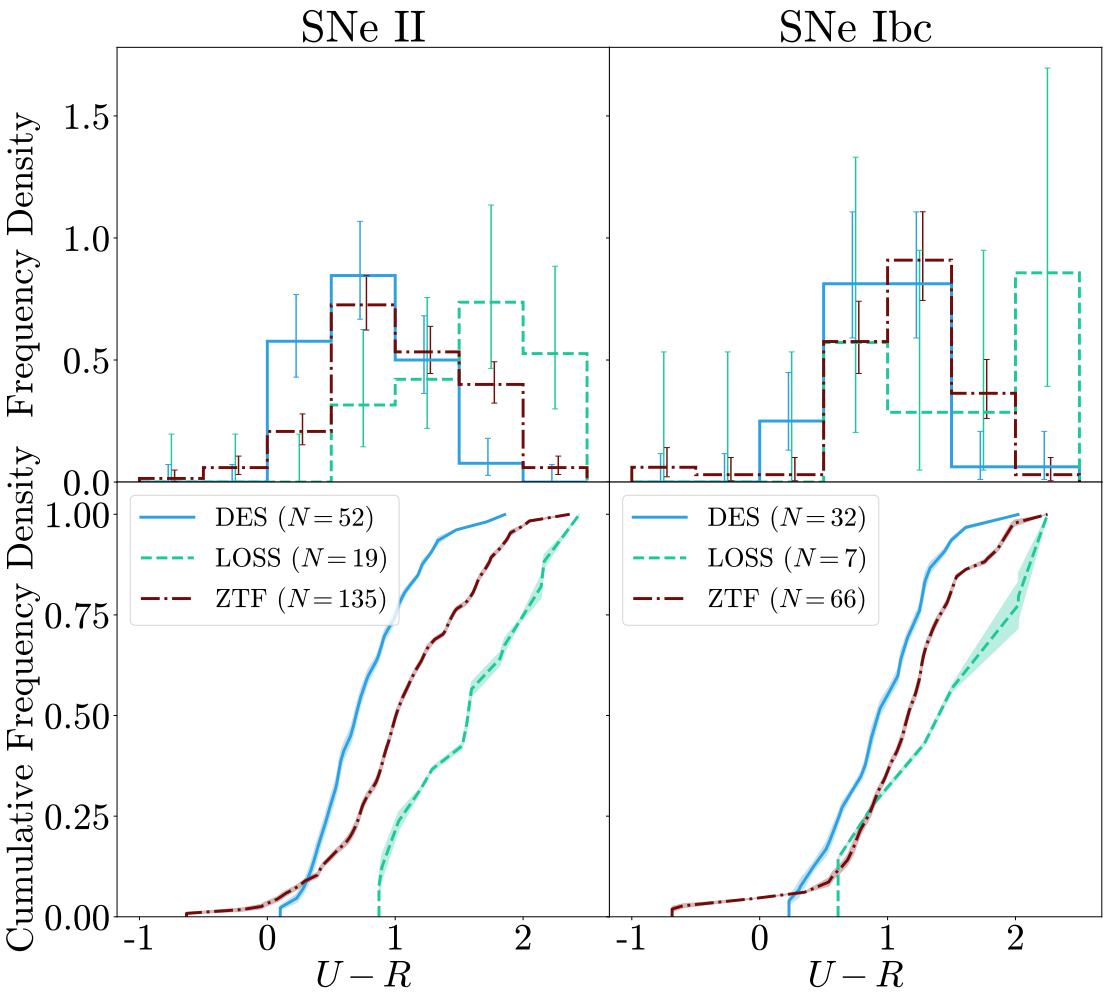

FIGURE 3.7: As Figure 3.6, but for the host galaxy rest-frame $U - R$ colour in place of stellar mass.

3.2.3.1 SNe II/Ibc Host Properties Comparison

Figure 3.9 and Figure 3.10 show the distributions of host stellar mass and $U - R$ colour comparing the host galaxies of SNe II and Ibc, and Table 3.4 shows the results of two-sample KS tests between these distributions. For host stellar mass, no significant differences are seen between the hosts of SNe II and SNe Ibc. The same result is found for host $U - R$ colour for LOSS and ZTF, the latter consistent with the findings of Perley et al. (2020). For the DES sample, the hosts of SNe Ibc appear redder with a significance of 2.0σ from the KS and AD tests. Taking $U - R$ as a proxy for star formation rate, this could indicate that SNe Ibc are exploding in galaxies with less star formation than SNe II. SNe Ibc have been shown to trace galaxy star formation more closely than SNe II (e.g. Anderson & James, 2009; Galbany et al., 2018) which would makes this result surprising, albeit with the caveats that these differences refer to local properties rather than the global host properties presented here and that the significance level is not high.

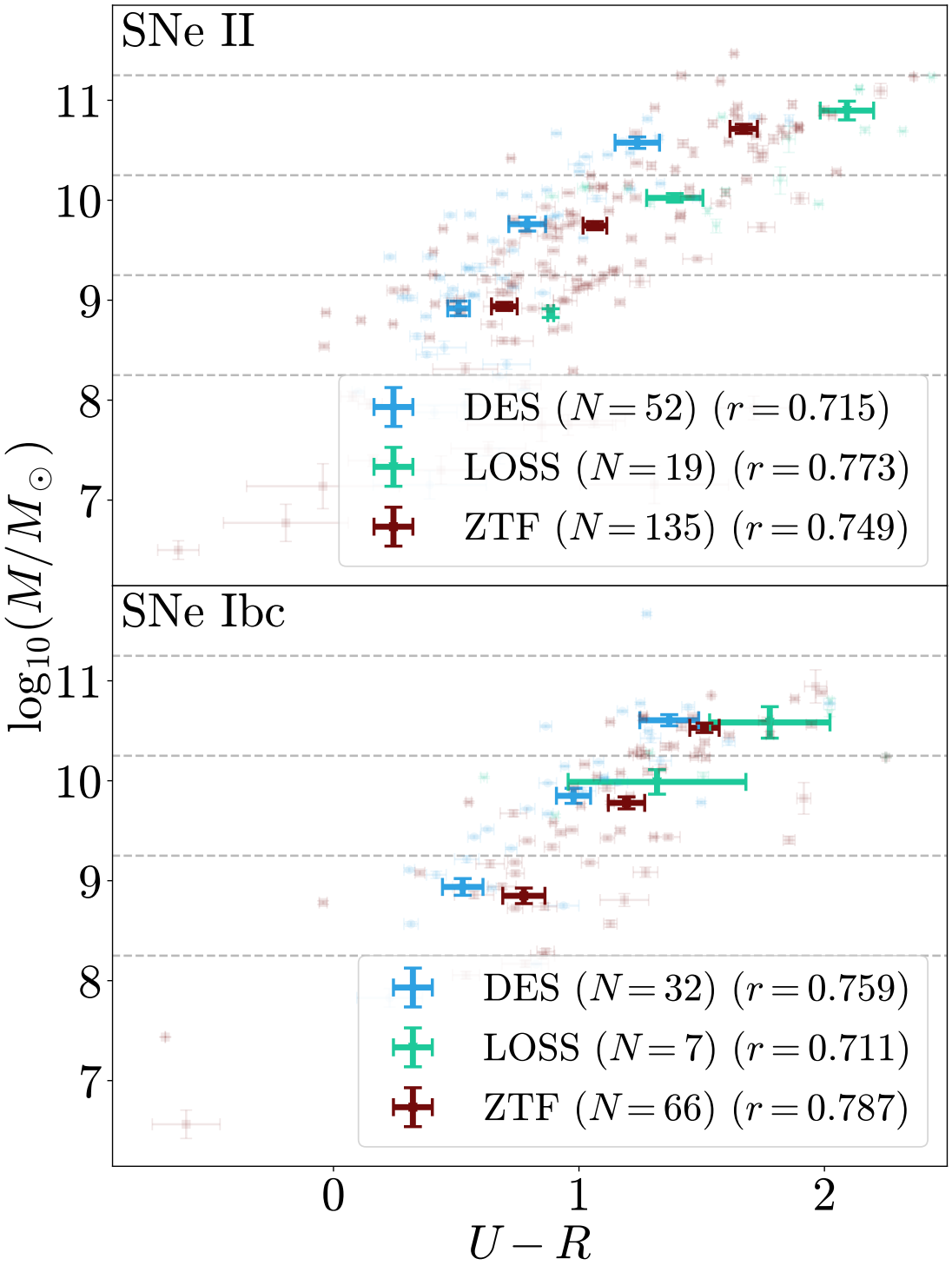

FIGURE 3.8: Host galaxy stellar mass plotted against host galaxy rest-frame $U - R$ colour for each sample along with correlation coefficients for each. Thick data points represent the mean and standard error for stellar mass and colour for each sample in stellar mass bins of $8.25 < \log(M/M_\odot) < 9.25$, $9.25 < \log(M/M_\odot) < 10.25$ and $10.25 < \log(M/M_\odot) < 11.25$. The horizontal dashed lines mark these bin boundaries.

TABLE 3.3: The results of two-sample KS and AD tests between the distributions of host galaxy stellar mass, rest-frame $U-R$ and $B-V$ colour. Also shown are metallicity values derived from stellar mass in Section 3.3.2.4 and $U-R$ (SFRcorr) and $U-R$ (Zcorr), the rest-frame $U-R$ colour corrected for SFR and metallicity evolution with redshift introduced in Section 3.3.3.3.

Property	Survey 1	Survey 2	KS test significance		AD test significance	
			SNe II	SNe Ibc	SNe II	SNe Ibc
Stellar mass	DES	LOSS	3.2σ	2.0σ	3.4σ	1.9σ
	DES	ZTF	0.4σ	0.5σ	0.8σ	0.3σ
	LOSS	ZTF	3.4σ	1.5σ	2.9σ	1.4σ
$U-R$	DES	LOSS	4.7σ	1.9σ	4.8σ	2.6σ
	DES	ZTF	3.4σ	1.6σ	3.8σ	1.8σ
	LOSS	ZTF	2.7σ	1.4σ	3.7σ	2.0σ
$B-V$	DES	LOSS	4.3σ	2.1σ	4.8σ	2.7σ
	DES	ZTF	3.6σ	1.9σ	3.9σ	2.3σ
	LOSS	ZTF	2.6σ	1.5σ	3.7σ	2.2σ
Metallicity	DES	LOSS	4.0σ	2.4σ	4.0σ	2.2σ
	DES	ZTF	1.4σ	0.9σ	1.8σ	0.8σ
	LOSS	ZTF	3.5σ	1.5σ	3.0σ	1.5σ
$U-R$ (SFRcorr)	DES	LOSS	4.3σ	1.4σ	4.7σ	2.0σ
	DES	ZTF	3.0σ	0.9σ	3.4σ	1.3σ
	LOSS	ZTF	2.8σ	1.4σ	3.6σ	2.0σ
$U-R$ (Zcorr)	DES	LOSS	3.8σ	1.6σ	4.5σ	2.4σ
	DES	ZTF	2.4σ	0.9σ	2.8σ	1.0σ
	LOSS	ZTF	2.7σ	1.4σ	3.6σ	2.1σ

TABLE 3.4: The results of two-sample KS tests between the SNe II and SNe Ibc host properties in each survey.

Property	Survey	KS test significance	AD test significance
Stellar mass	DES	1.1σ	1.4σ
	LOSS	0.1σ	0.2σ
	ZTF	1.2σ	1.3σ
$U-R$	DES	2.0σ	2.0σ
	LOSS	0.1σ	0.2σ
	ZTF	1.8σ	1.5σ

3.2.3.2 SN/host Correlations

I also consider relations between the properties of the host galaxy and the properties of the SN, studying correlations between peak SN luminosity and host stellar mass and rest-frame colour. Table 3.5 shows the Pearson correlation coefficients (r) between these properties for each of the DES, LOSS and ZTF samples.

For both SN II and SN Ibc samples, no significant trends are seen between the SN luminosities and the properties of the galaxies that host them – the correlations seen for SNe Ibc in LOSS are not statistically significant and correspond to only 7 galaxies. Gutiérrez et al. (2018) also finds no relation between stellar mass and peak SN

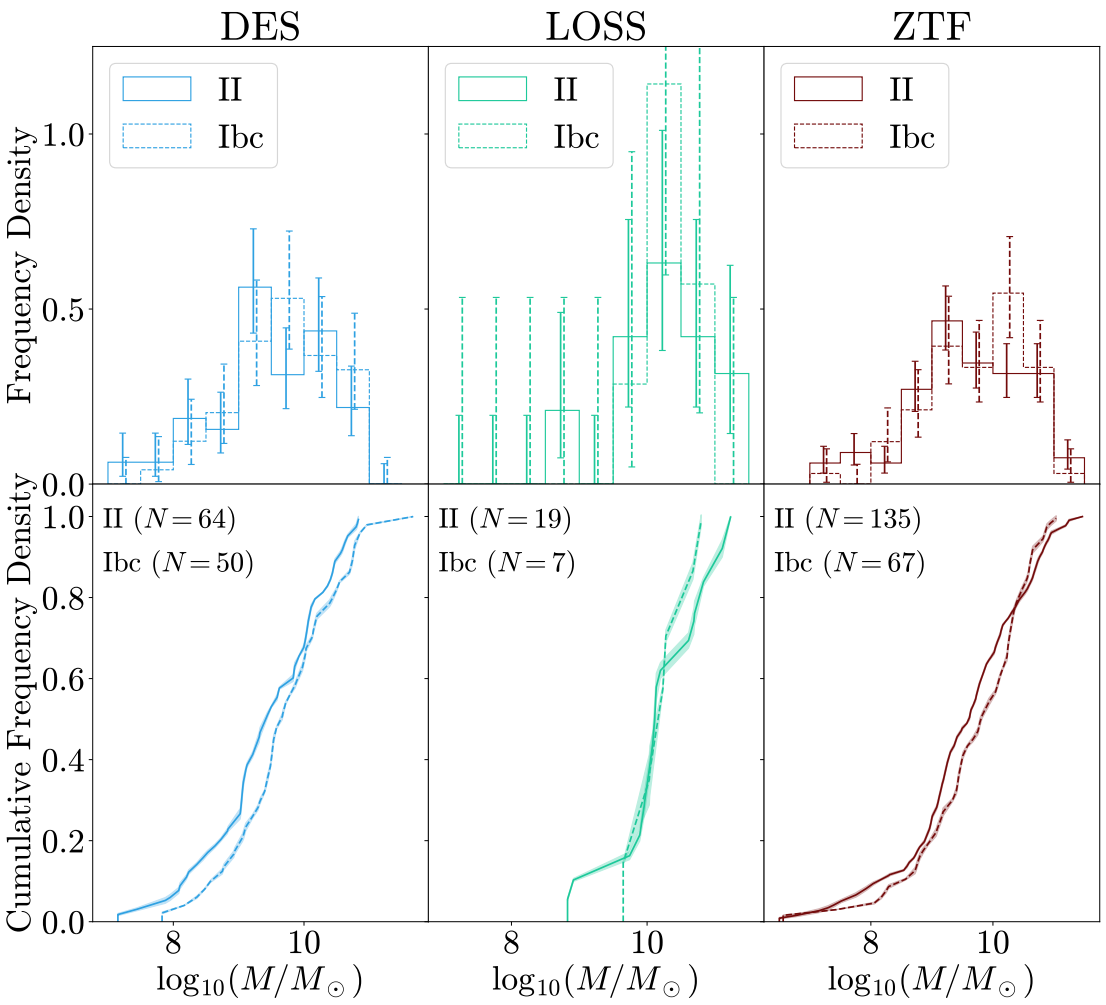

FIGURE 3.9: Host galaxy stellar mass distributions and cumulative distributions for each of the DES, LOSS and ZTF samples showing the properties of the hosts of SNe II and SNe Ibc for each sample.

luminosity for SNe II, and Wiseman et al. (2020b) finds a lack of strong evidence for a relation between peak transient luminosity and host mass and sSFR for RETs.

3.3 Discussion

In this section I explore these results, considering and assessing a number of potential causes for some of the noteworthy trends that are observed.

3.3.1 Impact of Photometric Misclassification

At this point, I have presented luminosity functions for CCSNe in DES and compared with LOSS and ZTF. However, it is important to consider the potential impact of misclassification of the sample of photometric CCSNe with host spectroscopic

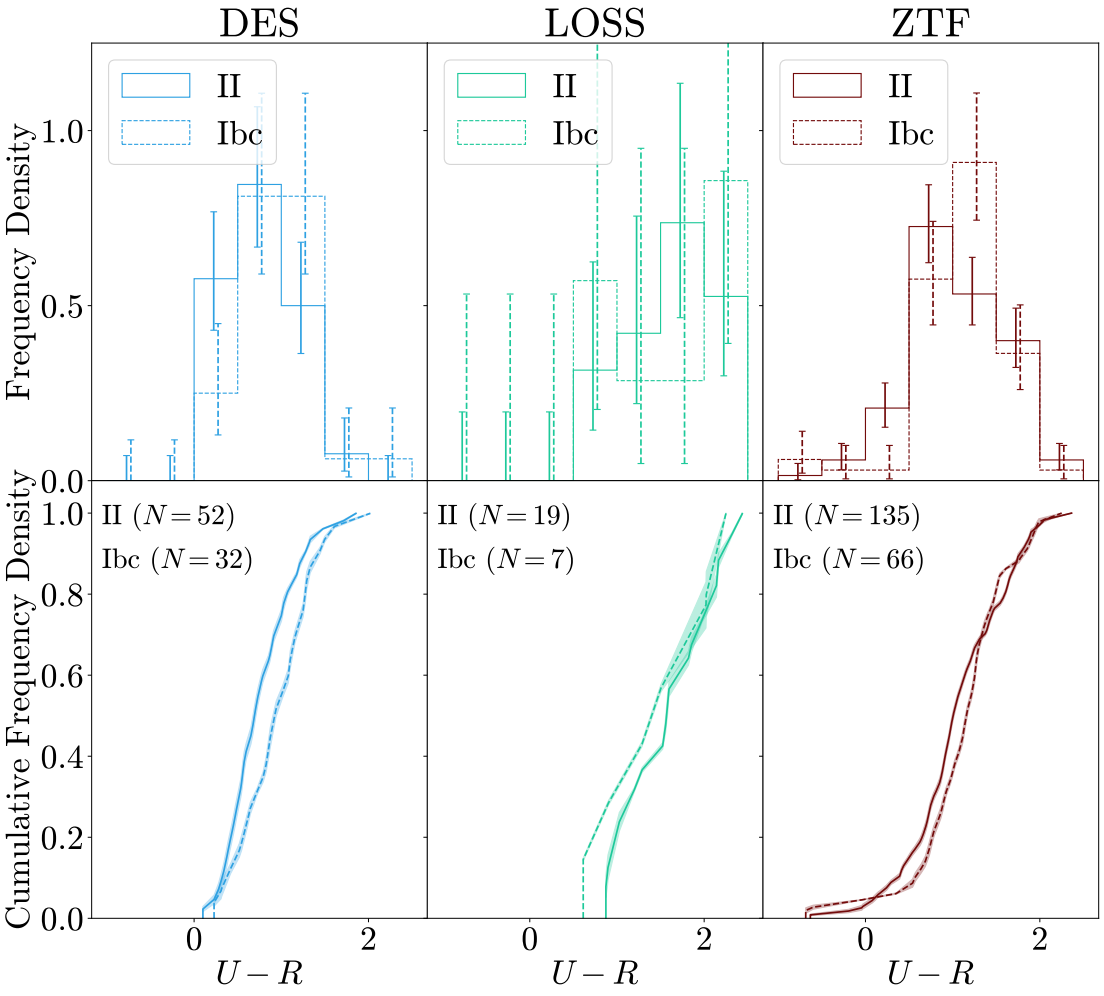

FIGURE 3.10: As Figure 3.9, but for host galaxy rest-frame $U - R$ colour instead of stellar mass.

TABLE 3.5: Correlation coefficients between peak SN R-band absolute magnitude and host galaxy stellar mass and rest-frame $U - R$ colour for SNe II and Ibc in DES, LOSS and ZTF.

Property	Survey	SN Type	Correlation with SN peak R-band absolute magnitude (r)
Stellar mass	DES	II	0.09
		Ibc	0.03
	LOSS	II	-0.28
		Ibc	0.57
	ZTF	II	-0.12
		Ibc	0.14
$U - R$	DES	II	-0.06
		Ibc	0.07
	LOSS	II	-0.12
		Ibc	0.55
	ZTF	II	0.07
		Ibc	0.21

redshifts in DES. SNe Ia have been removed using the SuperNNova model presented in Vincenzi et al. (2022), which has a high degree of accuracy upward of 98 per cent. As discussed in Section 2.2.1.2, the pSNid model used to split this sample into SNe II and Ibc has an accuracy of 86 per cent on the sample of DES CCSNe with spectroscopic classifications, with similar performance on each of the two classes. While this method works well, it does leave open the possibility that a small proportion of SNe in this sample are assigned to the wrong class.

To investigate what effect this may have on the analysis, I repeat the Monte Carlo process for CDF uncertainty outlined in Section 3.1.1 but this time in each iteration flipping 14 per cent of the classes, corresponding to the expected error rate, for the photometrically classified DES CCSNe (SNe II are changed to SNe Ibc and vice versa) to see what effect this has on the final CDF. Figure 3.11 shows the luminosity functions and host galaxy $U - R$ colour distributions for the three samples, with the randomised class flipping applied to DES photometrically classified SNe. Overall, these distributions appear very similar to those in Figure 3.1. I also try restricting the sample to only spectroscopically confirmed SNe from DES and see the same trends for SNe II, although there are too few spectroscopically confirmed SNe Ibc to make this comparison. Overall, the results presented in this analysis appear robust to the potential misclassification of SNe II and Ibc.

3.3.2 Difference in the Luminosity Function?

As part of my analysis, I have carried out two-sample KS tests between the luminosity functions of DES, LOSS and ZTF. For SNe II, DES is brighter than LOSS at a significance level of 3.0σ and appears brighter than ZTF although only at a significance of 1.4σ. For SNe Ibc, DES also appears brighter than both LOSS and ZTF although at a low significance of 1.9σ. Although the significance levels are not high, these differences raise the possibility of underlying differences in the luminosity functions of these samples. If there is a difference, one natural explanation would be redshift evolution in the underlying stellar populations and progenitor stars. However, I first consider other, simpler explanations.

3.3.2.1 Incompleteness

The most straight forward explanation for any difference between DES and LOSS is a lack of completeness in the DES sample due to lower sensitivity to fainter SNe. Figure 2.4 shows the peak absolute magnitudes of all objects in the samples plotted against redshift, prior to making any selection in absolute magnitude. Figure 3.1 shows the main differences between DES and LOSS for SNe II are in the $[-16, -16.5]$ luminosity bin and for SNe Ibc are in the $[-16, -16.7]$. DES is not complete in this

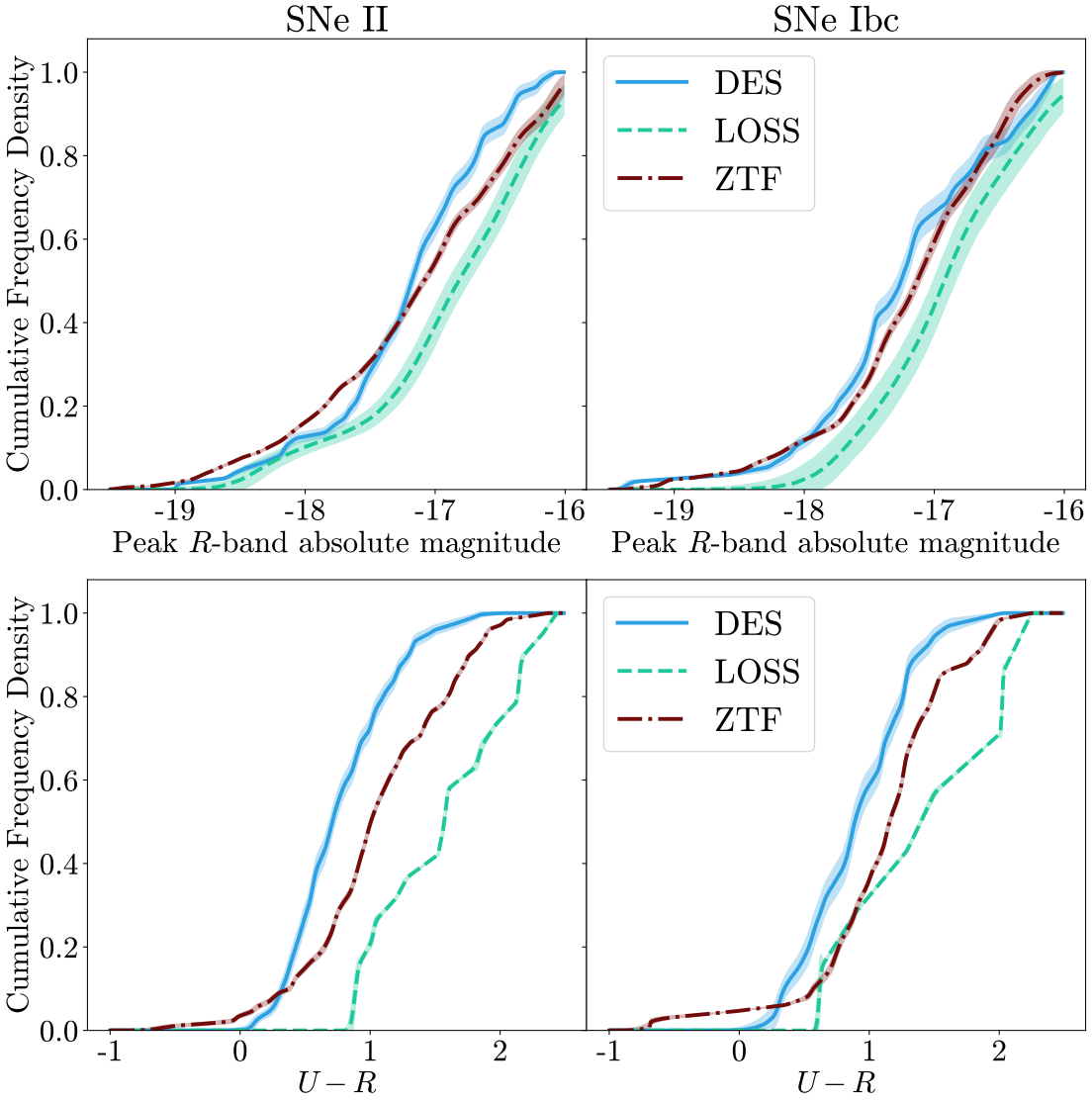

FIGURE 3.11: CDFs for the luminosity functions and rest-frame host galaxy $U-R$ colours for each of the DES, LOSS and ZTF samples, incorporating a 14 per cent misclassification rate for photometrically classified SNe in DES as outlined in Section 3.3.1.

range and the distribution is affected by the $V_{\rm max}$ correction, whereas the LOSS sample is not affected by this correction. The $V_{\rm max}$ correction for DES gives a maximum weighting of 2.9 but for ZTF this is much higher due to the lack of completeness in the sample, up to a maximum of 14.5 although this is typically around 2-3. This can be mitigated for with lower redshift cuts for DES and ZTF to obtain more complete samples – doing so reduces the significances from the KS test due to the smaller sample size but overall the trends that are seen appear unchanged. This suggests that incompleteness is not the cause of potential differences between the samples.

3.3.2.2 Host Properties

An alternative possibility is that any difference in luminosity function could be explained by a difference in host properties between the samples. For example, the host galaxies of the LOSS sample are significantly more massive and redder than that of DES, likely because of the galaxy-targeted nature of LOSS (Section 3.2). However, as there are no significant correlations between either host colour or mass and peak SN luminosity (Section 3.2.3) this is unlikely to cause any differences in the luminosity function.

3.3.2.3 Host Extinction

The difference in luminosity function could also result from differing levels of host galaxy extinction between the two samples. This could be due to both global and local host properties; for example, on average a higher level of host extinction might be expected in more massive, redder, dustier host galaxies and SNe closer to the central dusty regions of the host.

As discussed in Section 3.2.2, the DES hosts are on average bluer than those of LOSS and ZTF. This could indicate higher levels of host extinction in LOSS and ZTF that might explain any differences seen. To explore this possibility, I compare the luminosity functions of LOSS and ZTF with only SNe in DES that are in redder host galaxies. When making cuts at either $U - R > 0.5$, $U - R > 0.75$ or $U - R > 1.0$, the KS test significances are reduced due to the smaller sample size but the same overall trends are observed as for the full sample. This indicates that differing levels of host extinction do not cause any differences seen, though without measurements of the host extinction this cannot be ruled out as a possibility – local environment properties are likely to play a significant part in the level of extinction. I also consider the possibility of differing SN radial distributions across the three samples leading to differing levels of extinction, but do not find any significant differences in the physical separation between SN and host.

3.3.2.4 Metallicity

Differences in metallicity may also explain potential differences in the luminosity functions; for example, DES SNe may occur in lower metallicity environments than LOSS or ZTF. As previously mentioned, host metallicity affects the SN population as the most luminous classes of SNe preferentially occur in low-mass, low-metallicity environments. Metallicity varies with stellar mass, star formation rate, redshift (e.g. Zahid et al., 2013; Yates et al., 2012; Curti et al., 2020) and also radially within a galaxy (Parikh et al., 2021). There are a number of reasons why the DES hosts could be

expected to be lower metallicity than either the LOSS or ZTF hosts: the DES hosts are lower stellar mass than those of LOSS, they are bluer and hence more star forming than hosts in ZTF or LOSS (although the effect of increased SFR on metallicity will vary depending on galaxy mass) and they are at higher redshift. Metallicity differences are a possible cause of any differences in luminosity function.

While metallicity values calculated from host galaxy spectroscopy are not available for this sample, an indication of global host galaxy metallicity can be estimated using the relation between stellar mass and metallicity given in equation 4 of Zahid et al. (2013). I calculate global galaxy metallicity using the following approach:

- A straight line is fit to the relation between the redshifts and mass-metallicity relation parameters quoted in Table 1 of Zahid et al. (2013). I use only the samples from SDSS, the Smithsonian Hectospec Lensing Survey (SHELS; Geller et al., 2014) and the DEEP2 survey (Newman et al., 2013) quoted here as the higher redshift samples have very uncertain values for these parameters.
- For a galaxy at a given redshift, these linear fits are used to estimate the mass-metallicity relation parameters at that redshift. I then use the relation at that redshift to convert the measured stellar mass from SED fits to a metallicity.

The results of two-sample KS and AD tests between the global host metallicities of each of these samples are shown in Table 3.3 - as for stellar mass, DES and ZTF are consistent while both show differences to LOSS. This indicates differing host metallicity could explain differences between DES and LOSS but not between DES and ZTF.

Metallicity can also be probed by looking at the decline rates during the plateau phase after maximum light of SNe II. Theoretical models suggest that the metallicity of the progenitor star may affect the decline rate during the 'plateau' phase of the SN light curve (Dessart et al., 2013), however, observations do not show this dependence (Anderson et al., 2016). The absence of correlations could be related to the lack of SNe II in low-luminosity hosts. Nevertheless, some relations can be established when SNe II in faint hosts are included. Gutiérrez et al. (2018) finds that slower declining SNe II occur preferentially in low-luminosity (and therefore low-metallicity) hosts. For SNe II in DES and ZTF, I calculate the decline rate of this phase of the light curve (corresponding to s2 in Anderson et al., 2014) and find that the decline rates calculated are consistent across the two samples. This suggests that there is not a significant metallicity difference between the two samples, indicating that this is unlikely to explain any differences between DES and ZTF.

3.3.2.5 Does the Luminosity Function Evolve With Redshift?

The notion of a luminosity function which evolves with redshift is an interesting one - the differences seen in the luminosity functions of SNe II in DES and LOSS and SNe Ibc in DES, LOSS and ZTF raise this as a possibility, with the caveat that the significances are not especially high. Any differences could be explained by a lack of completeness in the DES sample, however this will have been significantly mitigated for by the V_{max} correction and making a lower redshift cut does not change the trends seen. Greater dust extinction from redder host galaxies is another possible explanation given that LOSS and ZTF hosts are bluer than DES, but selecting only DES SNe in redder hosts or ZTF and LOSS SNe in bluer hosts does not change the trends seen which suggests that this is not the case - despite this, without measurements of the host extinction this cannot be ruled out as a possibility. Differing metallicity also does not seem to explain the differences as I find consistent global host galaxy metallicities between DES and ZTF using the mass-metallicity relation of Zahid et al. (2013) and consistent decline rates after peak for SNe II.

3.3.3 Host Galaxy Colour Discrepancy

Section 3.2.2 uncovered a puzzling trend: SNe II in DES on average occur in bluer galaxies than those in ZTF and LOSS. A difference in host galaxy properties between DES/ZTF and LOSS can be explained, at least in part, by the differences in targeting between the surveys. However, the difference in host rest-frame colour between DES and ZTF is not so easily understood. In this section I explore possible explanations for this difference.

3.3.3.1 DES Spectroscopic Selection Bias

The DES sample in Figure 3.7 contains only CCSNe with a spectroscopic host redshift, obtained from a variety of sources (Vincenzi et al., 2021). Typically, galaxy redshifts are measured through the presence of narrow emission lines in their spectra, which will generally be stronger in bluer, star-forming galaxies. This may lead to a bias towards bluer galaxies in the DES sample, although Vincenzi et al. (2021) finds that the difference in spectroscopic selection efficiency in DES between red and blue galaxies is small. By contrast, ZTF has an automated SN spectroscopic follow-up programme which provides redshift information for 93 per cent of observed transients with $m < 18.5$ mag and 100 per cent with $m < 17$ mag. As a result, any possible host selection bias affecting DES would not affect ZTF.

To investigate whether such a bias occurs, I compare the DES samples with host spectroscopic redshifts (both the spectroscopically confirmed and photometric with

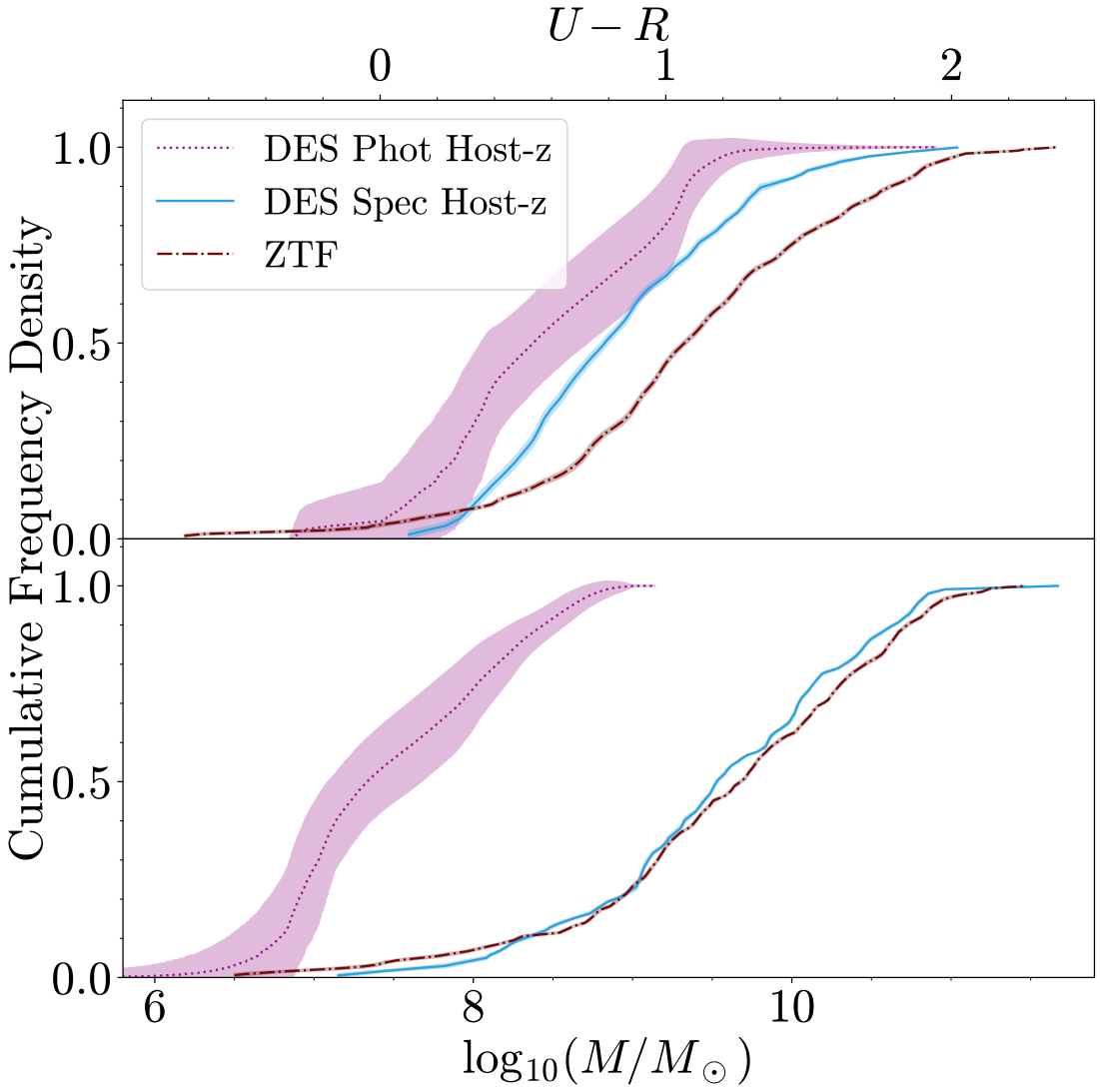

FIGURE 3.12: Host galaxy rest-frame $U-R$ (top) and stellar mass (bottom) cumulative distributions for all CCSNe in the the DES sample of objects without spectroscopic host redshifts, compared with the DES sample with spectroscopic host redshifts as well as the ZTF sample.

spectroscopic host samples) and ZTF samples to the DES CCSN sample with only photometric redshifts (Figure 3.12). However, rather than explaining the difference in host colour, this photometric sample appears bluer than the DES spectroscopic host sample. Considering the host stellar mass distribution for this sample, this is not unexpected: the DES hosts without spectroscopic redshifts are low stellar mass galaxies which are typically bluer and more strongly star-forming than higher mass galaxies. In summary, the difference in host rest-frame colour cannot be easily explained by a simple spectroscopic host selection bias in DES.

3.3.3.2 ZTF Spectroscopic Selection Effects

An alternative explanation is some selection bias in ZTF which favours SNe in redder hosts. The ZTF BTS sample has a very high level of spectroscopic completeness; however, spectroscopy is not captured exclusively by the ZTF spectroscopic instrument SEDMachine (SEDM) – in cases where the SEDM spectra are unreliable other instruments may be used, and in cases where an object is first classified by another survey ZTF do not take an additional spectrum. To understand whether this may introduce selection effects, I examine the sub-sample of ZTF SNe only with a classification reported by SEDM. However, no significant difference is found with this population: a two-sample KS test between the $U - R$ host colour distributions of DES and only ZTF SNe classified by SEDM has a significance of 3.2σ and 3.4σ from KS and AD tests, almost unchanged from the full ZTF sample.

3.3.3.3 Redshift Evolution of the Host Galaxies

Another possible explanation is redshift evolution. The mean redshift of the ZTF sample is ~ 0.03, corresponding to a lookback time of ~ 0.4 Gyr, while the mean redshift of the DES sample is ~ 0.2 which corresponds to a lookback time of ~ 2 Gyr. This leaves a period of $\sim$1–2 Gyr between most of the ZTF and DES SNe exploding; ZTF hosts are therefore on average older and less strongly star-forming. The host galaxy SFRs can be corrected for redshift evolution following the method of Section 4.2 of Taggart & Perley (2021), based on the star-forming sequences of galaxies outlined in Salim et al. (2007) and Noeske et al. (2007), correcting the SFR values to $z = 0$. However, I do not use SFR directly, and instead measure $U - R$ colour. As a result, I adapt the Taggart & Perley (2021) method to $U - R$ using the following steps:

- The SFR correction is calculated for each galaxy; this correction will be the same for sSFR as well.
- A linear relationship is fit between $U - R$ colour and sSFR for all host galaxies in the sample.
- The gradient of this line is used to convert the sSFR correction into a $U - R$ correction.

This allows the distributions of these corrected colours to be compared with those of the ZTF hosts.

Figure 3.13 shows the distributions of rest-frame $U - R$ colour corrected for the evolution of SFR, hereafter $U - R$ (SFRcorr). The correction factor between typical DES and ZTF redshifts is $\simeq 0.03$–0.04 mag and thus the effect is small: the significance

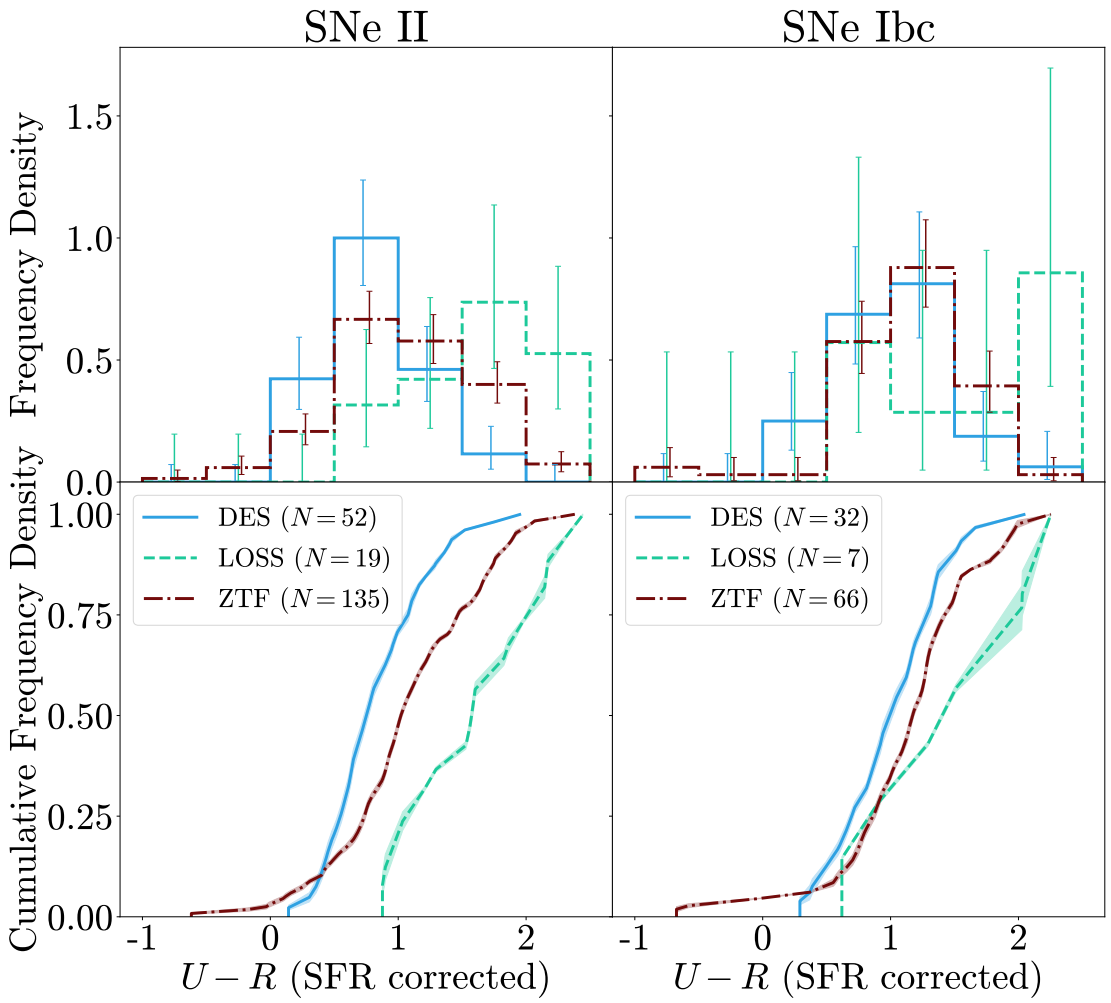

FIGURE 3.13: Host galaxy rest-frame $U - R$ colour distributions and cumulative distributions, corrected for the effects of SFR evolution with redshift, for both SNe II and SNe Ibc for DES, LOSS and ZTF samples.

of the difference between DES and ZTF from the two-sample KS test is reduced by only 0.4σ. Based on this, the difference in host colour seems unlikely to be caused by redshift evolution of the underlying galaxy populations.

However, another redshift evolution which should be considered is the evolution of the mass-metallicity relation. As galaxies age, their metallicity increases due to the synthesis of heavy elements in processes such as SNe which enrich their surroundings (Zahid et al., 2012, 2013, e.g.). Over time, the relation between galaxy mass and galaxy metallicity evolves. The metallicity of the host galaxies will have an effect on the emission lines produced, which will in turn affect galaxy colour. To investigate this, I use the following process to correct $U - R$ colour for the effects of metallicity evolution:

- Fit a relation between metallicity values inferred from Zahid et al. (2013) discussed in Section 3.3.2.4 and rest-frame host galaxy $U - R$ colours. Unlike the

SFR correction, this relationship is not linear. Instead, I fit an exponential relation with a linear term of the form $y = mx + c + e^{A(x-x_0)}$ where m, c, A and x_0 are the fitting parameters.

- Compare the metallicity difference for each galaxy of a given stellar mass between its actual redshift and $z = 0$.
- Use the fitted relation between metallicity and $U - R$ to estimate how much this change in metallicity would alter the rest-frame $U - R$ colour.
- Modify the calculated $U - R$ colours by this correction factor to calculate the rest-frame $U - R$ colour corrected for metallicity evolution, hereafter $U - R$ (Zcorr).

This correction involves the use of two relations that both show a large degree of scatter: the mass-metallicity relation from Zahid et al. (2013) and the relation between $U - R$ colour and metallicity observed in the samples used for this thesis. However, this does give an indication of the extent that evolving metallicity may have on $U - R$ colour.

Figure 3.14 shows the distributions of $U - R$ (Zcorr). This correction factor is larger than the previous correction for SFR evolution. For SNe II, this correction reduces the gap between DES and ZTF and the significance of this offset is reduced to 2.4σ and 2.8σ for both KS and AD tests, however the offset in $U - R$ between DES and ZTF across different galaxy masses as in Figure 3.8 is still seen. Overall, metallicity evolution with redshift may explain some but not all of the offset in rest-frame $U - R$ colour between host galaxies in DES and ZTF.

3.3.3.4 Systematic Differences in Host Galaxy Photometry Used

An additional possibility is that the different sources of host galaxy photometry between DES and ZTF is causing some systematic offset between the two samples. It may be that the inclusion of *u*-band data in the SED fits for the ZTF hosts is causing a systematic difference compared with the *griz*-only SED fits for the DES hosts (Section 2.4). I remove the *u*-band data from the ZTF host photometry and repeat the SED fits using only *griz*, but find that the ZTF rest-frame colours from *griz* fits are consistent with those from *ugriz* fits and thus that the difference between DES and ZTF host colours remains.

Alternatively, there may be differences between DES and SDSS photometry which cause an offset when considering the same bands. To investigate this possibility, I match DES SNe to the SDSS host catalogue using a 5″search radius, finding 47 objects with SDSS host galaxies, and then repeat the SED fits using SDSS photometry instead

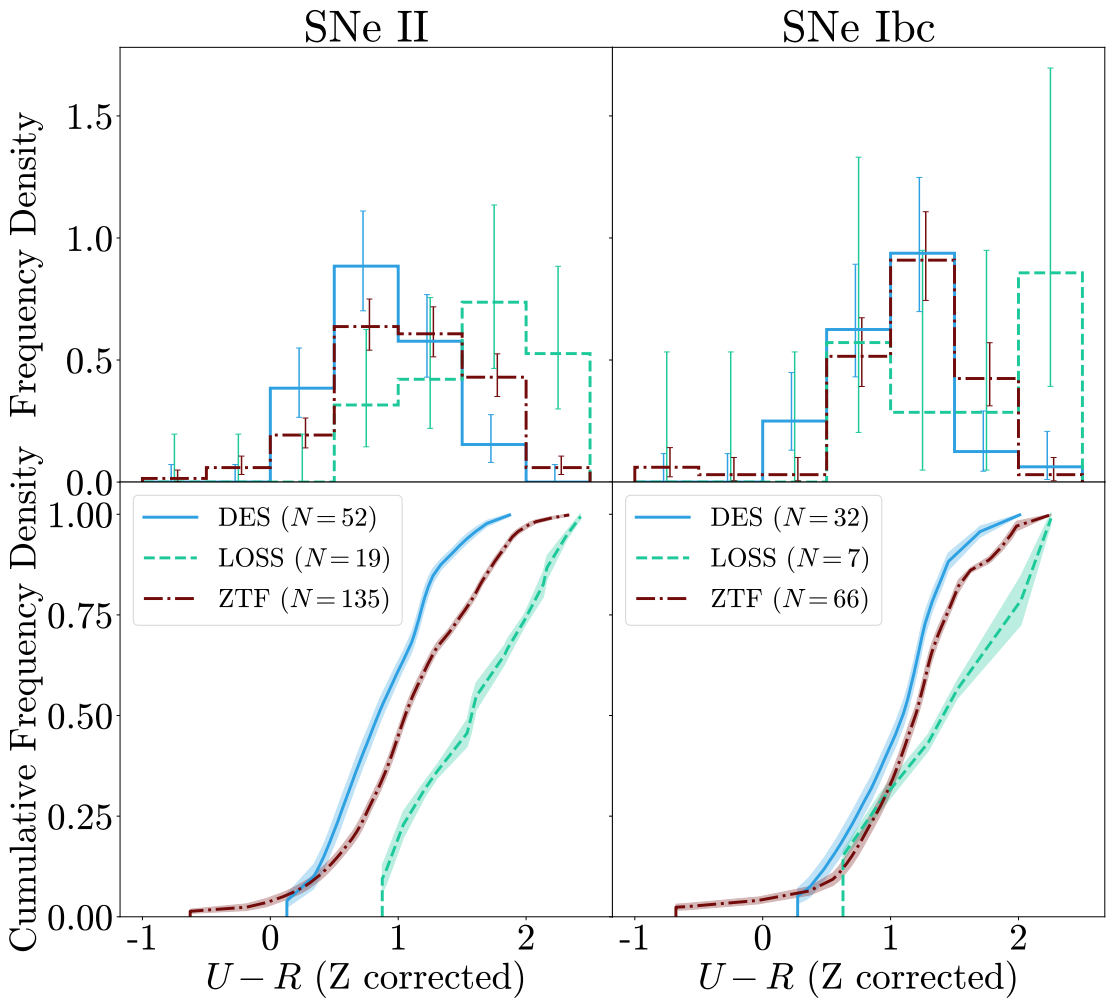

FIGURE 3.14: Host galaxy rest-frame $U - R$ colour distributions and cumulative distributions, corrected for the effects of metallicity evolution with redshift, for both SNe II and SNe Ibc for DES, LOSS and ZTF samples.

of DES. I find that rest-frame $U - R$ colours from SDSS photometry are consistent with those from DES with no systematic offset between the two. Overall, the difference in host colour does not seem to be caused by systematic differences in the data used to calculate host properties.

3.3.3.5 What Causes the Host Colour Discrepancy?

In summary, the difference in host galaxy rest-frame colour between the ZTF and DES samples is not obviously caused by selection biases in the two samples or systematic differences in the SED fitting for DES and ZTF, and metallicity evolution with redshift can only partially explain this offset. It should also be noted that the difference in host colour is much more pronounced in the SN II host sample: if there were some overall systematic bias, the same effect would expect to be seen in the SN Ibc sample as well.

It remains unclear what may be driving the difference in host colour, and more data is required to study this in further detail.

3.4 Summary

DES provides a large sample of high-redshift spectroscopically and photometrically-confirmed CCSNe. I have derived rest-frame luminosity functions for the DES sample using SED models to K-correct to the rest-frame and GP-interpolations to estimate the peak luminosity. To investigate the possible effect of redshift evolution on the luminosity function and host properties, I compare these to lower redshift CCSN samples from LOSS and ZTF. I also compare the properties of the corresponding host galaxies and examine relations between the SN and host galaxy properties for these samples. The main findings of this work are summarised as follows:

1. I have fit Gaussian and Lorentzian distributions to my calculated luminosity functions for DES and ZTF and present their corresponding parameter values to allow these to be used to simulate CCSN samples.
2. I explore differences between the different luminosity functions. The DES luminosity functions appear brighter than those of LOSS and ZTF, with differences of significance level 3.0σ and 1.8σ to each survey for SNe II and 1.9σ and 1.1σ for SNe Ibc. The ZTF samples are also brighter than LOSS with significances of 2.5σ and 1.8σ.
3. Any differences in the luminosity functions could result from higher levels of host galaxy extinction in LOSS and ZTF, however selecting a subset of DES SNe which explode in redder host galaxies does not change the trends seen which suggests this is not the case. This raises the possibility of a luminosity function which evolves with redshift, although at the significance levels calculated it cannot be definitively concluded that these differences are real. Assuming that these differences are significant, causes such as differing host extinction cannot be ruled out without measurements of this.
4. There are differences in the host galaxy properties of the LOSS CCSNe compared to the DES and ZTF CCSNe, but these are expected given that LOSS is a galaxy-targeted survey while DES and ZTF are untargeted.
5. There are also differences in the host galaxy properties of DES CCSNe compared with those in ZTF. The host galaxy stellar masses of both samples are consistent across both SNe II and SNe Ibc. However, for SNe II, DES host galaxies are significantly bluer than the ZTF hosts with a significance levels of 3.4σ and 3.8σ from two-sample KS and AD tests respectively.

6. I explore correcting the host galaxy colours to account for redshift evolution, and study the possibility that this difference is caused by selection biases in the DES or ZTF samples or systematic differences in the data used, but find that none of these effects are able to adequately explain the differences.

7. The host masses and rest-frame $U - R$ colours of SNe II compared to SNe Ibc are generally consistent in both the LOSS and ZTF samples. In the DES sample, hosts of SNe II appear bluer than those of SNe Ibc but only at a significance level of 2.0σ.

8. Overall, little environmental dependence on SN peak magnitude is observed across the three samples.

Chapter 4

Understanding the Extreme Luminosity of DES14X2fna

In the last chapter I detailed the luminosity functions and host galaxy properties of CCSNe in the Dark Energy Survey. During this analysis, an object stood out that was of particular interest: DES14X2fna, a SN IIb with a peak absolute magnitude of $\simeq$-19.5 in g-band. At the time of identification, this was the brightest SN IIb detected by nearly one mag. ASASSN-18am, another very luminous SN IIb, has since been identified (Bose et al., 2020) but even in comparison to that DES14X2fna stands out as it declines rapidly after peak. In the chapter, I present the spectroscopic and photometric properties of DES14X2fna and investigate potential mechanisms which power this unusual explosion.

4.1 SNe IIb

I have already introduced the large variety of CCSN subtypes in Chapter 1, but will begin here by recapping the physics of SNe IIb. These are an intermediate class of CCSN, displaying hydrogen lines at early times and helium lines at later times.

In the canonical picture of a SN IIb, the light curve is driven by the radioactive decay chain of ^{56}Ni synthesised in the explosion, which subsequently decays into ^{56}Co and then stable ^{56}Fe. Treatments of this radioactive decay model, for example the commonly used 'Arnett' model from Arnett (1982) and more recently Khatami & Kasen (2019), allow for various properties of the explosion to be estimated. For SNe with light curves driven by ^{56}Ni decay such as SNe IIb, a more luminous SN indicates a higher synthesised mass of ^{56}Ni to power the peak of the light curve.

As discussed in Chapter 1, whether SNe IIb, Ib, Ic and Ic-BL are distinct classes or part of a continuum remains an open question. Galbany et al. (2018) finds that SNe IIb

have unusual host properties compared with other core-collapse SN hosts, having particularly low metallicity and SFR. However, Schulze et al. (2021) finds that the host properties of SNe IIb are consistent with those of SNe II. SNe Ib, Ic and Ic-BL have been previously observed with peak absolute magnitudes from -16 up to and even brighter than -20, as shown in Figures 2 and 3 of Modjaz et al. (2019). Historically, SNe IIb have exhibited less diversity in peak luminosity, ranging from a peak r/R-band absolute magnitude of roughly -16.5 to -18. However, the discovery of ASASSN-18am with a peak $M_V \sim$ -19.7 (Bose et al., 2020) demonstrated that SNe IIb can reach considerable luminosities.

4.2 Observations

DES14X2fna was discovered by DES-SN in an r-band image captured by DECam at an apparent magnitude of $m_r = 19.1$ mag. This discovery was on 2014 October 1 (MJD 56931.2), with a previous non-detection on 2014 September 24 (MJD 56924.2) at $m_z \sim 23.7$. The transient was located in a faint host galaxy with $M_r \sim -16$ at $z = 0.0453$[1], at position α = $02^{\mathrm{h}}23^{\mathrm{m}}15\overset{\mathrm{s}}{.}64$, δ = -07°05′20.″8 (J2000). Based on the epochs of first detection and last non-detection, I use an explosion date of MJD 56927.7 $\pm$ 3.5 d.

After discovery, *griz* photometric coverage was acquired by DES-SN until January 2015. Photometric measurements were made using the processes outlined in Section 2.1.1. I correct this observed photometry for Milky Way extinction and K-correct to the rest-frame using the method outlined in Section 2.3.3; however, in this analysis the K-correction was done using SED templates of DES14X2fna from Hounsell et al. (in prep.) in order to focus on the specific SED of this object rather than the more general templates used for the luminosity functions in Chapter 3. For this work, I consider host galaxy extinction to be negligible based on Hα and Hβ flux ratios in spectroscopy of the host, finding these to be consistent with $E(B\text{-}V)_{\mathrm{host}} \sim 0$ (Osterbrock, 1989).

DES14X2fna is both luminous and relatively low redshift meaning that the observed photometry is very high signal-to-noise and the statistical uncertainties reach millimag levels at peak. In practice, the uncertainties will be larger than this - for this analysis, I add the statistical errors in quadrature with a value of 0.05 mag to represent systematic uncertainty. This value was selected as the smallest statistical error which lead to a stable GP fit across the full light curve with minimal unphysical undulations at late times. This late time behaviour was not significant when considering the peak luminosity of the SN in Chapter 3 but becomes more significant here when considering the full evolution of DES14X2fna. The observed photometry without any corrections is detailed in Table 4.1, and the corrected rest-frame light curves, incorporating this systematic error, are shown in Figure 4.1 and also detailed in

[1]Obtained from narrow host galaxy emission features

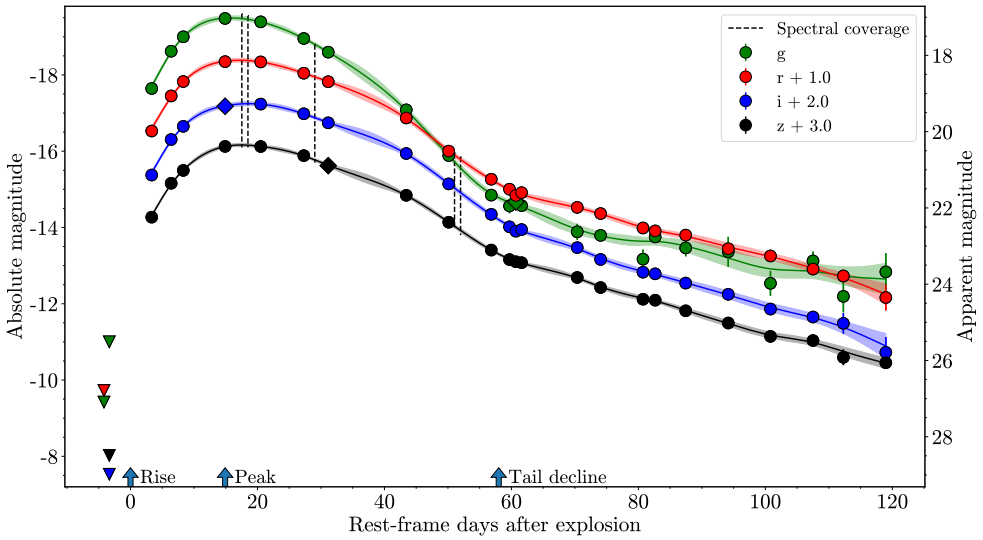

FIGURE 4.1: *griz* light curves of DES14X2fna, corrected for Milky Way extinction and k-corrected to the rest frame. Missing epochs of data have been interpolated using GP-interpolation. The dashed vertical lines indicate the epochs of spectral coverage, and the triangles prior to explosion denote upper limits. Diamond markers for data points indicate that they were reconstructed based on GP-interpolation of the full observer-frame light curve.

Table 4.1. The GP-interpolated light curve used to reconstruct missing data was applied in the observer-frame - as such, it is not plotted with the rest-frame data in this figure. Instead, the GP-interpolation shown is obtained from this rest-frame data and is included to illustrate the fits obtained from GP-interpolation to photometry of DES14X2fna.

Spectroscopy of DES14X2fna was taken between +17.5 and +52 d (all phases stated in this chapter are in the rest-frame and with respect to explosion epoch). These spectra were obtained with three different instruments: the AAOmega spectrograph at the Anglo-Australian Telescope (AAT) as part of the OzDES spectroscopic follow-up program, the Kast Double Spectrograph at Lick Observatory (LO) and the Blue Channel Spectrograph at the MMT Observatory. Details of the spectroscopic observations are in Table 4.2. Spectroscopic reductions were performed using standard procedures; the AAT spectrum was reduced following the procedure outlined in Childress et al. (2017).

The spectral evolution of DES14X2fna is shown in Figure 4.2. Note that as these spectra are only used for classification and calculating line velocities, they have not been calibrated to match photometry. Based on the presence of hydrogen at 18.5 days, it was initially classified as a SN II (Graham et al., 2014). The appearance of helium at 52 days led to a reclassification as a SN IIb (Kuehn et al., 2014).

TABLE 4.1: Observed and rest-frame photometry of DES14X2fna, quoted in AB magnitudes in the natural DECam system. Note that this observer-frame photometry has not been corrected for Milky Way extinction and quoted uncertainties are purely statistical. For this analysis, these have been added in quadrature with an error of 0.05 mag to represent systematic uncertainty, and these are included in the rest-frame photometry. Phases are given with respect to explosion.

MJD	UT date	Rest-frame phase (d)	g (mag)	(rest) (mag)	r (mag)	(rest) (mag)	i (mag)	(rest) (mag)	z (mag)	(rest) (mag)
56923.3	20140923	-4.2	>23.7	–	>23.5	–	–	–	–	–
56924.2	20140924	-3.3	>23.9	–	–	–	>23.9	–	>23.7	–
56931.1	20141001	3.3	18.980±0.005	18.87±0.07	19.13±0.01	18.98±0.06	19.30±0.01	19.14±0.06	19.44±0.01	19.24±0.05
56934.4	20141004	6.4	18.115±0.003	17.89±0.05	18.281±0.004	18.06±0.05	18.42±0.01	18.21±0.05	18.60±0.01	18.35±0.05
56936.3	20141006	8.3	17.504±0.002	17.51±0.05	17.727±0.002	17.69±0.05	17.911±0.002	17.86±0.05	18.077±0.003	18.02±0.05
56943.2	20141013	14.9	17.137±0.001	17.03±0.05	17.278±0.001	17.16±0.05	–	17.33±0.05	17.569±0.002	17.39±0.05
56949.1	20141019	20.5	17.240±0.002	17.12±0.05	17.291±0.002	17.17±0.05	17.40±0.01	17.28±0.05	17.524±0.003	17.39±0.05
56956.2	20141026	27.3	17.655±0.002	17.56±0.05	17.604±0.002	17.47±0.05	17.688±0.002	17.53±0.05	17.782±0.002	17.63±0.05
56960.2	20141030	31.1	17.986±0.002	17.92±0.06	17.826±0.002	17.69±0.05	17.906±0.002	17.77±0.05	–	17.89±0.05
56973.0	20141112	43.4	19.405±0.005	19.43±0.07	18.726±0.003	18.64±0.06	18.716±0.003	18.57±0.06	18.780±0.004	18.67±0.05
56980.0	20141119	50.1	20.55±0.01	20.63±0.07	19.57±0.01	19.51±0.06	19.49±0.01	19.37±0.05	19.43±0.01	19.38±0.05
56987.0	20141126	56.8	21.53±0.02	21.66±0.07	20.32±0.01	20.25±0.06	20.28±0.01	20.17±0.06	20.08±0.01	20.11±0.05
56990.1	20141129	59.7	21.85±0.14	21.95±0.19	20.51±0.06	20.51±0.08	20.51±0.17	20.50±0.09	20.37±0.04	20.35±0.06
56991.1	20141130	60.7	–	21.84±0.11	20.81±0.04	20.67±0.06	20.73±0.04	20.61±0.06	20.41±0.04	20.41±0.05
56992.1	20141201	61.6	21.83±0.06	21.94±0.10	20.65±0.02	20.60±0.06	20.65±0.02	20.57±0.05	20.36±0.02	20.44±0.05
57001.3	20141210	70.4	22.46±0.15	22.63±0.21	21.07±0.03	20.99±0.07	21.13±0.03	21.04±0.06	20.72±0.03	20.82±0.05
57005.0	20141214	74.0	22.55±0.08	22.72±0.12	21.26±0.03	21.15±0.07	–	21.35±0.07	–	21.09±0.06
57005.1	20141214	74.1	–	–	–	–	21.44±0.05	–	20.93±0.03	–
57012.0	20141221	80.7	23.14±0.20	23.34±0.25	21.63±0.05	23.34±0.25	21.77±0.07	23.34±0.25	21.24±0.05	23.34±0.25
57014.0	20141223	82.6	22.67±0.07	22.76±0.12	21.71±0.03	22.76±0.12	21.79±0.04	22.76±0.12	21.29±0.03	22.76±0.12
57019.1	20141228	87.5	22.93±0.16	23.05±0.22	21.84±0.06	23.05±0.22	22.07±0.07	23.05±0.22	21.54±0.07	23.05±0.22
57026.1	20150104	94.2	23.12±0.32	23.15±0.39	22.21±0.11	23.15±0.39	22.36±0.11	23.15±0.39	21.90±0.07	23.15±0.39
57033.0	20150111	100.8	23.80±0.29	23.98±0.33	22.40±0.07	23.98±0.33	22.76±0.12	23.98±0.33	22.17±0.08	23.98±0.33
57040.0	20150118	107.5	23.42±0.21	23.39±0.24	22.76±0.09	23.39±0.24	22.90±0.12	23.39±0.24	22.34±0.09	23.39±0.24
57045.1	20150123	112.3	24.22±0.39	24.32±0.42	22.89±0.13	24.32±0.42	23.19±0.26	24.32±0.42	22.92±0.26	24.32±0.42
57052.1	20150130	119.0	23.77±0.46	23.68±0.49	23.58±0.34	23.68±0.49	23.78±0.34	23.68±0.49	22.86±0.15	23.68±0.49

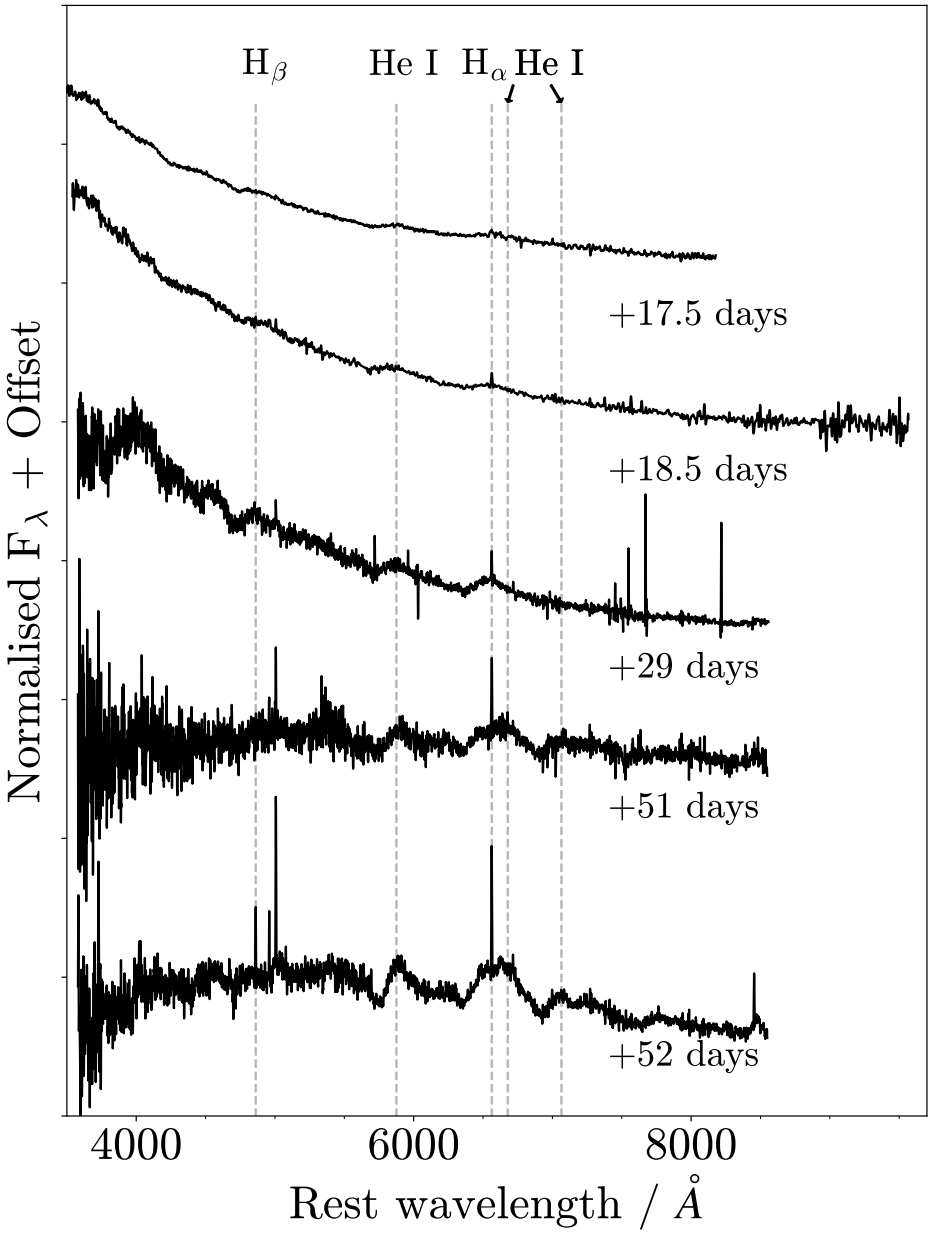

FIGURE 4.2: Optical spectra of DES14X2fna. Each spectrum has been smoothed using a Savitzky-Golay filter. Spectra have been offset by an arbitrary amount for clarity, and corrected for redshift and Milky Way reddening using the extinction model of Fitzpatrick & Massa (2007).

TABLE 4.2: Details of spectroscopy available for DES14X2fna. Phases are given with respect to explosion.

UT date	MJD	Rest-frame phase (d)	Telescope + Instrument	Range (Å)
20141016	56946	+17.5	MMT+BCS	3340-8550
20141017	56947	+18.5	LICK+Kast	3400-10000
20141028	56958	+29	AAT+2dF/AAOmega	3740-8950
20141120	56981	+51	AAT+2dF/AAOmega	3740-8940
20141121	56982	+52	AAT+2dF/AAOmega	3740-8950

NOTES:
BCS – Blue Channel Spectrograph on MMT 6.5m telescope
Kast – Kast Double Spectrograph on the 3m Shane telescope at Lick Observatory
2dF/AAOmega – 2dF fibre positioner and AAOmega spectrograph on the 3.9-metre Anglo-Australian Telescope (AAT)

4.3 Characterising DES14X2fna

4.3.1 Host Galaxy

DES14X2fna was located in an anonymous host galaxy at a redshift of 0.0453. Assuming peculiar velocity dispersion of 200 km s^{-1}, this corresponds to a distance of 200.7±3.0 Mpc or a distance modulus of $\mu = 36.51 \pm 0.03$ mag. Global properties of the host were inferred using *griz*-band photometry from the deep stacked templates of the DES-SN fields from Wiseman et al. (2020a) described in Chapter 2. A composite *gri*-band image of the host galaxy from these templates is shown in Figure 4.3. The neighbouring galaxy is at $z = 0.207$. This photometry corresponds to an absolute magnitude of $M_r = -16.35 \pm 0.03$. Stellar mass ($M_{stellar}$) and star formation rate (SFR) are estimated using stellar population synthesis models based on the templates of Bruzual & Charlot (2003) with a Chabrier (2003) IMF, as per Wiseman et al. (2020b), measuring $\log_{10}(M_*/M_\odot)=8.13^{+0.16}_{-0.07}$ and $\log_{10}(\mathrm{SFR}/M_\odot \mathrm{yr}^{-1})=-1.53^{+0.23}_{-0.47}$. These results are consistent with those from fitting with PÉGASE templates and a Kroupa IMF using the method of Smith et al. (2020b).

Abundance measurements are derived from nebular emission lines in the host galaxy spectrum[2] from the OzDES survey (Lidman et al., 2020), a spectroscopic redshift follow-up programme for DES. Emission line measurements and abundance calculations are performed using the method outlined in Wiseman et al. (2020b). Briefly, the stellar continuum is subtracted along with any Balmer line absorption using the Penalized PiXel-Fitting software (pPXF; Cappellari & Emsellem, 2004; Cappellari et al., 2012; Cappellari, 2017) with the MILES library of single stellar

[2]Host spectrum of the host of DES14X2fna was taken in September 2018, by which time the SN had completely faded from view.

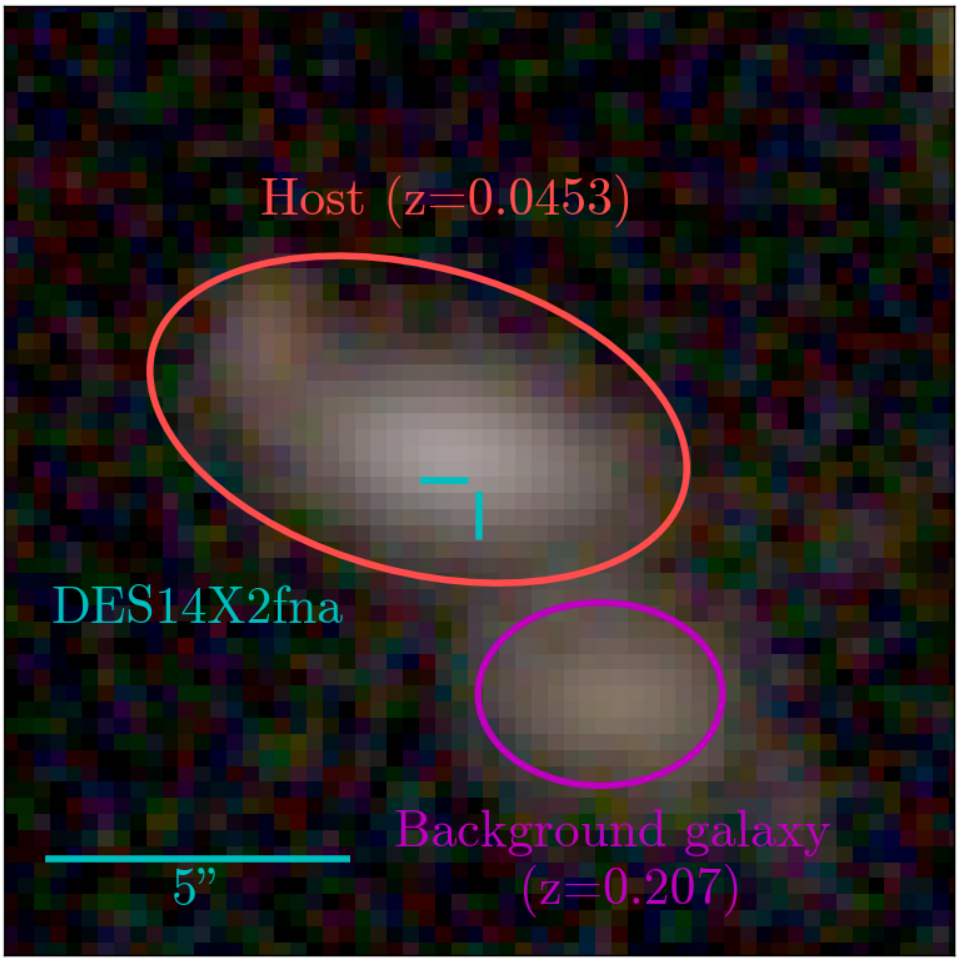

FIGURE 4.3: A composite *gri*-band image of the host galaxy of DES14X2fna, from the stacked templates of the DES-SN field of Wiseman et al. (2020a). The location of the SN is indicated by the blue markers. The adjacent galaxy, shown by the purple circle, is at higher redshift and not in proximity to the host.

populations (Vazdekis et al., 2010), and the resulting gas spectrum is fit with Gaussian profiles. Line fluxes are used to derive metallicities based on a number of different calibrations: S2N2 (Dopita et al., 2016), N2 and O3N2 (Pettini & Pagel, 2004), and R23 (Kewley et al., 2004) (Table 4.3).

Comparing the mass of the host of DES14X2fna with previous studies of stellar masses of core-collapse SN hosts (e.g. Figure 4 of Galbany et al. 2018, Figure 11 of Wiseman et al. 2020a, Figure 14 of Schulze et al. 2021) indicates that this is a relatively low mass host although not unusually low for a SN IIb. The PISCO sample of host galaxies presented in Galbany et al. (2018) contains 13 SNe IIb host environments - this sample varies in PP04 O3N2 metallicity between approximately 8.4 to 8.7 and in $\log_{10}(\mathrm{sSFR}/\mathrm{yr}^{-1})$ between approximately -11.2 to -9.5. DES14X2fna is lower metallicity than any of these hosts but falls in the upper end of the distribution in terms of sSFR. The PTF sample presented in Schulze et al. (2021) contains 61 SNe IIb

TABLE 4.3: Properties of the host galaxy of DES14X2fna.

Property	Host Value
M_g	-16.01 $\pm$ 0.04 mag
M_r	-16.34 $\pm$ 0.04 mag
M_i	-16.50 $\pm$ 0.05 mag
M_z	-16.56 $\pm$ 0.05 mag
Redshift	0.0453 $\pm$ 0.0005
E(B-V)$_{MW}$	0.0225 mag
$\log_{10}(M_*/M_\odot)$	$8.13^{+0.16}_{-0.07}$
$\log_{10}(\mathrm{SFR}/M_\odot \mathrm{yr}^{-1})$	$-1.53^{+0.26}_{-0.48}$
$\log_{10}(\mathrm{sSFR}/\mathrm{yr}^{-1})$	$-9.66^{+0.10}_{-0.41}$
Metallicity: S2N2 D16	$7.76^{+0.31}_{-0.54}$ dex
Metallicity: PP04 N2	$8.17^{+0.11}_{-0.17}$ dex
Metallicity: PP04 O3N2	$8.19^{+0.09}_{-0.14}$ dex
Metallicity: KK04 R23	$8.17^{+0.20}_{-0.23}$ dex

hosts which extend down to $10^6 M_\odot$. For this sample, $\log_{10}(\mathrm{sSFR}/\mathrm{yr}^{-1})$ varies from approximately -12 to -8. The host of DES14X2fna sits towards the upper end of this distribution, although it is not as standout as compared to the PISCO sample.

In summary, the host of DES14X2fna is a low-mass, low-metallicity but relatively highly star-forming galaxy. The majority of core-collapse SNe are observed across a wide range of star-forming hosts (Anderson et al., 2010). However, as discussed in Chapter 1, the most energetic form of stripped envelope SN, SNe Ic-BL, are observed preferentially in low-mass, low-metallicity, star-forming environments similar to DES14X2fna (Japelj et al., 2018; Modjaz et al., 2020).

4.3.2 Photometry

The rest-frame *griz* light curves of DES14X2fna are shown in Figure 4.1. After explosion, DES14X2fna rises to a peak *g*-band absolute magnitude of $\simeq -19.5$, and $\simeq -19.3$, $\simeq -19.2$ and $\simeq -19.1$ in *riz*-bands respectively. After peak *g*-band declines by $\sim$5 mags in $\sim$40 days, while *riz* decline by $\sim$3 mags over the same period. After approximately 60 days, each band appears to show a roughly linear decline. GP-interpolation can be used to estimate the rise time and peak absolute magnitude, but does not directly provide uncertainties on rise time. This is estimated using a Monte Carlo approach, randomising the rest-frame photometry within error bars and GP-interpolating this to estimate the rise time and peak absolute magnitude. This is repeated 1000 times, with the mean and standard deviation taken as the final values and uncertainties. These values are shown in Table 4.4.

To characterise the light curve of DES14X2fna relative to the population of SNe IIb, I have gathered a comparison sample of spectroscopically confirmed SNe IIb. Objects

TABLE 4.4: Peak absolute magnitudes of DES14X2fna estimated from GP interpolation. Statistical errors in rise time estimated from MC approach, systematic errors correspond to uncertainty in explosion epoch between last non-detection and first detection in rest-frame.

Filter	Peak absolute magnitude (mag)	Rise time (d)
g	-19.47 $\pm$ 0.06	$16.67 \pm 0.53_{\rm stat} \pm 3.35_{\rm sys}$
r	-19.37 $\pm$ 0.05	$18.00 \pm 0.56_{\rm stat} \pm 3.35_{\rm sys}$
i	-19.23 $\pm$ 0.06	$18.90 \pm 0.58_{\rm stat} \pm 3.35_{\rm sys}$
z	-19.14 $\pm$ 0.05	$18.35 \pm 0.57_{\rm stat} \pm 3.35_{\rm sys}$

included have publicly-available photometry with good coverage around peak and a well-constrained explosion epoch, either through light curve modelling or a short period between last non-detection and first detection (15 days is the maximum in this sample). This leaves a sample of 22 SNe IIb (see Table 4.5).

The top panel of Figure 4.4 shows the rest-frame r-band light curve of DES14X2fna along with r/R-band light curves of the SNe comparison sample. Note that SN 2009mg, SN 2011ei and SN 2013cu lack sufficient r/R-band coverage and so I have used V-band photometry as the closest wavelength band available to R. For each object GP-interpolation is used to estimate the rise time and peak absolute magnitude. I estimate the epoch at which the linear decline phase of the light curve begins for each SN, $t_{\rm tail}$ and the absolute magnitude at this epoch, $M_{\rm tail}$, by eye, where these could be inferred from the data. In addition, linear fits are used to calculate the tail decline rate where possible. Details and parameter values of each SN in the comparison sample are given in Table 4.5. Light curves are corrected for redshift and Milky Way extinction based on values reported in the respective papers outlined in this table. However, as these objects are all at low redshift, these light curves are not K-corrected into the rest frame since the effect will be small. Uncertainties in quoted peak absolute magnitude ($M_{\rm peak,MW}$) incorporate uncertainty in GP-interpolation to observed photometry and Milky Way extinction correction. Distances are estimated by cross-matching SNe with their hosts using the NASA Extragalactic Database (NED[3]) and obtaining a luminosity distance in the assumed cosmology for this analysis corrected for Virgo infall. This approach is chosen for consistency as some of these hosts do not have redshift-independent distance estimates and where they do these are often calculated for different cosmologies. The exception to this is SN 1993J, as the negative redshift of the host means that a redshift distance is not appropriate - instead, the literature value of 2.9$\pm$0.4 Mpc from Lennarz et al. (2012) is adopted. Distance uncertainties are included in this analysis. Where data is available, I correct for host extinction and factor this into the peak absolute magnitude $M_{\rm peak,host}$. However, as this data was not available for all objects and only an upper limit in some

[3] http://ned.ipac.caltech.edu/

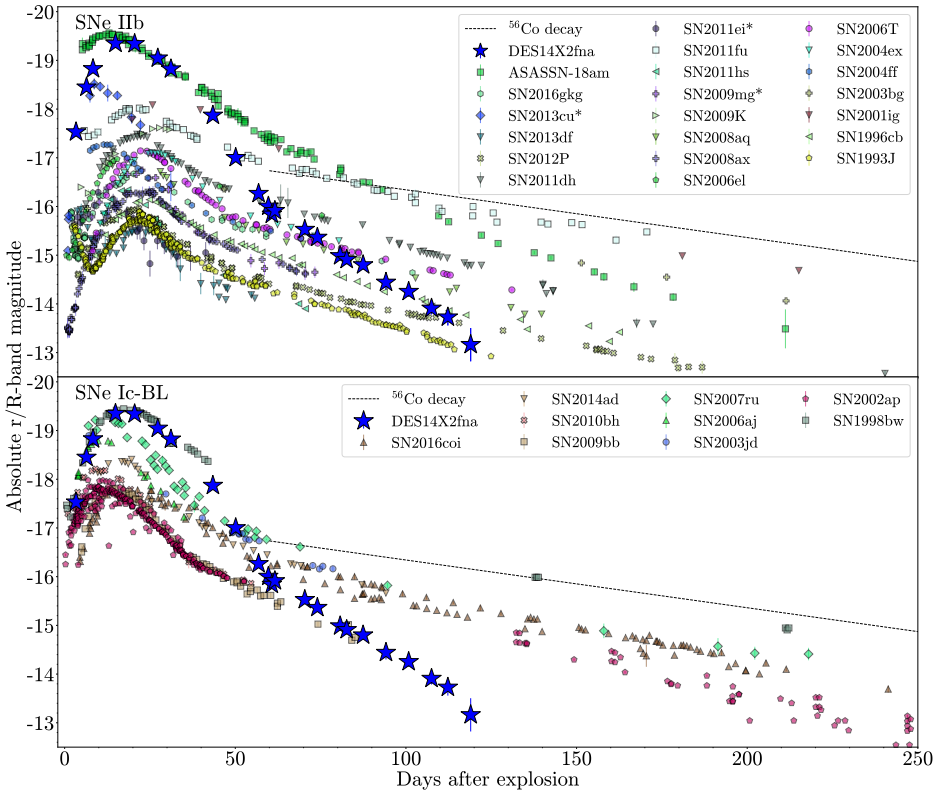

FIGURE 4.4: **Upper:** *r*-band light curve of DES14X2fna alongside the *r*/*R*-band light curves of the SN IIb comparison sample. The dashed line indicates the decline rate expected for fully-trapped ^{56}Co decay. Objects denoted with * in the legend show *V*-band photometry due to a lack of available *r*/*R*-band data **Lower:** Same as upper panel but for a comparison sample of SNe Ic-BL. All light curves are corrected for MW extinction, and DES14X2fna is k-corrected to the rest-frame.

cases I do not correct for host extinction when considering bolometric luminosities in order to be consistent across all objects.

The most noticeable feature of DES14X2fna is its very high peak luminosity, 0.2 mag fainter than the very luminous ASASSN-18am at peak but nearly one mag brighter than the next brightest object in the sample, SN 2013cu. It is important to note that host extinction can make a significant difference to the luminosity of each object, as in the case of SN 2008ax which shows an increase in peak luminosity of greater than 1 mag. However, as most objects have a host extinction considerably less than this and DES14X2fna is significantly more luminous than most of the sample, DES14X2fna still stands out for its considerable luminosity even when accounting for this possibility. DES14X2fna rises to peak in *r*-band in 18 days, similar to ASASSN-18am and SN 2011hs and fairly typical for SNe IIb based on the sample of SN IIb rise times presented in Figure 4 of Pessi et al. (2019). After rising to maximum, DES14X2fna

declines at a similar rate to ASASSN-18am until $\sim$ 30 days after explosion, after which DES14X2fna begins to decline far more rapidly.

DES14X2fna has a single-peaked light curve similar to SN 2008ax and unlike the well-studied SN 1993J. However, as there is a period of $\simeq$7 days between the last non-detection and first detection it is possible that an initial peak did occur but was not observed, as this has been observed to last only a few days in previous SNe (Okyudo et al., 1993; Helou et al., 2013; Tartaglia et al., 2017).

Motivated by the bright peak luminosity of DES14X2fna, I also compare to SNe Ic-BL to study any resemblance to this very energetic class of stripped envelope SNe. Following the method for the SN IIb sample, I form a similar comparison sample of SNe Ic-BL (Table 4.6), and light curves for these objects are shown in the lower panel of Figure 4.4. Overall, the peak of DES14X2fna resembles that of a SN Ic-BL more closely than a typical SN IIb. Most notably, in *r*-band DES14X2fna matches SN 1998bw well until $\simeq$ 30 days after explosion. After this time DES14X2fna declines more rapidly than SN 1998bw.

As is evident from both panels of Figure 4.4, after peak DES14X2fna exhibits a very rapid tail decline compared to both SNe IIb and SNe Ic-BL. The top panel of Figure 4.5 focuses on this decline phase for each SN in the SN IIb comparison sample where a tail is apparent. For each SN in the plot, a line is fit to the tail to estimate the decline rate (Table 4.5). DES14X2fna has an *r*-band decline rate of 4.30 ± 0.10 mag $(100\mathrm{d})^{-1}$, significantly faster than ASASSN-18am, the next fastest decliner in the sample (3.03 ± 0.06 mag $(100\mathrm{d})^{-1}$). The lower panel of Figure 4.5 also shows a histogram of the estimated decline rates for the sample, where DES14X2fna is a clear outlier.

It is evident that DES14X2fna exhibits both a very luminous peak and a faster tail evolution than other previously observed SNe IIb. Assuming that this object follows the canonical ^{56}Ni decay model for a SN IIb, high ^{56}Ni and ejecta masses would be required to power the high maximum luminosity and broad peak of DES14X2fna. However, a high ejecta mass would be expected to lead to complete trapping of the γ-rays produced in ^{56}Co decay at late times as there would be significant surrounding material to absorb these γ-rays. Not only does DES14X2fna decline at a rate far faster than expected for fully-trapped ^{56}Co decay, it declines more than 1.0 mag $(100\mathrm{d})^{-1}$ faster than any other SN IIb in the comparison sample. This raises the question of whether the light curve of DES14X2fna is consistent with a ^{56}Ni decay model or if an alternative mechanism to power the light curve is required.

4.3.3 Bolometric Luminosity

I next consider the bolometric and pseudo-bolometric light curves of DES14X2fna. Observed *griz* light curves are converted to luminosities by fitting with a black body

TABLE 4.5: Details and light curve properties of the SN IIb comparison sample. These properties were calculated using r/R-band photometry with the exception of SNe marked with *, for which V-band light curves were used due to a lack of r/R-band data. Missing host extinction values have been labelled as either negligible based on spectroscopy or N/A if no host extinction data was available. All presented magnitudes are in AB system. Where SN explosion dates were calculated using the dates of first detection and last non-detection, rise time uncertainties have quoted systematic errors as in Table 4.4. These values are not quoted where explosion epochs were sourced from literature using other methods.

SN	Redshift	$E(B-V)_{MW}$ (mag)	$E(B-V)_{host}$ (mag)	Rise time (d)	$M_{peak,MW}$ (mag)	$M_{peak,host}$ (mag)	t_{tail} (d)	M_{tail} (mag)	Tail decline rate (mag 100d^{-1})	References
DES14X2fna	0.0453	0.0225±0.0003	Negligible	$18.00\pm0.56_{stat}\pm3.35_{sys}$	-19.37±0.05	–	60	-16	4.30±0.10	–
ASASSN-18am	0.0301	0.0086±0.0011	Negligible	$18.89\pm0.42_{stat}\pm0.39_{sys}$	-19.53±0.04	–	60	-17.3	3.03±0.06	(1)
SN 2016gkg	0.0049	0.0166±0.0002	$0.09^{+0.08}_{-0.07}$	$20.39\pm1.11_{stat}\pm0.16_{sys}$	-16.69±0.06	$-16.97^{+0.26}_{-0.22}$	43	-16	1.63±0.08	(2), (3), (4), (5), (6), (7)
SN 2013cu*	0.0252	0.0105±0.0003	N/A	$9.79\pm1.08_{stat}\pm0.97_{sys}$	-18.51±0.07	–	–	–	–	(2), (8)
SN 2013df	0.0024	0.0168±0.0002	0.081 ± 0.016	$22.32\pm0.68_{stat}$	-15.54±0.04	-15.80±0.06	40	-14.8	1.96±0.02	(2), (9), (10), (11), (12)
SN 2012P	0.0045	0.0437±0.0005	$0.29^{+0.08}_{-0.05}$	$20.32\pm0.19_{stat}$	-15.93±0.03	$-16.83^{+0.25}_{-0.16}$	[50,60]	[-14,-14.2]	1.44±0.02	(2), (13)
SN 2011dh	0.0016	0.0309±0.0017	j0.05	$21.89\pm0.19_{stat}\pm0.88_{sys}$	-17.47±0.03	–	48	-15.8	2.02±0.03	(2), (9), (14), (15), (16)
SN 2011el*	0.0093	0.0505±0.0008	0.18	$11.84\pm0.70_{stat}$	-16.14±0.07	-16.70±0.07	–	–	–	(2), (17)
SN 2011fu	0.0185	0.0648±0.0008	0.15±0.11	$20.47\pm0.54_{stat}$	-18.01±0.03	-18.48±0.34	[40,45]	[-17.2,-17.4]	1.69±0.05	(18), (19)
SN 2011hs	0.0057	0.0104±0.0004	0.16±0.07	$17.91\pm0.29_{stat}$	-16.35±0.03	-16.85±0.22	35	-15.1	2.14±0.02	(2), (20)
SN 2009K	0.0117	0.0491±0.0014	N/A	$27.46\pm0.41_{stat}\pm1.21_{sys}$	-17.61±0.03	–	–	–	–	(21), (22), (23), (24)
SN 2009mg*	0.0076	0.0388±0.0005	0.09±0.02	$21.06\pm1.00_{stat}$	-16.70±0.05	-16.98±0.08	–	–	–	(2), (25)
SN 2008aq	0.008	0.0386±0.0009	0.027	$20.11\pm0.44_{stat}$	-16.91±0.04	-17.00±0.04	47	-15.7	2.18±0.04	(2), (21), (22), (26)
SN 2008ax	0.0019	0.0188±0.0002	0.38±0.1	$23.92\pm1.07_{stat}$	-16.32±0.04	-17.50±0.31	40	-15.3	2.13±0.03	(2), (22), (27), (28)
SN 2006el	0.017	0.0975±0.0012	N/A	$22.21\pm1.00_{stat}$	-17.14±0.09	–	–	–	–	(22), (29)
SN 2006T	0.0081	0.0643±0.0007	N/A	$22.83\pm0.23_{stat}\pm7.63_{sys}$	-17.15±0.03	–	48	-15.9	1.79±0.02	(2), (21), (22)
SN 2004ex	0.018	0.0184±0.0016	N/A	$25.67\pm0.56_{stat}\pm10.43_{sys}$	-17.10±0.03	–	54	-15.9	2.06±0.08	(22)
SN 2004ff	0.023	0.0274±0.001	N/A	$11.82\pm0.37_{stat}$	-17.27±0.03	–	40	-16	1.88±0.08	(21), (29), (30)
SN 2003bg	0.0046	0.018±0.001	Negligible	$49.41\pm0.81_{stat}$	-16.36±0.04	–	–	–	1.29±0.06	(31)
SN 2001ig	0.0031	0.0089±0.0004	j0.09	$30.14\pm3.86_{stat}$	-18.01±0.07	–	–	–	–	(32)
SN 1996cb	0.0024	0.0261±0.0005	j0.12	$24.09\pm0.67_{stat}$	-16.10±0.05	–	44	-15.6	2.21±0.03	(33)
SN 1993J	-0.0001	0.069±0.0001	0.12±0.07	$20.99\pm4.42_{stat}$	-15.75±0.04	-16.12±0.22	40	-14.7	2.18±0.02	(9), (34), (35), (36), (37), (38), (39), (40), (41), (42), (43)

References: (1) Bose et al. (2020); (2) Brown et al. (2014); (3) Bersten et al. (2018); (4) Tonry et al. (2016); (5) Arcavi et al. (2017b); (6) Nicholls et al. (2016); (7) Kilpatrick et al. (2016); (8) Ofek et al. (2014); (9) Tinyanont et al. (2016); (10) Szalai et al. (2016); (11) Maeda et al. (2015); (12) Morales-Garoffolo et al. (2014); (13) Fremling et al. (2016); (14) Ergon et al. (2015); (15) Sahu et al. (2013); (16) Helou et al. (2013); (17) Drake et al. (2009); (18) Kumar et al. (2013); (19) Ciabattari & Mazzoni (2011); (20) Bufano et al. (2014); (21) Stritzinger et al. (2018); (22) Bianco et al. (2014); (23) Hicken et al. (2017); (24) Pignata et al. (2009); (25) Monard (2009); (26) Chu et al. (2008); (27) Tsvetkov et al. (2009); (28) Pastorello et al. (2008); (29) Drout et al. (2011); (30) Pugh et al. (2004); (31) Galbany et al. (2016); (32) Kato et al. (2004); (33) Qiu et al. (1999); (34) Richmond et al. (1996); (35) Barbon et al. (1995); (36) Metlova et al. (1995); (37) Richmond et al. (1994); (38) Lewis et al. (1994); (39) Benson et al. (1994); (40) van Driel et al. (1993); (41) Okyudo et al. (1993); (42) Mikuz et al. (1993); (43) Zhou (1993).

TABLE 4.6: Details of SN Ic-BL comparison sample.

SN	Redshift	$E(B-V)_{\rm MW}$	References
SN 2016coi	0.003646	0.0737	(1)
SN 2014ad	0.0057	0.038	(2)
SN 2010bh	0.0593	0.1004	(3)
SN 2009bb	0.0104	0.0847	(4), (5)
SN 2007ru	0.0155	0.2217	(6), (7)
SN 2006aj	0.033023	0.1261	(6)
SN 2003jd	0.019	0.0378	(6)
SN 2002ap	0.002108	0.0616	(6), (8), (9), (10), (11)
SN 1998bw	0.0085	0.0494	(12), (13), (14), (15)

(1) Prentice et al. (2018); (2) Sahu et al. (2018); (3) Cano et al. (2011); (4) Stritzinger et al. (2018); (5) Pignata et al. (2011); (6) Bianco et al. (2014); (7) Sahu et al. (2009); (8) Foley et al. (2003); (9) Yoshii et al. (2003); (10) Pandey et al. (2003); (11) Gal-Yam et al. (2002); (12) Sollerman et al. (2002); (13) Patat et al. (2001); (14) Sollerman et al. (2000); (15) Galama et al. (1998)

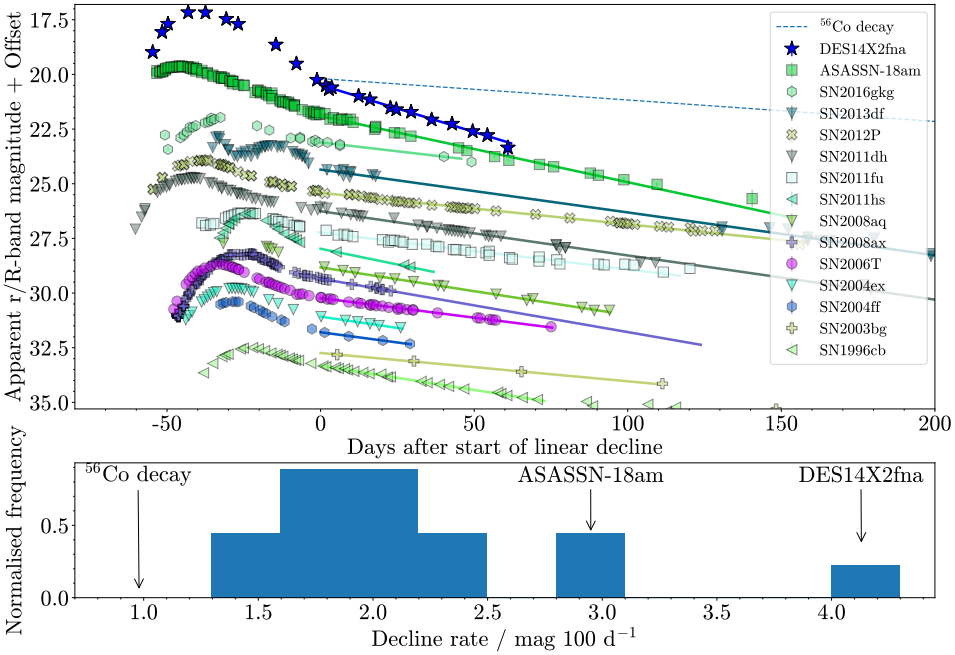

FIGURE 4.5: **Upper:** r-band light curve of DES14X2fna and the r/R-band light curves of the SNe in the SN IIb comparison sample that exhibit a linear decline. The solid lines show a linear fit to the post-peak linear decline of each SN. **Lower:** Histogram showing r/R-band decline rates estimated from the linear fits in upper panel, with DES14X2fna annotated.

curve to compute an SED. The exact values and uncertainties in bolometric luminosities were estimated using a Monte Carlo approach:

- An initial black body fit is carried out to estimate photospheric radius and temperature along with their uncertainties.
- Randomised radius and temperature values are then drawn from a Gaussian distribution using the best-fit values and uncertainties and used to generate a randomised black body SED.
- Each randomised SED is integrated over the wavelength range covered by *griz* bands to produce a pseudo-bolometric luminosity, L_{griz}. A bolometric luminosity $L_{\rm bol}$ is estimated by integrating the fitted SED over all wavelengths.
- This process is then repeated, with the final values of L_{griz} and $L_{\rm bol}$ as well as their uncertainties calculated from the mean and standard deviation of values from all the randomised black body SEDs.

I also considered estimating bolometric luminosity using mangled SED models and the bolometric corrections outlined in Lyman et al. (2013), but find that these obtain consistent results with the black body approach. As a result, black body fits were favoured since these provide information on photospheric temperature and radius as well as luminosity. Of course, the black body approximation is not valid at later times as the SN enters the nebular phase hence bolometric luminosity is not estimated more than 120 days after explosion, after the last observation of DES14X2fna. At later times the decreasing quality of a black body fit is reflected in larger fit uncertainties and hence much larger uncertainties in $L_{\rm bol}$ and L_{griz}. In addition to this, further uncertainty in $L_{\rm bol}$ arises from the lack of flux information beyond optical wavelengths, particularly in the UV. Without observations at these wavelengths, this effect cannot be quantified although I acknowledge that it will serve to increase uncertainty.

To calculate bolometric light curves for the SNe IIb comparison sample, I make cuts to select only SNe with observations in at least 3 photometric bands around peak luminosity to allow reasonable black body fits. Unlike DES14X2fna, this sample of SNe IIb includes objects with photometric data at very different epochs and phases of the light curve, which restricts the epochs at which bolometric luminosities can be calculated. At each epoch with available photometry, other observed bands were GP-interpolated to provide simultaneous photometry, after which the same procedure outlined for DES14X2fna was carried out to estimate black body fit parameters and bolometric luminosities. To ensure consistency with estimates of the pseudo-bolometric luminosity of DES14X2fna, I use the same wavelength limits for integration regardless of which photometric bands were available for each SN. The

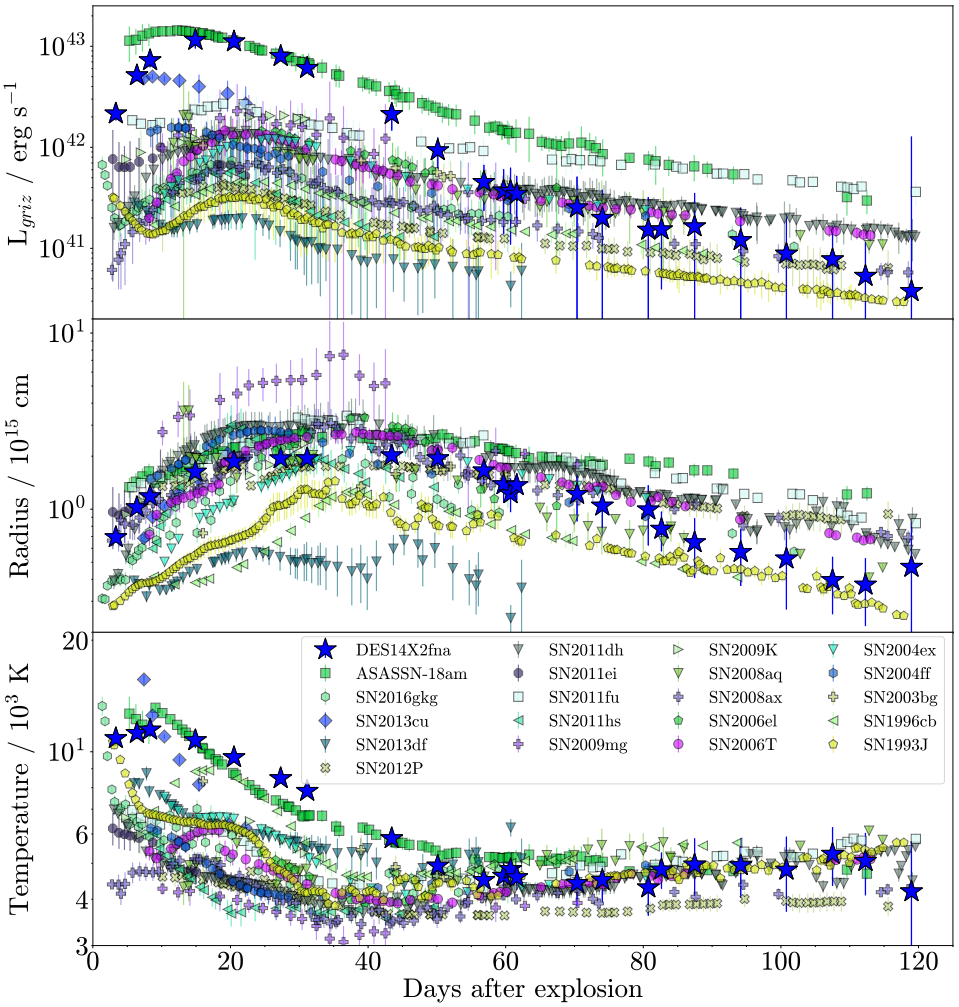

FIGURE 4.6: **Upper:** Bolometric light curves of DES14X2fna and the SN IIb comparison sample, estimated from black body fits to observed photometry. **Middle:** Photospheric radii for DES14X2fna and the SN IIb comparison sample estimated from black body fits. **Lower:** Effective temperatures for DES14X2fna and the SN IIb comparison sample.

bolometric luminosities, photospheric radii and temperatures obtained from these black body fits are shown in Figure 4.6.

As with the r/R-band photometric data, aside from ASASSN-18am DES14X2fna is the most luminous object in the SN IIb sample and has a relatively broad light curve peak. The true peak bolometric luminosity and rise time are estimated using GP-interpolation, which gives a peak luminosity of $L_{\rm bol} = (2.44 \pm 0.41) \times 10^{43}$ erg s^{-1} and $L_{griz} = (1.17 \pm 0.08) \times 10^{43}$ erg s^{-1}, with a rise time to peak, t_p of 15.38 days. Except for ASASSN-18am and SN 2013cu, DES14X2fna is brighter at peak than any

other SN in the sample by more than a factor of 2. This reiterates the findings from broad-band photometry: DES14X2fna is very luminous at maximum, comparable only to ASASSN-18am, and has a relatively broad light curve peak.

The photospheric radius of DES14X2fna shows an initial fast rise, reaching $(1.86 \pm 0.08) \times 10^{15}$ cm after 20.5 days, suggesting a photospheric velocity of $\sim$7,900 km s^{-1}. The radius then remains roughly constant for $\sim$ 30 days, before slowly decreasing again. This radius evolution is fairly typical for a SN IIb, most closely resembling SN 2011dh and SN 2004ff. ASASSN-18am also shows a similar radius evolution to DES14X2fna at early times, although declines more slowly after peak.

DES14X2fna and ASASSN-18am both show a similar temperature evolution, rising to $\sim 12,000$ K at peak after $\sim 8-9$ days, before declining roughly linearly to $\sim$ 5000 K after $\sim$50 days and staying roughly constant thereafter, although ASASSN-18am declines more rapidly between $\sim 10-20$ days. While SN 2016gkg and SN 2013cu do reach comparable temperatures, this occurs very soon after explosion due to shock cooling while DES14X2fna and ASASSN-18am show temperatures in excess of the rest of the SNe IIb sample until 50 days after explosion, with a far more prolonged temperature decline.

4.3.4 Spectroscopy

Spectroscopy of DES14X2fna is shown in Figure 4.2. After $\sim$ 17.5 days, weak Hβ and He I 5876 lines become visible. Approximately one day later a more noticeable broad Hα feature is visible. From $\sim$ 29 days, the features become more prominent, with Hα, Hβ and He I 5876 all visible. These are still present in the later spectra at $\sim$ 50 days, albeit with Hβ becoming increasingly noisy, and further He I features at 6678Å and 7065Å also appear in these later spectra.

Where possible, the expansion velocities of these lines are estimated from their P-Cygni profiles, fitting a Gaussian with a pseudo-continuum to estimate the minimum and using this to infer velocity. I follow the process outlined in Maguire et al. (2012), fitting to a small wavelength range around each feature and considering a 30 Å range for the cut-off on either side of the feature when searching for the best fit. The velocity evolution of DES14X2fna is shown in Table 4.7.

Overall, Hα and Hβ maintain a relatively constant velocity throughout all the spectra of roughly 9000 km s^{-1}. He I 5876 has a velocity of 9254 ± 517 km s^{-1} after 17.5 days, comparable to the H lines, before decreasing gradually in each spectrum and reaching 6074 ± 119 km s^{-1} after 52 days. He I 7065 is not visible in the early spectra but has velocities of 6616 ± 766 km s^{-1} and 6219 ± 489 in the final two spectra respectively, similar to He I 5876. The decreasing velocity of He but not H could occur if almost all

Line	Phase	v_{exp} / km s^{-1}
H_α	+29	8670 ± 660
–	51	8880 ± 740
–	52	9540 ± 510
H_β	+17.5	8250 ± 150
–	29	9110 ± 450
–	52	9620 ± 1830
He I 5876	+17.5	9250 ± 520
–	29	8480 ± 300
–	51	6550 ± 970
–	52	6070 ± 490
He I 7065	+51	6620 ± 770
–	52	6220 ± 490

TABLE 4.7: Expansion velocities of DES14X2fna at different phases calculated from position of minimum of P-Cygni profile.

H present is located in the outer ejecta, meaning that there is little or no H below 8000-9000 km s^{-1}.

Figure 4.7 shows a comparison of the spectra of DES14X2fna with the similarly luminous SN IIb ASASSN-18am and the 'prototypical' SN IIb SN 1993J. While DES14X2fna shows similar hydrogen and helium features to these objects, there are significant differences in the spectral evolution. Temperatures inferred from black body fits in the lower panel of Figure 4.6 show that DES14X2fna and ASASSN-18am are significantly hotter than SN 1993J until $\sim$50 days after explosion, and this is reflected in the continuum.

After $\sim$ 17.5 days, DES14X2fna and ASASSN-18am have only subtle features and are dominated by a blue continuum while SN 1993J has clear features. SN 1993J displays Hα and He I 6678 lines which overlap to create a broader feature and an absorption feature appearing to correspond to Hβ, as well as He I 5876 features.

After 29 days, DES14X2fna is still hotter than SN 1993J and comparable to ASASSN-18am. DES14X2fna again appears very similar to ASASSN-18am with both showing a broad Hα feature as well as Hβ and He I 5876. For SN 1993J, at this epoch the broad feature at $\sim$ 6600 Å shows dips around the wavelength of Hα, indicating that the contribution of H to this broad feature has reduced. After 52 days, the Hβ feature in DES14X2fna is no longer visible though may still be contained in the noise. However, Hα is still visible and He I 6678 and 7065 lines are now apparent along with the He I 5876 line seen previously. ASASSN-18am lacks wavelength coverage above $\sim$6700 Å but still appears similar to DES14X2fna at this epoch, with Hα and He I 5876 features as well as a noticeable Hβ feature. At this epoch, SN 1993J continues the trend of a dip in the broad feature at $\sim$6600 Å around Hα, and now displays clear He I 7065 lines.

Overall, the spectral evolution of these objects shows that DES14X2fna maintains its H envelope for far longer than SN 1993J, with H features visible in the spectra of DES14X2fna at later epochs. This suggests that although the H envelope of the progenitor of DES14X2fna partially stripped, it still has a more massive H envelope than a typical SN IIb. This is also seen in ASASSN-18am, and Bose et al. (2020) discusses that this SN is also richer in H than other SNe IIb. Overall, DES14X2fna shows strong resemblance to ASASSN-18am over the epochs where both have spectroscopic coverage.

4.4 Semi-analytic Light Curve Modelling

This analysis has shown significant differences between DES14X2fna and previously observed SNe IIb, with regard to both its luminosity and fast decline rate. I next consider the possible sources of luminosity of DES14X2fna by making use of the fitting code MOSFiT (Guillochon et al., 2018). This uses a semi-analytic approach to light curve fitting, combining models for different sources to drive luminosity in the system with others to model diffusion through the SN ejecta to produce an observed luminosity over time. From these, model photometric light curves can be generated by assuming a modified black body SED. By using a Markov chain Monte Carlo (MCMC) approach to sample the parameter space for all of the models included, MOSFiT calculates the best fit light curve and parameters for a given model. I consider three different mechanisms included in MOSFiT to model the light curve of DES14X2fna:

1. Nickel-cobalt decay: The canonical model of a SN IIb, using the treatment of the radioactive decay of ^{56}Ni and ^{56}Co from Nadyozhin (1994).
2. Nickel-cobalt decay + CSM interaction: The nickel-cobalt decay model above along with extra luminosity resulting from interaction of the ejecta with a surrounding CSM, using the model from Chatzopoulos et al. (2013). Although the narrow spectral features associated with CSM interaction are not observed in DES14X2fna, this does not rule out the possibility that CSM interaction occured. Given a sufficiently low density CSM (Reynolds et al., 2020), or if the SN ejecta collides with the CSM outside the broad-line forming region (Arcavi et al., 2017a), CSM interaction can occur without clear narrow-line spectral features.
3. Nickel-cobalt decay + magnetar: SN driven by a combination of nickel-cobalt decay, using the model outlined above, and a magnetar, using the model from Nicholl et al. (2017). This is the proposed model for SN 1998bw in Wang et al. (2017), which shows a close resemblance to DES14X2fna at peak. It is also suggested as an explanation for the light curve of ASASSN-18am in Bose et al. (2020).

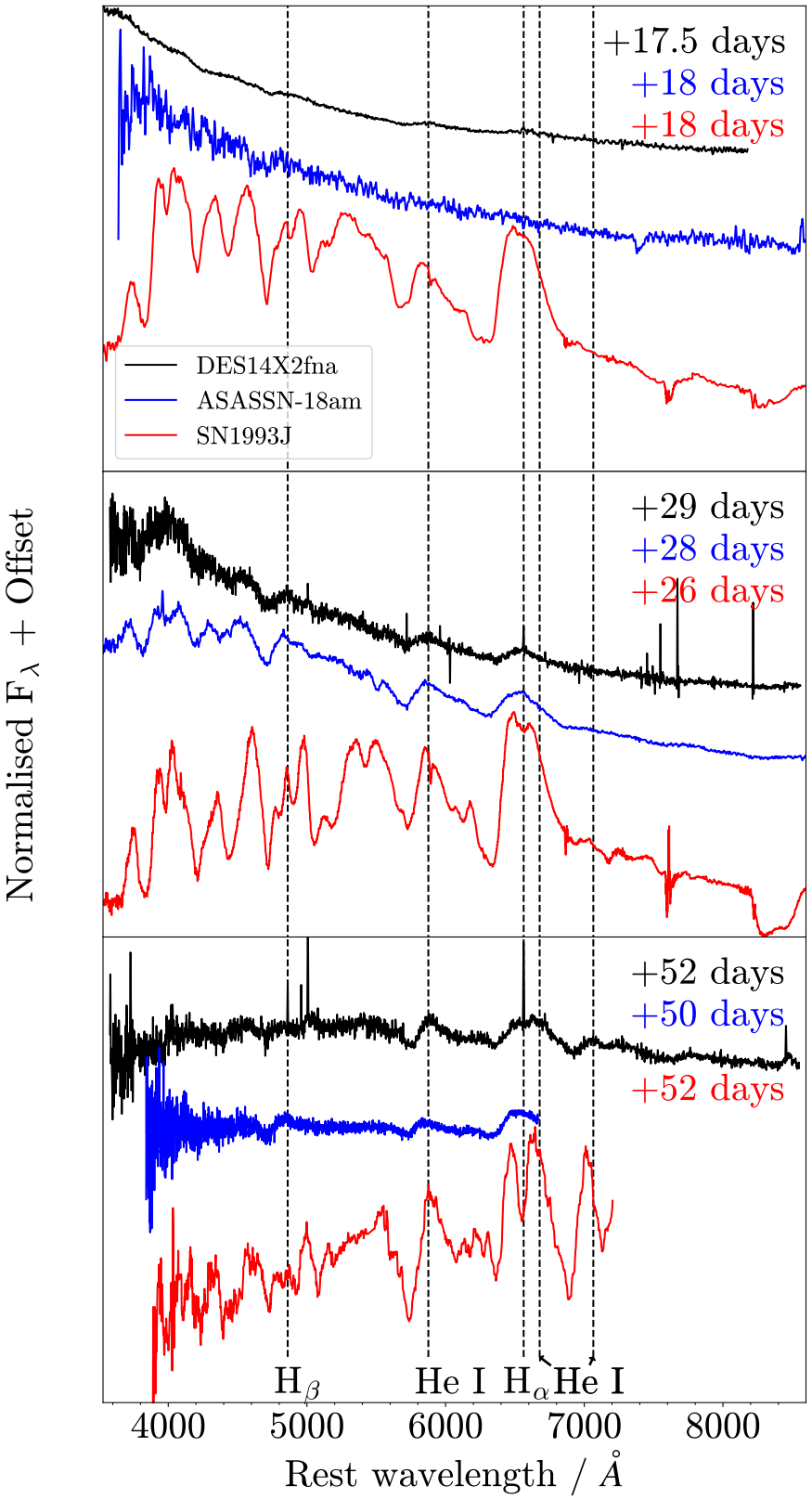

FIGURE 4.7: Spectroscopy of DES14X2fna between 17.5 and 52 days after explosion, alongside spectra of ASASSN-18am and SN 1993J. Spectra have been arbitrarily shifted for presentation and corrected for Milky Way reddening using the extinction model of Fitzpatrick & Massa (2007). Phases displayed in top right are with respect to explosion.

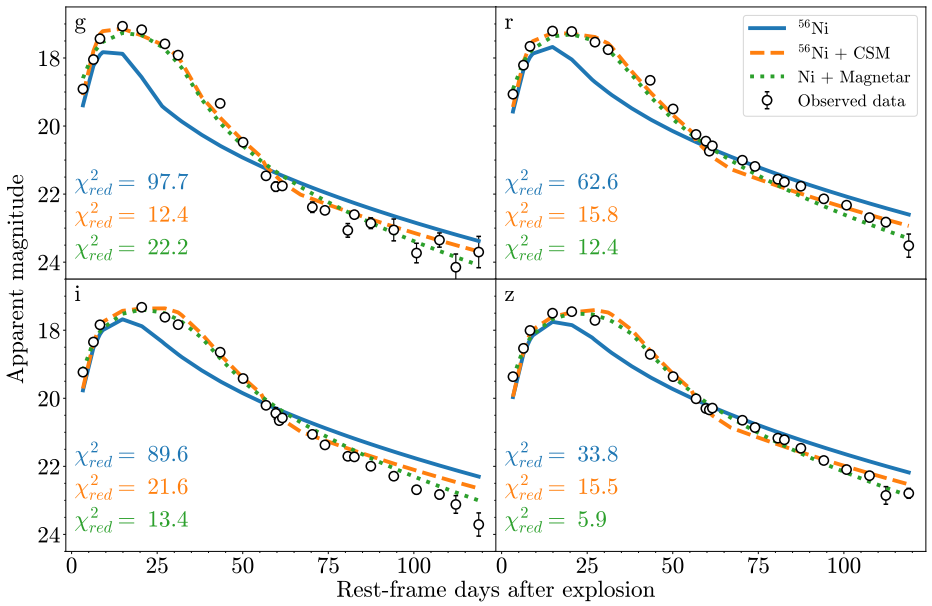

FIGURE 4.8: The best-fit light curves to observations for a variety of physical models after 10,000 MCMC iterations, along with the observed values in *griz* bands.

For each of these models, I run an MCMC-based MOSFiT simulation comprising 1000 walkers for 10,000 iterations. Each model utilises the PHOTOSPHERES.TEMPERATURE_FLOOR photospheric model as outlined in Nicholl et al. (2017). For each walker, MOSFiT calculates model photometry at each epoch and compares with observed photometry - model and observed photometry are used to calculate the reduced χ^2 value, $\chi^2_{\rm red}$ and identify the best-fit model to observations. These model fits are run assuming a fixed opacity to UVOIR radiation κ=0.07 cm^2 g^{-1}, following Prentice et al. (2019), as well as a fixed opacity to gamma rays produced in ^{56}Ni decay of $\kappa_{\gamma,\rm Ni}$=0.03 cm^2 g^{-1} (Wang et al., 2017). Figure 4.8 shows the best-fit light curve for each of these methods in DES *griz* bands, along with the reduced χ^2 value for each of these fits in each band. I will now discuss the fits and results for each of these three models.

4.4.1 Nickel Decay

The first model considered is the canonical nickel-cobalt decay model. Table 4.8 gives the details of the priors used on parameter values in MOSFiT simulation for the ^{56}Ni decay model. Flat and log-flat values were left at their default values, Gaussian priors were selected based on physical observations which can be used to infer ejecta mass and velocity. These priors were selected to restrict the parameter space to physically reasonable solutions. MOSFiT models the photosphere as expanding and cooling with

TABLE 4.8: Details of priors selected for ^{56}Ni decay model for each parameter, detailing minimum and maximum values, prior type and mean and standard deviation in the case of a Gaussian prior.

Parameter	Description	Unit	Minimum Value	Maximum Value	Prior	μ	σ
f_{Ni}	^{56}Ni fraction of ejecta	–	10^{-3}	1	flat	–	–
T_{min}	Minimum photosphere temperature	K	10^{3}	10^{5}	log-flat	–	–
M_{ejecta}	Ejecta mass	$M_{\odot}$	1	4	Gaussian	3	0.3
v_{ejecta}	Ejecta velocity	km s^{-1}	6000	18000	Gaussian	9000	1000

the ejecta before receding at a constant final temperature as described in Nicholl et al. (2017) - this is the parameter T_{min}. Nuisance parameters including $n_{H,host}$ (the line-of-sight H number density of the host used to calculate extinction which is not constrained by the data) and the white-noise variance (the additional magnitude uncertainty required to give a reduced χ^2 equal to one, see Nicholl et al. (2017)) have been marginalised over. Figure 4.9 shows the corner plot detailing best-fit parameter values and their correlations with each other for the ^{56}Ni decay model.

It is clear that nickel-cobalt decay alone is unable to accurately model the light curve of DES14X2fna, with an overall $\chi^2_{red} = 58.2$. This model predicts a narrower peak in *r*-band and a slower tail decline rate, especially in higher-wavelength bands, than observations. Additionally, this model overall underestimates luminosity in *r*-band and overestimates at late times in longer wavelength bands suggesting that it also fails to fit the high temperature and slow temperature decline of DES14X2fna. This model fails to give a reasonable value of ejecta mass and is consistent with a value below the chosen lower limit of 1 $M_{\odot}$. Prolonged H features in spectroscopy of DES14X2fna indicate a more massive hydrogen envelope than the prototypical SN IIb SN 1993J, indicating that the ejecta mass cannot be substantially smaller than other objects - this motivated the choice of lower limit and rules out such a low value. This was obtained even when using a Gaussian prior with a mean and standard deviation of 3 $M_{\odot}$ and 0.3 $M_{\odot}$ respectively, selected arbitrarily to try and force the model to identify a minimum with a physically reasonable ejecta mass. Overall, this model is unable to match observations and does not have realistic best-fit values for all parameters.

4.4.2 CSM Interaction and Nickel Decay

The next model considered was the combined ^{56}Ni decay and CSM interaction model. Table 4.9 gives the details of the priors used on parameter values in MOSFiT simulations for this model. As in Section 4.4.1, flat and log-flat values were left at their default values and Gaussian priors were selected to restrict the parameter space to physically reasonable solutions based on observations. Figure 4.10 shows the corner plot detailing best-fit parameter values and their correlations with each other for the combined ^{56}Ni decay and CSM interaction model.

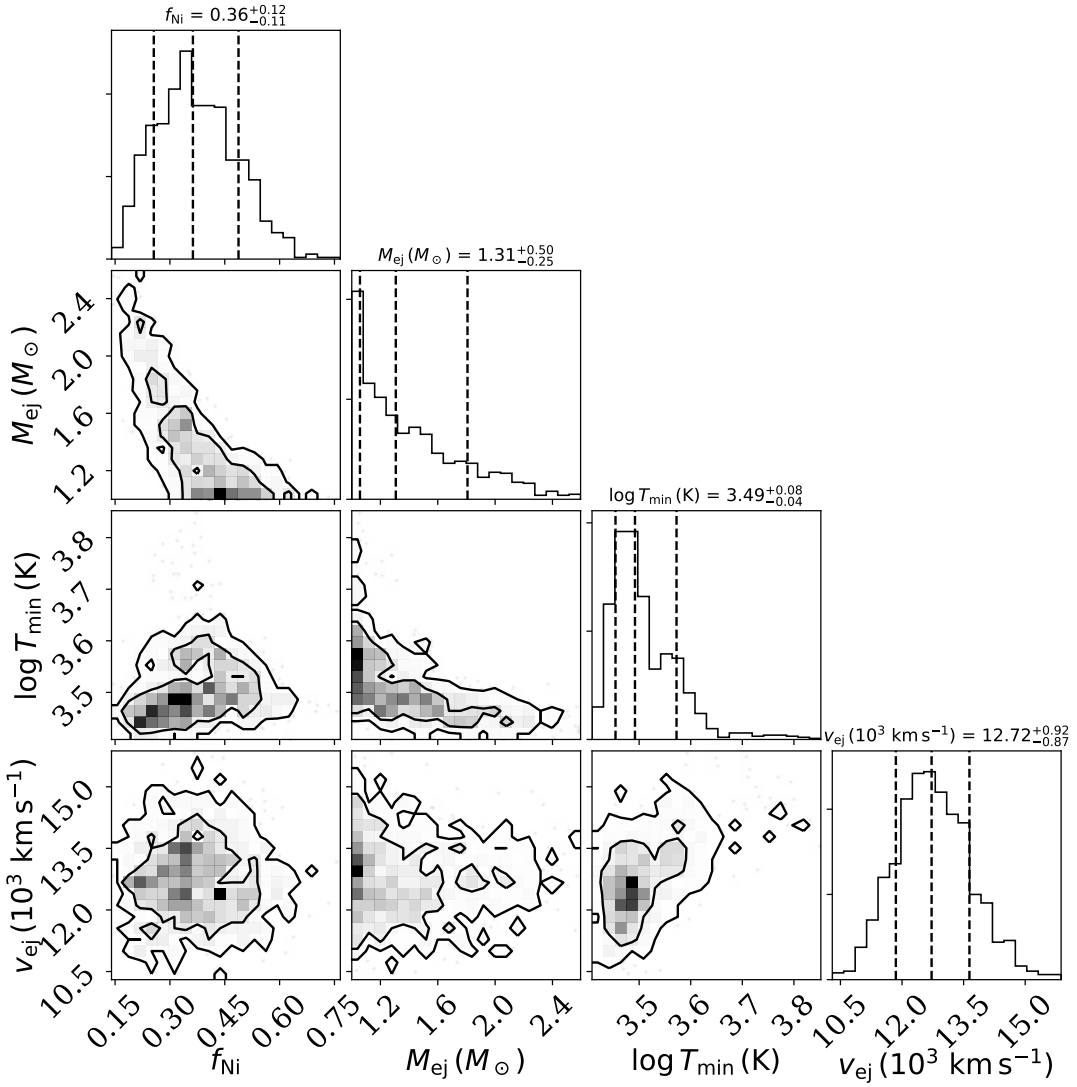

FIGURE 4.9: Corner plot of the ^{56}Ni decay model fit to photometry of DES14X2fna using MOSFiT, showing the best-fit parameter values and their correlations and degeneracies. Dashed lines represent 16th, 50th and 84th percentiles and contours represent 1σ and 2σ confidence levels.

TABLE 4.9: Details of priors selected for combined ^{56}Ni decay and CSM interaction model for each parameter, detailing minimum and maximum values, prior type and mean and standard deviation in the case of a Gaussian prior.

Parameter	Description	Unit	Minimum Value	Maximum Value	Prior	μ	σ
$f_{\rm Ni}$	^{56}Ni fraction of ejecta	–	10^{-3}	1	flat	–	–
$T_{\rm min}$	Minimum photosphere temperature	K	10^3	10^5	log-flat	–	–
$M_{\rm CSM}$	Mass of CSM	$M_\odot$	10^{-2}	10	Gaussian	0.3	0.1
$M_{\rm ejecta}$	Mass of ejecta	$M_\odot$	1	4	Gaussian	2	0.5
E_K	Kinetic energy of ejecta	10^{51} erg	0.5	2.5	Gaussian	1.0	0.5
ρ	Density of CSM	g cm^{-3}	10^{-15}	10^{-11}	log-flat	–	–

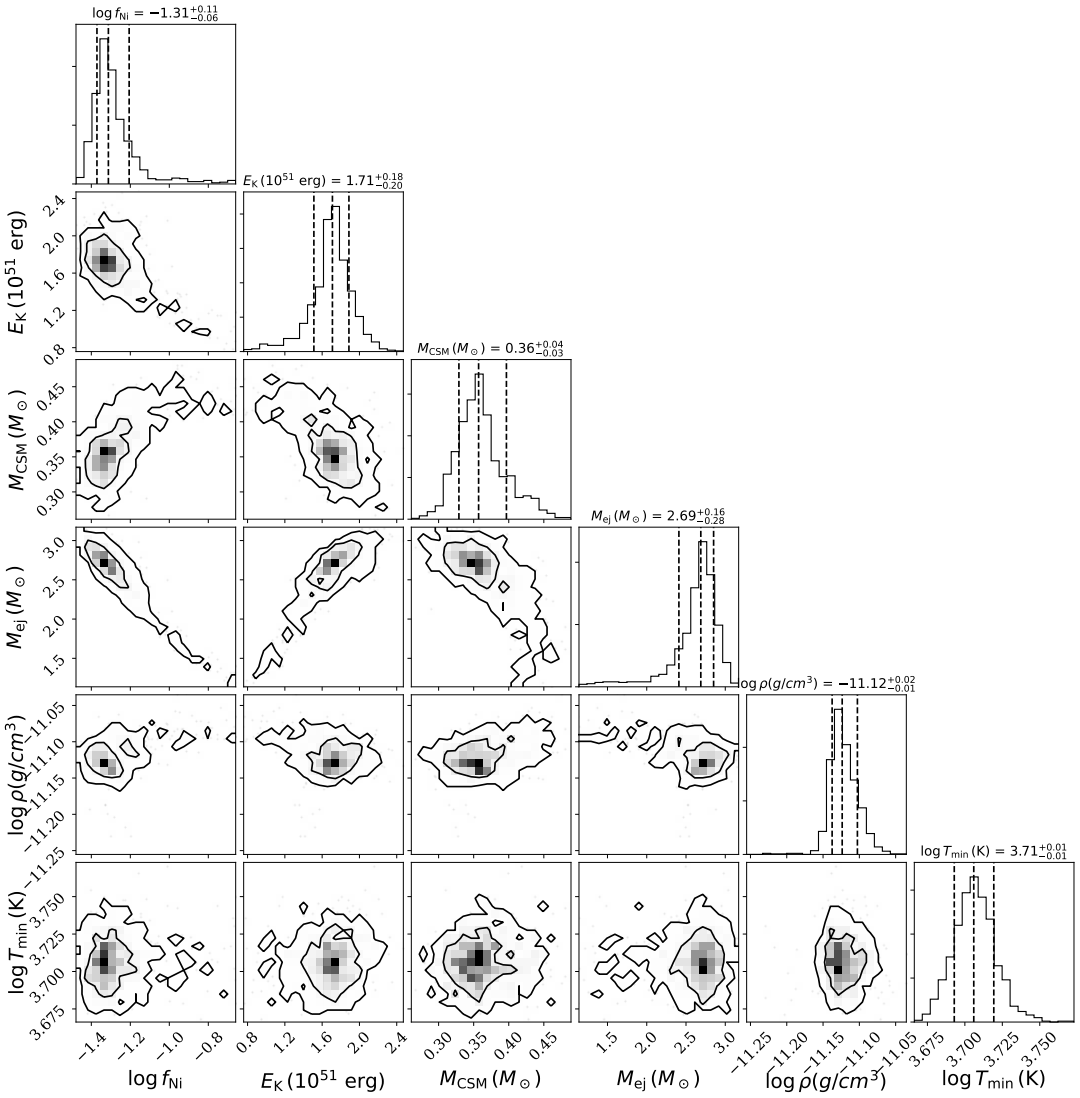

FIGURE 4.10: Corner plot of the combined ^{56}Ni decay and CSM interaction model fit to photometry of DES14X2fna using MOSFiT, showing the best-fit parameter values and their correlations and degeneracies. Dashed lines represent 16th, 50th and 84th percentiles and contours represent 1σ and 2σ confidence levels.

The addition of CSM-interaction to the nickel-cobalt decay model significantly improves the quality of the model, with a reduced χ^2 of 12.1. This model fits both the peak and the decline much more accurately, although the decline rate is still slower than observed in higher wavelength bands. The best-fit ejecta mass is $2.69^{+0.16}_{-0.28}$ M$_\odot$, very typical for a SN IIb based on the sample in Prentice et al. (2019). This model fits kinetic energy rather than ejecta velocity directly, but using the best-fit kinetic energy of $1.71^{+0.18}_{-0.20} \times 10^{51}$ erg s^{-1} along with the ejecta mass, the ejecta velocity is estimated to be ∼8,000 km s^{-1}, comparable to the velocities inferred from spectroscopy. This model is able to match most features of the observed photometry and the physical parameter values are consistent with properties expected for a SN IIb.

TABLE 4.10: Details of priors selected for combined ^{56}Ni decay and magnetar spin-down model for each parameter, detailing minimum and maximum values, prior type and mean and standard deviation in the case of a Gaussian prior.

Parameter	Description	Unit	Minimum Value	Maximum Value	Prior	μ	σ
f_{Ni}	^{56}Ni fraction of ejecta	–	0	1	flat	–	–
T_{min}	Minimum photosphere temperature	K	10^3	10^5	log-flat	–	–
B	Magnetar magnetic field strength	10^{14}G	0.1	20	flat	–	–
P_{spin}	Initial spin period of magnetar	ms	2	20	flat	–	–
M_{ejecta}	Ejecta mass	$M_\odot$	0.1	10	Gaussian	2	0.5
v_{ejecta}	Ejecta velocity	km s^{-1}	7500	10500	Gaussian	9000	500

4.4.3 Magnetar and Nickel Decay

The final model considered was the combination of magnetar spin-down and nickel-cobalt decay. Table 4.9 gives the details of the priors used on parameter values in MOSFiT simulation for the magnetar model. As mentioned in Section 4.4.1, most flat and log-flat priors were left at their default values and Gaussian priors were selected to restrict the parameter space to physically reasonable solutions based on observations. The neutron star mass is fixed at 1.4 $M_\odot$. In comparison with some other parameters, a relatively strict Gaussian prior has been imposed on ejecta velocity. With a more flexible prior many walkers were moving towards an unphysical local minimum with an ejecta velocity less than observations indicate and a magnetar spin period of less than 1 ms, hence the strict prior. Figure 4.11 shows the corner plot detailing best-fit parameter values and their correlations with each other for the combined ^{56}Ni decay and magnetar model.

The addition of a magnetar to nickel-cobalt decay further improves the quality of the fit, with a reduced χ^2 of 10.0. Compared with the CSM model, this model matches the observed decline rate of DES14X2fna in the tail more accurately. The best-fit ejecta mass is $2.85^{+0.61}_{-0.55}$ $M_\odot$, also very typical for a SN IIb compared with the Prentice et al. (2019) sample. For this fit, a fixed value of $\kappa_{\gamma,mag}$ = 0.01 cm^2 g^{-1} is assumed. This was originally left as a free parameter but the MCMC favoured a value below the range of expected values for a magnetar, between 10^{-2} and 10^6 cm^2 g^{-1} (Kotera et al., 2013). As a result, this was fixed to the lowest value considered reasonable.

As an independent check, an alternative semi-analytic magnetar code based on the model outlined in Inserra et al. (2013), hereafter I13, was also considered. Unlike MOSFiT, I13 fits directly to bolometric luminosities rather than observed photometry - as such, the black-body estimated luminosities from Section 4.3.3 are used. I have again assumed a fixed value of $\kappa_{\gamma,mag}$ = 0.01 cm^2 g^{-1}. The fit to this data using I13 is shown in Fig 4.12 - overall, this model fits the black-body luminosities well both around peak and in the tail.

As previously noted, the *r*-band light curve of DES14X2fna shows strong resemblance around peak to that of SN 1998bw (SN Ic-BL), which Wang et al. (2017) finds can be accurately fit with a combination of a magnetar and nickel-cobalt decay. The MOSFiT

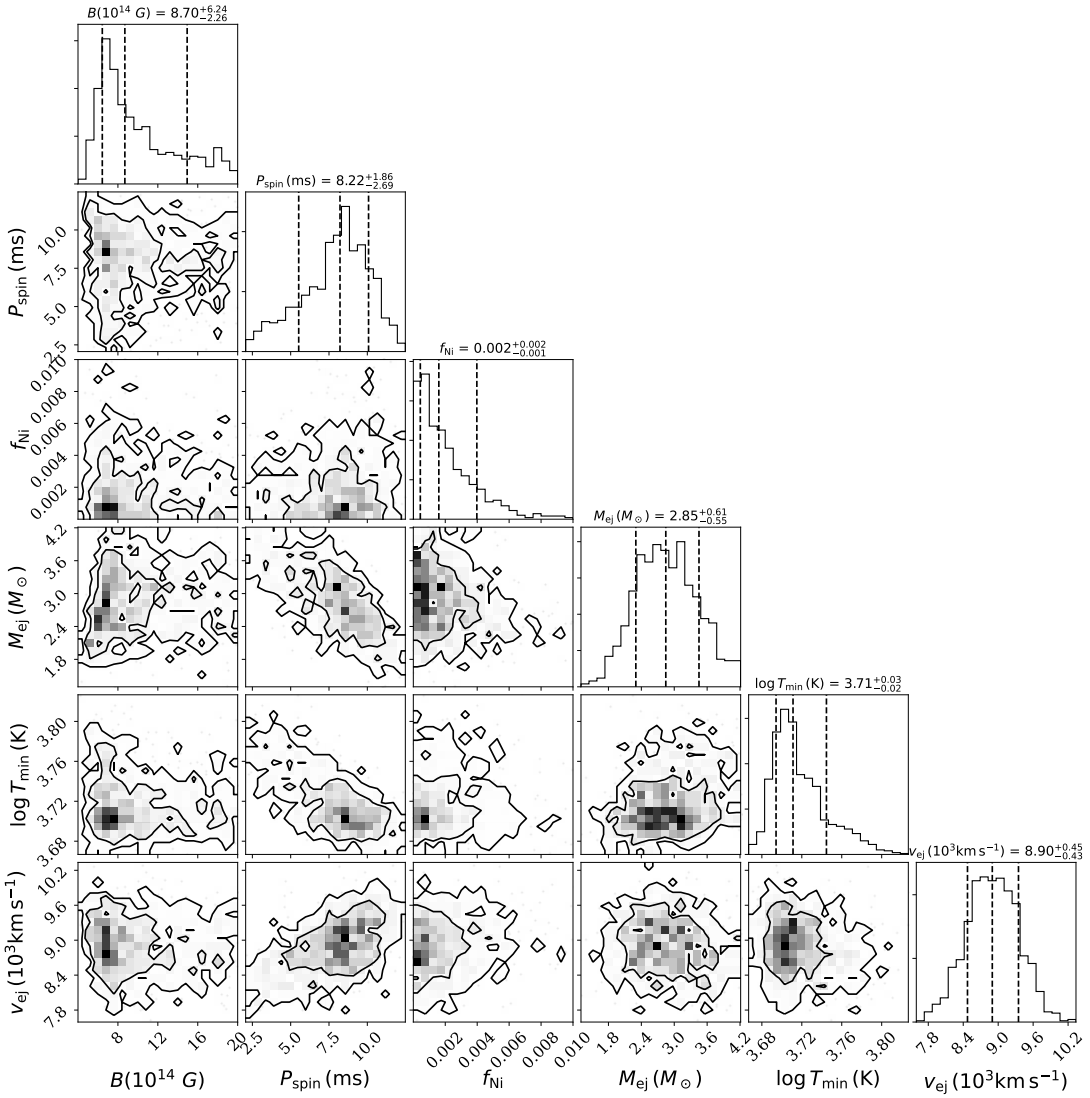

FIGURE 4.11: Corner plot of the combined ^{56}Ni decay and magnetar model fit to photometry of DES14X2fna using MOSFiT, showing the best-fit parameter values and their correlations and degeneracies. Dashed lines represent 16th, 50th and 84th percentiles and contours represent 1σ and 2σ confidence levels.

and I13 magnetar fits indicate that a similar mechanism could power DES14X2fna. Table 4.11 shows the best-fit properties of the magnetar model fit for DES14X2fna along with those of SN 1998bw. For both models, the predicted initial ejecta velocity v_{ejecta} is consistent with velocity measurements from spectroscopy and the ejecta mass is consistent with the SNe IIb population in Prentice et al. (2019). Comparing DES14X2fna to SN 1998bw, there are differences of a factor of ∼2-2.5 for the estimated values of magnetar magnetic field strength and spin period. Ejecta velocity is lower for DES14X2fna although only by less than 1.5σ, and the ejecta mass is comparable for both objects. One key difference between the two objects is that for DES14X2fna, the ^{56}Ni mass is considerably less than for SN 1998bw. The quoted ^{56}Ni mass for I13, <0.023 $M_\odot$, is a 1σ upper limit from the fitting uncertainty - the parameter value itself

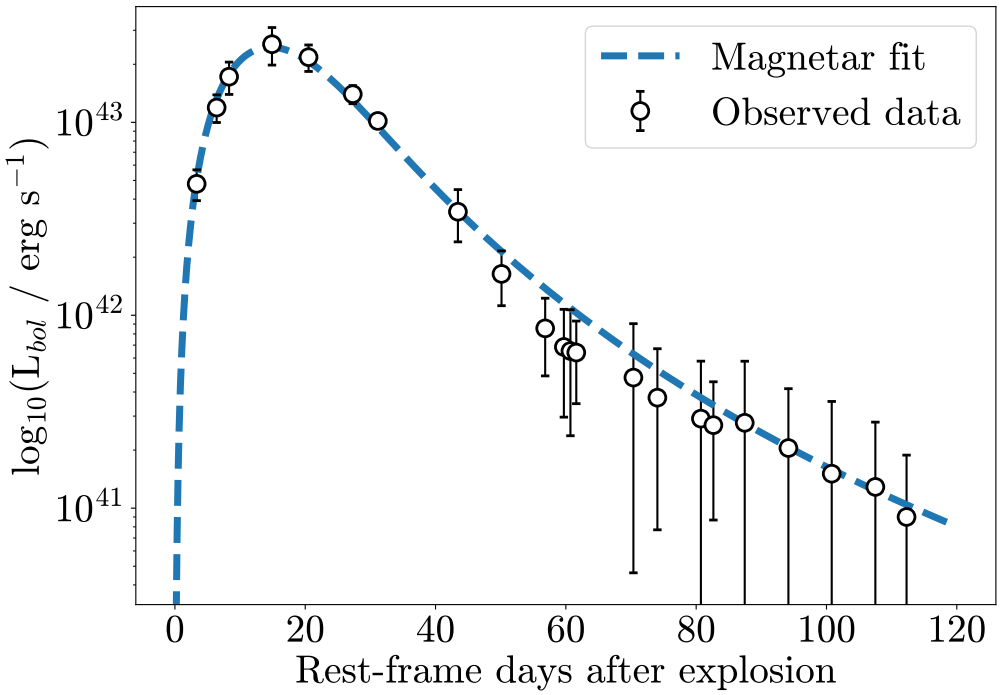

FIGURE 4.12: Bolometric luminosities of DES14X2fna calculated from black body fits to observed photometry along with a magnetar fit to this data based on the model detailed in Inserra et al. (2013).

TABLE 4.11: The best fit properties of the combined magnetar and ^{56}Ni fit to photometry of DES14X2fna using both MOSFiT and I13, along with the best-fit magnetar properties of SN 1998bw from Wang et al. (2017).

SN	B (10^{14} G)	P_{spin} (ms)	M_{ejecta} ($M_\odot$)	v_{ejecta} 10^3 km/s	M_{Ni} ($M_\odot$)	$\kappa_{\gamma,mag}$ (cm^2 g^{-1})
DES14X2fna (MOSFiT)	$8.70^{+6.24}_{-2.26}$	$8.22^{+1.86}_{-2.69}$	$2.85^{+0.61}_{-0.55}$	$8.90^{+0.45}_{-0.43}$	$(4.41^{+6.87}_{-3.25}) \times 10^{-3}$	0.01**
DES14X2fna (I13)	7.80±2.32	11.96±0.28	2.10±0.43	9.04±2.22	<0.023*	0.01**
SN 1998bw	$16.6^{+2.1}_{-1.4}$	20.8±0.8	$2.6^{+0.5}_{-0.4}$	$11.05^{+1.50}_{-1.59}$	$0.10^{+0.03}_{-0.02}$	$0.29^{+0.19}_{-0.17}$

*: 1σ upper limit

**: Fixed value

is $\sim 10^{-4}$. Under the assumption that DES14X2fna is powered in part by a magnetar, this demonstrates that the contribution of ^{56}Ni decay to the light curve is minimal. The different magnetar properties of DES14X2fna compared to SN 1998bw have the effect of increasing the initial energy output of the magnetar and increasing the timescale over which it declines. This leads to DES14X2fna and SN 1998bw showing similar light curve peaks before DES14X2fna declines far more rapidly at later times.

4.5 Discussion

4.5.1 Peak Luminosity

By studying both the *r*-band and bolometric light curves of DES14X2fna, I have demonstrated that it is considerably more luminous than any other SN IIb in the comparison sample with the exception of ASASSN-18am. Under the assumption that this object follows the canonical ^{56}Ni decay model for a SN IIb, the peak must be powered by a very considerable mass of ^{56}Ni far in excess of what is typical for a SN IIb. Using the bolometric light curve for DES14X2fna I can make some initial estimates of the mass of ^{56}Ni synthesised in the explosion. Equation 3 of Prentice et al. (2016) from the commonly-used, analytically-derived 'Arnett model' (Arnett, 1982) allows estimation of the ^{56}Ni mass using the peak bolometric luminosity, L_p, and the rise time to peak bolometric luminosity, t_p. Using values for these from Section 4.3.3 gives an estimate of $M_{Ni} = 1.02 \pm 0.20$ M$_\odot$. Please note this is not a Gaussian uncertainty, rather a maximum possible deviation based on uncertainty in explosion epoch, constrained only between the last non-detection and first detection. Equation 19 of Khatami & Kasen (2019) proposes an updated relation between peak time and luminosity, with the effect of opacity and mixing encapsulated in a parameter β. Assuming that the proposed β value for SNe IIb in Khatami & Kasen (2019), 0.82, is valid for DES14X2fna, the mass is calculated as $M_{Ni} = 0.633^{+0.083}_{-0.079}$ M$_\odot$. Again, this is not a Gaussian uncertainty, instead reflecting the maximum possible deviation due to uncertainty in explosion epoch. Meza & Anderson (2020) finds SNe IIb and Ib ^{56}Ni masses which typically vary from $\sim 0.03 - 0.2$ and $\sim 0.02 - 0.13$ M$_\odot$ using these methods respectively. DES14X2fna would require a ^{56}Ni mass that is $\sim$ 4-5 times larger than is typical for SNe IIb.

The breadth of the peak of the light curve of DES14X2fna also indicates an ejecta mass at the very least typical for a SN IIb. The ejecta mass can be estimated using equation 1 in Prentice et al. (2019), based on the Arnett model,

$$M_{ej} = \frac{1}{2}\left(\frac{\beta c}{\kappa}\right)\tau_m^2 v_{sc} \tag{4.1}$$

where $\beta \approx 13.7$ is a constant of integration, κ is the opacity of the ejecta and v_{sc} is a characteristic velocity of the ejecta. I again follow Prentice et al. (2019) in assuming κ = 0.07 cm^2 g^{-1} and $\tau_m = t_p$, and use the velocity of Hα around peak of $\simeq$9000 km s^{-1} as an estimate of the characteristic ejecta velocity. This gives an estimate for ejecta mass of $M_{ej} = 2.35^{+1.11}_{-0.90}$ M$_\odot$, consistent with the mean and median M_{ej} for SNe IIb in Prentice et al. (2019), 2.7 ± 1.0 M$_\odot$ and $2.5^{+1.3}_{-0.7}$ M$_\odot$, respectively. This suggests that the light curve of DES14X2fna is consistent with a fairly typical SN IIb ejecta mass.

4.5.2 Tail Decline

As well as the high peak luminosity and broad peak of DES14X2fna, I have also demonstrated that DES14X2fna declines far more rapidly at late times than any other SN in the comparison sample. However, under the assumption that this object is powered by ^{56}Ni decay, this creates a discrepancy with the very luminous peak of DES14X2fna.

In the canonical picture of a SN IIb, after any hydrogen present has recombined the light curve is driven by radioactive decay of ^{56}Co, as any ^{56}Ni produced will have already decayed. The source of optical luminosity at this stage is the deposition of γ-rays and positrons produced in the radioactive decay process. Under the assumption that γ-rays produced are fully trapped and all deposit their energy, the luminosity of the SN will decline at a rate of 0.98 mag (100d)$^{-1}$ (Woosley et al., 1989). A decline rate faster than this indicates that γ-rays produced are not fully trapped and therefore some of their energy is not observed in the optical light curve. In *griz* photometric bands, DES14X2fna has decline rates of 3.96 $\pm$ 0.45 mag (100d)$^{-1}$, 4.30 $\pm$ 0.10 mag (100d^{-1}), 5.15 $\pm$ 0.13 mag (100d)$^{-1}$ and 4.70 $\pm$ 0.08 mag (100d)$^{-1}$, far in excess of the rate expected for complete trapping. Such a fast decline rate indicates a very low ejecta mass, allowing most of the γ-rays produced to escape. However, as discussed in Section 4.5.1, if DES14X2fna were to be powered by ^{56}Ni it would require a mass of ^{56}Ni at least four times that of any other SN IIb observed and an ejecta mass at least typical for a SN IIb. This high mass of material would lead to significant trapping of the γ-rays produced in ^{56}Co decay and therefore preclude the fast decline which is observed in DES14X2fna. Assuming ^{56}Ni alone, DES14X2fna cannot have an ejecta mass typical for a SN IIb while also displaying a significantly faster decline rate.

^{56}Ni mass can also be estimated from the bolometric tail decline, which helps to reiterate the discrepancy between peak and decline rate for DES14X2fna. For a canonical SN IIb, in this phase ^{56}Ni mass will have almost entirely decayed and the light curve is powered solely by ^{56}Co. Assuming complete γ-ray trapping, in this phase the light curve will follow (Jerkstrand et al., 2012),

$$L(t) = 1.42 \times 10^{43} \frac{M_{Ni}}{M_{\odot}} (e^{-t/t_{Co}} - e^{-t/t_{Ni}}) \text{ erg s}^{-1}, \tag{4.2}$$

where $L(t)$ is the luminosity, M_{Ni} is the mass of ^{56}Ni synthesised in the explosion and t_{Co} and t_{Ni} are the characteristic decay timescales for ^{56}Co and ^{56}Ni respectively. Assuming that other SNe follow this relation and have similar γ-ray deposition, SNe ^{56}Ni masses will share the same ratio as bolometric luminosity at the same epoch. SN 1987A is commonly used for this analysis, although as it does not reach the linear decline phase of its light curve until after the last data for DES14X2fna, this method cannot be directly used. However, a bolometric luminosity at later times for

DES14X2fna can be inferred by extrapolating the linear decline in $\log(L_{bol})$. After 159.1 days since explosion SN 1987A has a UV-optical-infrared (UVOIR) bolometric luminosity of $\log_{10}(L_{\rm UVOIR}/\ {\rm erg\ s^{-1}})$ = 41.381 (Suntzeff et al., 1991), whereas extrapolating the light curve of DES14X2fna gives a luminosity at this epoch of $\log_{10}(L_{bol}/\ {\rm erg\ s^{-1}})$ = 40.22±0.11. Note that the uncertainty for the SN 1987A luminosity is less than 0.02 dex, although no exact value is given. As a result, its uncertainty is considered to be negligible compared to DES14X2fna. The ratio of luminosities is (6.93±1.74) $\times 10^{-2}$, leading to an estimate for ^{56}Ni mass for DES14X2fna of (5.20±1.35) $\times 10^{-3}$ $M_\odot$. The underlying assumption that these objects share similar γ-ray deposition is clearly not valid as DES14X2fna exhibits a very rapid decline not seen in SN 1987A, so this value is only a lower limit on the ^{56}Ni mass produced. While only a lower limit, the fact that this value is nearly two orders of magnitude less than the mass of ^{56}Ni predicted from peak luminosity demonstrates the inconsistency between peak and tail of DES14X2fna.

It is also possible to take into account the effect of incomplete trapping of γ-rays when estimating the ^{56}Ni mass from the bolometric decline. Clocchiatti & Wheeler (1997) proposes a simple model to take this into account, also given in equation 2 of Terreran et al. (2016). This is the most logical method to estimate ^{56}Ni mass for DES14X2fna given its fast decline rate. However, in practice this model is unable to constrain the ^{56}Ni mass of DES14X2fna despite working for every other object in the SNe IIb comparison sample. The reason for this appears to be that DES14X2fna declines too fast to be well fit by this model. Equation 7 of Clocchiatti & Wheeler (1997),

$$\frac{d}{dt}m(t) = \frac{d}{dt}m_0(t) + \frac{5\log_{10}(e)}{e^{(T_0/t)^2}-1}\frac{T_0^2}{t^3} \tag{4.3}$$

gives an expression for the decline rate in magnitude for ^{56}Co decay, where $\frac{d}{dt}m_0(t)$ is the decline rate for fully trapped ^{56}Co decay, 0.98 mag (100d)$^{-1}$, T_0 is the characteristic decay time for the γ-ray optical depth and the complete second term corresponds to the shift in decline rate as a result of incomplete trapping, $\frac{d}{dt}m_1(t)$. Assuming a fixed value of t, the second term increases with decreasing T_0 and is maximised in the limit T_0 tends to zero. Applying this, the maximum value of the second term is,

$$\lim_{x\to 0}\frac{d}{dt}m_1(t) = \frac{5\log_{10}(e)}{t}.$$

At the start of the tail after 60 days, this term is 3.62 mag (100d)$^{-1}$ giving a maximum decline rate of 4.60 mag (100d)$^{-1}$, which does not rule out the fast decline rate of DES14X2fna at this epoch. However, at later times the maximum decline rate decreases - for example, 100 days after explosion the maximum possible decline rate is 3.15 mag (100d)$^{-1}$ which is more than 1 mag (100d)$^{-1}$ less than the observed decline rate of DES14X2fna at this epoch. This discrepancy only increases at later stages of the

observed light curve. Overall, this suggests that DES14X2fna declines too rapidly to be explained by ^{56}Ni decay alone.

4.5.3 Power Source

Throughout this analysis, I have demonstrated that DES14X2fna has very different properties when compared with other SNe IIb. DES14X2fna reaches a peak absolute magnitude in *r*-band of -19.37, comparable only to ASASSN-18am and nearly 1 mag brighter than any other SN IIb. DES14X2fna also displays a relatively broad light curve peak. As discussed in Section 4.5.1, this is indicative of a very high ^{56}Ni mass and an at least comparable ejecta mass when compared to other SNe IIb. However, as discussed in Section 4.5.2, these ^{56}Ni and ejecta masses are not consistent with the very fast post-peak decline observed across all photometric bands of DES14X2fna. DES14X2fna appears to decline too rapidly for this to be explained simply by incomplete trapping of γ-rays produced in ^{56}Co decay. In Section 4.4, I consider a semi-analytic model of ^{56}Ni decay. This model is unable to accurately model the light curve of DES14X2fna, predicting a narrower peak in *r*-band and a slower tail decline rate, especially in higher-wavelength bands, than observations. This model is also unable to reproduce the temperature of DES14X2fna, underestimating luminosity at peak in shorter wavelength bands and overestimating at longer wavelengths at later times. Based on the contradictions between the peak and decline of the light curve of DES14X2fna as well as the inability of the semi-analytic model to fit observed photometry, I rule out the possibility that DES14X2fna can be powered by ^{56}Ni decay alone.

Having established that DES14X2fna requires an additional source of luminosity besides ^{56}Ni, the question to address is what that source of luminosity might be. One possibility is that interaction with a surrounding CSM helps to power the light curve. Such a model allows for a faster decline than ^{56}Ni decay alone as the decline rate is no longer limited by the decay timescale of ^{56}Co - a decrease in the luminosity from CSM interaction can lead to a much more rapid decline (Taubenberger et al., 2019). There is precedent for SNe IIb which also show signs of interaction. SN 2018gjx (Prentice et al., 2020) was an object which spectroscopically resembled a SN IIb before going on to show narrow spectral features typical of a SN Ibn after $\sim$40 days, although DES14X2fna is two mags brighter at peak and does not show narrow spectral features during available spectroscopic coverage so is not directly comparable. Semi-analytic fits using MOSFiT suggest that CSM interaction combined with ^{56}Ni decay could power the light curve of DES14X2fna. Although the narrow spectral features associated with CSM interaction are not observed in spectroscopy of DES14X2fna, as previously mentioned this does not rule out that it occurred - interaction has been

invoked for other objects which no not display narrow lines (e.g. SN 2016gsd, Reynolds et al. 2020; iPTF14hls Arcavi et al. 2017a).

I have also shown that the *r*-band peak of DES14X2fna shows close resemblance to the *R*-band peak of SN 1998bw, potentially suggesting that they share a source of luminosity at this phase of the light curve. However, DES14X2fna is also seen to decline far more rapidly than SN 1998bw at late times. If they are to share a source of luminosity, this source must be capable of powering the peak before quickly decreasing in luminosity. Wang et al. (2017) finds that the bolometric light curve of SN 1998bw is likely powered by a combination of ^{56}Ni decay and a magnetar, with this model favoured over the traditional two-component model for SNe Ic-BL as it can explain the late time shift in decline rate. Crucially, Wang et al. (2017) finds that the magnetar dominates the light curve only during peak and at very late times, with the post-peak decline dominated by ^{56}Ni decay. The very luminous peak and fast decline of DES14X2fna could therefore potentially be explained by a magnetar. Semi-analytic model fits find that a combination of a magnetar and ^{56}Ni decay is able to fit the light curve of DES14X2fna far better than ^{56}Ni decay, accurately modelling the peak and decline rate of DES14X2fna.

The similarity of DES14X2fna to SN 1998bw and the good fit to observed photometry given by the combined magnetar and ^{56}Ni model provides evidence that DES14X2fna could also partially be powered by a magnetar. This model also demonstrates that ^{56}Ni makes a minimal contribution to the light curve. This helps to explain the differences between DES14X2fna and SN 1998bw. As shown in Wang et al. (2017), the light curve of SN 1998bw is dominated by a magnetar only around peak and at very late times, far later than photometry is available for DES14X2fna. At intermediate times, the light curve is dominated by ^{56}Co decay. In the case of DES14X2fna, it may be that the light curve is still dominated by a magnetar at intermediate times, which would allow for a faster decline rate than is typically associated with ^{56}Co decay. This would explain why DES14X2fna declines far more rapidly after peak than SN 1998bw. Overall, a magnetar model provides a good fit to observations of DES14X2fna.

An additional possibility to consider is whether the rapid decline of DES14X2fna could result from the onset of dust formation. This process has been invoked to explain fast declines observed in SNe Ibn such as SN 2006jc (Anupama et al., 2008). For this object, the optical light curve was seen to flatten $\sim$30-50 days after maximum before a sudden increase in optical decline rate was accompanied by an increase in NIR luminosity as a result of dust reprocessing. In the absence of NIR observations for DES14X2fna I cannot be sure whether this might have occurred, although it is important to note that SN 2006jc was an object which showed strong interaction and had a much faster evolution than DES14X2fna - even during the flattening phase, it still declined faster than DES14X2fna at optical wavelengths. As a result, I consider the possibility that this decline rate is due to dust formation unlikely although cannot rule it out.

4.5.4 DES14X2fna as a Photometric Contaminant

DES14X2fna has a very high luminosity at peak, reaching a peak $M_r \simeq$ -19.3, and therefore into the range of peak luminosities expected for SNe Ia. While the H and He features of DES14X2fna clearly distinguish it from a SN Ia, it is a possibility that a similar object could be mistakenly included in a photometric sample of SNe Ia in the absence of spectroscopy. To assess this, I use the SNe Ia light curve template fitter SALT2 (Guy et al., 2007) to fit observed photometry using the Python package SNCOSMO. SALT2 calculates the stretch and colour parameters for a SN Ia light curve, x_1 and c. For the DES cosmological sample of SNe Ia, only SNe with $\sim -0.3 < c < 0.3$ and $-3 < x_1 < 3$ are included. Fitting the observed light curve between -15 and +45 days relative to explosion gives a poor quality fit, particularly in higher wavelength bands, with $\chi^2_{red} = 6041$. This fit also has a value of $x_1 = -3.08$ and $c = -1.20$, meaning that it would not pass the cuts to be included in a cosmological sample. However, the large χ^2_{red} value obtained also results partly from the fact that DES14X2fna has very high signal-to-noise data. If a similar object were observed at a higher redshift, it is possible that it could be misclassified as a SN Ia.

To assess the likelihood of an object similar to DES14X2fna acting as a photometric contaminant, the object is simulated based on SED templates from Hounsell et al. (in prep.) over the 5 years of DES using SNANA (Kessler et al., 2009). These templates can extend into the UV based on extrapolation of the optical SED but effects such as line blanketing mean that these are not reliable. As a result, objects are simulated up to z<0.59 meaning that the effective wavelength of DES g-band never falls below 3000 Å. In total, 23,870 DES14X2fna-like events are simulated at different redshifts in DES up to this limit. Each of these synthetic light curves is fit using SALT2, a standard template fitter for SNe Ia light curves (Guy et al., 2007), and the RNN-based photometric classifier SUPERNNOVA (Möller & de Boissière, 2019) is used to estimate the probability that each light curve corresponds to a SN Ia, hereafter referred to as P_{Ia}. The model used for classification was trained on a set of templates which did not include DES14X2fna and so has not previously seen an object with these properties. To identify the synthetic light curves with the potential to be mistakenly included in cosmological samples of SNe Ia, I apply a number of cuts:

1. Select only SNe with valid SALT2 fits: This identifies SNe with light curves with the potential to be included in the DES 3-year cosmological sample based on the cuts outlined in Brout et al. (2019b). Any objects outside the redshift range of [0.05, 1.2], with a Milky Way E(B-V) > 0.25, without data both before and after peak or without data points with a signal-to-noise ratio > 5 in at least two bands are excluded from the SALT2 fits entirely, leaving a total of 18,520 objects.
2. Select only SNe with $-0.3 < c < 0.3$ and $-3 < x_1 < 3$ based on SALT2 fits: As previously mentioned, this cut is used in Brout et al. (2019b) to select the

cosmological sample. Performing this cut leaves a total of 15,101 objects in the sample.

3. Select only SNe with a high value of P_{Ia}: This identifies only the synthetic SNe with a high probability of being classified as a SN Ia by SUPERNNOVA. Note that SUPERNNOVA has two models, one for photometric classification with a host spectroscopic redshift and one without. Here only the model for classification with a redshift is considered as objects without host redshifts would not be included in a cosmological sample. This confidence threshold for inclusion is arbitrary - a lower threshold will give a larger sample but increases the likelihood of sources being included incorrectly. Using a high threshold of $P_{Ia} > 0.9$ gives a total of 270 synthetic SNe which would be misclassified as SNe Ia, 1.1 per cent of the sample. Lowering this threshold to 0.8 increases the number of misclassifications to 372, 1.6 per cent of the sample. At a threshold of $P_{Ia} > 0.5$, where an object is simply more likely than not to be a SN Ia, there are 565 misclassifications corresponding to 2.4 per cent of the sample.

Overall, in these simulations a DES14X2fna-like object is misclassified as a SN Ia in $\sim$1.1-2.4 per cent cases depending on the threshold used for P_{Ia}. While rare, it does show that such an object does have the potential to contaminate a cosmological sample. Analysing the light curves of the synthetic SNe which were classified shows that this generally occurs when the fast linear decline of DES14X2fna is undetected, due to either dropping below the detection limit of the survey or the end of the observing season, or is observed with very low signal-to-noise. This suggests that DES14X2fna is difficult to differentiate from a SN Ia based on photometry around peak, but can be differentiated from its late time decline. This is to be expected given DES14X2fna does not show the second peak typical for SNe Ia and has a very fast tail decline.

Given that DES14X2fna is near unique, it is clear that this type of object is rare with a rate only a small fraction of the rate of SNe Ia. In addition to this, only a small fraction of similar events will be misclassified as SNe Ia. While DES14X2fna is an interesting case of a potential contaminant, in practice the effect that these objects have on cosmological analyses is unlikely to be significant.

4.6 Summary

In this chapter I presented the observed properties and explored the physical mechanisms of the unusual SN IIb DES14X2fna, which has both a very high peak luminosity and very fast late-time decline compared to other members of its class. At peak, this SN reaches an *r*-band absolute magnitude of -19.37 $\pm$ 0.05, comparable to

the recently discovered very luminous SN IIb ASASSN-18am and 0.88 mag brighter than any other SN IIb. The main findings of this analysis are as follows:

1. The light curve of DES14X2fna cannot be explained by ^{56}Ni decay alone. The peak luminosity and peak time of DES14X2fna indicate a ^{56}Ni mass synthesised in the explosion more than four times greater than observed in any other SNe IIb in Khatami & Kasen (2019) and an ejecta mass of $2.35^{+1.11}_{-0.90}$ $M_{\odot}$ which is consistent with other SNe IIb in Prentice et al. (2019). However, DES14X2fna declines at more than three times the rate expected for fully-trapped ^{56}Co decay in *g*-band and more than four times in *riz*-bands. This decline is more than 1 mag 100 d^{-1} faster than any other SN IIb in the tail.

2. DES14X2fna displays signs of H for far longer than the prototypical SN IIb SN 1993J, indicating it has a more massive H envelope than a typical SN IIb. Bose et al. (2020) obtains a similar finding for ASASSN-18am.

3. Semi-analytic ^{56}Ni decay models using MOSFiT are unable to fit the peak and the fast tail decline of the light curve of DES14X2fna.

4. DES14X2fna declines too rapidly at late times to be fit by the treatment for incomplete trapping of γ-rays produced in ^{56}Co decay in Clocchiatti & Wheeler (1997), providing further evidence that an additional source of luminosity is required.

5. The addition of CSM interaction to the ^{56}Ni decay model provides a significantly better fit to the observed photometry of DES14X2fna than ^{56}Ni decay alone, indicating that it could in part power this object.

6. The light curve of DES14X2fna is well fit by a magnetar model. DES14X2fna also shows resemblance to SN 1998bw around peak, which is well fit by a magnetar model in Wang et al. (2017).

7. Based on simulations of DES14X2fna in SNANA using templates from Hounsell et al. (in prep.) in DES, an object similar to DES14X2fna is misclassified as a SN Ia suitable for cosmology in $\sim$1.1-2.4 per cent cases depending on the probability threshold used. This typically occurs when the fast decline of such an object is not observed with sufficient signal-to-noise. However, given the rarity of such events they are unlikely to act as a significant contaminant to cosmological samples.

Chapter 5

Generating Synthetic Supernova Light Curves using Generative Adversarial Networks

As discussed in Section 1.4, upcoming surveys such as LSST are incredibly exciting in terms of the science questions they will help to tackle but also raise challenges in that follow-up spectroscopy will only be feasible for a very small subset of the sample. Photometric classification will therefore be a vital tool for SN science. However, one limiting factor faced by these methods is the quality of the data sets on which they are trained. In this chapter, I will introduce a method of generating synthetic SN light curves to boost training sets.

5.1 Motivation and Objectives

Neural networks, and machine learning techniques in general, are seeing increasingly widespread use within astronomy for a variety of applications such as photometric classification (e.g. Muthukrishna et al., 2019; Möller & de Boissière, 2019; Boone, 2019), outlier detection (e.g. Boone, 2021) and candidate identification (e.g. Cañameras et al., 2020; Ayyar et al., 2022). They can be a very powerful tool, but their success is dependent on the quality of the data sets they are trained on. Some of the most powerful neural networks for image classification are trained on data-sets such as ImageNet (Deng et al., 2009) which consist of millions of training examples. When it comes to training models for transient classification, performance is limited by the total numbers of these transients which we have observed. As discussed in Chapter 1, CCSNe show very heterogeneous properties and span a myriad of subtypes. For rarer subtypes, the total number of observed objects may be small which makes training

classifiers to detect these objects difficult. Of course, the best approach to boost training the size of training samples is to observe large quantities of spectroscopically confirmed transients. In the longer term, the data collected by photometric surveys such as LSST combined with spectroscopic surveys such as 4MOST may well provide these observations. However, this clearly will not be the case prior to the start of LSST which means that other techniques are required in order to create training sets.

One approach, as was used for PLAsTiCC, is to create synthetic training sets using simulations. Training based on simulated data sets has led to a number of successful models, including Möller & de Boissière (2019) and Muthukrishna et al. (2019). Some simulations are based on physical models of the explosion mechanisms of SNe; for example, as part of the PLAsTiCC data semi-analytic models of the explosion created using MOSFiT (Guillochon et al., 2018) were used for some classes of CCSNe. However, one limitation of this approach is that the physical models must be able to reproduce the full variability of light curves that is seen in nature in order to generate a representative training sample, whereas in reality there is a great deal not understood about the physical processes in CCSNe. If a model is trained on light curves based on physical simulations, the model will only be able to classify objects similar to those the simulations are able to create.

An alternative approach to take is to use data-driven methods to simulate SN populations. The advantage of this approach is that no assumptions have to be made about the underlying physics of the explosion; in this way, the simulated data set should be able to reproduce the full heterogeneity seen in the sample from which it is simulated. The PLAsTiCC data set applies Non-negative Matrix Factorisation (NMF), a technique for dimensionality reduction of data similar to Principal Component Analysis (PCA), to generate half of the SNe II included. An alternate technique to generate synthetic SN light curves is to use Generative Adversarial Networks (GANs). GANs are a class of neural network which can be used to produce realistic synthetic data which closely resembles the data set on which they are trained. GANs have been successfully used in other fields and within astronomy to generate synthetic data which can be used to augment the training set; this has been shown to improve the performance of classifiers compared with only using the original training set (e.g. Motamed et al., 2021; García-Jara et al., 2022).

Motivated by the previous success achieved by others in augmenting training sets using GANs, my ambition is to apply this approach to photometric SN classification. The objective of this project is to train a GAN which is able to generate realistic CCSN light curves as a proof-of-concept. There are a number of different approaches which could be taken for the generator. For example, the GAN could be trained to produce rest-frame light curve templates. However, for this work I focus on the generation of observer-frame light curves with associated uncertainties which could in theory be used directly as the input for a photometric classifier. In particular, I focus on the

generation of DES-like *griz* light curves. One challenge this poses is that some classifiers, including RAPID, also take spectroscopic host redshift as an input, meaning that a generator would also be required to generate a corresponding redshift for each SN which creates additional complexity. Other classifiers, however, support classification based only on photometry which is desirable as a pre-existing host redshift is not required for classification. For example, SUPERNNOVA supports classification based only on an observed light curve. For this work, I focus solely on the generation of observer-frame photometry which could in theory be used to train such a classifier.

5.2 Introduction to Neural Networks

Having detailed the goals of this work in the previous section, I will now introduce the general principles of a neural network, before going on to outline specific types of network that are relevant for this chapter.

5.2.1 Artificial Neural Networks

Artificial neural networks (ANNs) are models inspired by the structure of biological neural networks which make up the brain. ANNs consist of interconnected nodes called neurons, with each node able to receive information from and transmit to other neurons (Rosenblatt, 1957).

5.2.1.1 Neurons

While there are a wide variety of different architectures which have been developed for ANNs, in the simplest case each neuron has a structure as shown in Figure 5.1. A neuron is in practice a set of calculations which are described as follows:

- The neuron is connected to n different inputs denoted by x_i, and each connection has an individual associated weight w_i.
- At the neuron, the sum of the product of each input value x_i and its corresponding weight w_i is calculated, $\sum_{i=1}^{n} x_i w_i$.
- This sum is then added to the value b, which is a value associated with the neuron known as a bias, i.e. $\sum_{i=1}^{n} x_i w_i + b$.
- A function f, known as the activation function, is then applied to this value which leaves the final output of the neuron as $y = f(\sum_{i=1}^{n} x_i w_i + b)$.

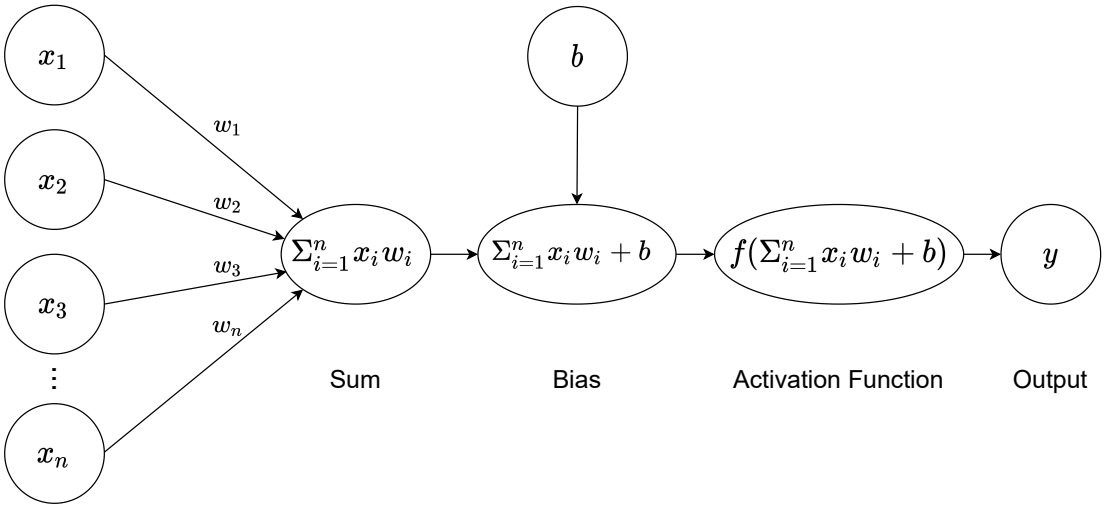

FIGURE 5.1: Structure of a single neuron in a neural network.

The values w_i and b are properties of the neuron. The activation function f is used to introduce non-linearity into the model on top of the linear sums of input values and weights and processes the output into a form which can be used by the next neuron. The bias b is used to apply a linear offset to the value at the neuron before the activation function. In effect, each neuron is a function mapping the inputs it receives to an output y.

5.2.1.2 Networks

By combining large number of neurons, ANNs can be used to learn complex non-linear equations by modifying the parameters of each individual neuron (w_i and b introduced in Section 5.2.1.1).

Figure 5.2 shows the generalised structure of an ANN. This begins with a layer of nodes called the input layer, consisting of N different nodes where N is the number of dimensions of the input data - the input is a column vector $\mathbf{x}$ with N elements which describes a single data point in an N-dimensional parameter space:

$$\mathbf{x} = \begin{pmatrix} x_1 & x_2 & x_3 & ... & x_N \end{pmatrix}^T. \tag{5.1}$$

Each node in the input layer is then connected to each neuron in the next layer, the hidden layer. This layer is named as such because only the input and output layers are visible to the end user. Each neuron has the structure outlined in Section 5.2.1.1. For hidden layer of M different neurons, the weights of connections to the previous layer can collectively be treated as an $N \times M$ matrix $\underline{\underline{\mathbf{W}}}$ such that

$$\underline{\underline{\mathbf{W}}} = \begin{pmatrix} w_{11} & w_{12} & w_{13} & ... & w_{1N} \\ w_{21} & w_{22} & w_{23} & ... & w_{2N} \\ w_{31} & w_{32} & w_{33} & ... & w_{3N} \\ \vdots & & & & \\ w_{M1} & w_{M2} & w_{M3} & ... & w_{MN} \end{pmatrix} \tag{5.2}$$

where w_{ij} is the weight for the connection between node i in the input layer and neuron j in the hidden layer. Similarly, the biases of the M different neurons in the hidden layer can be treated as a column vector $\mathbf{b}$ such that

$$\mathbf{b} = \begin{pmatrix} b_1 & b_2 & b_3 & ... & b_M \end{pmatrix}^T. \tag{5.3}$$

In this way, the output of the hidden layer is a column vector $\mathbf{y}$,

$$\mathbf{y} = \begin{pmatrix} y_1 & y_2 & y_3 & ... & y_M \end{pmatrix}^T \tag{5.4}$$

which can be described as a matrix operation such that

$$\mathbf{y} = f(\underline{\underline{\mathbf{W}}}\mathbf{x} + \mathbf{b}) = f \begin{pmatrix} w_{11}x_1 + w_{12}x_2 + w_{13}x_3 + ... + w_{1N}x_N + b_1 \\ w_{21}x_1 + w_{22}x_2 + w_{23}x_3 + ... + w_{2N}x_N + b_2 \\ w_{31}x_1 + w_{32}x_2 + w_{33}x_3 + ... + w_{3N}x_N + b_3 \\ \vdots \\ w_{M1}x_1 + w_{M2}x_2 + w_{M3}x_3 + ... + w_{MN}x_N + b_M \end{pmatrix} \tag{5.5}$$

where f is the activation function as outlined in Section 5.2.1.1. Each neuron in the hidden layer is then connected to each neuron in the final layer which processes the output of the network, the output layer. Mathematically speaking, this layer operates in the same way as the hidden layer. The main difference is that while the hidden layer can consist of any number of neurons, the output layer must be of the right shape for a given problem. For example, a neural network being trained to differentiate between three different classes will have an output layer containing three different nodes; one for each class. The activation function will also be chosen to ensure that the values output by the network are in the expected range - it is typical to apply a function which ensures that all the values in the final layer sum to one meaning that they can be interpreted as probabilities.

In practice, ANNs span a variety of structures. The model described here consists of a single hidden layer and in theory, any function can be accurately treated using a single hidden layer. However, in practice better results are often achieved using multiple hidden layers between the input and output layers. The use of models with more than one hidden layer is known as *deep learning*. There are also numerous architectures for

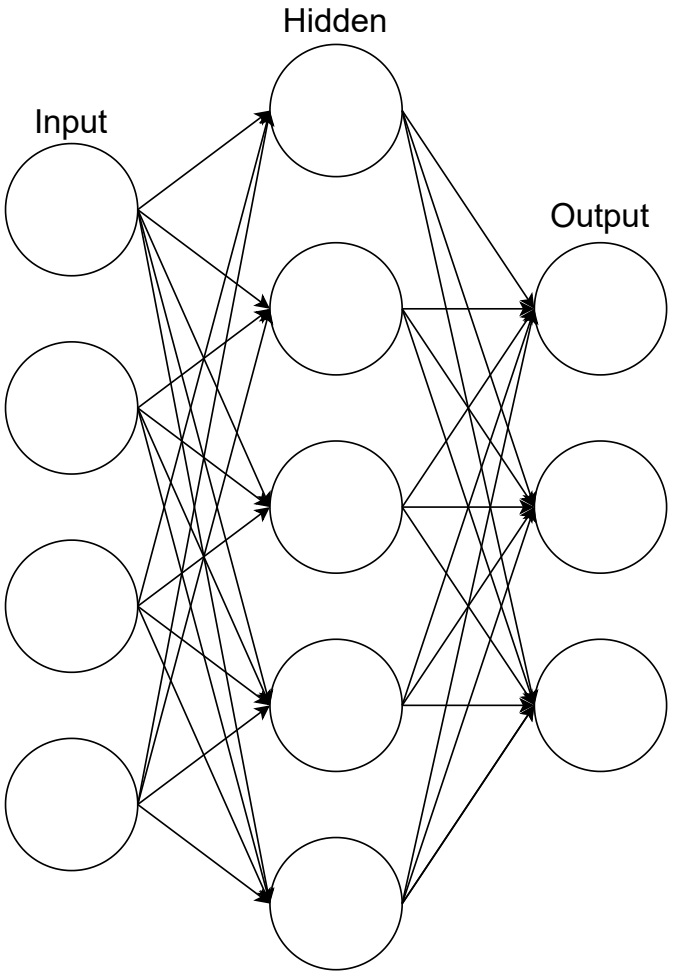

FIGURE 5.2: Structure of simple neural network showing input, hidden and output layers as well as connections between them.

different layers which are well suited for working with different types of data such as images or time series.

5.2.1.3 Training ANNs

In the previous sections, I have introduced the structure of ANNs and the idea that they can be used to learn complex non-linear equations by modifying the weights and biases associated with each individual neuron. I will now go on to outline how ANNs can be trained for specific problems, using as a specific example a three class classification problem.

The main strength of neural networks is for situations where the desired outputs for given input data are known but the function to map the inputs to their desired outputs is very complex. For three class classification, the network is trained with known examples of each class in order to learn a function which maps the input data

onto a class prediction. As mentioned in Section 5.2.1.2, a network trained for multi-class classification will have one node in the output layer for each class, three in total for this case. In order to train the model, the desired outputs are column vectors such that for each of the three classes the output of the model will be:

$$\text{Class 1: } \hat{\mathbf{y}} = \begin{pmatrix} 1 & 0 & 0 \end{pmatrix}^T$$
$$\text{Class 2: } \hat{\mathbf{y}} = \begin{pmatrix} 0 & 1 & 0 \end{pmatrix}^T$$
$$\text{Class 3: } \hat{\mathbf{y}} = \begin{pmatrix} 0 & 0 & 1 \end{pmatrix}^T.$$

Here, I will distinguish between the desired output of the model $\hat{\mathbf{y}}$ from the actual output $\mathbf{y}$. The column vector $\hat{\mathbf{y}}$ in this case represents the desired output values in the three nodes of the output layer. With this setup, the node with the highest value in the output layer then becomes the predicted class. For this kind of problem, it is typical to use a *softmax* activation function in the output layer of the form,

$$y_i = \frac{e^{z_i}}{\sum_{j=1}^{K} e^{z_j}} \tag{5.6}$$

where y_i is the ith element of the output column vector $\mathbf{y}$ after the activation function, z_i is the ith element of the output column vector prior to the activation function and K is the number of nodes in the output layer. In this way, all values in the output layer are positive and sum to one allowing them to be interpreted as probabilities that the input data belongs to each class.

Training a neural network is akin to fitting a model using χ^2 minimisation; the parameters of the model are adjusted to minimise some goodness-of-fit/performance metric. In the case of a neural network, this metric is known as the *loss function*. When the loss function is equal to zero the network is performing perfectly, although this is not achieved in practice. The network is trained by calculating the gradient of the loss function with respect to each of the parameters across all the neurons, and updating the parameter values based on these gradients in order to minimise the loss function. As this process continues, the actual output of the network gets increasingly close to the desired output.

The loss function that is used will depend on what the network is being trained for and there are a number of different options. For a three class classification problem, a common choice is a categorical cross-entropy. In this case, the loss function L is given by,

$$L = -\sum_{i=1}^{K} \hat{y}_i \log y_i \tag{5.7}$$

where $\hat{y}_i$ is the ith element of the desired output $\hat{\mathbf{y}}$, y_i is the ith element of the actual output $\mathbf{y}$ and K is again the number of nodes in the output layer.

Model training is conducted in an iterative process, with each step referred to as an *epoch*. During each epoch, batches of the input data are passed to the network along with their true labels and the weights in the network are adjusted based on the gradient for each batch. Each epoch corresponds to a full pass through of the data set. The model weights are updated based on the stochastic gradient descent method, with gradients calculated based on a subset of the data corresponding to each batch. Training the model also involves a number of hyperparameters which are not updated in the training process, such as the number of hidden layers and neurons in each hidden layer. One important hyperparameter here is the *learning rate*, which relates to the amount that the parameters of the network are updated for each batch. If the learning rate is too high, the training process will struggle to minimise the loss function as the parameter values are likely to keep overshooting the minimum. However, if the learning rate is too low then model training will take a very long time to converge to an optimal set of parameter values. In recent years, a number of optimisers have been developed which refine the stochastic gradient descent process and adjust the learning rate of each parameter throughout the training process, which can help to improve both model performance and speed of convergence. A commonly used example is the Adam optimiser (Kingma & Ba, 2014).

One major concern which needs to be taken into account when training a neural network is *overfitting*. This occurs when the network begins to learn the specific input data it receives rather than generalised functions, meaning that it will perform well when classifying the data it is trained on but poorly on unseen data. The generalisation performance of a network can be assessed by splitting the data set into train and test samples: the train set is fed to the network to optimise the parameters, while the train set is used simply to assess the performance on unseen data for each epoch and is not used to update the model weights. There are a number of ways to combat overfitting: in this chapter, I will make use of *Dropout* layers, which are regularly used for this purpose. These randomly deactivate a specified percentage of connections in the network during each epoch, which prevents all parameters being optimised simultaneously and converging to the same solution.

5.2.2 Recurrent Neural Networks

I have now introduced the general structure of ANNs and described how they can be trained to learn different functions. I will next introduce a class of ANNs known as recurrent neural networks (RNNs). RNNs are of particular interest for working with time series data such as SN light curves, and have previously been used for

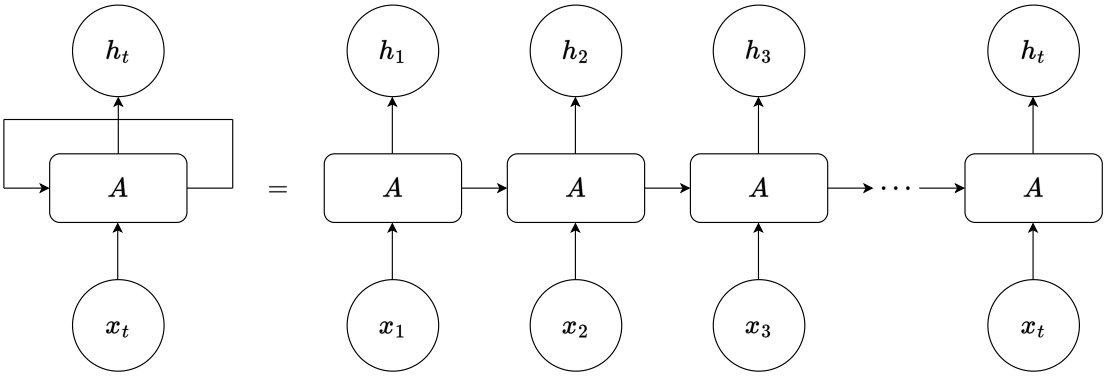

FIGURE 5.3: Structure of recurrent neural network, with rolled architecture on the left and the equivalent unrolled architecture on the right.

photometric classification of SNe (e.g. Möller & de Boissière, 2019; Muthukrishna et al., 2019).

Many neural networks are *feed-forward networks*, such as the general ANN introduced in Section 5.2.1.3. In these networks, information is passed through the networks forward along connections from the input to the output once. RNNs differ in that they are cyclic - neurons receive both their current input and the state of the network at previous steps as input. This allows RNNs to build a representation of previous steps in the time series, allowing them 'memory' of full sequences and making them perfect for working with time series data. Figure 5.3 shows a simple RNN architecture, with the inputs at each time step i represented by x_i, the function applied by the network represented by A and the output at each time step represented by h_i. On the left of the figure is the 'rolled' representation of the RNN, where the output from the neuron is cycled through to the same neuron for the next step of the time series. On the right is the same architecture but now 'unrolled', with the output of the neuron at each step taken as part of the input for the next step.

One issue with this type of RNN, however, is that they have short-term memory - if a sequence is very long, an RNN does not factor in the early steps in the sequence when working with later steps. As discussed in Section 5.2.1.3, model weights are updated based on the gradient of the loss function with respect to the weights. For RNNs, this is proportional to the product of the gradients at each step in the sequence which will in turn depend on the derivatives of the activation function. With typical activation functions used in RNNs, these are less than one meaning the product of many of these gradients will approach zero. This is referred to as a *vanishing gradient*. For long sequences the gradient of the loss function with respect to the early steps becomes very small meaning these have little impact on training the network - this is what causes the short-term memory.

A number of modified RNN architectures have been created to avoid this issue. One of these is the Long Short-term Memory network (LSTM). An LSTM contains a number of smaller networks known as 'gates' which are used to control the flow of information. For a full overview of the LSTM architecture please see Hochreiter & Schmidhuber (1997), but in brief a combination of gates known as forget, input and output gates are used in an LSTM to determine the information from past steps which is relevant to use, the information from the current step which should be used to update the state of the network and the output for the current step. With this setup, the gradient for each parameter weight is given by the sum of four different terms from the different gates. This allows the network better control of the gradients and helps to prevent the vanishing gradient problem when taking the product across multiple steps, allowing the network to learn from full sequences. More recently, the Gated Recurrent Unit (GRU; Cho et al., 2014) has been proposed as an alternative architecture. This is similar to the LSTM architecture but has only two gates; update and reset gates. GRUs have fewer parameters than LSTMs, making them faster to train, but achieve similar performance.

5.2.3 Generative Adversarial Networks

Thus far in this chapter, I have introduced the general concept of ANNs and a particular ANN architecture ideally suited for working with time series data known as RNNs. I will now introduce the ANN architecture which will be the main focus on this chapter; the Generative Adversarial Network (GAN).

GANs are a class of neural network which can be used for data generation, first proposed in Goodfellow et al. (2014). These networks actually consist of two separate ANNs which are trained in parallel, typically referred to as the generator and the discriminator, with a typical GAN architecture shown in Figure 5.4. A GAN is trained on a set of real data and, if trained correctly, allows for the generation of synthetic data which closely resembles this data set. GANs are trained with the following steps:

- The generator network is fed random noise z, processes this and produces an output of the same data structure as the real data - I will refer to this output as $G(z)$.
- The discriminator is fed the synthetic data $G(z)$ as well as the real data. The purpose of this network is to differentiate between inputs from each of these two sources, with the output of the discriminator predicting whether each input is from the real or fake data sets.
- The value of the loss function for the discriminator is calculated by comparing its predicted outputs to the true labels, and the gradients of this loss function are used to update the weights of the discriminator.

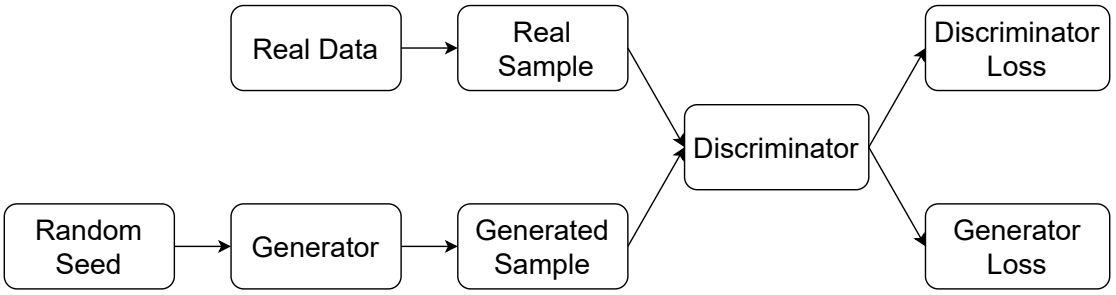

FIGURE 5.4: Structure of a generative adversarial networks, showing the various steps involved in training this type of model.

- Simultaneously, the loss function is also calculated for the generator. The aim of the generator is to produce an output $G(z)$ close enough to the real data to be classed as real by the discriminator - as a result, the generator's performance can only be assessed based on the output of the discriminator. The loss function is calculated in the same way as for the discriminator, except only considering inputs which are from the generator and this time with the labels inverted so that the loss function considers these inputs to come from the real data set. The generator is updated by calculating the gradient of the loss function with respect to each weight in the generator, with the weights in the discriminator kept frozen for this. In this way, the generator is updated to produce an output which more closely resembles the real data set to the current state of the discriminator.
- This process is repeated for a number of epochs, allowing the generator and discriminator to train off of each other and improve at their respective tasks. If trained well, the generator will become able to generate realistic examples of the real data set.

The type of network used for the generator and discriminator depends on the type of data the GAN is being trained to generate. One common application is image generation - for example, GANs have been used to generate realistic human faces (e.g. Karras et al., 2017) and fingerprints (e.g. Minaee & Abdolrashidi, 2018). In these cases, convolutional neural networks (CNNs) are used for both the generator and discriminator as they are perfectly suited to working with image data. However, RNNs have also been applied in GANs for the generation of sequential data such as music (e.g. Mogren, 2016).

When trained correctly, GANs can be an incredibly powerful tool for generation of synthetic data. However, there are a number of possible issues which can arise when training a GAN (Arjovsky & Bottou, 2017):

- Vanishing gradients: If the discriminator becomes very good at differentiating between the real and synthetic inputs, the gradients of the loss function for the

generator become very small because they will have little effect on the output of the discriminator. This causes the generator to stop learning and the training fails.

- Mode collapse: A well-trained GAN will produce a variety of outputs in order to generate varied synthetic data. However, if the generator produces an output which seems very realistic to the discriminator, it may start to produce only that output in order to trick the discriminator. Typically, the discriminator will then learn to reject that specific input and the generator will continue learning different outputs. However, if the discriminator is stuck in a local minimum and is unable to do so, it is easy for the generator to compensate for changes in the discriminator and so the GAN begins only producing a very small range of outputs.

A modified GAN architecture known as a Wasserstein GAN (WGAN) was proposed in Arjovsky et al. (2017). This architecture is similar to a GAN but with a modified discriminator, and requires use of a Wasserstein loss function. In a traditional GAN, the discriminator simply aims to distinguish between real and synthetic inputs and the output layer will use an activation function such as the sigmoid function to scale the output between 0 and 1 - the two classes can then be distinguished based on whether the output is greater than or less than 0.5. For the critic in a WGAN, the output layer does not have an activation function and instead returns an unbound scalar.

The loss function in a GAN is effectively a measure of the distance between the real data set and the generated data set. The WGAN architecture uses an approximation of the Earth-Mover distance between two distributions (Rubner et al., 2000), given by:

$$W(p_r, p_g) = \sup_{\|f\|<K} \left[\mathbb{E}_{x\sim p_r}[f(x)] - \mathbb{E}_{\tilde{x}\sim p_g}[f(\tilde{x})]\right] \tag{5.8}$$

where $W(p_r, p_g)$ is the distance between the data distribution over a real samples x (p_r) and over generated data $\tilde{x}$ (p_g) and f is the function applied by the critic, mapping the input data to an output scalar. In this equation, $\mathbb{E}_{x\sim p_r}[f(x)]$ and $\mathbb{E}_{\tilde{x}\sim p_g}[f(\tilde{x})]$ then represent the expected output of the critic for real and generated data. The supremum sup represents the maximum value of the differences between these two terms, with the restriction applied $\|f\| < K$ meaning that the function f must be K-Lipschitz continuous. This means that for the function f, there exists some real scalar K such that for all real pairs of x-values x_1 and x_2,

$$|f(x_1) - f(x_2)| \leq K|x_1 - x_2|. \tag{5.9}$$

Assuming that f satisfies this condition, for training a WGAN the loss function in practice then can be written as:

$$L = \mathbb{E}_{x\sim p_r}[f(x)] - \mathbb{E}_{\tilde{x}\sim p_g}[f(G(z))] \tag{5.10}$$

where $\mathbb{E}_{x\sim p_r}[f(x)]$ is the mean output of the critic applied to the real data set and $\mathbb{E}_{\tilde{x}\sim p_g}[f(G(z))]$ is the mean output of the critic applied to the generated data set. When the critic is trained, it aims to minimise L which it can do by minimising the former and maximising the latter. When the generator is trained, $G(z)$ is treated as if it is from the real data set by the loss function meaning that it is trained by minimising $\mathbb{E}_{\tilde{x}\sim p_g}[f(G(z))]$. With this treatment, the discriminator can never classify perfectly since the difference in output between $\mathbb{E}_{x\sim p_r}[f(x)]$ and $\mathbb{E}_{\tilde{x}\sim p_g}[f(G(z))]$ can always be further increased. This helps to counteract the zero gradient problem which can occur for a regular GAN.

One difficulty that arises from this treatment is enforcing the condition that f must be K-Lipschitz continuous. Arjovsky et al. (2017) applies a simple, practical method to approximately enforce this constraint by clipping the weights to be between -0.01 and 0.01 to restrict the sample to a compact parameter space. As acknowledged in this paper, this solution is not an ideal way to enforce this condition. Gulrajani et al. (2017) presented an improved method of enforcing this condition based on the norm of the gradients of the critic's output with respect to the input. This work shows that for a 1-Lipschitz function (K-Lipschitz with K=1), an input randomly interpolated between the real and generated data will have a gradient of norm 1. The condition of being 1-Lipschitz continuous is instead enforced by an additional term in the loss function such that:

$$L = \mathbb{E}_{x\sim p_r}[f(x)] - \mathbb{E}_{\tilde{x}\sim p_g}[f(G(z))] + \lambda\mathbb{E}_{\hat{x}\sim p_{\hat{x}}}[(||\nabla_{\hat{x}} f(\hat{x})||_2 - 1)^2] \tag{5.11}$$

where $\hat{x}$ drawn from a linear interpolation between x and $\tilde{x}$ such that $\hat{x} = tx + (1-t)\tilde{x}$ where t is uniformly distributed between 0 and 1. This extra term enforces the condition of 1-Lipschitz continuity by penalising solutions which do not have a gradient norm of 1 and therefore do not follow this condition; the term λ is a scalar which sets the size of the gradient penalty, which is set to 10 in Gulrajani et al. (2017).

5.3 Model Architecture

I will now describe the model architectures used in this work. As discussed, the objective of this work is to train a GAN capable of generating realistic SN light curves. There are a number of different types of neural network which could be used for this application, including CNNs as is typical for GANs to generate images. However, these types of network are only able to generate outputs of a fixed shape meaning that they would only be able to generate light curves of a fixed length. In practice, SN light

curves can have highly variable total numbers of data points. As such, I elect to use RNNs for both the generator and the critic due to their ability to handle sequences of variable length, as well as perfect suitability for handling sequential data. In addition, I opt to use the WGAN with gradient penalty formulation presented in Gulrajani et al. (2017), introduced in Section 5.2.3, based on the advantages offered over a traditional GAN.

5.3.1 Critic Architecture

I will begin by outlining the structure of the critic model. For this discussion I will refer to the number of time steps in a given time series as T, the batch size (the number of light curves fed to the critic in each batch) as B, the number of nodes in each layer of the critic as N and the number of columns in the input light curve data as C. The value of C depends on the data that is to be included. As discussed in Section 5.1, in this work I focus on the generation of observer-frame light curves which requires C= 12; four columns for the time of observation in each of *griz* filters, four columns for the magnitude in each band and an additional four for the uncertainties in each band. If uncertainties are not required, the last four columns can be dropped and if the generator is only required to generate simultaneous observations in each band then only one column is required to represent time of observation. This demonstrates that the generator can be easily altered depending on the data format required.

The structure of the critic is as follows:

- Layer 1: Input - Shape (B, C, T)
  The first layer takes as an input B different light curves with C columns and T time steps giving an overall shape of (B, C, T).
- Layer 2: GRU - Shape (B, N, T)
  The first hidden layer consists of N different GRU units, with each unit returning the full time series (in keras this corresponds to RETURN_SEQUENCES=TRUE). The use of N units means that this layer encodes each time step of the input light curve into an N dimensional representation, with the full time series kept meaning that the output is of shape (B, N, T).
- Layer 3: Dropout - Shape (B, N, T)
  The next layer is a dropout layer; this has no parameters and is simply used to randomly deactivate a certain fraction of nodes during each batch of training in order to prevent overfitting as discussed in Section 5.2.1.3. The dropout fraction of this layer is experimented with during training.
- Layer 4: GRU - Shape (B, N, T)
  The next layer is another GRU layer similar to layer 2, except this layer returns

only the most recent state rather than the full sequence (this time corresponding in keras to RETURN_SEQUENCES=FALSE).

- Layer 5: Dropout - Shape (B, N, T)
  The next layer is another dropout layer, with the same dropout rate as layer 3.

- Layer 6: Dense (Output) - Shape (B, 1)
  The output of the network is a dense layer, which is just a set of typical nodes connected to all nodes in the previous layer as shown in Figure 5.2. This layer consists of only one neuron and has an output of shape (B, 1), corresponding to a single value for each input light curve.

For the first two GRU layers, I use the hyperbolic tangent function $\tanh(x)$ as the activation function for the output. For the final output GRU layer, no activation function is used for the output which allows the network to produce an unbound scalar. This allows the Wasserstein loss function to be used.

5.3.2 Generator Architecture

I will now outline the structure of the generator. For this discussion C again refers to the number of columns, this time in the generated light curves; this must match C in the critic. L refers to the number of latent dimensions from which the input noise to the generator in drawn, M refers to the number of nodes in each layer of the generator and B and T again refer to the batch size and the number of time steps. The structure of the generator is identical and is as follows:

- Layer 1: Input - Shape (B, L, T)
  The input to the generator is essentially noise, a random seed which the generator will learn to map to a realistic output. This random noise is initially drawn from an L-dimensional Normal distribution giving an array of shape (L, 1). As mentioned, the advantage of using an RNN for the generator is that it will be able to generate variable length time series. The random input is then repeated T times to give a shape of (L, T) – the purpose of this is to ensure that the same random seed is used at each time step of the RNN. The value of T sets the total length of the time series output by the generator. In effect, the generator is able to generate time series with a length determined by the size of the noise used as input. The overall shape of the input is (B, L, T) as separate noise is generated for each input of the batch.

- Layer 2: GRU - Shape (B, M, T)
  The first hidden layer consists of M different GRU units, with each unit returning the full time series (in keras this corresponds to RETURN_SEQUENCES=TRUE).

- Layer 3: Dropout - Shape (B, M, T)
  The next layer is a dropout layer; this has no parameters and is simply used to randomly deactivate a certain fraction of nodes during each batch of training in order to prevent overfitting as discussed in Section 5.2.1.3. The dropout fraction of this layer is experimented with during training.
- Layer 4: GRU - Shape (B, M, T)
  The next layer is a second GRU layer identical in structure to the first.
- Layer 5: Dropout - Shape (B, M, T)
  The next layer is another dropout layer, with the same dropout rate as layer 3.
- Layer 6: GRU (Output) - Shape (B, C, T)
  The output layer is another GRU layer, this time with C units. The value of C depends on the data that is to be generated as outlined in Section 5.3.1. The generator is not given any information about which columns correspond to which data; the output simply needs to be of the same shape as the real light curves which will be fed to the critic. The output light curves have T different time steps and in total B light curves will be generated, giving an output shape of (B, C, T).

This architecture allows the generator to map an input of a random seed sampled from an L-dimensional Normal distribution to a time series with the same structure as the real data. If trained correctly, the generated time series should then resemble real SN light curves. As for the critic, I use the hyperbolic tangent function as the activation function for the GRU layers. This means that the output of the generator is restricted to values between -1 and 1.

5.4 Training Process

In this section I will give an overview of the process followed to train the models.

5.4.1 Data Set

A key part of training a GAN is the set of real data on which it is trained. For this work, I opt to train on DES-like light curves from the simulation framework detailed in Vincenzi et al. (2021). This approach uses the SED time-series SN templates presented in Vincenzi et al. (2019) along with the observed CCSN luminosity functions, rates and fractions from LOSS presented in Li et al. (2011) and Shivvers et al. (2017) to create a population of CCSNe. Using the simulation code SNANA (Kessler et al., 2009), the observing conditions of DES are used to obtain

observer-frame DES-like photometry of these objects. In total, this sample contains $\sim 220,000$ simulated CCSNe. While the ultimate aim for this work would be to train on sets of real light curves such as the DES sample presented in Chapters 2 and 3, the use of a large data set from simulations allows for experimentation to see how the GAN is able to perform with training samples of different sizes.

To train the GAN I focus specifically on a subset of the full simulation of light curves which show both a rise to peak and decline after peak - light curves where either the first data point or last data point is the maximum across the whole light curve in any of *griz* bands are excluded. In addition, cuts were made to select only light curves with at least 8 detections in each band to ensure good coverage of the evolution of each SN. I also apply redshift cuts to the training sample for two separate reasons; this cut can be used to control the sample size and will also select only more local SNe with higher signal-to-noise photometry. The redshift cut applied and final sample size will be presented when discussing the results of each model.

Prior to training, a number of pre-processing steps were applied. While RNNs are able to work with variable length time series, a complete set of data is still required for each time step which means that the number of observations must be the same in each band. For light curves where some bands had fewer observations than others, data points were dropped at the beginning and end of the longer time series to fix the number of time steps across each band. After this step, each light curve was interpolated using GPs (as in Section 2.3.1) with the magnitudes and uncertainties recalculated at the same times as the raw light curve but based on the GP fit. This step was applied in order to smooth the light curves, preventing the generator from having to learn to reconstruct artefacts in the data.

5.4.2 Scaling Input Data

The hyperbolic tangent activation function used in the output layer of the generator means that this model is only capable of generating values between -1 and 1. As a result, prior to training it is important that the real data is also scaled to values between -1 and 1 so that the generator is able to create outputs which can resemble the real data.

For this setup, the training data consists of a combination of phases, magnitudes and magnitude errors. These are each scaled using the following:

- Phases: The phases of each observation are quoted in MJD. The first step involved in scaling was to adjust these phases to be with respect to the time of maximum for each object, giving them a common reference point. After doing this, the phases were scaled to values between -1 and 1 using the expression

$t' = 2\left[\left((t - t_{\min})/(t_{\max} - t_{\min})\right) - 0.5\right]$ where t' is the scaled phase, t is the phase with respect to maximum and $t_{\min}$ and $t_{\max}$ are the minimum and maximum values of t across all objects.

- Magnitudes: These values could be scaled between -1 and 1 by converting magnitudes to fluxes and then scaling in flux space, however this would require the generator to generate data covering several orders of magnitude. Instead, I opt to leave these values as logarithmic magnitudes and scale them using the expression $m' = 2\left[\left((m - m_{\max})/(m_{\min} - m_{\max})\right) - 0.5\right]$ where m' is the scaled magnitude, m is the original magnitude and $m_{\min}$ and $M_{\max}$ are the minimum and maximum values of m across all objects. This formulation flips the inverted magnitude system so that brighter magnitudes are closer to 1 and fainter closer to -1.

- Magnitude errors: Magnitude errors are also scaled between -1 and 1 using $\sigma_{m'} = 2\left[\left((\sigma_m - \sigma_{m_{\max}})/(\sigma_{m_{\min}} - \sigma_{m_{\max}})\right) - 0.5\right]$ where $\sigma_{m'}$ is the scaled magnitude, σ_m is the original magnitude and $\sigma_{m_{\min}}$ and $\sigma_{m_{\max}}$ are the minimum and maximum values of σ_m across all objects.

5.4.3 Hyperparameters

The GAN model I have used include a number of hyperparameters that are not estimated by the training process, which relate to both the structure of the model itself and also the training process.

As discussed in Section 5.2.1.3, there are a number of optimisers which have been developed to improve the stochastic gradient descent process used to train neural networks. Gulrajani et al. (2017), which proposed the WGAN model implementation with gradient penalty that I have used here, utilised the Adam optimiser Kingma & Ba (2014) which calculates individual adaptive learning rates for each parameter based on the first and second moments of the gradients of the loss function with respect to each parameter. The Adam algorithm has two hyperparameters, $\beta 1$ and $\beta 2$, which each relate to the decline rate of these two moments. In this work I use $\beta 1 = 0.5$ and $\beta 2 = 0.9$ as suggested. The third hyperparameter is the learning rate, α, which is the initial learning rate used by the optimiser. For this work, I use a value of $\alpha = 0.00002$, which was found to give promising results.

The main hyperparameters involved in the network itself relate to the number of GRU units in each layer of the critic and generator models, corresponding to the values N and M in Section 5.3. Throughout this work I experimented with a number of different values for these parameters. The final values used were $M = N = 100$. Another hyperparameter used in the network was the dropout rate, d, the fraction of connections disabled in each training iteration to prevent overfitting as outlined in

Section 5.2.1.3. During this work, I found that including dropout layers in the generator and critic led to significantly more stable training and more realistic light curves. However, if the dropout fraction was set too high, the generated light curves would only occupy a small fraction of the full parameter space covered by the training data. For this work, I have used a dropout fraction of $d = 0.25$. The final hyperparameter of relevance here is n_{critic}, which represents the number of times the critic is updated for each time the generator is updated. As outlined in Arjovsky et al. (2017), for a WGAN the critic should be trained more often than the generator - this paper uses $n_{\text{critic}} = 5$. For this work, I use $n_{\text{critic}} = 3$, finding that this speeds up training compared to a higher value while still giving good results.

It was possible to explore other hyperparameters, including the number of different GRU layers in both the critic and generator, and to experiment with varying the number of GRU units in each layer. Muthukrishna et al. (2019) used two GRU layers for light curve classification, which motivated my decision to use two GRU layers for both the critic and generator. I have considered different architectures with more layers but found that this did not make a significant difference to the results. As a result, I elect to focus only on models with two layers of GRU units.

5.4.4 Training

Having finalised the data set and model hyperparameters, the only remaining step is to train the model. As discussed in Section 5.2.1.3, this process involves a number of epochs which are in turn divided up into smaller batches. As each batch is passed to the generator, the following steps occur:

- First, an L dimensional Normal distribution is sampled for each of the B different light curves in the input and repeated T times to give an array of shape (B, L, T).
- This randomised input is then passed to the generator and used to produce B different randomised light curves with T time steps.
- The B different real and generated light curves are fed to the critic, with the loss function calculated for this sample.
- A random number is drawn from a uniform distribution between 0 and 1 and the interpolated light curves between the real and generated samples are calculated as outlined in Section 5.2.3. These are then used to calculate the gradient penalty term for these inputs.
- The overall loss function of the critic, combining both the output of the critic from the real and generated light curves and the gradient penalty term, is calculated. The gradients of the loss function with respect to each parameter in the critic are then used to update the model.

- All previous steps are repeated n_{critic} times, meaning that the critic is updated multiple times depending on the value of n_{critic}.
- After the critic is updated, more light curves are generated following the first two steps. The generated light curves only are now passed to the critic and used to calculate the loss function, with the generated light curves this time treated as if they come from the real data-set by the loss function.
- The generator is then updated based on the gradients of this loss function with respect to each of the generator's parameters.

The weights of the generator and critic are updated after each batch. While the RNN-based generator and critic are able to handle variable length time series, each individual batch must consist only of light curves of the same length since each batch must have a fixed size. To work with this restriction, for this work I use a batch size B= 1 so that each light curve is passed to the model separately. An alternate approach would be to group together light curves of the same size, however this would lead to variable batch sizes during the training which is not desirable as the model would be updated at irregular intervals.

5.5 Summary

In this chapter I gave an introduction to neural networks, detailing their overall function and describing different architectures which are well suited for working with time series. I also gave an overview of GANs, describing how they can be used to generate synthetic data.

After introducing the various technologies involved, I then detailed a GAN architecture which can be used to generate variable length synthetic SN light curves and described how this model can be trained. In the next chapter, I will look at the results of this work to see if the GAN is able to generate realistic light curves.

Chapter 6

Results of Synthetic Light Curve Generation

Now that I have given an overview of GANs and described the process of training a GAN model for the generation of synthetic SN light curves, it is time to switch attention to analysis of the light curves which are generated by this model. In this chapter I will present individual generated light curves as well as analysing the overall population properties.

6.1 Assessing Generated Light Curves

There are two main criteria that must be satisfied by the data generated by a GAN in order for it to be considered to be performing well:

1. The generated data must show good *fidelity* i.e. close resemblance to the real data.
2. The generated data must capture the *diversity* present in the real data.

The latter point is of great importance; a generator which is able to produce realistic light curves but with little diversity will only allow for reliable classification of a small subset of the real population.

When training a GAN, it is typically clear to see when it is generating realistic data by visually comparing the generated data to the training set. However, this does not allow for quantitative assessment of either of the two criteria mentioned above. The ideal way to assess the performance of a GAN is to train a classifier only on generated data from the GAN and test it on real data. In this way, the extent to which the

generated data resembles the real data can be measured based on the performance of the classifier. In addition, training a classifier typically involves extracting features which describe the input data, allowing this data to be encoded into a column vector. Comparing the real and generated data sets in this encoded feature space also allows for assessment of the performance of the GAN. However, this requires a classifier to be trained repeatedly at different epochs of the GAN training which adds additional computational expense and complexity and falls beyond the scope of this work.

In this chapter, I assess the quality of the generated light curves in this chapter by extracting light curve parameters from both the real data used to train the GAN and from the generated light curves which allows for comparison between the samples. In this way, the fidelity and diversity of the generator can be assessed based on their physical characteristics. I focus on the following properties of each individual light curve:

- m_{Peak}, the peak apparent magnitude reached in each of *griz* bands.
- Δm_{15}, the decline in mags in the 15 days after maximum in each of *griz* bands in the observer frame.
- Rise time, the time taken for the light curve to rise to peak in each of *griz* bands. Typically, this would be defined with respect to explosion but the generated light curves do not have an associated explosion date. Instead, the rise time is defined as the time between the first data point in any of the bands and the time of peak in each band.
- The colours at peak e.g. $g - r$ colour at g-band peak, $r - i$ colour at r-band peak.

These features are estimated based on GP interpolation of the real and generated light curves, as outlined in Section 2.3.1.

I consider the distributions of each separate physical property to ensure the generated distributions are consistent with the real distributions. However, it is also important to compare these two distributions across all physical properties simultaneously to ensure that the generated light curves are realistic. As mentioned earlier in this section, a trained classifier can be used to encode input data into a single column vector and the performance of the GAN can be assessed by comparing real and generated data in this feature space. Rather than using a trained classifier, in this case I use the 15 physical properties outlined above to describe each light curve and compare the two data sets in this 15-dimensional feature space. To do this, I use the metrics *density* and *coverage* introduced in Ferjad Naeem et al. (2020); these respectively relate to the fraction of the generated data set covered by the real data set, and the fraction of the real data set covered by the generated data set. Density is a

measure of fidelity, while coverage is a measure of diversity. These metrics are calculated by constructing a manifold consisting of the union of the spheres around each data point, where the radius of each sphere is given by the distance to the kth nearest neighbour in the feature space, and seeing if data points from the other data set lie within this manifold. For identical data sets these metrics will both have a value of 1, while for data sets which do not overlap at all they will have values of 0. I follow Ferjad Naeem et al. (2020) in using $k = 5$ when calculating these metrics.

In addition, I also compare the real and generated light curves at a population level, studying:

- The mean light curve, calculating the mean of all light curves in the data-set in 5 day phase bins as well the standard deviations to represent the diversity of the sample.
- The mean light curve, calculated in the same way as the previous point except shifted so that all light curves in each data-set are set to the same peak magnitude. This allows the diversity of the rises and declines of the real and generated light curves to be studied independently of the peak magnitude.
- The mean colour curves, calculated based on GP fits to the generated light curves, as well as their standard deviation to represent the diversity.

6.2 Results

I will now focus on the generated light curves themselves and their overall properties. Throughout this discussion, I will refer to both real and generated data sets. Here, the real data set corresponds to the set of simulated light curves which are used to train each model while the generated data set corresponds to the set of synthetic light curves generated by the GAN.

As described in Section 6.1, I focus on a variety of different light curve parameters when assessing the performance of the GAN. The training process covers numerous epochs with the quality of the generated light curves varying considerably throughout the training; the fidelity and diversity of different parameters will improve and worsen at different epochs. It may be that at one stage, the colours of the generated light curves match closely with the real set but the generated uncertainties are unrealistic, while at a later stage the generated uncertainties become more realistic but the generated colours decrease in fidelity. As such, it can be difficult to identify the epoch of training at which the generator produces the best results.

To determine the best performing state of the model, I utilise the density and coverage metrics introduced in Section 6.1. Due to the randomness involved in light curve

TABLE 6.1: Sample sizes, redshift cuts, number of training epochs elapsed and density and coverage metrics for various GAN models trained on different CCSN types.

SN Type –	z_{lim} –	N_{SN} –	N_{epochs} –	Density (Individual)	Coverage –	Density (Combined)	Coverage –
Ic	0.25	324	2400	0.83±0.04	0.71±0.03	0.84	0.94
Ic (small)	0.08	32	4400	0.80±0.09	0.89±0.08	0.80	1.0
II	0.1	354	1950	0.97±0.04	0.67±0.03	0.96	0.92
Ib	0.15	256	3500	0.79±0.04	0.60±0.03	0.79	0.86
IIn	0.15	295	6650	0.76±0.03	0.71±0.04	0.76	0.97
IIb	0.15	282	4120	0.58±0.03	0.57±0.04	0.58	0.90
Ic-BL	0.25	113	5460	0.75±0.06	0.77±0.04	0.75	0.94

generation, the values of these metrics will vary each time a data set is generated. To reduce the effect of this, I calculate these metrics for a generated data set 10 times the size of the real set. The models that are presented were selected by finding the epoch which had the highest values for these metrics as well as showing consistent physical properties with the training set. I also calculate these metrics for 10 separate data sets of the same size as the real data set to see how much these metrics vary between each run. The real sample consists of SN light curves with different numbers of time steps; to create the generated sample, I use the same distribution of time series lengths as for the real sample.

The number of training epochs required for good performance varies for different SN types due to the random nature of model training. The number of epochs elapsed and density and coverage metrics, both across 10 individual data sets the size of the real data set and across all 10 combined, are shown in Table 6.1. Part of the motivation for using a WGAN was to give a more stable training process where the model can continuously improve with further training. It may be the case that leaving the model to train for much longer periods of time will lead to the generator approaching an optimal state for all light curve parameters, however this is very computationally expensive.

As discussed in Section 5.4.1, when training the models I apply a redshift cut to control the sample size and select only SNe with higher signal-to-noise photometry. For most SN types I consider, I use a sample of $\sim 250 - 350$ for training as a compromise between sample size and computational expense of training. This involves a redshift cut at either 0.1, 0.15 or 0.25 depending on the SN type. The exception to this is for SNe Ic-BL, where a redshift cut at 0.25 gave a smaller sample size of 113. This reduced sample was used to ensure consistent redshift ranges with the other SN types. In one case, I also made a lower redshift cut at 0.08 for SNe Ic to test the GAN on a smaller training sample. The redshift cuts and sample sizes used for each SN type are shown in Table 6.1.

6.2.1 SNe Ic

I will begin with a model trained on SNe Ic light curves, with a redshift cut applied at 0.25 to give a total sample size of 324 SNe. SNe Ic were chosen arbitrarily as an initial class to explore the performance of the GAN. Figure 6.1 shows some examples of generated light curves for this model. Overall, the light curves have the expected morphology in each band, but it is important to verify that their physical properties are realistic. Figures 6.2, 6.3, 6.4 and 6.5 show the distributions for peak apparent magnitudes, Δm_{15} and rise times for each of *griz* bands as well as peak colours. The peak apparent magnitudes in each band for the generated sample agree well with the real sample. For both rise time and Δm_{15}, the real data set does not follow a simple distribution such as a Gaussian or skewed Gaussian and the generated data set struggles to perfectly match this. However, both distributions cover the same broad set of values and the generated data set does give physically reasonable light curves. Based on peak colour, the generated data set gives a slightly broader set of colours compared to the real data set but covers a similar range of values.

To assess whether the generated data set is physically reasonable across all parameters, I consider the density and coverage as outlined in Section 6.1 and presented in Table 6.1. This model has a density value of $\sim$0.84, demonstrating that the vast majority of generated light curves sit within the distribution of real light curves and that this model has good fidelity. Moreover, with a generated data set 10 times the size of the real data set the coverage of this model is 0.94 demonstrating that it has very high diversity and is able to almost entirely reproduce the light curve variability seen in the real data set.

Based on these physical properties, the light curves generated by the GAN show good agreement with the real data set. To consider the full light curve evolution, I also examine the overall light curve morphology produced by the generator. Figure 6.6 shows the mean light curves and their associated standard deviation for each of the real and generated data sets, and Figure 6.7 also shows the light curves, this time expressed as a shift from peak magnitude. Overall, the mean light curves from the two samples are in good agreement and the generated sample is able to capture most of the diversity in the real sample. Discrepancies are noticeable between the two; for example, the generated data set lacks fast declining light curves in *z*-band which can also be seen in the Δm_{15} distributions in Figure 6.3.

Figure 6.8 shows the $g-r$, $r-i$ and $i-z$ colour curves for the real and generated samples. The $g-r$ curve for the generated data set is in close agreement with the real data set though does not fully capture the diversity of the real data set. For $r-i$, the generated data set shows the same overall evolution as the real data set, albeit with a larger spread around peak and with an early decrease that is not present in the real light curves. For $i-z$, generated and real data sets also agree well although the

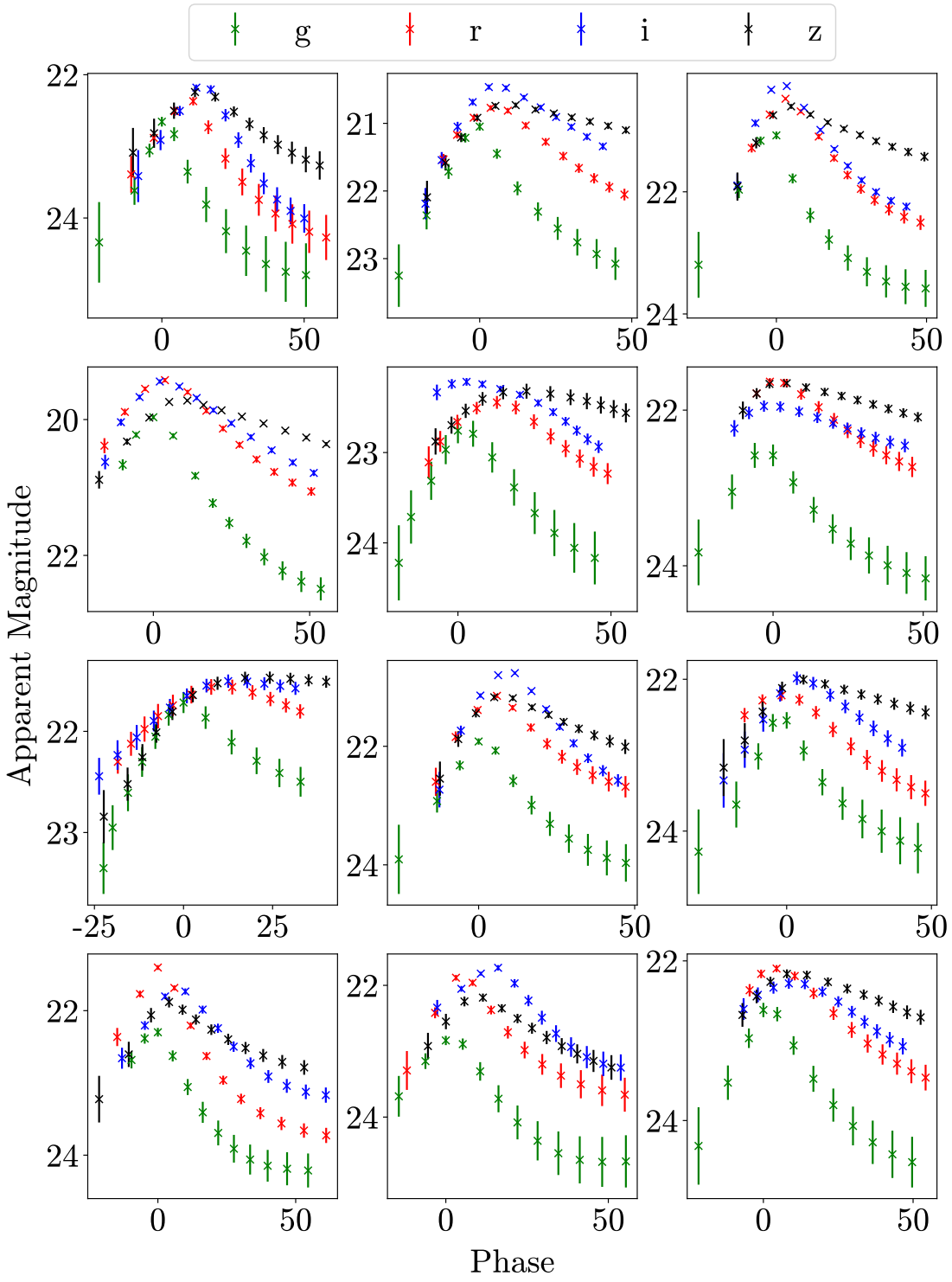

FIGURE 6.1: Example light curves for the GAN model trained to generate SNe Ic.

generated light curves are slightly bluer at later times. Overall, the GAN is able to capture the expected colour evolution of the real data set.

Figure 6.9 shows the apparent magnitude uncertainty plotted as a function of apparent magnitude for each of the real and generated data sets, in magnitude bins

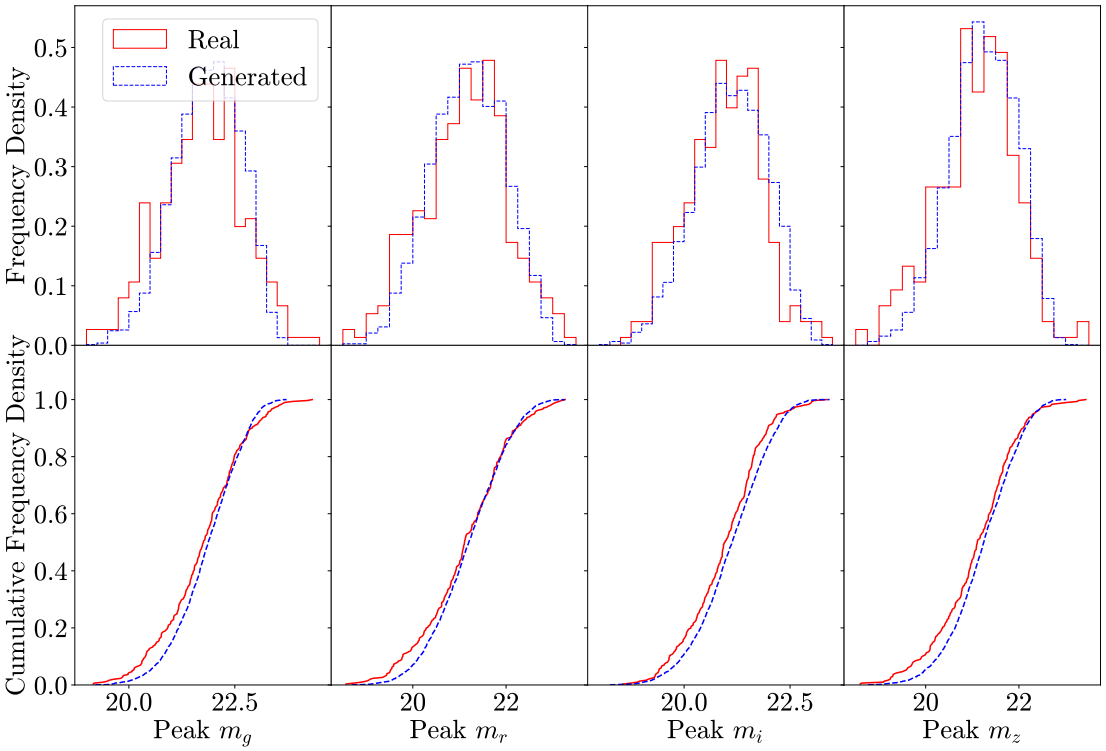

FIGURE 6.2: Peak apparent magnitude distributions in *griz* bands for both the real data set used to train the SN Ic GAN model and the synthetic data set generated by the GAN.

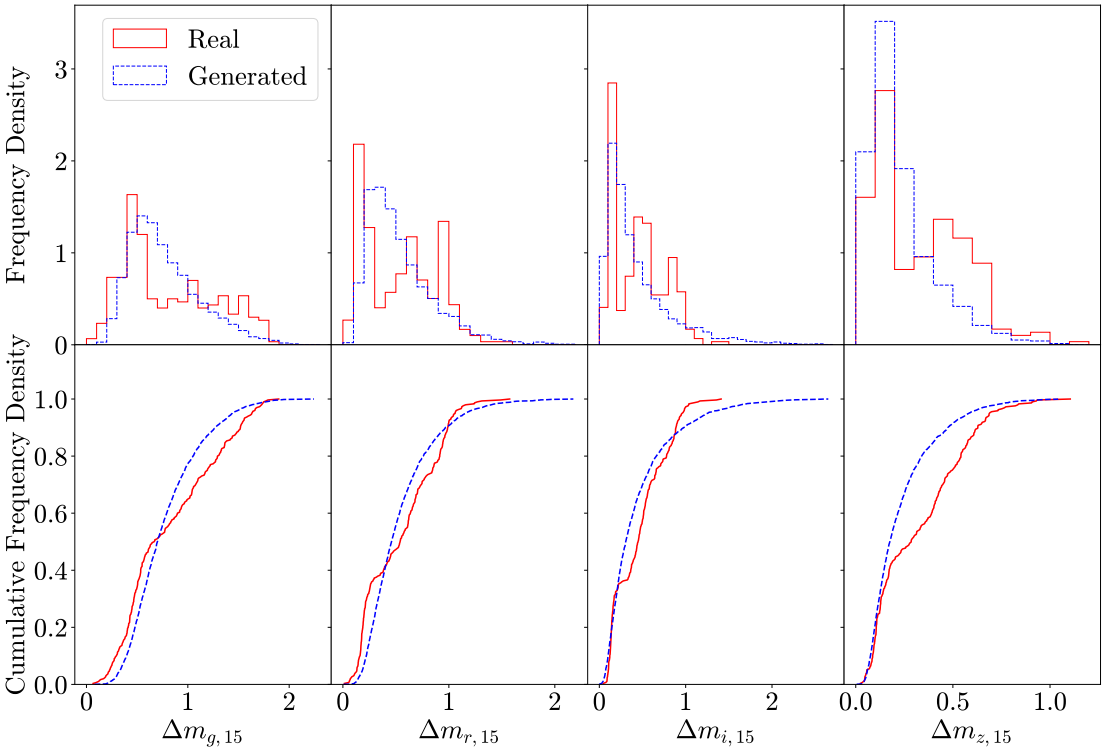

FIGURE 6.3: As per Figure 6.2 but for Δm_{15}.

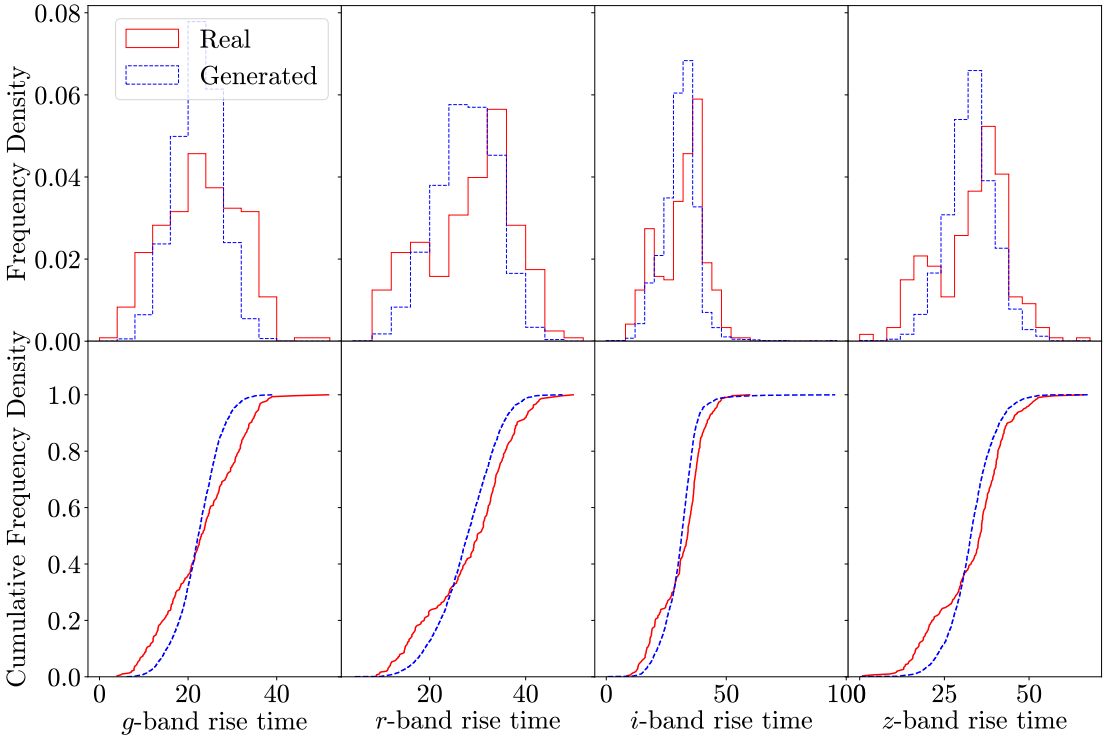

FIGURE 6.4: As per Figure 6.2 but for rise time.

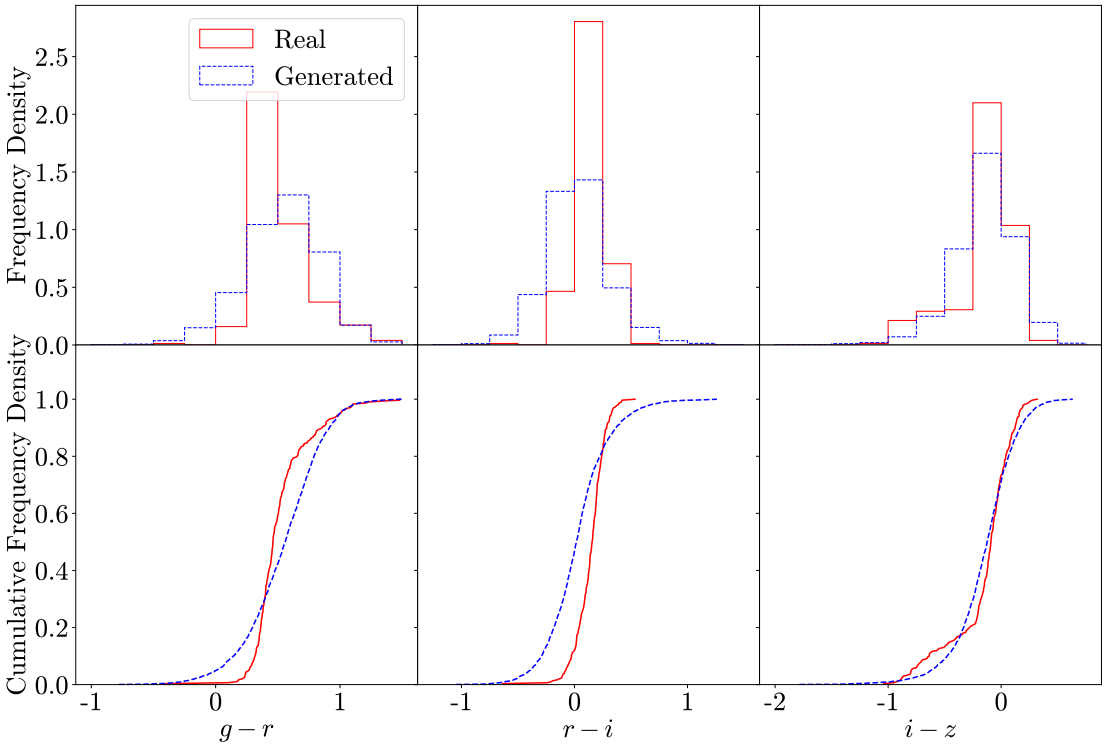

FIGURE 6.5: As per Figure 6.2 but for peak $g-r$, $r-i$ and $i-z$ colours.

from 18 to 25 mag with a width of 0.5 mag. The y-values and their uncertainties respectively represent the median and 16th and 84th percentiles for the values in each bin. Comparing the real and generated data sets, the median values of the errors are

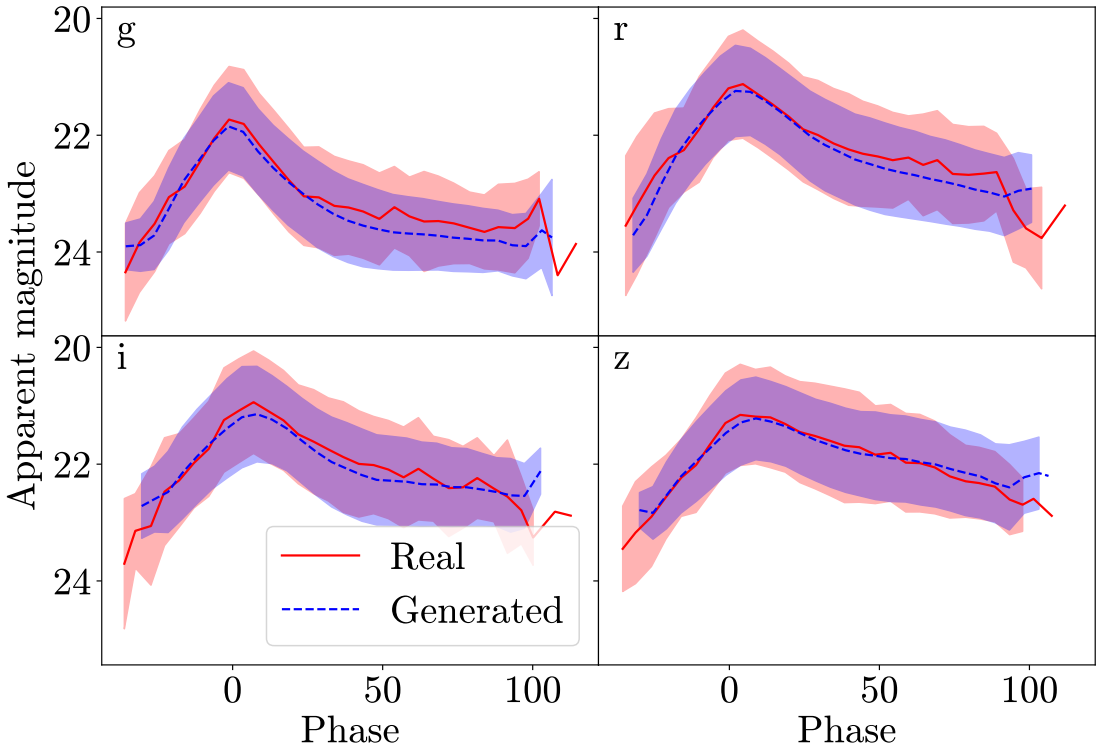

FIGURE 6.6: The mean and standard deviation of all light curves in the real and generated SNe Ic samples for *griz* bands.

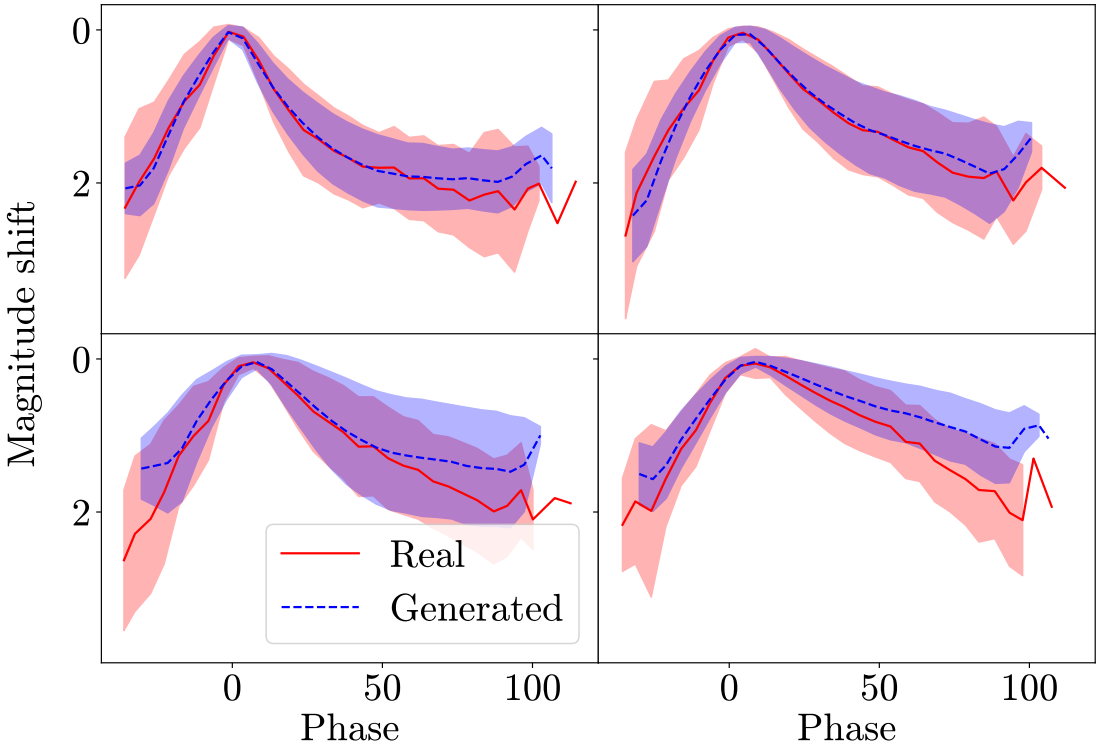

FIGURE 6.7: As per 6.6 except with light curves scaled to give the decline from peak in mags.

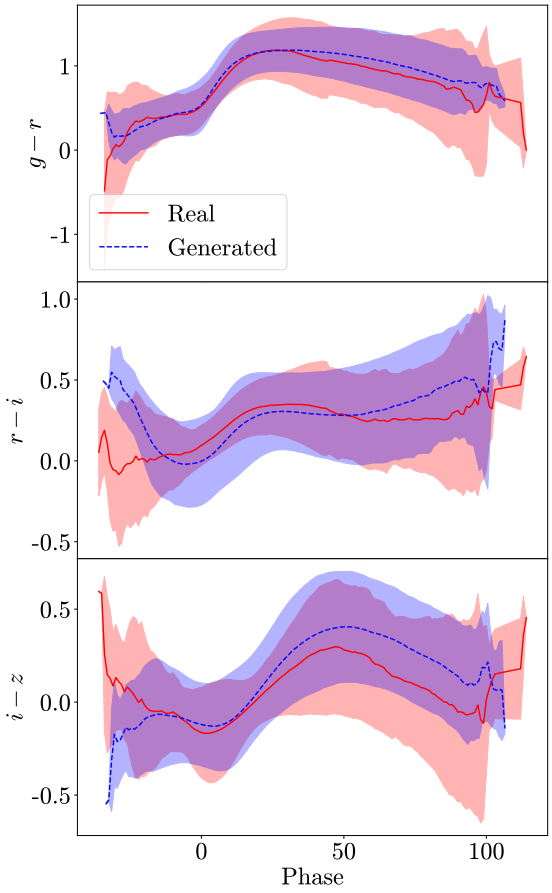

FIGURE 6.8: As per 6.6 except showing $g-r$, $r-i$ and $i-z$ colour curves.

very similar and both show the same rise in magnitude error at fainter magnitudes. The main difference is that the spread in uncertainty values is much smaller for generated data than for real data. There is also an unrealistic drop in magnitude uncertainty below $\sim$24 mag in z-band, likely because there are few data points in the real data set in these bins so the GAN has not learned to generate these points accurately. Overall, the model is generating physically realistic errors although there is further room for improvement.

As discussed at the beginning of this section, it is not easy to judge the number of training epochs after which the GAN produces the best light curves. For example, at earlier epochs the GAN was better able to reproduce the decline rates of the real data set and Figure 6.7 showed closer agreement between the real and generated data sets. However, at these epochs the distribution of peak apparent magnitudes was not as well represented by the generator meaning that Figure 6.6 shows worse agreement between the data sets. The main challenge involved is making sure that all physical properties are represented well simultaneously. Nevertheless, these generated light curves show good agreement with the real data across all physical properties. Further refinement of the structure of the model and training process will only serve to improve this.

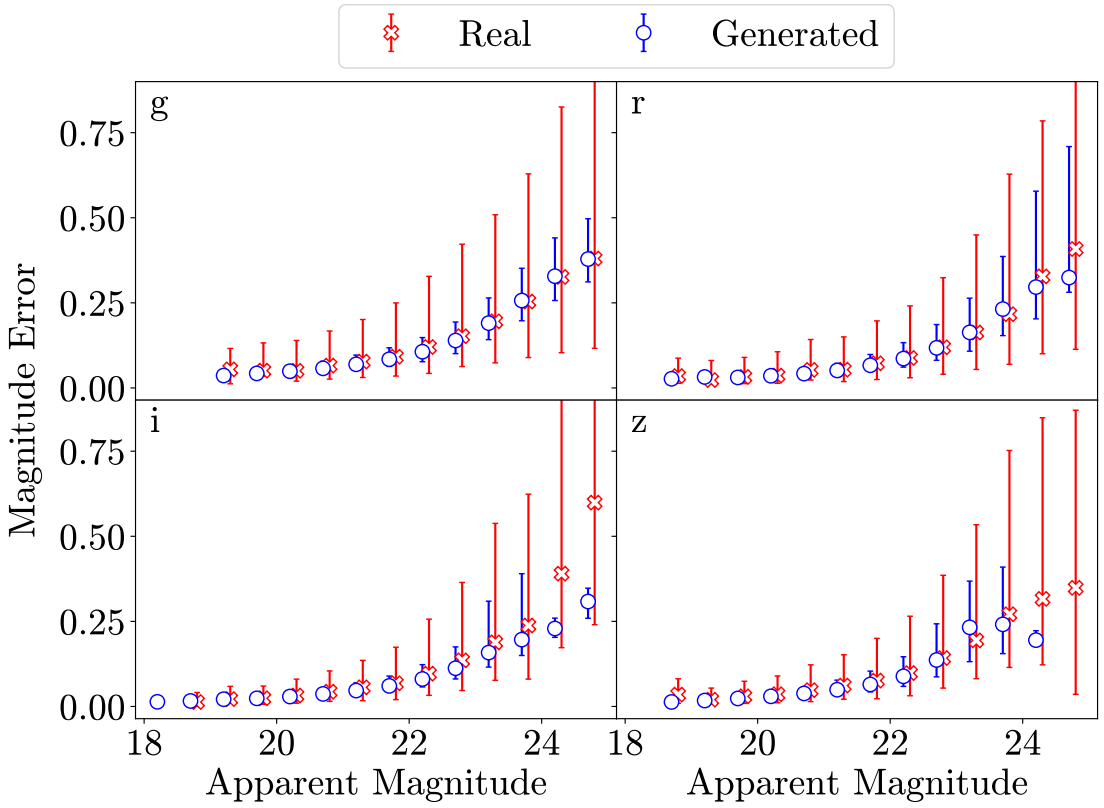

FIGURE 6.9: Apparent magnitude uncertainty as a function of apparent magnitude for each of the real and generated SNe Ic data sets. Values shown are the mean and standard deviation of all uncertainties in magnitude bins from 18 to 25 mag with a width of 0.5 mag.

6.2.2 SNe Ic (Small Training Sample)

After verifying that the GAN is indeed able to generate physically realistic light curves, I next repeat the process with a much smaller training set. The goal of this is to investigate whether GANs can be used to augment small data sets, which would allow this technique to be used for rare SN subtypes with few examples. I again focus on SNe Ic but this time use a much lower redshift cut of 0.08 which gives a sample size of 32 SNe. In Section 6.2.1, I presented generated light curves as well as physical analysis of the generated light curves. From hereon in, generated light curves will be presented here but for brevity all remaining plots will be presented in Appendix A.

Figure 6.1 shows some examples of generated light curves for this model. As for the model presented in Section 6.2.1, the generator is able to learn the correct morphology of the light curves despite having been trained on $\sim$ 10 per cent of the data. The ability of the GAN to learn to generate SN light curves despite the small size of the training set is very reassuring and demonstrates that this method has the potential to be used for SN types where only a few examples are available. Based on the physical properties of the light curves as presented in Appendix A.1, the generated light curves

also closely resemble the training set physically despite the small data set. Across all 15 calculated physical properties combined, the density of the model is 0.80 demonstrating that the generated light curves have good fidelity. For a generated data set with 10 light curves for each real light curve, the coverage of this model is 1.0 demonstrating that the model is able to completely reproduce the diversity seen in the training sample.

The only way in which this model performs noticeably worse than the model in Section 6.2.1 is for the generated uncertainties, with the generator failing to produce uncertainties consistent with the training data for apparent magnitudes with little coverage in the training set. Despite this, the generated uncertainties are still overall in agreement with the training set at brighter magnitudes and further refinement of the model will help to minimise the discrepancies.

6.2.3 SNe II

I next consider training a GAN to generate light curves for SNe II; Figure 6.11 shows some examples of generated light curves for this model. As for the SNe Ic models, this model has also learned the correct overall light curve morphology including the plateau that is associated with some SNe II. Based on the density and coverage of the generated data set, this model is able to produce light curves with very high fidelity and diversity; across a generated data set 10 times the size of the training set, the density is 0.96 and the coverage is 0.92. The light curve analysis presented in Appendix A.2 also shows that the generated data set closely matches the real data set in terms of physical properties. The most significant difference is the reduced spread in magnitude error in the generated data set compared to the real data set at brighter magnitudes, similar to the SNe Ic models. There are also some discrepancies in the colour evolution between the real and generated data sets, particularly at later times for $r - i$, although overall both data sets show similar trends. Taking all this into account, the GAN performs well when generating SNe II.

6.2.4 SNe Ib

Figure 6.12 shows some examples of generated light curves for the model trained on SNe Ib. As for SNe Ic, this model has learned the correct bell-shaped light curve for SESNe. Furthermore, Appendix A.3 presents comparison of the real and generated light curves for this model and demonstrates that the model generates SNe with comparable properties to the training set and encompassing the variability seen. Across a generated data set 10 times the size of the training set, the density is 0.79 and the coverage is 0.86. While this is lower than for SNe Ic and II, this still demonstrates that the model achieves good fidelity and diversity.

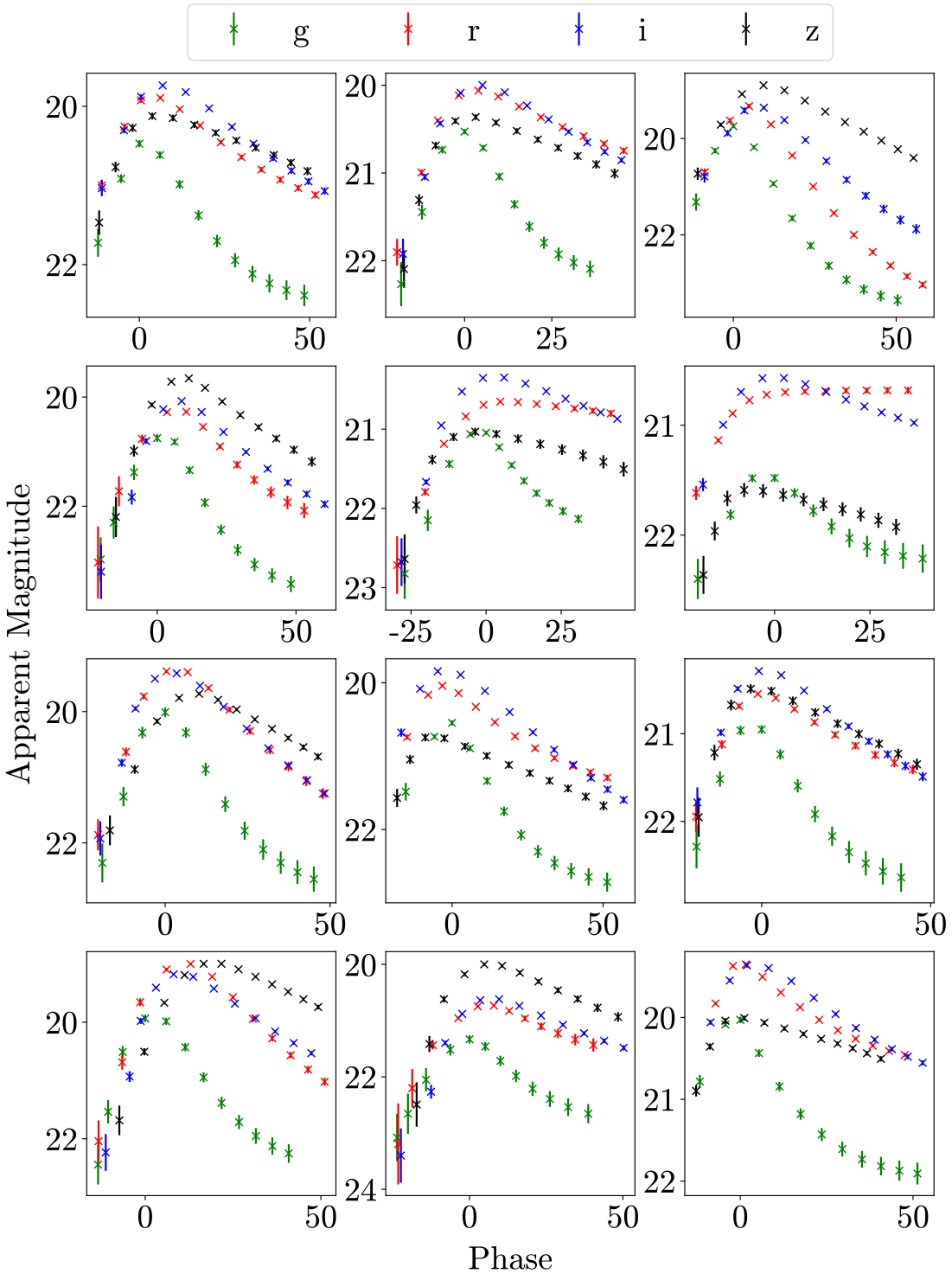

FIGURE 6.10: Example light curves for the GAN model trained to generate SNe Ic on a small data set of 32 SNe.

6.2.5 SNe IIn

Figure 6.13 shows some examples of generated light curves for SNe IIn, and Appendix A.4 presents comparison of the real and generated light curves for this model. Across

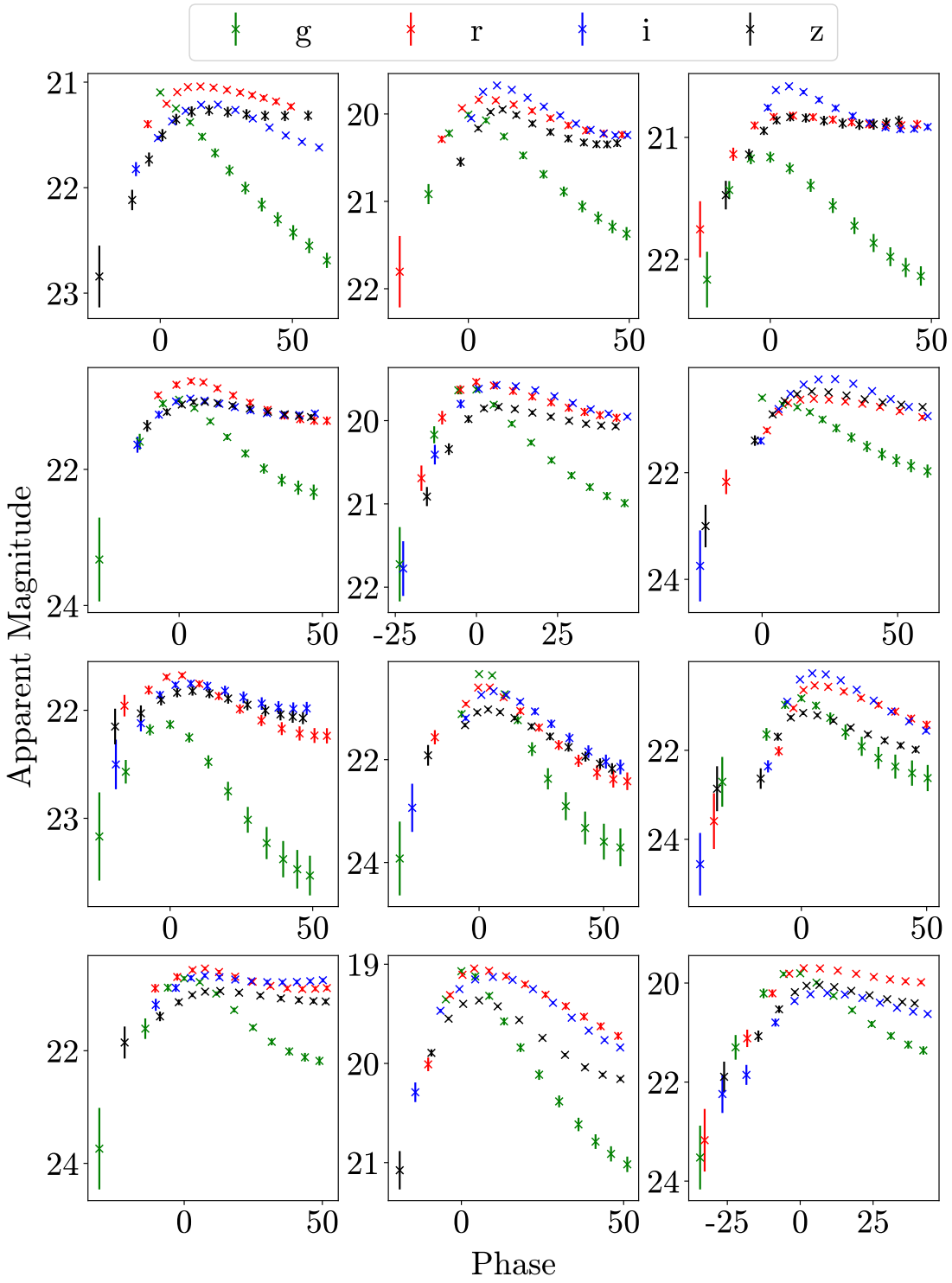

FIGURE 6.11: Example light curves for the GAN model trained to generate SNe II.

light curve morphology, peak apparent magnitude, rise time and colour evolution the generated data matches the training set well. The main discrepancies are in Δm_{15} where the GAN does not capture the double peaked nature of these distributions and in the $i - z$ colour curve. Across a generated data set 10 times the size of the training set, the density is 0.76 and coverage is 0.97. While this model is lower fidelity than

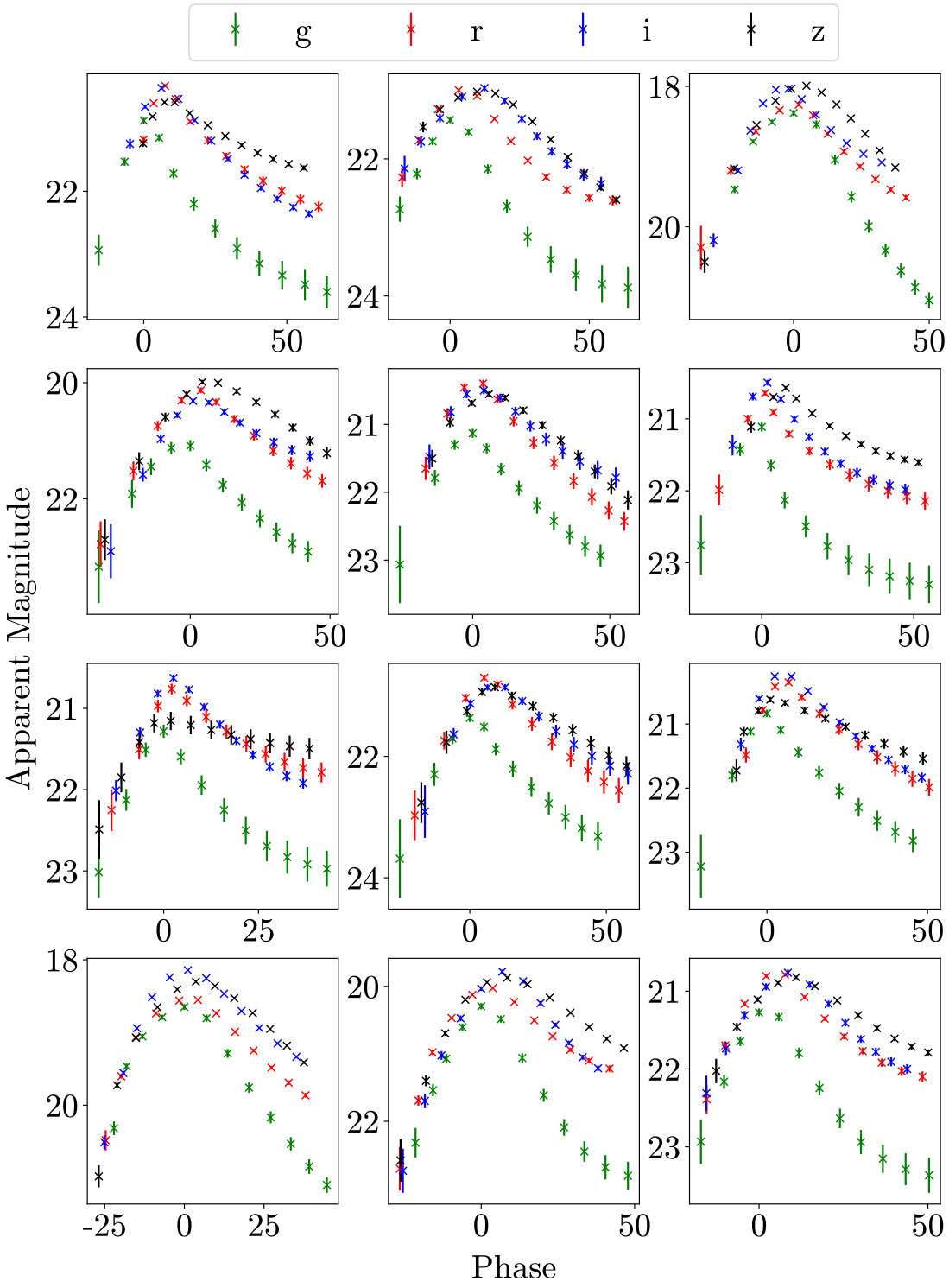

FIGURE 6.12: Example light curves for the GAN model trained to generate SNe Ib.

others so far, the high coverage demonstrates that it is still able to capture the full variability of the training set. It would therefore be possible to select only generated light curves which lie on the real data set manifold outlined in Section 6.1 and obtain a data set with much higher fidelity which also encompasses the diversity of the real data.

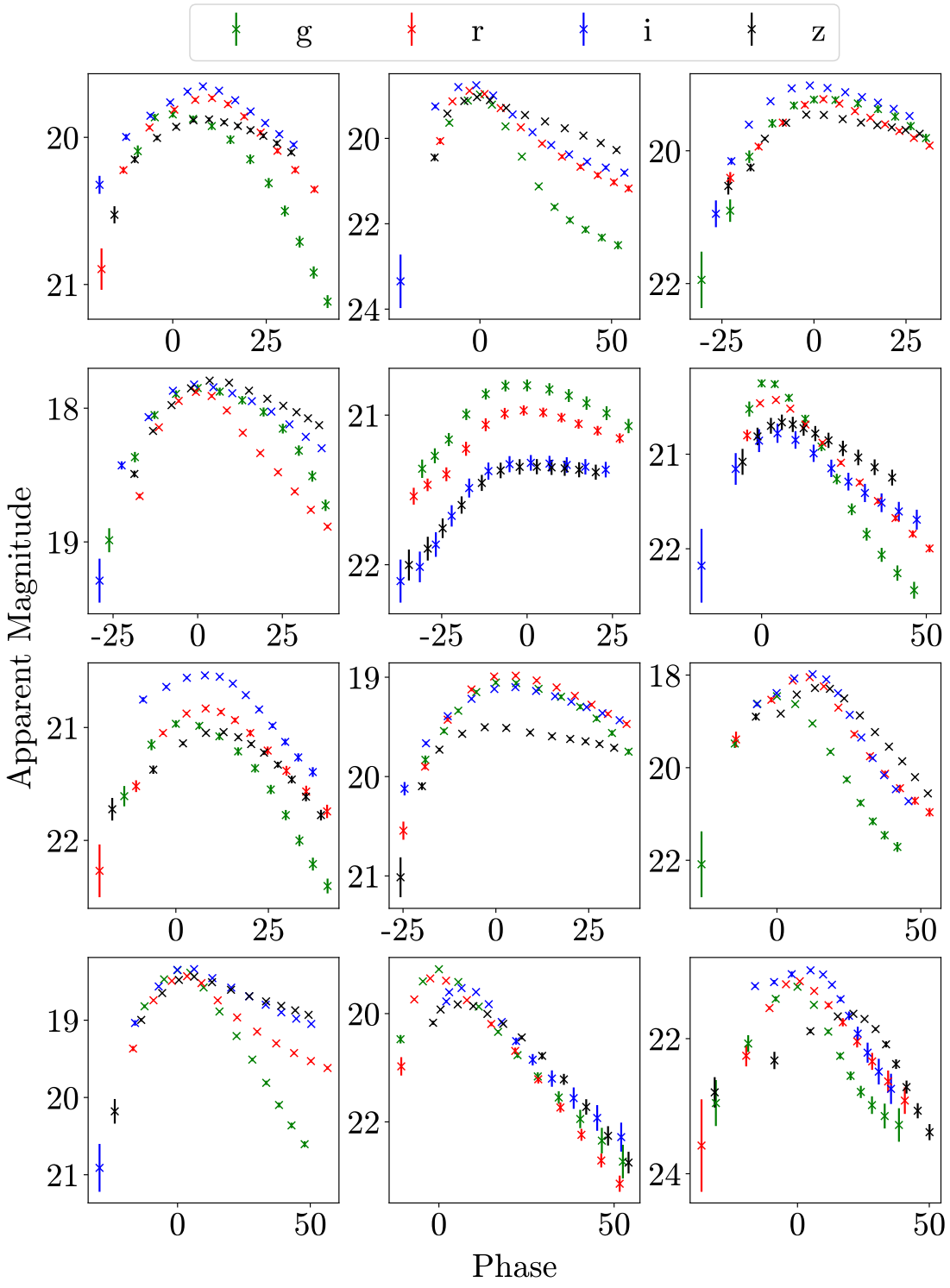

FIGURE 6.13: Example light curves for the GAN model trained to generate SNe IIn.

6.2.6 SNe IIb

Figure 6.14 shows some examples of generated light curves for SNe IIb, and Appendix A.6 presents comparison of the real and generated light curves for this model. As for SNe Ib and Ic, this model has learned the correct bell-shaped light curve for SESNe,

although some light curves show an unexpected rise in g-band at late times. Physical properties such as peak apparent magnitude and rise time, and the overall light curve and colour evolution, indicate that this model is generating physically realistic light curves. However, across a generated data set 10 times the size of the training set this model has a density metric of only 0.58. This is far lower than for any other SN type, suggesting that this model produces much less realistic light curves when considering all light curve properties at once. Despite this lower fidelity, the coverage obtained is 0.90 demonstrates that it is still able to capture most of the variability of the training set. As mentioned in Section 6.2.5, a data set with much higher fidelity could be obtained by selecting only generated light curves which lie on the real data set manifold outlined in Section 6.1. Overall, while this model is worse for other SN types it is still of use for realistic light curve generation.

6.2.7 SNe Ic-BL

Figure 6.15 shows some examples of generated light curves for SNe Ic-BL, the final SN type considered, and Appendix A.6 presents comparison of the real and generated light curves for this model. Light curve morphology, peak apparent magnitude, rise time and colour evolution overall agree well between these data sets. The main differences are that the generated data set lacks faster declining objects in i and z bands and that the colour evolution at late times for the generated data shows unusual behaviour, but this will be dominated by only a few light curves which continue this late. Across a generated data set 10 times the size of the training set, the density and coverage of this model are 0.75 and 0.94, similar to the model for SNe IIn.

6.3 Discussion

As demonstrated by work such as Motamed et al. (2021) and García-Jara et al. (2022), augmenting data sets using GANs can help to improve the performance of classifiers. The question posed in the previous chapter is whether a similar approach could be used within the field of SNe in order to improve the performance of photometric classifiers. In this section, I will summarise the findings from Section 6.2 and discuss how the work I have presented here can be developed for wider use.

6.3.1 Summary of Findings

The aim of this work was to assess whether GANs could be used to generate physically realistic light curves. In Section 6.2, I presented individual examples and population demographics for generated light curves of a variety of types of CCSNe. In

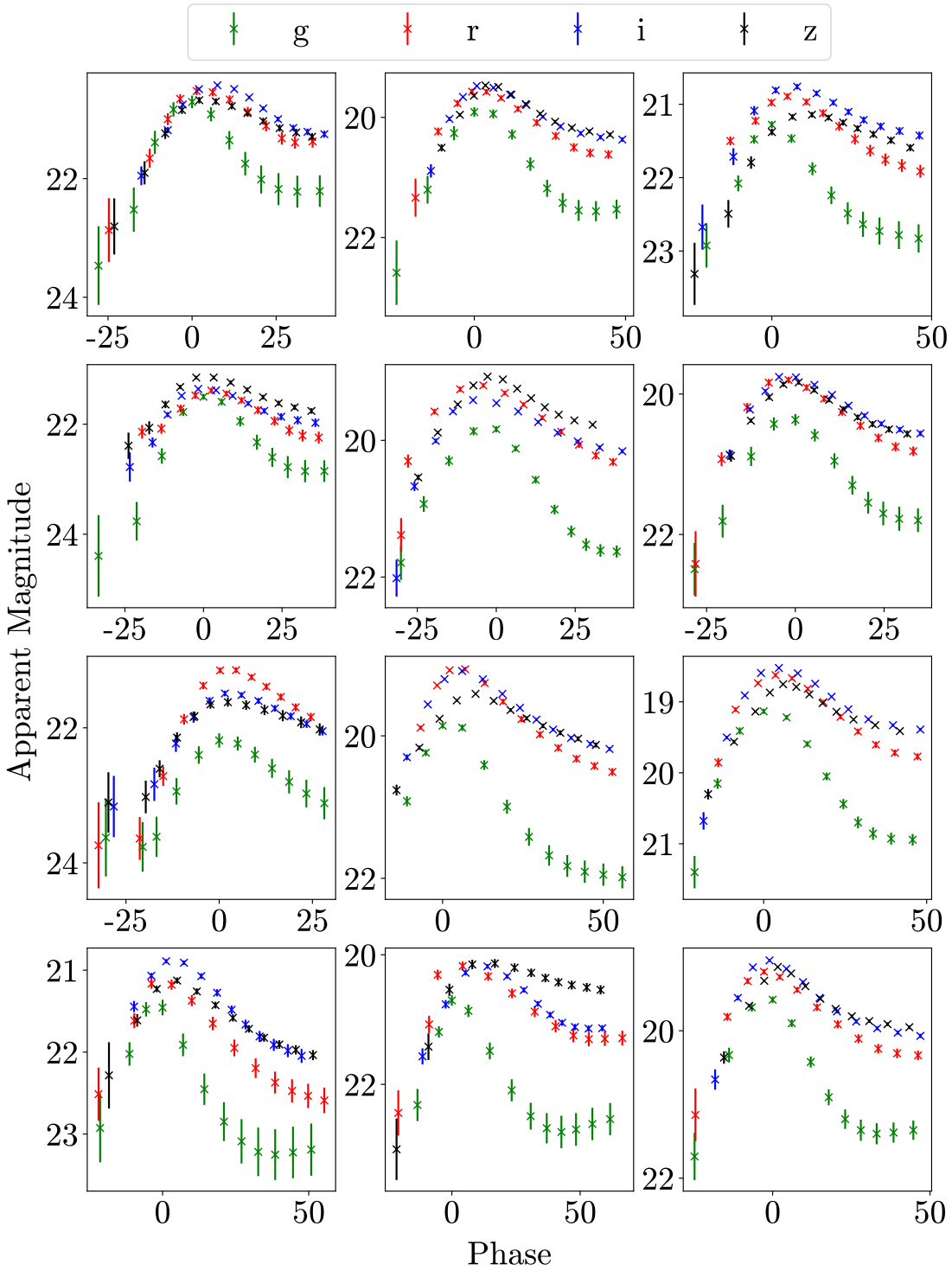

FIGURE 6.14: Example light curves for the GAN model trained to generate SNe IIb.

brief, I find that this method can indeed be used for light curve generation. While there remains room for improvement and performance varies across SN type, GANs were able to generate physically realistic light curves based on characteristics such as rise time, decline rate and colour. Populations of generated light curves also closely follow the samples they were trained on in terms of peak apparent magnitude, and

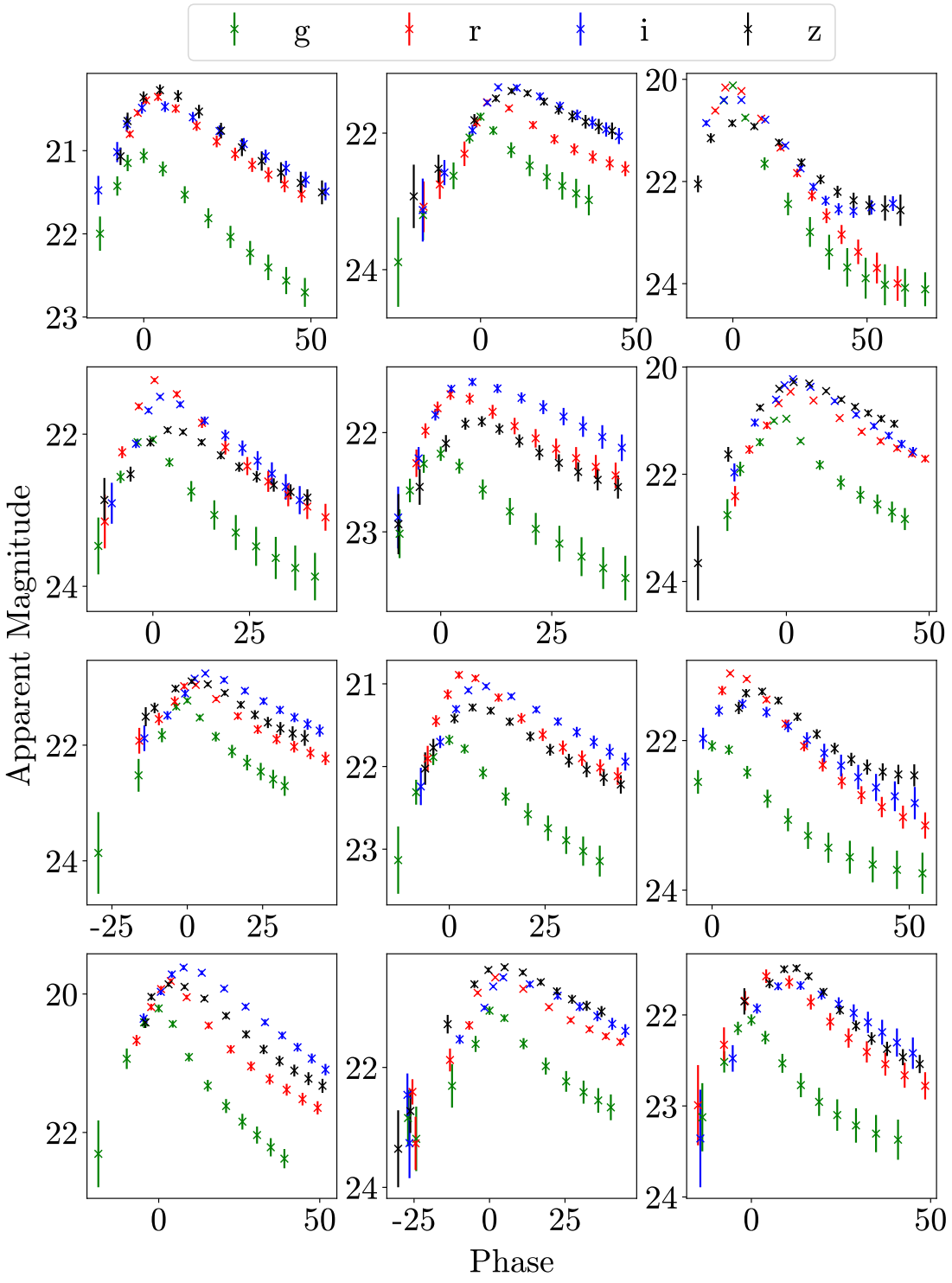

FIGURE 6.15: Example light curves for the GAN model trained to generate SNe Ic-BL.

the generated light curves encompass well the diversity seen in the samples used to train these models. In terms of light curve morphology, different classes also show expected features; for example, generated SNe II show the plateau associated with SNe IIP while SESNe have light curves with the expected bell-shaped rise and decline.

Most of these models were trained on data sets consisting of $\sim 250 - 350$, however even a GAN model trained on 32 SNe Ic light curves was still able to generate a data set that closely resembled the sample on which it was trained. This demonstrates the power of GANs to augment even small data sets, which means that this approach could be used for rare SN types which do not have many observed examples and which are not understood well enough to be simulated. The results presented in this thesis underline the potential of GANs to be a valuable asset for photometric classification.

6.3.2 Future Improvements

This work was intended as a proof-of-concept to test whether GANs could be used for light curve generation, and succeeds in demonstrating that this is the case. Now that this has been established, there are a number of improvements that can be made to enhance this approach for use within the wider community.

6.3.2.1 Hyperparameter Optimisation

A simple and yet significant improvement to the model would be to focus more on hyperparameter optimisation. The hyperparameter values I have used have mostly been based on what has been used in other work; while I have done some exploration of different hyperparameter values, particularly for the learning rate of the optimiser, the training process is too computationally expensive to have allowed for more exploration in the time available. Further refinement of the hyperparameters of the model will allow for improved light curve generation.

6.3.2.2 Redshift Generation

A major addition that could be made to this approach is to incorporate redshift generation. This was not included at this stage as it adds additional complexity for the generator to learn; the model would be required to generate a realistic redshift on top of realistic observer-frame photometry. However, incorporating redshift generation to the model would not be technically challenging; redshift would simply be included as an extra column in the data produced by the generator and would also be passed to the critic, which would be able to assess whether the generated redshifts were realistic. Now that this technique has been shown as able to generate realistic light curves, the addition of redshift generation would be valuable as this would allow the GAN augmentation approach to be applied to photometric classifiers which do use redshift for prediction.

6.3.2.3 Generation of SNe Ia

Given that samples of CCSNe are typically smaller than SNe Ia, for this work I have focused solely on generation of the former. However, the exact same techniques could be easily applied to the generation of SNe Ia light curves given a suitable training set. Numerous light curve fitting tools for SNe Ia are currently used when carrying out cosmological analyses with SNe Ia, for example SALT2 (Guy et al., 2007), SNooPy (Burns et al., 2011) and BayeSN (Mandel et al., 2022). After the incorporation of redshift generation to the GAN model, these light curve fitters could be applied to GAN-generated SNe Ia light curves to further test whether their physical properties are consistent with the sample on which they are trained.

6.3.2.4 Combining All Models

Throughout this analysis, I have focused on training separate models for each SN type. This approach has worked well and has been shown to reproduce the expected light curve characteristics of the different SN types. However, it would be preferable to include all of these SN types into a single model. A modified GAN architecture known as a Conditional GAN (CGAN), which is able to generate data based on a specified label, was proposed in Mirza & Osindero (2014). With this approach, it would be possible to train a single GAN model that is able to generate different light curves depending on the SN type specified.

During the early stages of this work, I did in fact experiment with CGANs though opted against using them because I found that the generator produced very similar light curves regardless of the label specified meaning that the CGAN did not work as expected. This motivated the decision to train separate models for separate SN types to ensure that the different classes were represented properly by the generator. However, this was prior to the use of the WGAN with gradient penalty approach discussed in Section 5.2.3, which gave far better performance than a traditional GAN. With this in mind, revisiting the CGAN architecture while also incorporating the benefits of the WGAN approach could well allow realistic light curve generation across multiple SN types in a single model.

6.3.2.5 More Realistic Noise

As part of this work, I have made a number of decisions to assist the generator. The light curves in the training set were smoothed using GP interpolation, and redshift cuts were applied to ensure that the training set consisted of high signal-to-noise photometry. These decisions were made to simplify the data the generator was required to produce when establishing whether GANs could be used to produce SN

light curves. Now that I have shown this is possible, a GAN could be trained without these selections and fits in favour of smooth, high signal-to-noise light curves to assess whether the model is able to generate realistic noise.

6.3.2.6 Training on Real Photometry

On a related note to the previous point, for this work I have trained based on simulated data. This provided a large data-set to test the GANs on and allowed for experimentation with different sample sizes. However, were this approach to be used for augmenting data-sets for photometric classifiers it would be important to apply the light curve generation technique to real observed SN photometry to provide a fully data-driven augmented data-set.

6.3.2.7 Using GAN-generated Photometry to Train Classifier

One final key test of the GAN models presented here would be to train a photometric classification model entirely on GAN-generated light curves, as mentioned in Section 6.1. Testing how well this classifier is able to generalise to real light curves would provide an additional quantitative method of assessing the performance of the GAN.

6.4 Summary

The key question this work sought to address was whether GANs could be used to generate physically realistic light curves. In this chapter I presented light curves generated by GAN models trained on a variety of different CCSN types, as well as their corresponding physical properties. The results of this work can be summarised as follows:

- GANs can be used to generate physically realistic light curves based on peak apparent magnitude, Δm_{15}, rise time and peak colour as well as the overall light curve and colour distributions. While there are some discrepancies, overall the light curves generated by the GAN models have similar physical properties to the real data sets the models were trained on. Characteristic features, such as the plateau often seen in the light curve of SNe II, are produced by the GAN.
- GANs can be trained on small data sets, consisting of ~ 30 light curves, and still produce physically realistic light curves which would make them suitable for use with rare SN types with few known examples.

- The ability of GANs to generate realistic SN light curves means that they can be used to augment training sets for photometric classifiers and have the potential to significantly improve their performance.
- Further work will serve to improve the quality of generated light curves and add additional functionality. Hyperparameter optimisation will allow the GANs to generate even more realistic light curves, and the GAN can be trained to generate redshifts as well as photometry and used to generate multiple SN types in a single model.

Chapter 7

Conclusions

In this thesis, I have focused on the study of the population of CCSNe in three separate ways; analysing their broad population demographics, carrying out detailed analysis of a single unusual object and exploring ways to improve photometric classification of these objects to assist future work. In this final chapter, I summarise the main results and impact of this work, and consider the future of such analyses.

7.1 Summary of Results

I will begin this section by summarising the key results presented in this thesis.

7.1.1 Core-collapse Luminosity Functions

In Chapter 3, I presented luminosity functions of samples of SNe II and Ibc observed by DES. The deep photometry provided by DES means that this luminosity function is based on CCSNe at higher redshift than previous work, which allows the possibility of redshift evolution in the luminosity function to be investigated. To this end, I compare the DES luminosity function with previous work from LOSS presented in L11 as well as another luminosity function I calculate for the ZTF core-collapse sample. To analyse the significance of differences in the luminosity functions, I carry out two-sample KS tests between these populations, taking into account a V_{max} correction to mitigate for the effects of Malmquist bias.

Comparisons between the samples of SNe II do indicate some differences, with differences of 3.0σ when comparing DES with LOSS and 2.7σ between ZTF and LOSS. Visually, SNe Ibc appear to follow the same trend although with much lower significances of below 2.0σ, meaning that these differences may not be real. Overall, these results do raise redshift evolution in the luminosity function as a possibility. I

consider a number of other explanations for this difference, including incompleteness in the samples, differences in the host galaxies properties, metallicity differences and differing levels of host galaxy extinction, but find no clear evidence that any of these effects could explain the differences seen. However, without measurements of the level of host extinction for these SNe the possibility that differences are caused by differing host extinction cannot be ruled out.

7.1.2 Host Galaxy Demographics

Within Chapter 3, I also focus on the corresponding host galaxies for SNe in the luminosity function samples. The properties of these host galaxies are calculated based on SED fits to photometry taken from DES for the DES SNe and from SDSS for the LOSS and ZTF SNe. This analysis uses rest-frame $U - R$ colour as a proxy for star formation, since this correlates well with sSFR and is better constrained from SED fitting.

My results show an unexpected and as-yet unexplained difference in rest-frame $U - R$ colour between CCSN hosts in DES and ZTF; overall, DES hosts are bluer than their ZTF counterparts for SNe II, with differences in excess of 3.5σ from both two-sample KS and AD tests. I explore numerous possible causes for this effect including evolution of galaxy SFR and metallicity with redshift, selection bias and systematic effects due to the different photometry used. However, none of these effects are able to explain the difference between the galaxy populations. For the higher redshift DES sample, CCSNe appear to be exploding in bluer host galaxies than for the more local ZTF sample for some unknown reason.

7.1.3 An Unusual SN IIb

In Chapter 4, I carry out an in depth analysis of DES14X2fna, an unusual SN IIb identified while analysing the full CCSN sample. This object had a peak r-band absolute magnitude of -19.37$\pm$0.05, but also declined rapidly after peak with a decline rate in the tail of 4.30 $\pm$ 0.10 mag (100d)$^{-1}$ in r-band. To put this into context, I compared DES14X2fna with a sample of 22 other SNe IIb. DES14X2fna was nearly one mag brighter at peak than any other member of its class save for the similarly unusual ASASSN-18am, and also declined significantly faster than any other member of its class in the tail.

The unusual properties of DES14X2fna raised the question of whether it could be powered by ^{56}Ni decay as is typical for SNe IIb or whether an additional power source is required. To consider this possibility, I performed semi-analytic fits to the observed photometry of DES14X2fna for a variety of different power sources. I find that ^{56}Ni

decay alone is not able to power DES14X2fna and that the addition of either interaction with surrounding CSM or a magnetar improves the quality of the model fits to observations. No signs of CSM interaction are observed in spectroscopy of DES14X2fna, although that does not rule out the possibility that it may have occurred. Overall, DES14X2fna shows that some SNe IIb require additional physics beyond ^{56}Ni decay to explain their properties. In addition, I also consider the possibility that similar objects could be misclassified as SNe Ia by photometric classifiers - while this can happen in some instances, the effect is small and the rarity of these events means that they are unlikely to be significant contaminants.

7.1.4 Generating Synthetic Supernovae

In Chapter 5, I focus on training a GAN to generate realistic synthetic SN light curves which could be used to augment data-sets used to train photometric classifiers and ultimately improve their performance. Similar techniques have been applied both elsewhere in astronomy and in other fields. I explore the use of an RNN-based GAN, which would allow for the generation of variable length time series. The purpose of this work was to test whether GANs can be used to generate physically realistic SN light curves, and the results I obtain demonstrate that this is the case – the GANs I have trained are able to generate realistic observer-frame light curves in terms of rise times, post-peak decline and peak apparent magnitude across a variety of CCSN types. While further work is required to allow for the generation of redshifts and more realistic noise, the results obtained are very promising for the use of GAN augmentation in photometric classification.

7.2 Impact and Future Perspectives

The analysis and results presented in this thesis have given new insights into the properties of CCSNe and their host galaxies as well as laying significant groundwork for future study of these objects. I will now consider the impact of my findings and future perspectives of the study of CCSNe.

7.2.1 An Evolving Supernova Population?

The luminosity functions I present for DES and ZTF will be of great benefit going forward from the perspective of survey simulations. Previous work has relied on the very local sample from LOSS, and the construction of these luminosity functions means that future work looking to simulate CCSNe at higher redshifts will be able to base analysis on real SN samples at those redshifts.

Beyond this, the comparison of the CCSN luminosity functions from DES, LOSS and ZTF has raised the possibility of redshift evolution in the intrinsic luminosity function of these objects. It is important to note that while the results I have presented do show some differences between the samples, they do not rule out the possibility that such differences could simply be caused by differing levels of extinction from the host galaxies of these SNe. This analysis does not provide conclusive evidence in favour of an evolving luminosity function. Nevertheless, the differences that are seen are of great interest. A luminosity function which evolves with redshift would signify that the CCSN population evolves with cosmic time, which in turn would open the question as to what might cause this. Galaxy properties, and therefore the properties of SN hosts, are known to evolve with redshift which may in turn cause an evolution of the CCSN population. However, my results have not indicated any dependence of SN luminosity on the global properties of the host. An evolution may instead occur due to differences in the local environment around a SN; understanding what drives this effect would help to constrain our knowledge of the physics of CCSNe. In addition, a luminosity function which evolves with redshift would have major implications for the simulation of SN surveys going forward. Future work would need to take this into account in order to create realistic SN populations, which in turn would require accurate measurement of the extent of this evolution.

My analysis of the host galaxy properties of CCSNe have also indicated differences in the host galaxy properties of different samples. Hosts in DES and ZTF have consistent stellar mass distributions but show an offset in rest-frame colours that is particularly prevalent in the SN II population. This offset is seen across the full range of stellar masses; for a fixed host mass, a DES host is bluer than its ZTF counterpart. The cause of this difference remains unexplained, even after considering simple explanations such as typical redshift evolution of galaxy properties, selection bias and systematic differences.

Upcoming time domain surveys will provide much larger sample sizes to investigate these effects in more detail. ZTF is set to continue over the coming years and will observe hundreds of CCSNe, however these objects will be at comparable redshifts to the current sample – higher redshift SNe are required to investigate these effects in more detail, in particular for the luminosity. As discussed in Section 1.4, LSST is expected to observe millions of SNe which will include a sample of CCSNe far in excess of what is currently available. This sample, combined with the sample from ZTF, will allow for further comparison of the luminosities of CCSNe at different redshifts to confirm whether the differences presented in this work are caused by redshift evolution or another effect. If the sample is shown to evolve with redshift, the large sizes of this sample will assist with measurement of the extent of this evolution. In addition, analysis of the host galaxies of these samples will reveal whether the

differences in host galaxy properties between DES and ZTF are seen more widely between different CCSN samples and uncover what might be causing this difference.

7.2.2 Study of Unusual Supernovae

The increasing number of SNe discovered has led to the identification of more unusual SNe, such as DES14X2fna, which resemble existing classes in some ways but display uncharacteristic properties in others. My analysis of DES14X2fna indicated that its bright luminosity and fast evolution could not be powered by ^{56}Ni decay - the ^{56}Ni and ejecta masses which would be required for such a luminous SN would be expected to trap most of the γ-rays produced by radioactive decay, which does not agree with the fast decline that is observed. Overall, my results have demonstrated that other physical processes can significantly contribute to the light curves of SNe IIb.

The discovery of even a single unusual object can challenge our assumptions about the physical processes involved in different types of SN explosion. In the era of LSST, more of these types of objects are expected to be discovered. This will help to fill in the gaps between different classes of SNe, for example the gaps between different classes of SESNe and also the gaps between typical CCSNe and extremely luminous SLSNe. The discovery of unusual SNe will allow us to probe whether there is a continuum between these transients or if these are distinct types of explosion with different physical processes.

7.2.3 Improving Photometric Classification of Supernovae

As detailed in Section 1.4, the advent of transient surveys including DES and LSST has led to significant work in the area of photometric classification. However, despite the progress that has been made in applying new machine learning tools for this application, the performance of these models is still limited by the data sets used to train them.

In this thesis, I have introduced a new technique for the generation of synthetic SN light curves to augment data-sets used to train photometric classifiers, based on the use of GANs. GANs have previously been applied for data generation for the generation of variable star light curves (García-Jara et al., 2022), but never for SNe. Compared with García-Jara et al. (2022), this work also has the advantage of being able to generate variable length time series since I have used a GAN based on RNNs. Boone (2021) presents a variational autoencoder which can be used to generate SN light curves, however this method requires a distribution of latent variables as input and would generate light smooth light curve templates rather than observed light curves. The benefit of using GANs is that this approach is completely data-driven,

with no external variables required as input to generate a light curve. In addition, this method is able to generate uncertainties on each observation without the requirement for a simulation with full details of the survey observing conditions as was used for the light curves in the PLAsTiCC data-set derived from SNANA simulations.

The methods and models I have described in this thesis can be of great benefit to future study of CCSNe. Data-set augmentation using GANs has been shown to improve classifier performance both within astronomy (García-Jara et al., 2022) and in other fields (e.g., Motamed et al., 2021). This work has shown that GANs can be used to generate realistic synthetic SNe. Future work can utilise this method for augmentation, improving our ability to accurately classify CCSNe based purely on photometry.

7.3 Closing Remarks

The diversity of extreme explosion physics showcased by CCSNe, as well as the strong impact they have on the evolution of their surroundings, makes them an exciting target for astrophysical study. Many unknowns remain about the processes involved in these events and a combination of large population studies and detailed single object analysis will allow us to refine our understanding of CCSN physics. Upcoming surveys, most notably LSST, will provide a fantastic data set for these kinds of analyses and the future of CCSN study is incredibly promising.

Beyond the study of CCSN physics, I have looked at methods to improve photometric classification of these objects. The ability to reliably classify objects based only on photometry is essential to leverage the vast data sets that surveys like LSST will provide. The techniques I have developed have the potential to significantly improve classification of both CCSNe and other astrophysical events.

Appendix A

Synthetic Light Curve Plots

In this appendix I present plots showing the physical properties of light curves generated using GANs as presented in Chapter 6.

A.1 SNe Ic (Small Training Set)

A.1, A.2, A.3 and A.4 show the distributions for peak apparent magnitudes, Δm_{15} and rise times for each of *griz* bands as well as peak colours for the SNe Ic GAN model trained on a small data set of 32 SNe. Figure A.5 shows the mean light curves and their associated standard deviation for each of the real and generated data sets, and Figure A.6 shows the light curves expressed as a shift from peak magnitude. Figure A.7 shows the $g - r$, $r - i$ and $i - z$ colour curves for the real and generated samples, and Figure A.8 shows the apparent magnitude uncertainty plotted as a function of apparent magnitude as in Figure A.8.

A.2 SNe II

Figures A.9 to A.16 show the same plots as figures A.1 to A.8 but for SNe II.

A.3 SNe Ib

Figures A.17 to A.24 show the same plots as figures A.1 to A.8 but for SNe Ib.

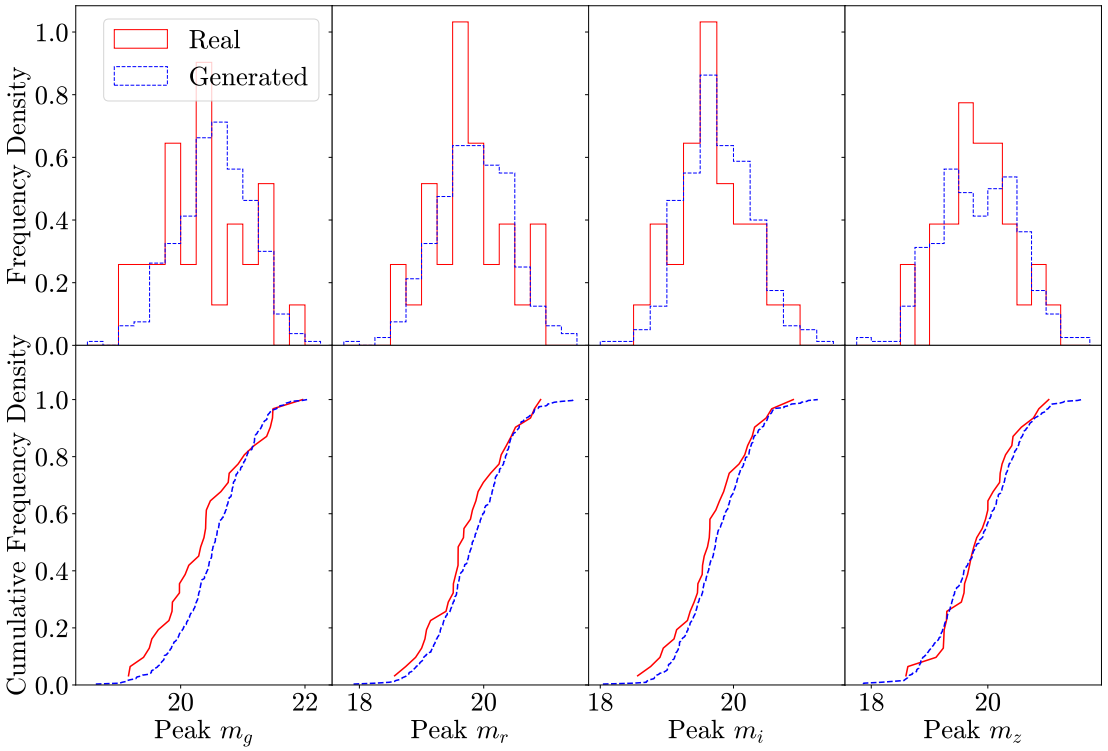

FIGURE A.1: As per Figure 6.2 but for the smaller data set trained on 32 SNe Ic.

A.4 SNe IIn

Figures A.25 to A.32 show the same plots as figures A.1 to A.8 but for SNe Ib.

A.5 SNe IIb

Figures A.33 to A.40 show the same plots as figures A.1 to A.8 but for SNe IIb.

A.6 SNe Ic-BL

Figures A.41 to A.48 show the same plots as figures A.1 to A.8 but for SNe Ib.

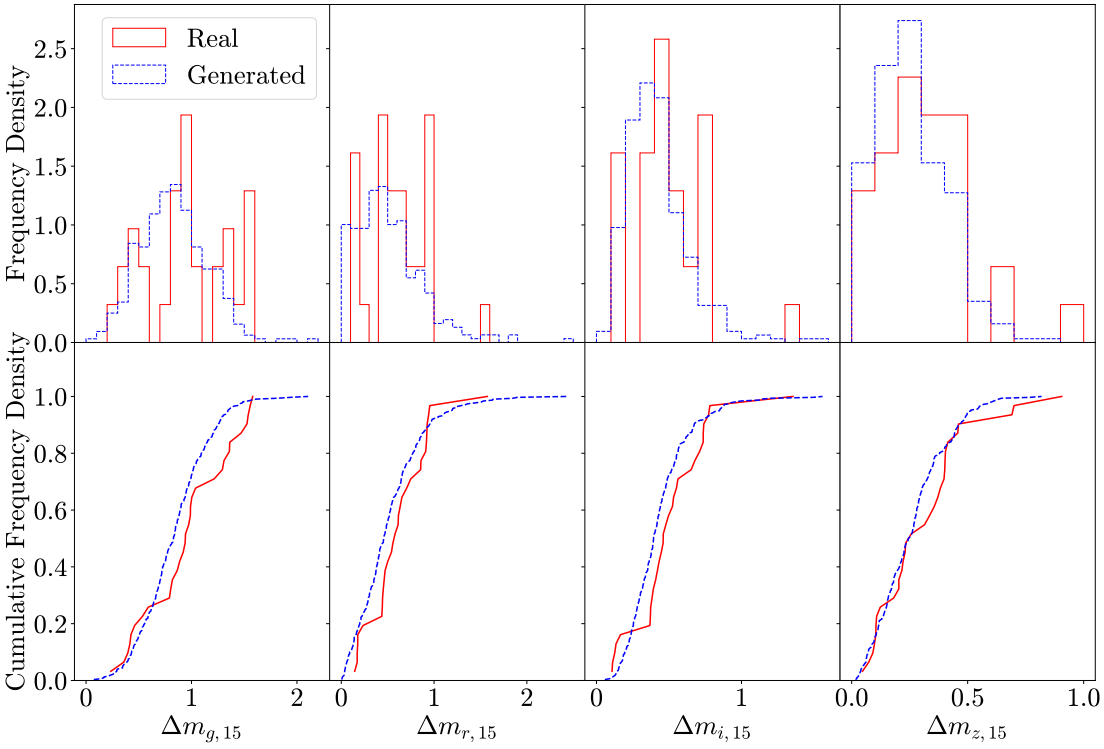

FIGURE A.2: As per Figure 6.3 but for the smaller data set trained on 32 SNe Ic.

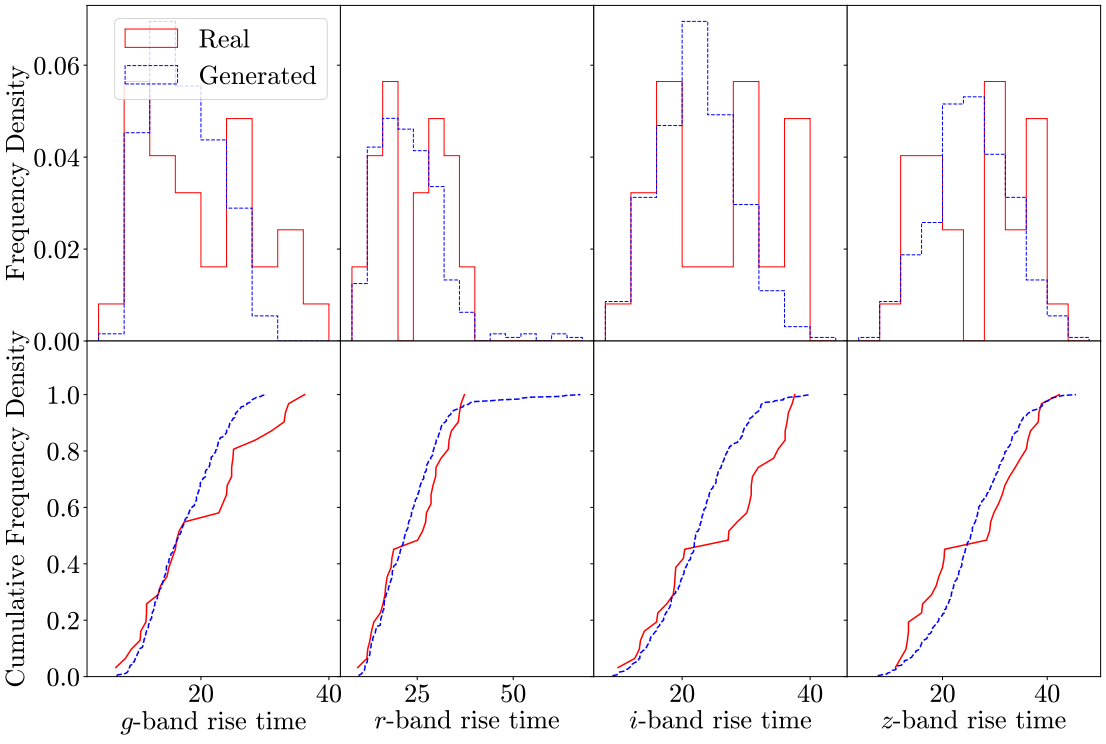

FIGURE A.3: As per Figure 6.4 but for the smaller data set trained on 32 SNe Ic.

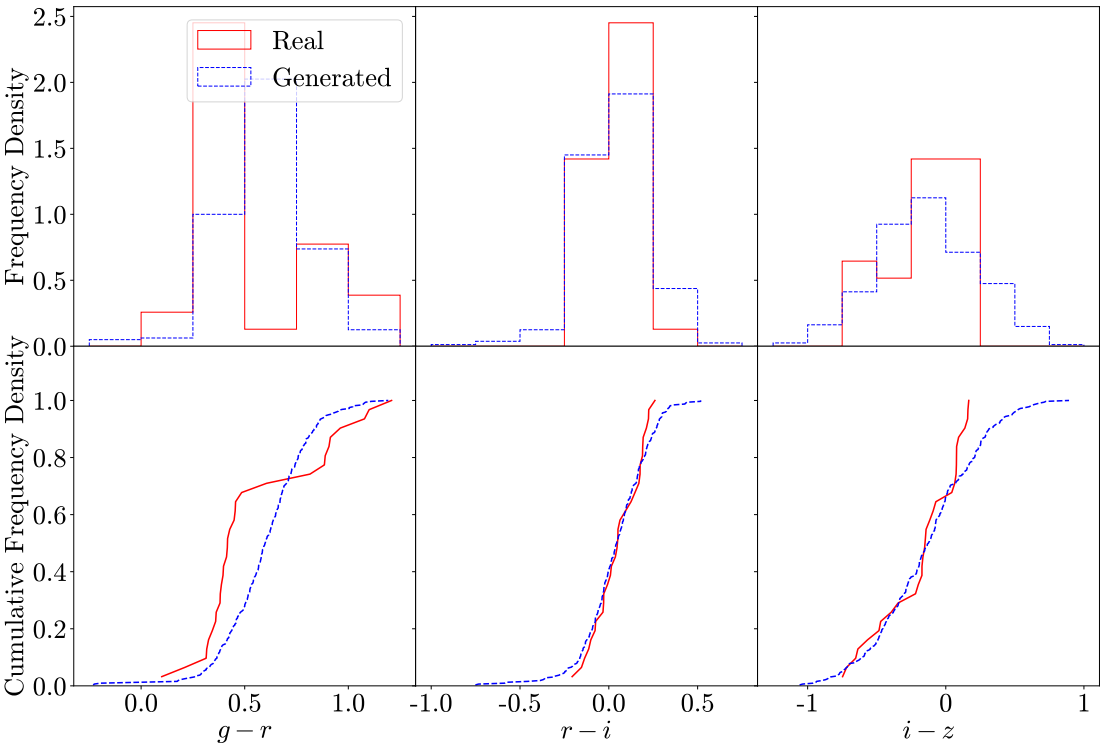

FIGURE A.4: As per Figure 6.5 but for the smaller data set trained on 32 SNe Ic.

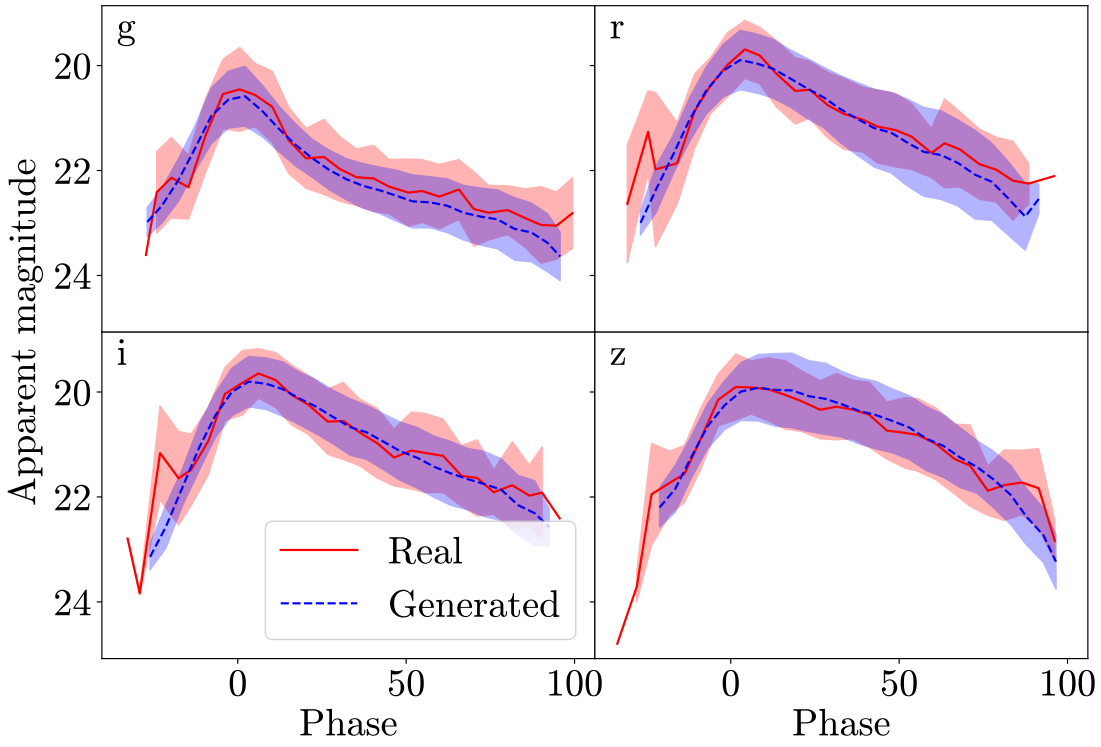

FIGURE A.5: As per Figure 6.6 but for the smaller data set trained on 32 SNe Ic.

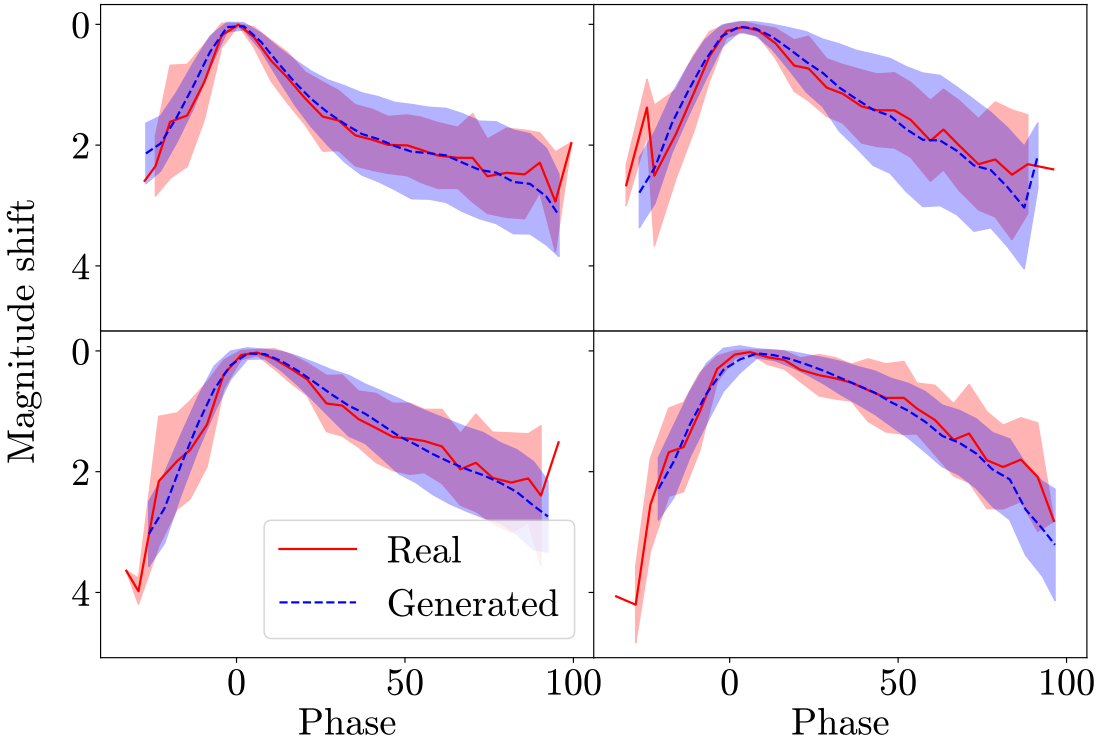

FIGURE A.6: As per Figure 6.7 but for the smaller data set trained on 32 SNe Ic.

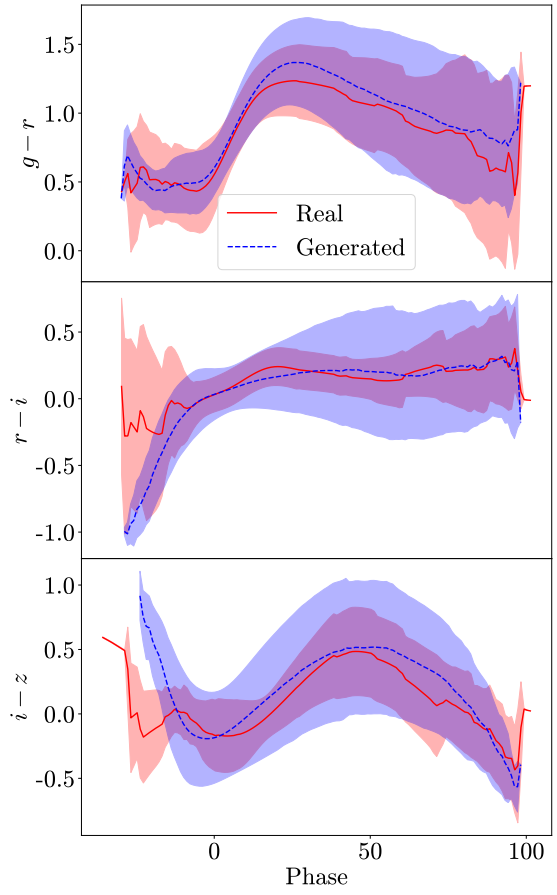

FIGURE A.7: As per Figure 6.8 but for the smaller data set trained on 32 SNe Ic.

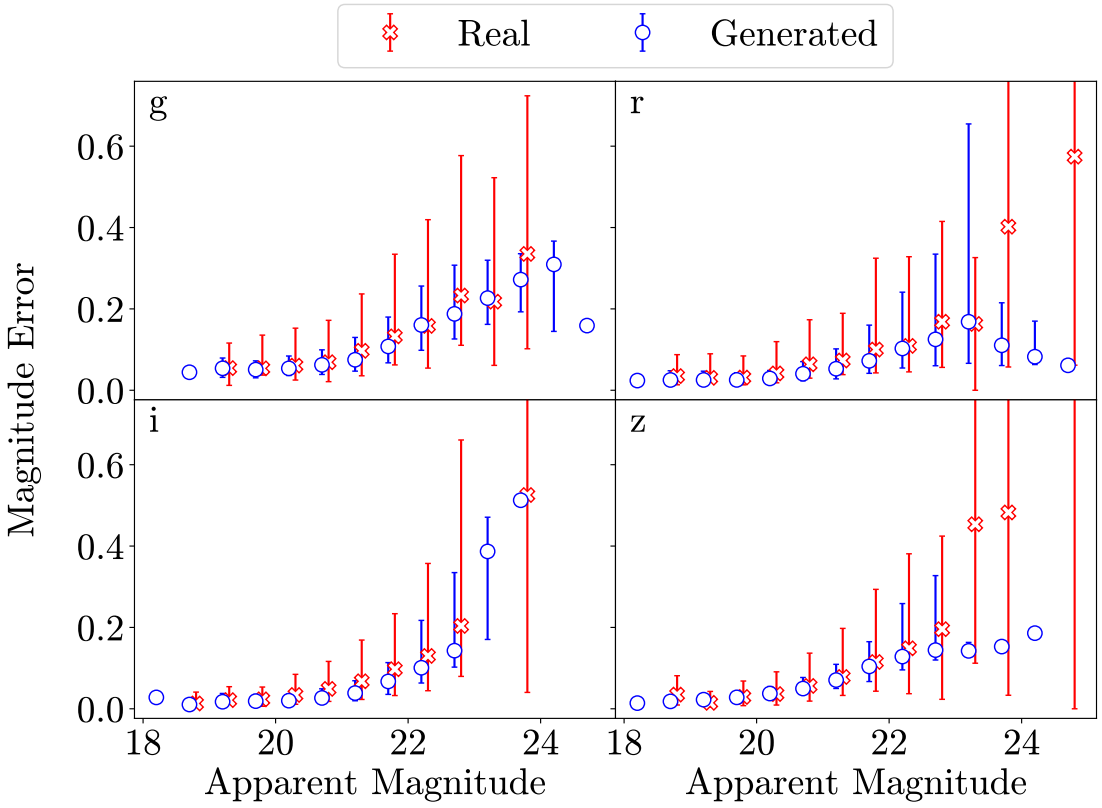

FIGURE A.8: As per Figure 6.9 but for the smaller data set trained on 32 SNe Ic.

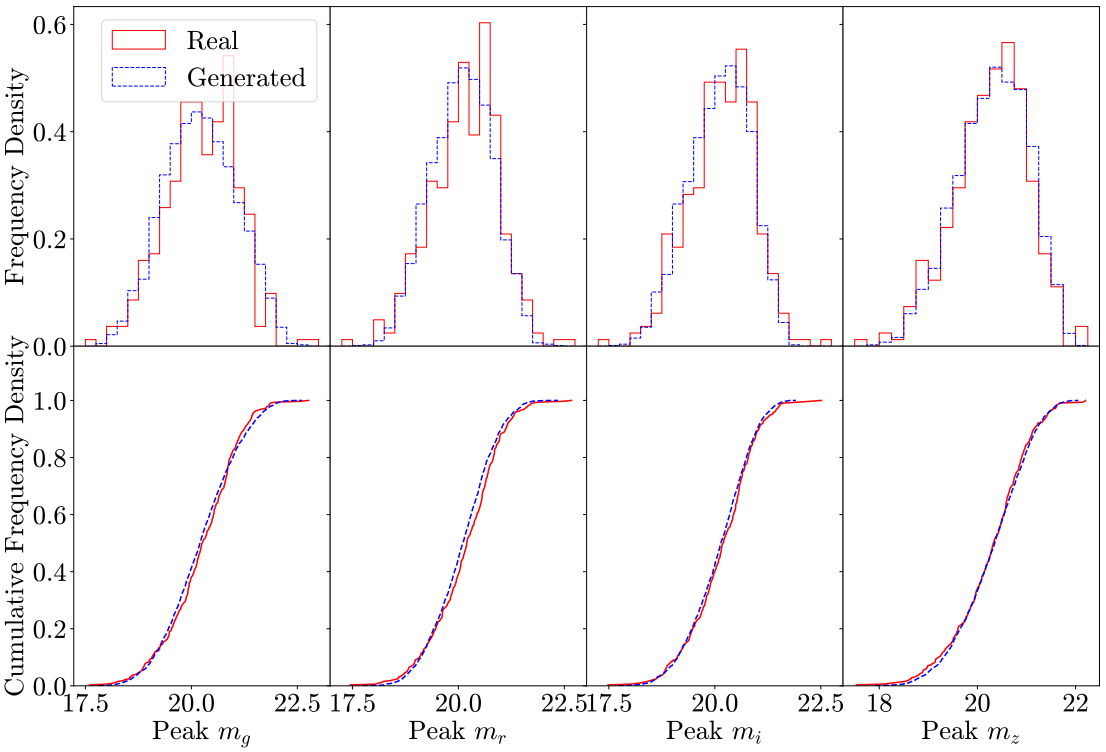

FIGURE A.9: As per Figure 6.2 but for SNe II.

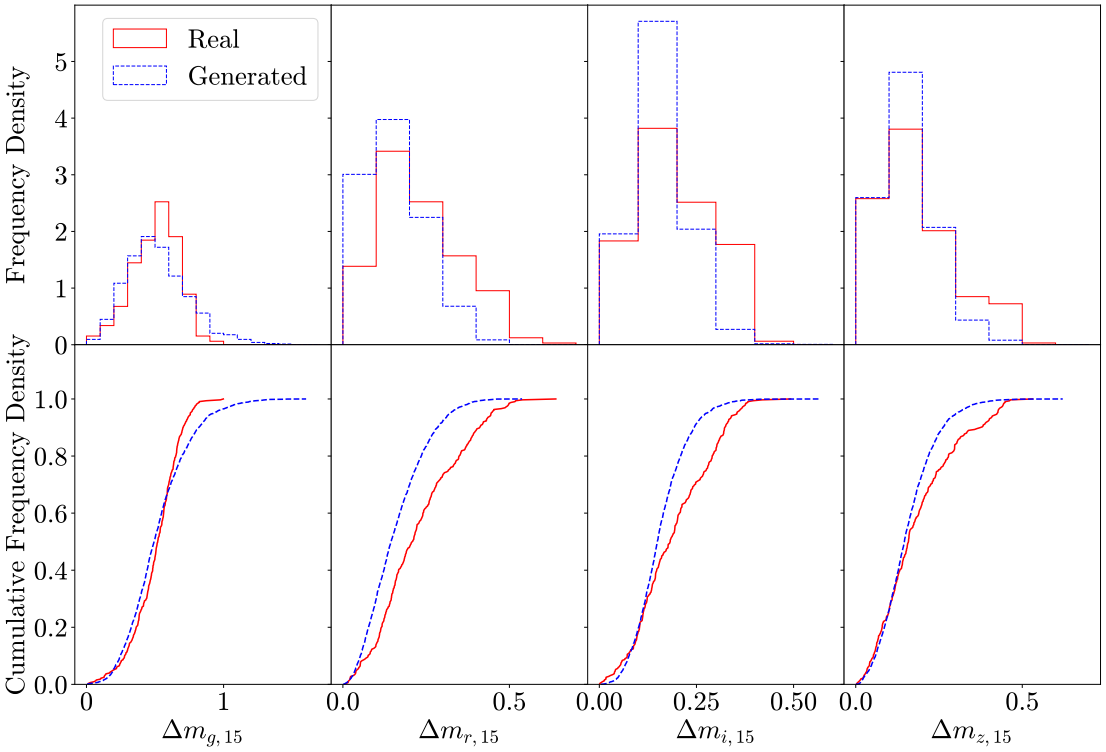

FIGURE A.10: As per Figure 6.3 but for SNe II.

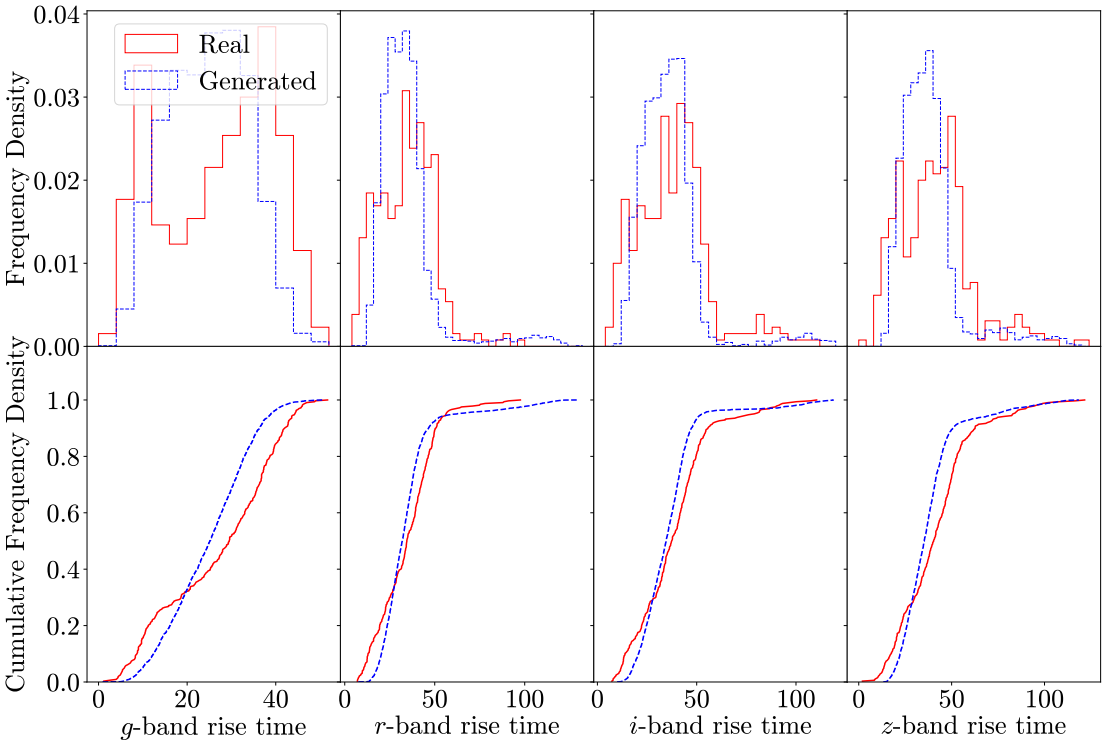

FIGURE A.11: As per Figure 6.4 but for SNe II.

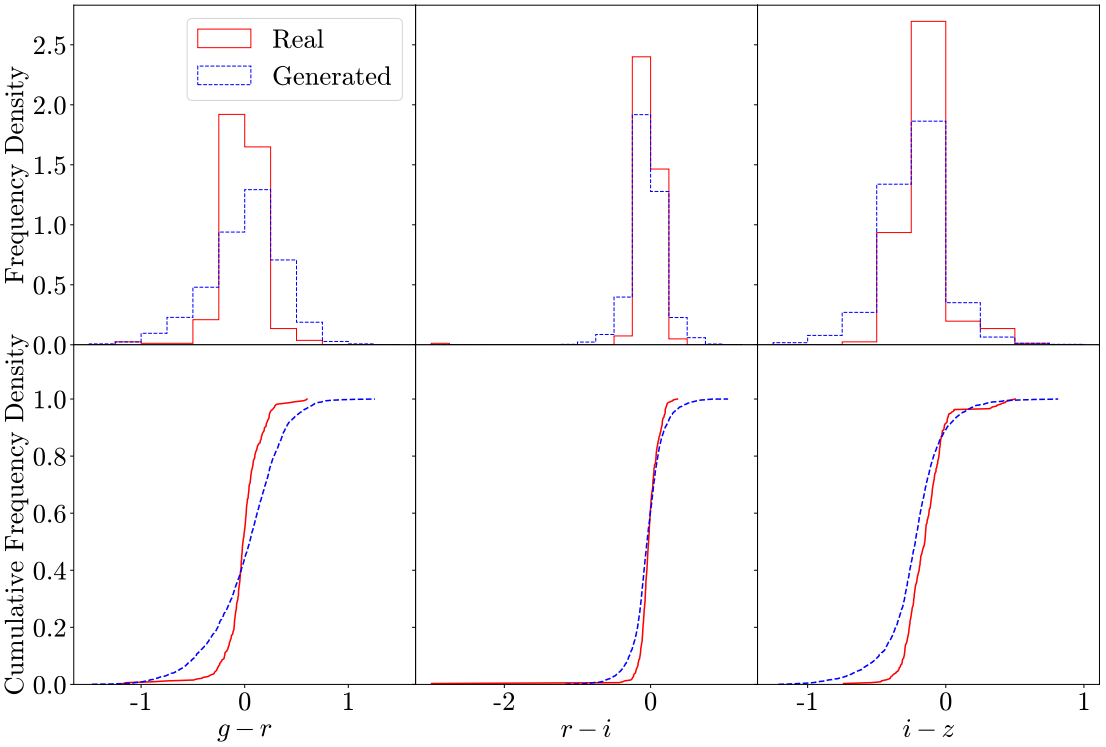

FIGURE A.12: As per Figure 6.5 but for SNe II.

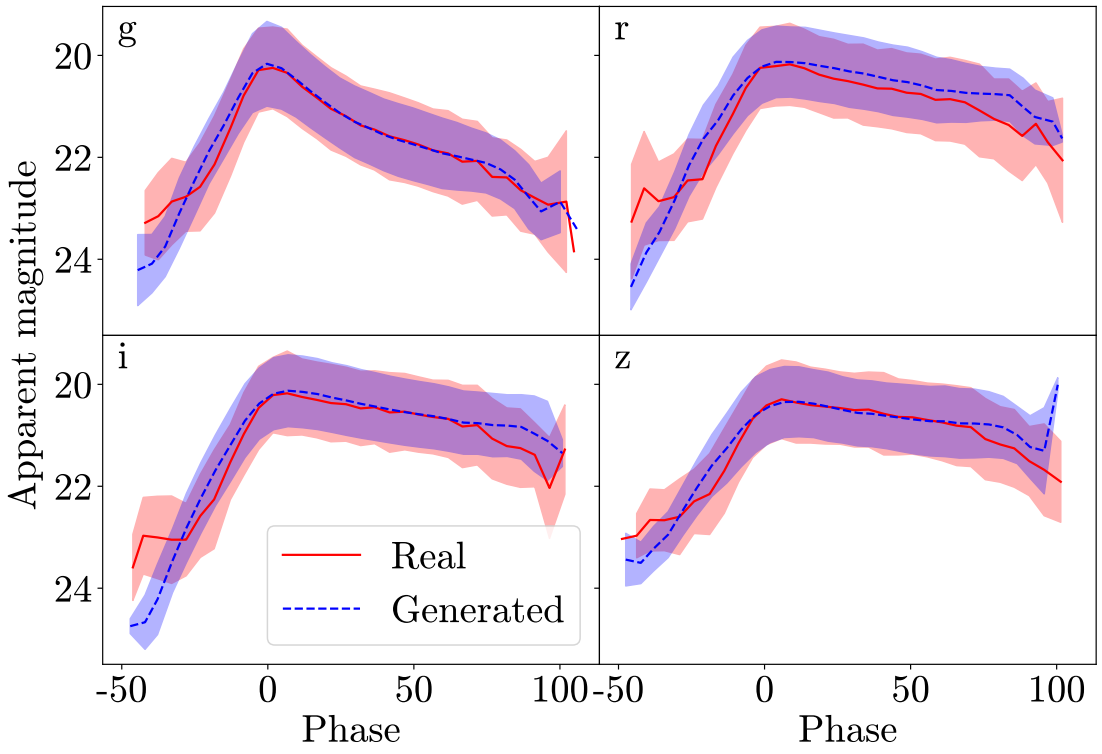

FIGURE A.13: As per Figure 6.6 but for SNe II.

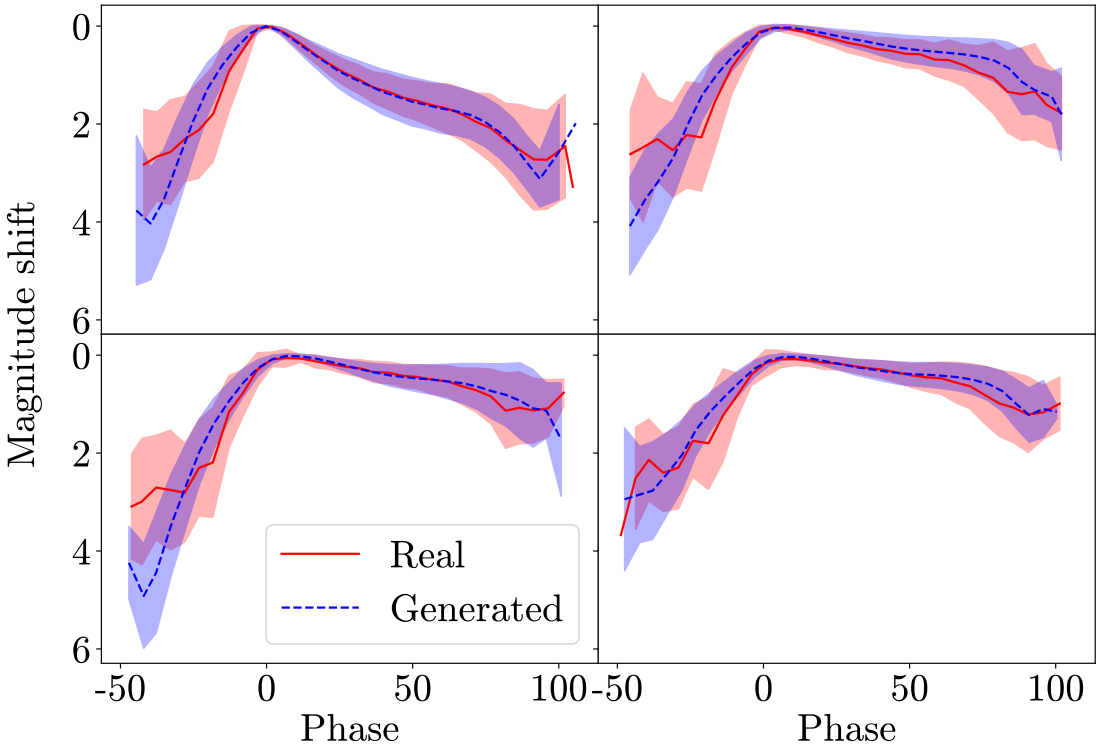

FIGURE A.14: As per Figure 6.7 but for SNe II.

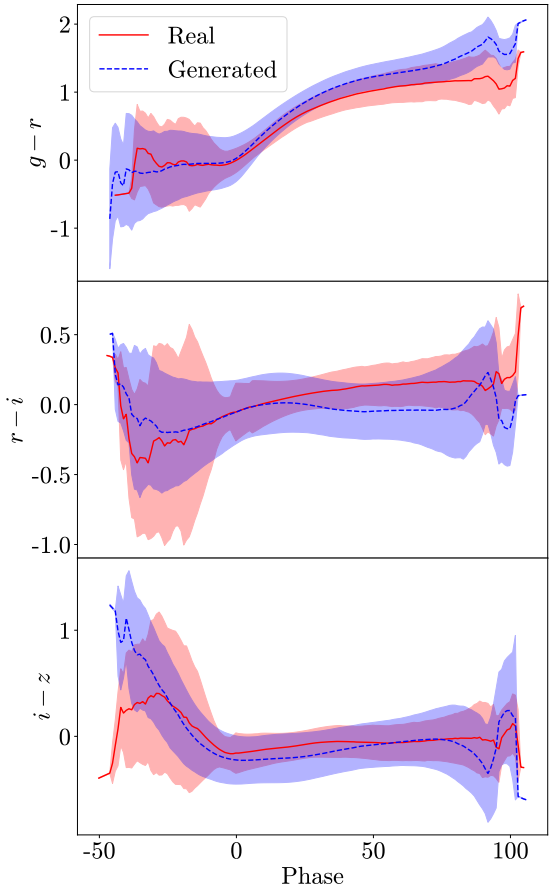

FIGURE A.15: As per Figure 6.8 but for SNe II.

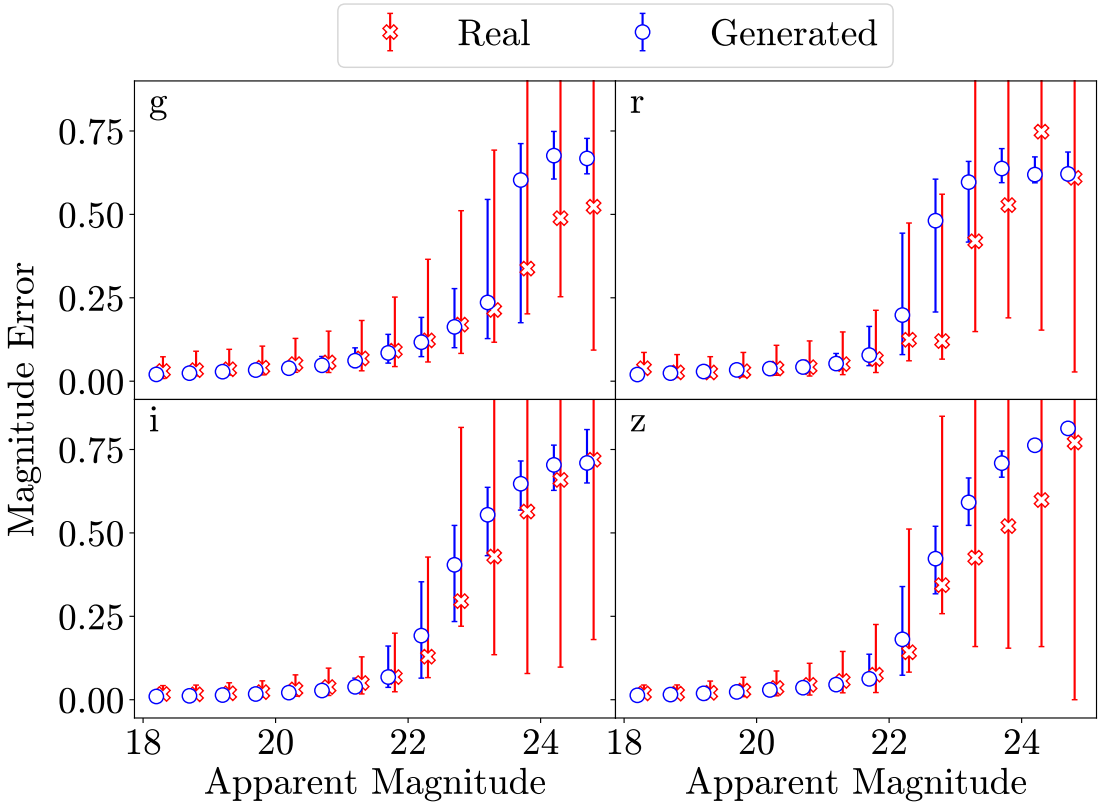

FIGURE A.16: As per Figure 6.9 but for SNe II.

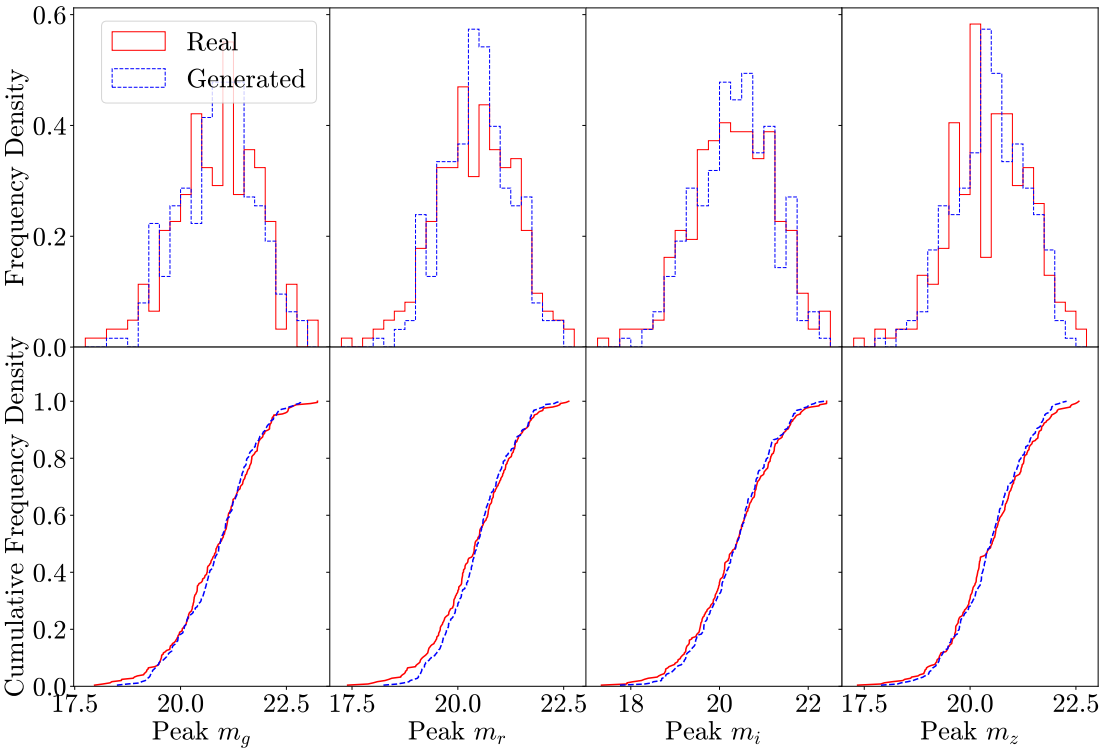

FIGURE A.17: As per Figure 6.2 but for SNe Ib.

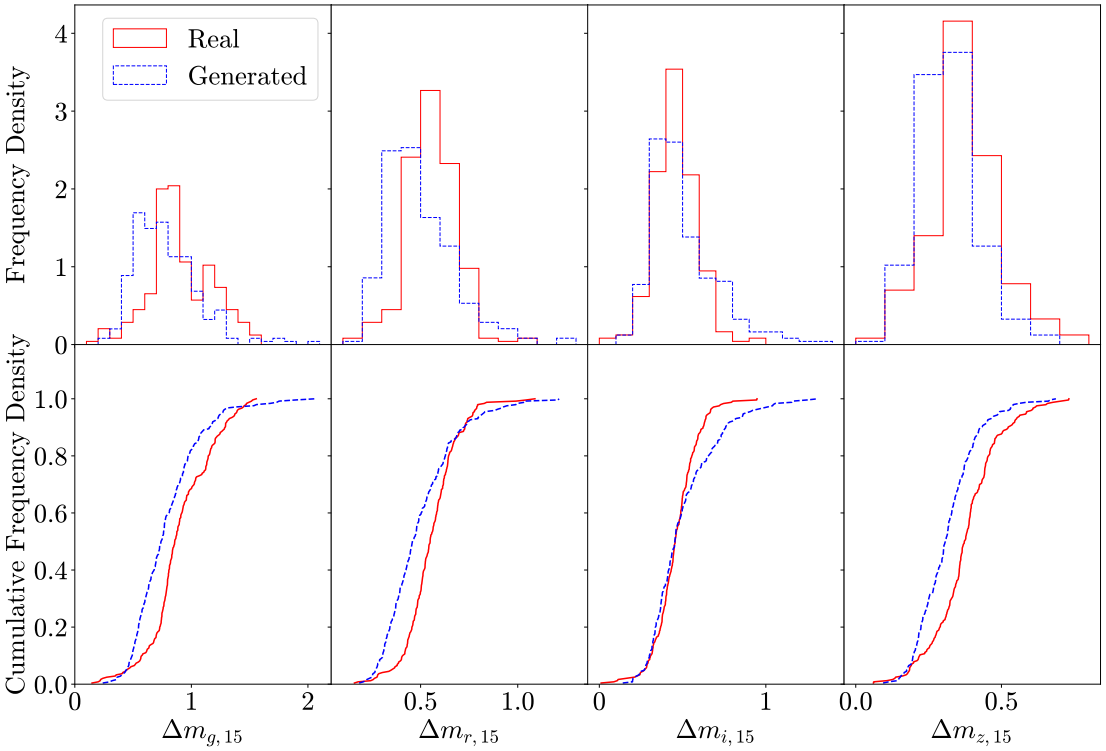

FIGURE A.18: As per Figure 6.3 but for SNe Ib.

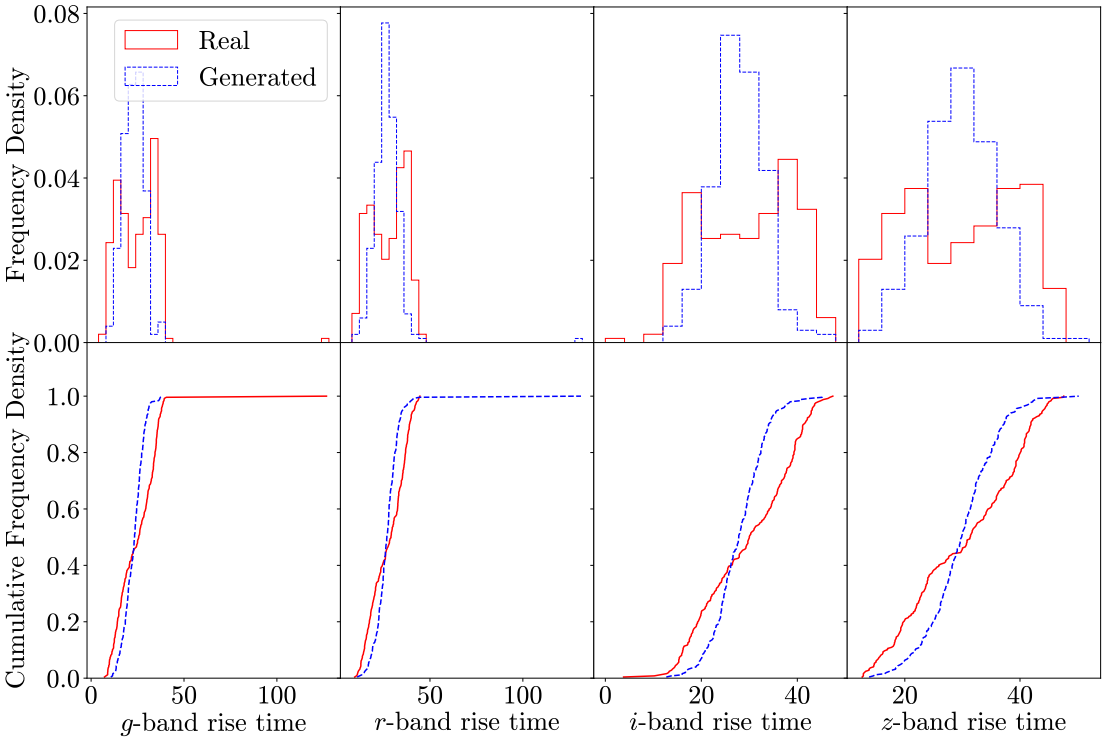

FIGURE A.19: As per Figure 6.4 but for SNe Ib.

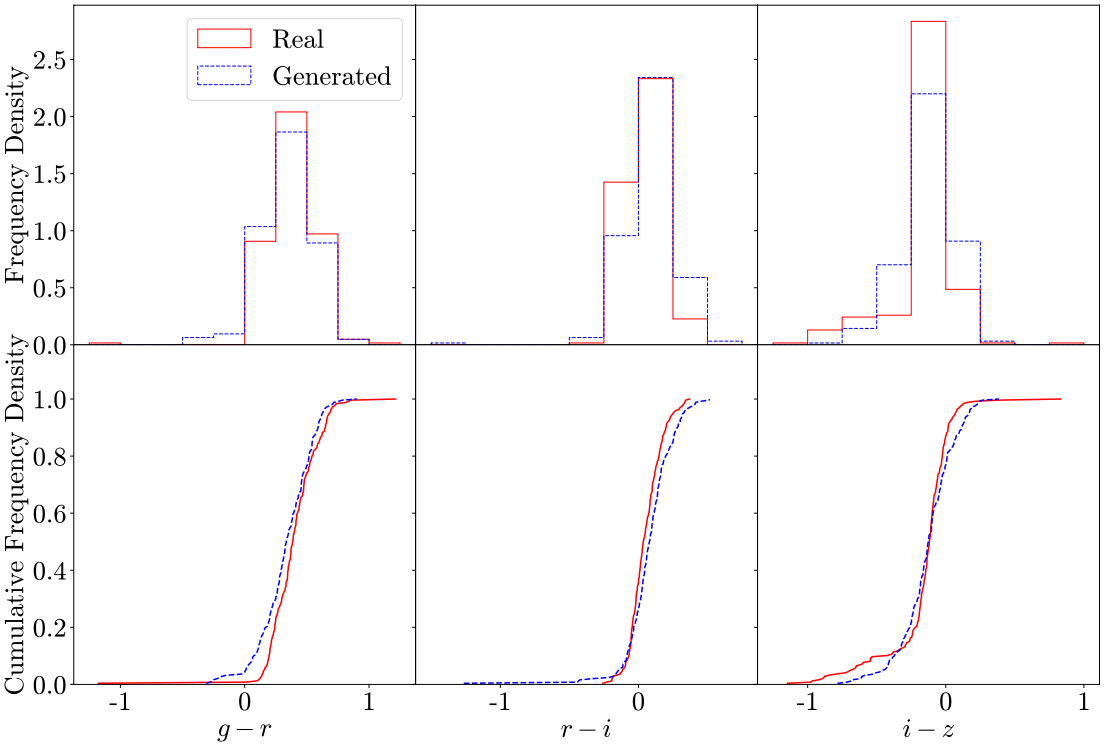

FIGURE A.20: As per Figure 6.5 but for SNe Ib.

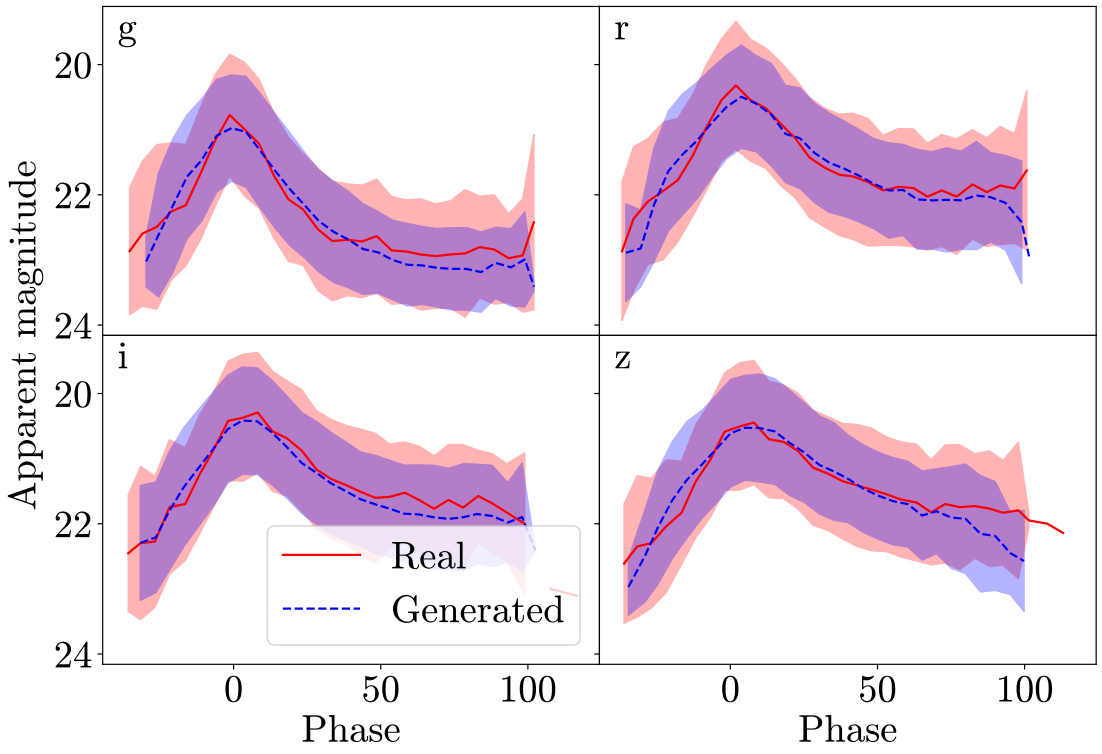

FIGURE A.21: As per Figure 6.6 but for SNe Ib.

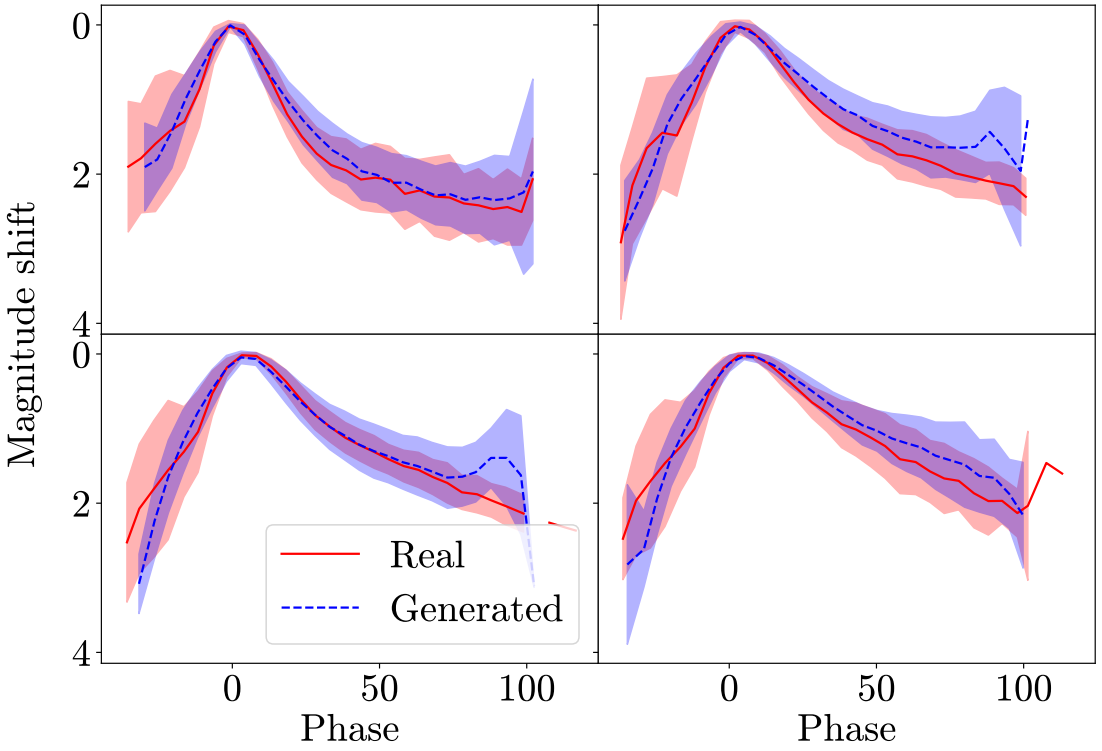

FIGURE A.22: As per Figure 6.7 but for SNe Ib.

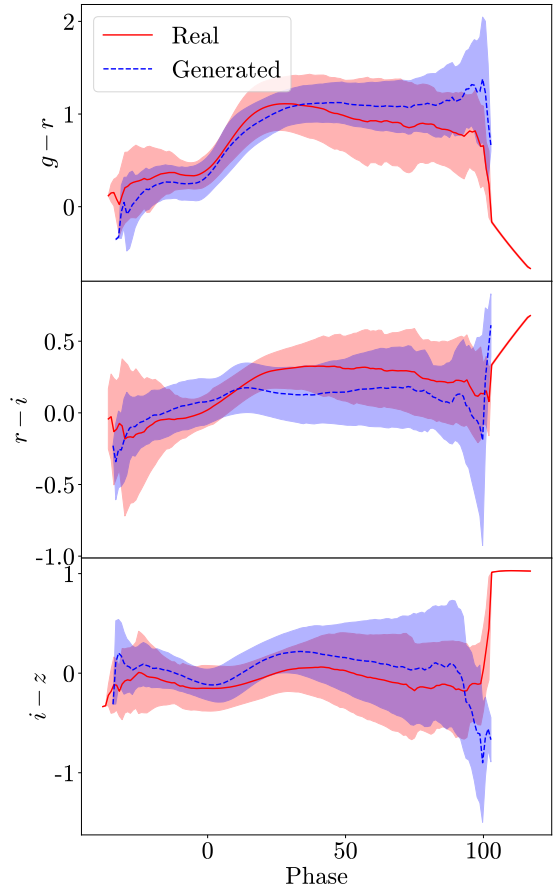

FIGURE A.23: As per Figure 6.8 but for SNe Ib.

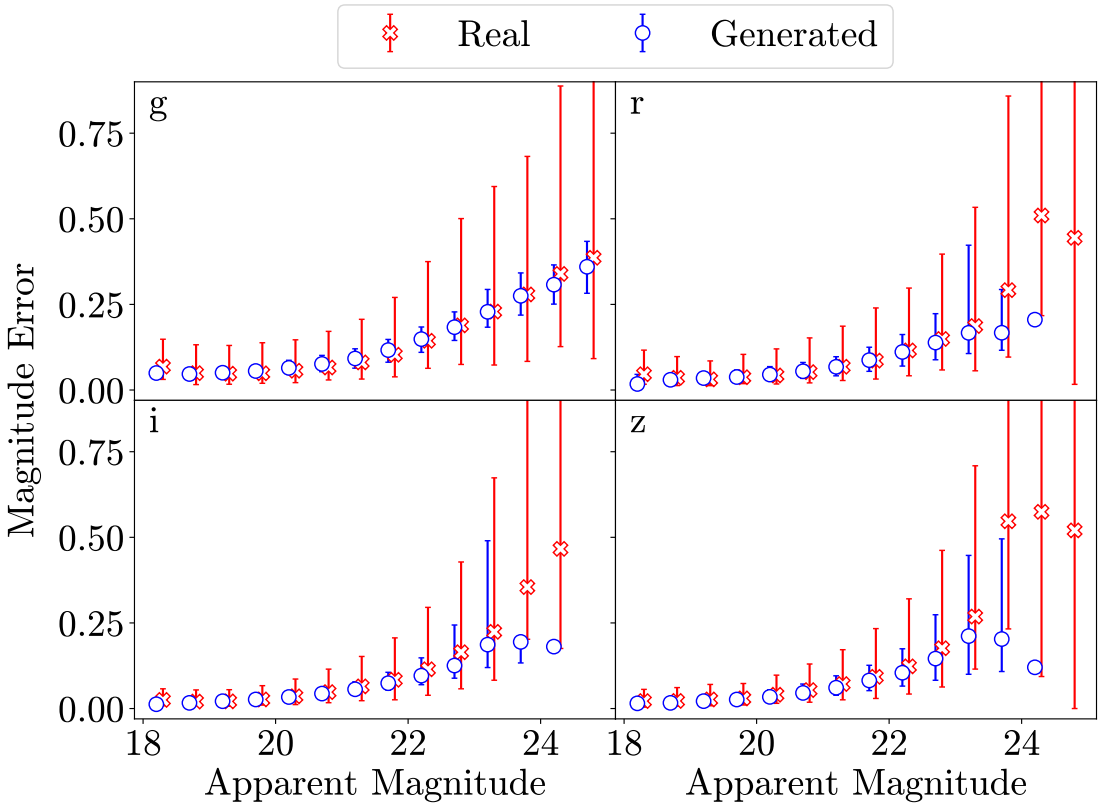

FIGURE A.24: As per Figure 6.9 but for SNe Ib.

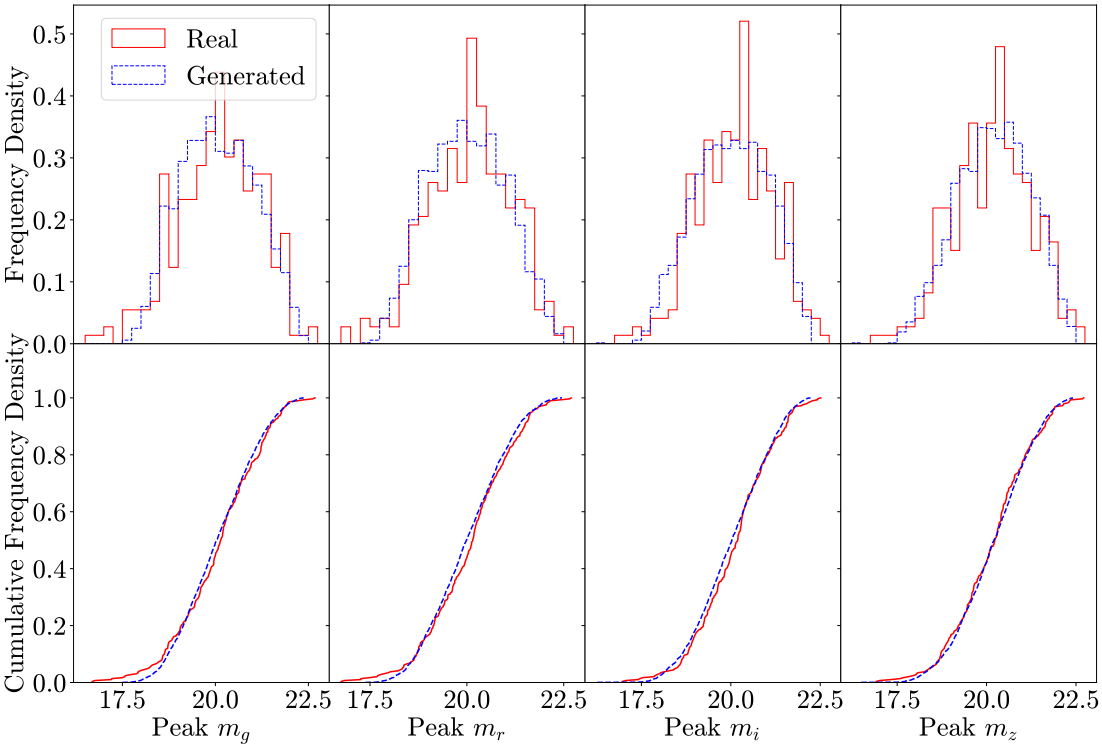

FIGURE A.25: As per Figure 6.2 but for SNe IIn.

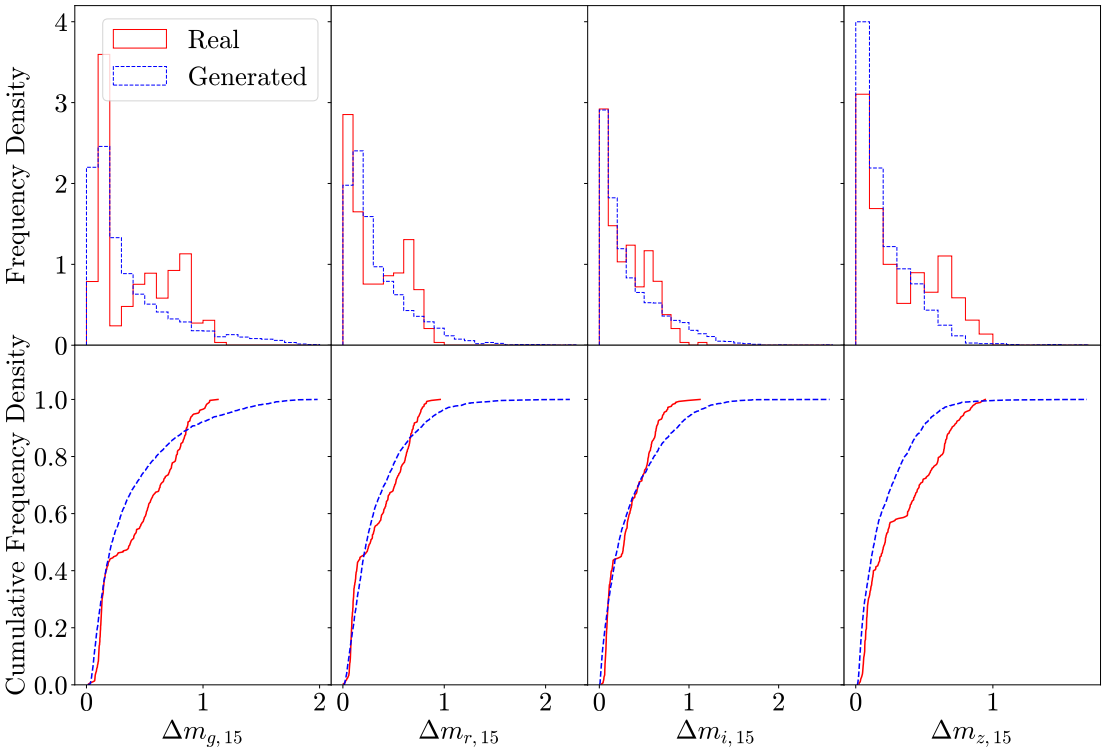

FIGURE A.26: As per Figure 6.3 but for SNe IIn.

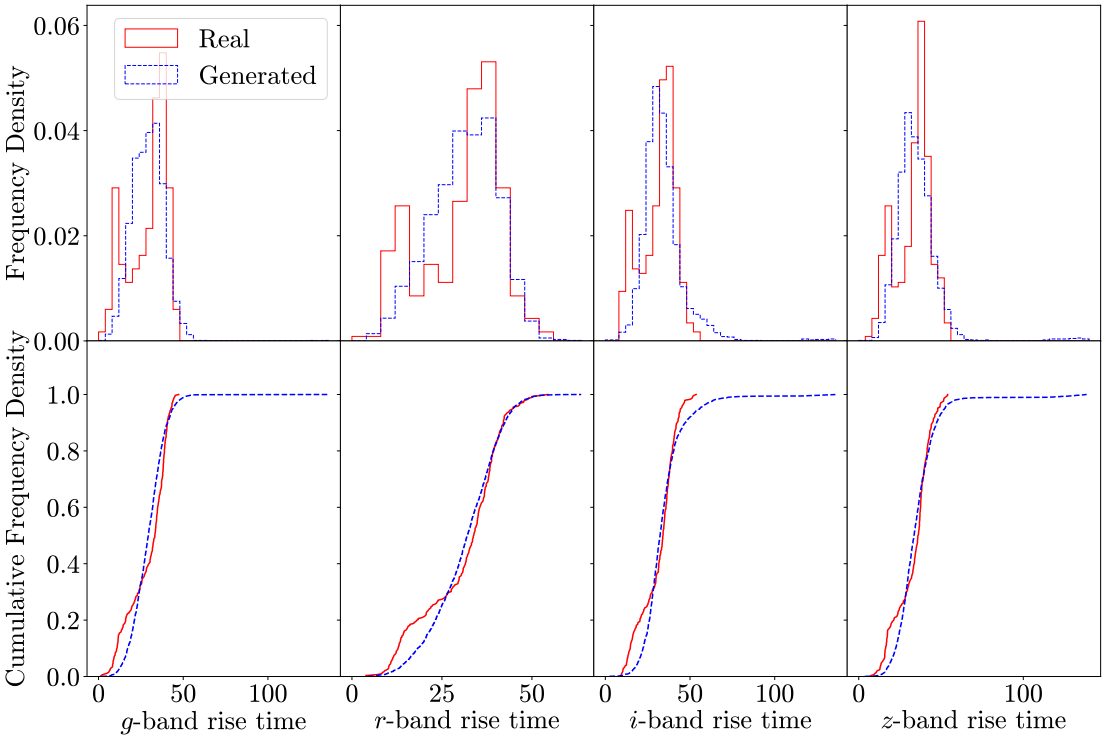

FIGURE A.27: As per Figure 6.4 but for SNe IIn.

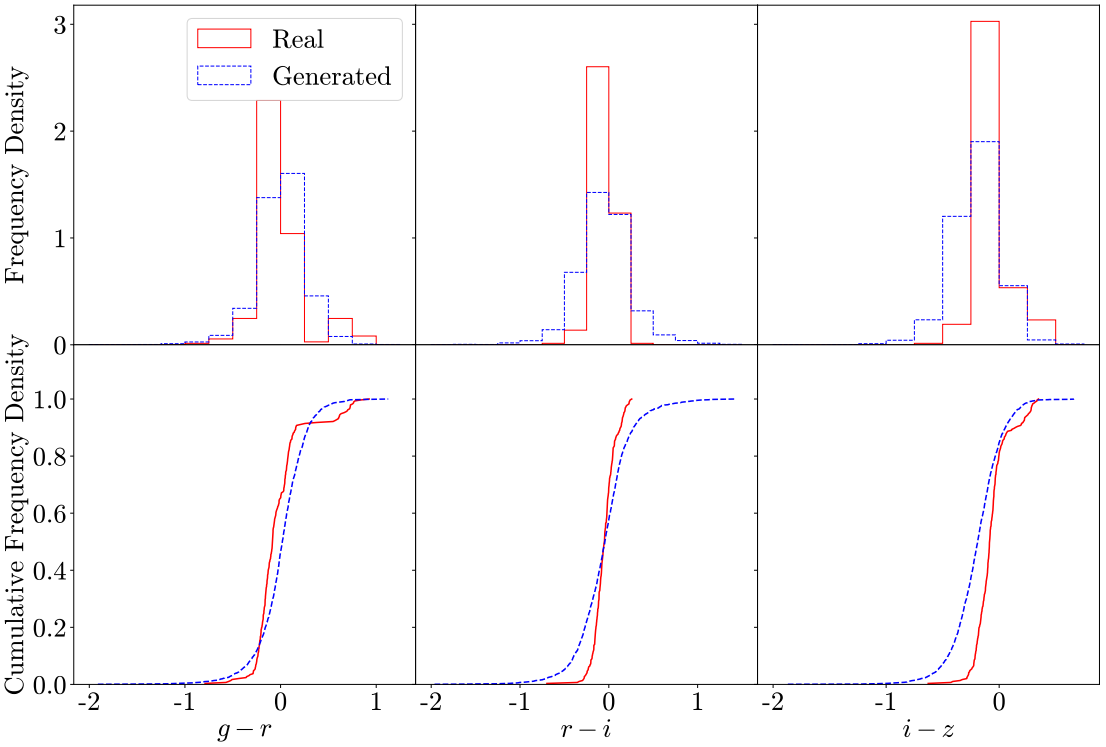

FIGURE A.28: As per Figure 6.5 but for SNe IIn.

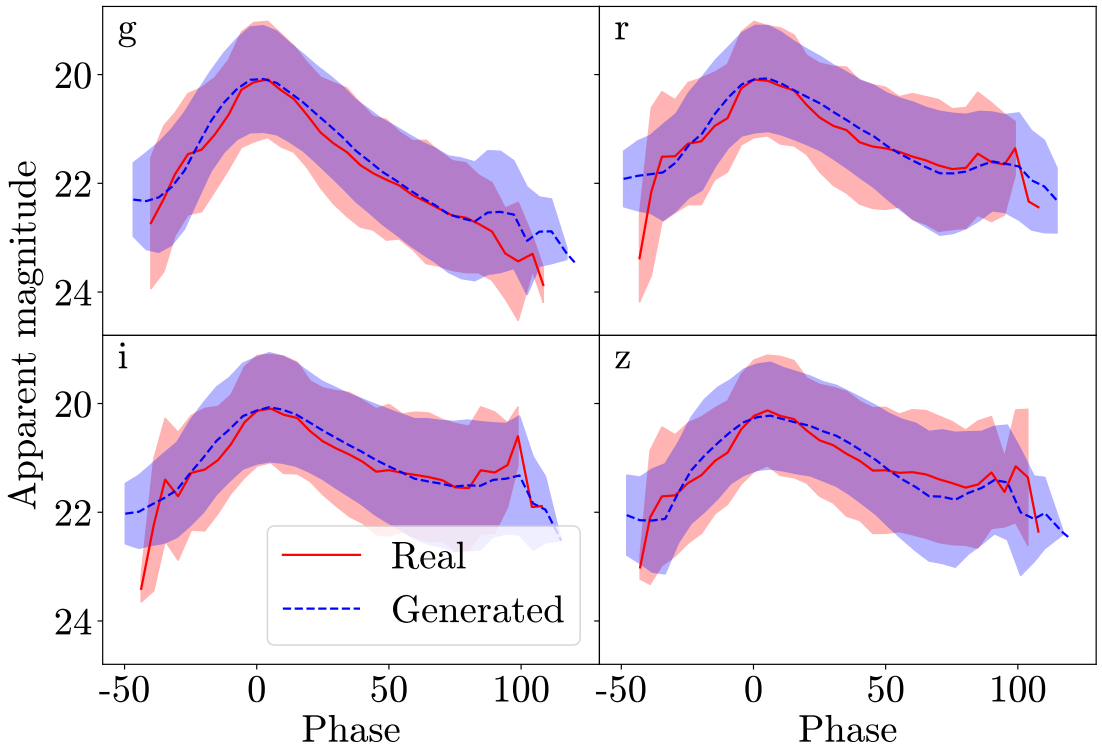

FIGURE A.29: As per Figure 6.6 but for SNe IIn.

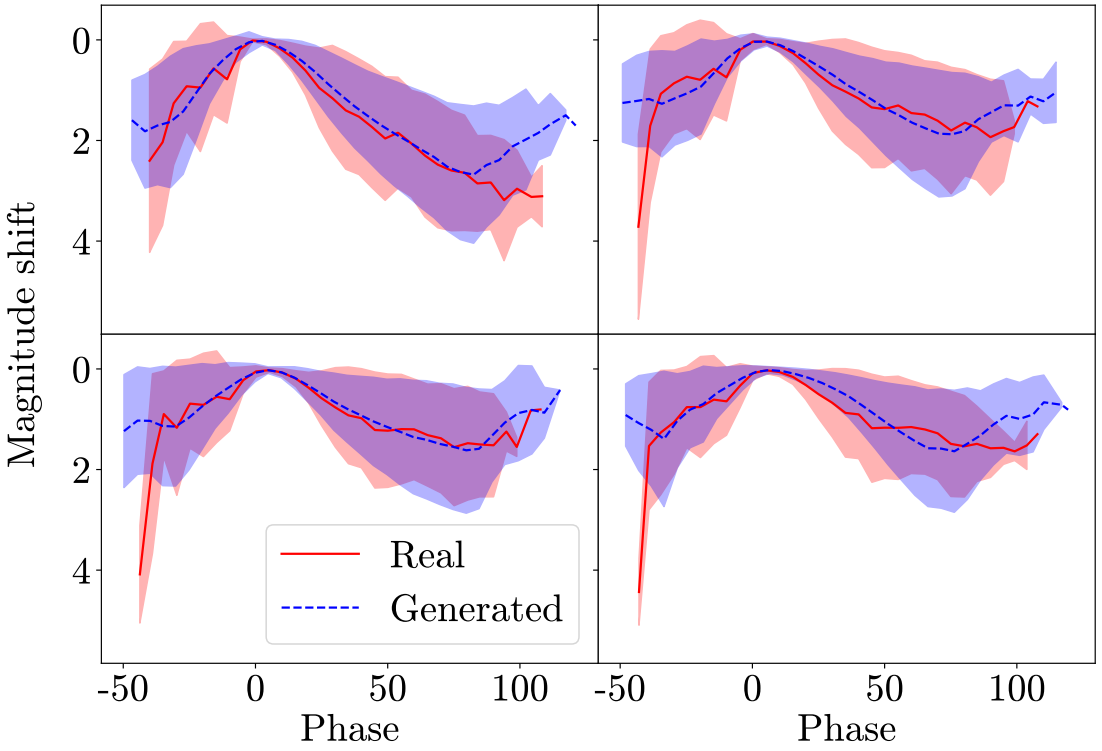

FIGURE A.30: As per Figure 6.7 but for SNe IIn.

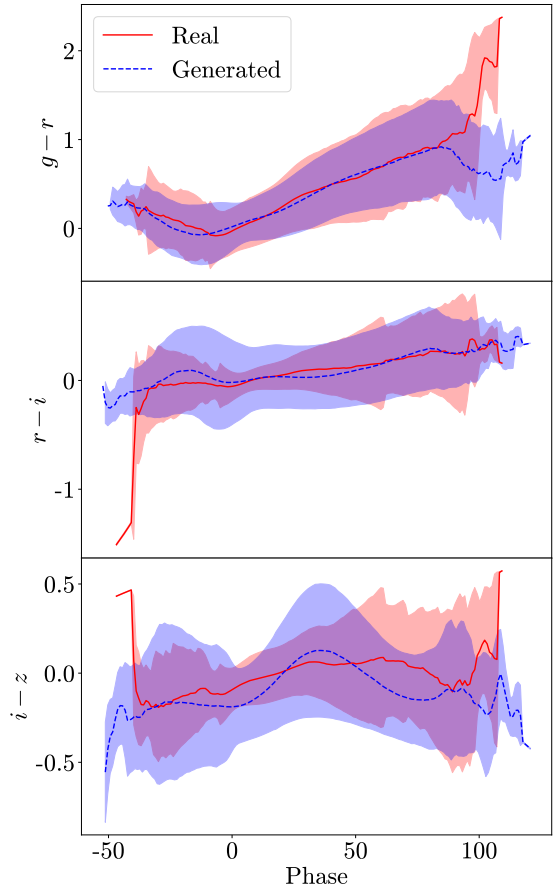

FIGURE A.31: As per Figure 6.8 but for SNe IIn.

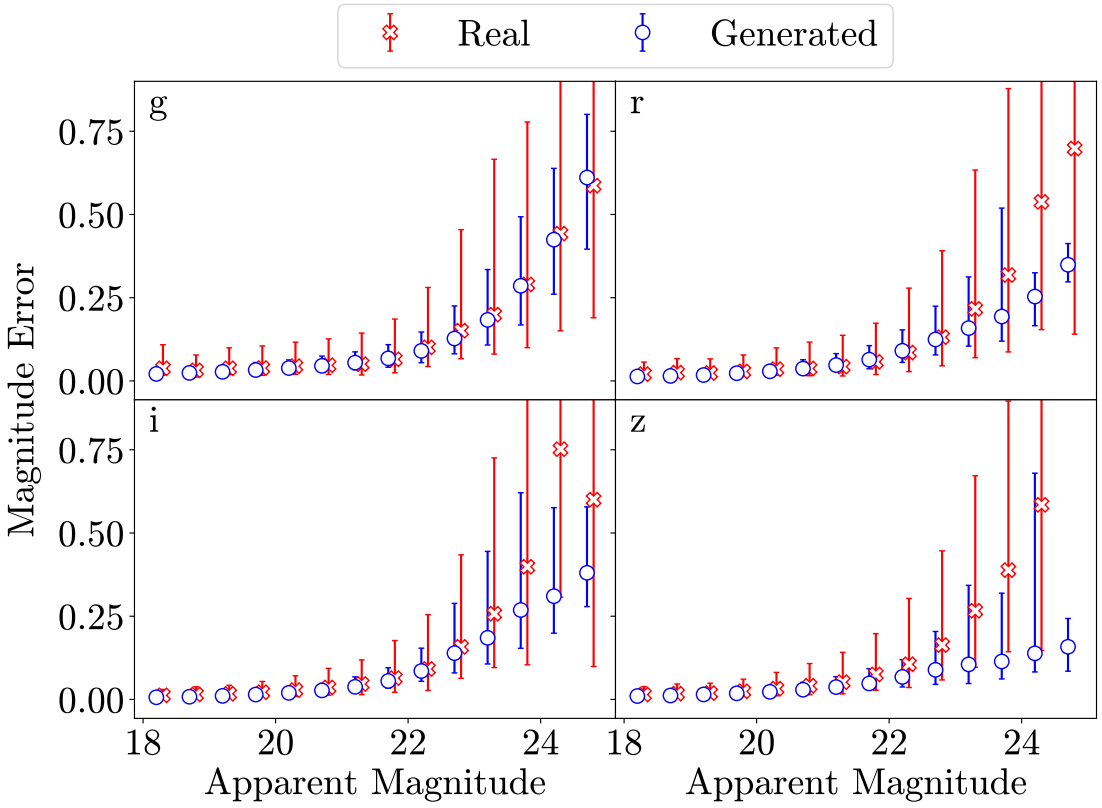

FIGURE A.32: As per Figure 6.9 but for SNe IIn.

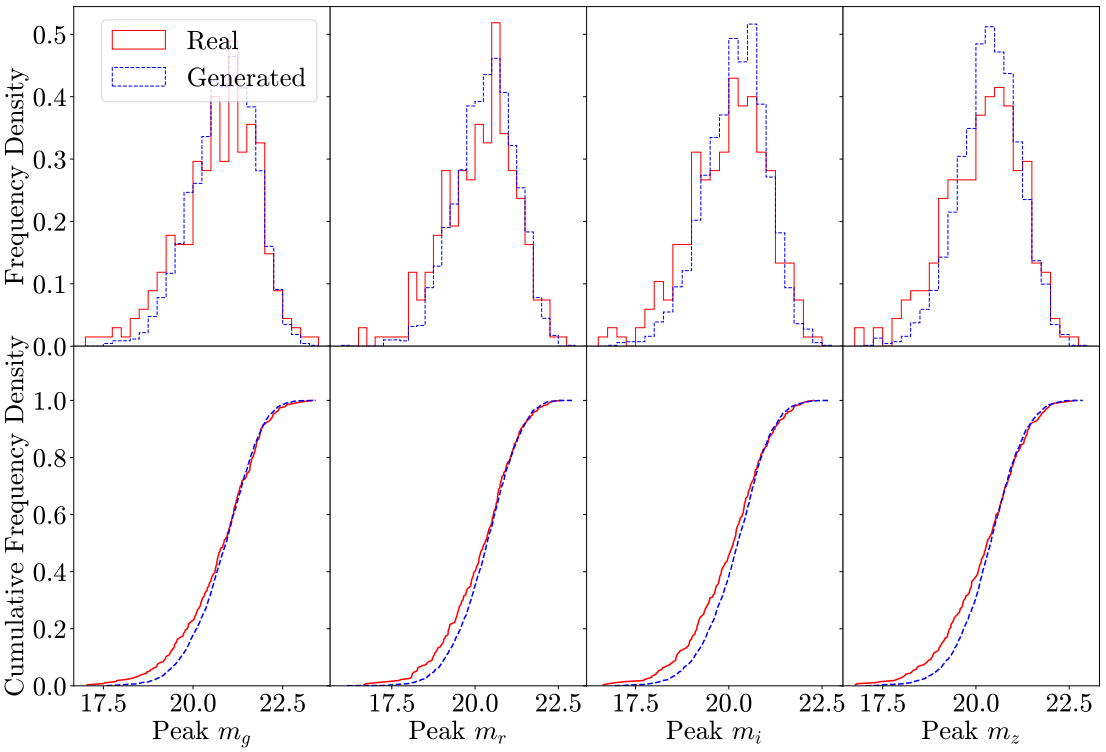

FIGURE A.33: As per Figure 6.2 but for SNe IIb.

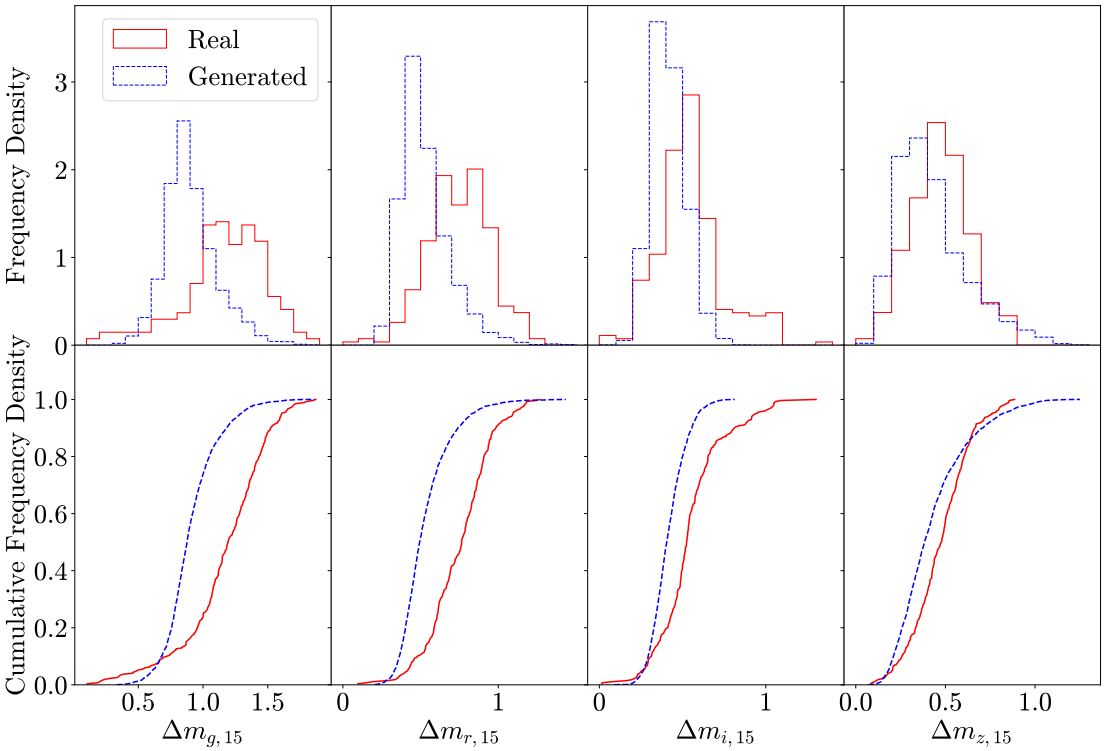

FIGURE A.34: As per Figure 6.3 but for SNe IIb.

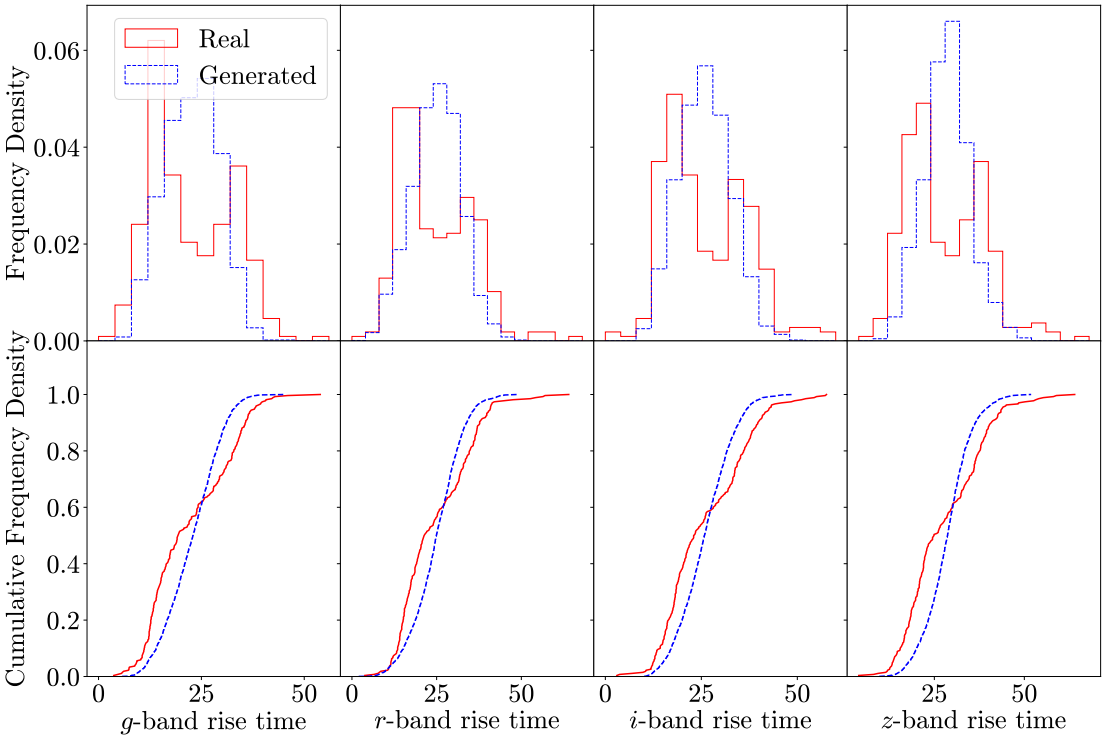

FIGURE A.35: As per Figure 6.4 but for SNe IIb.

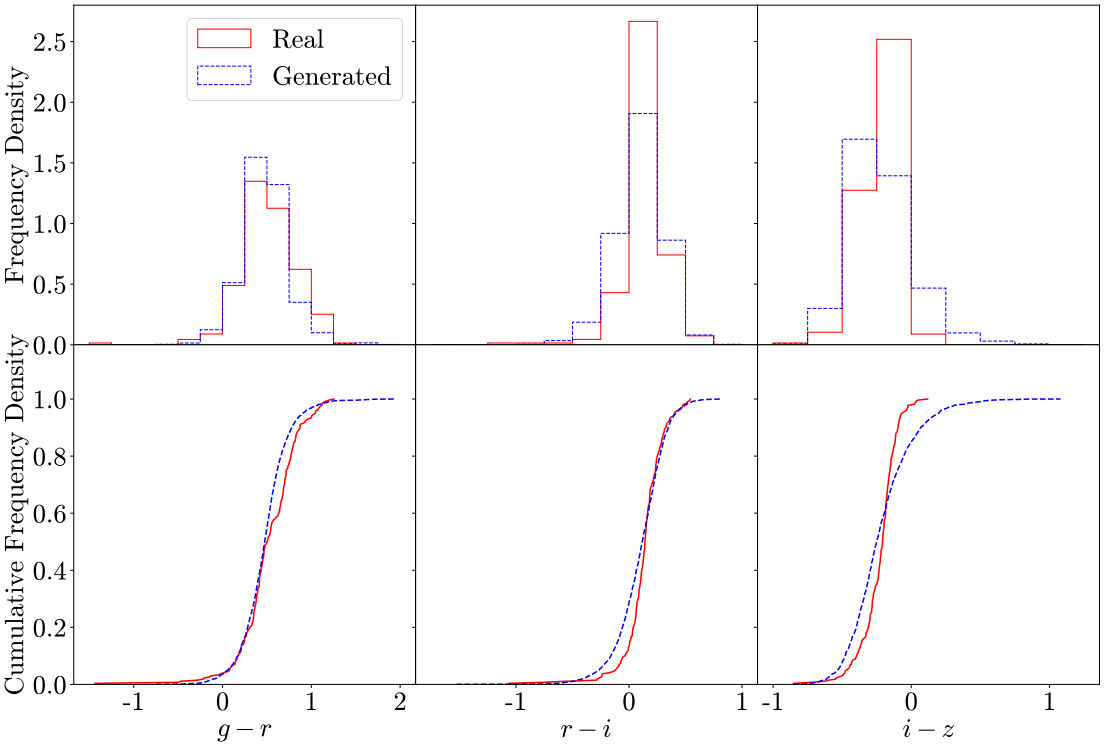

FIGURE A.36: As per Figure 6.5 but for SNe IIb.

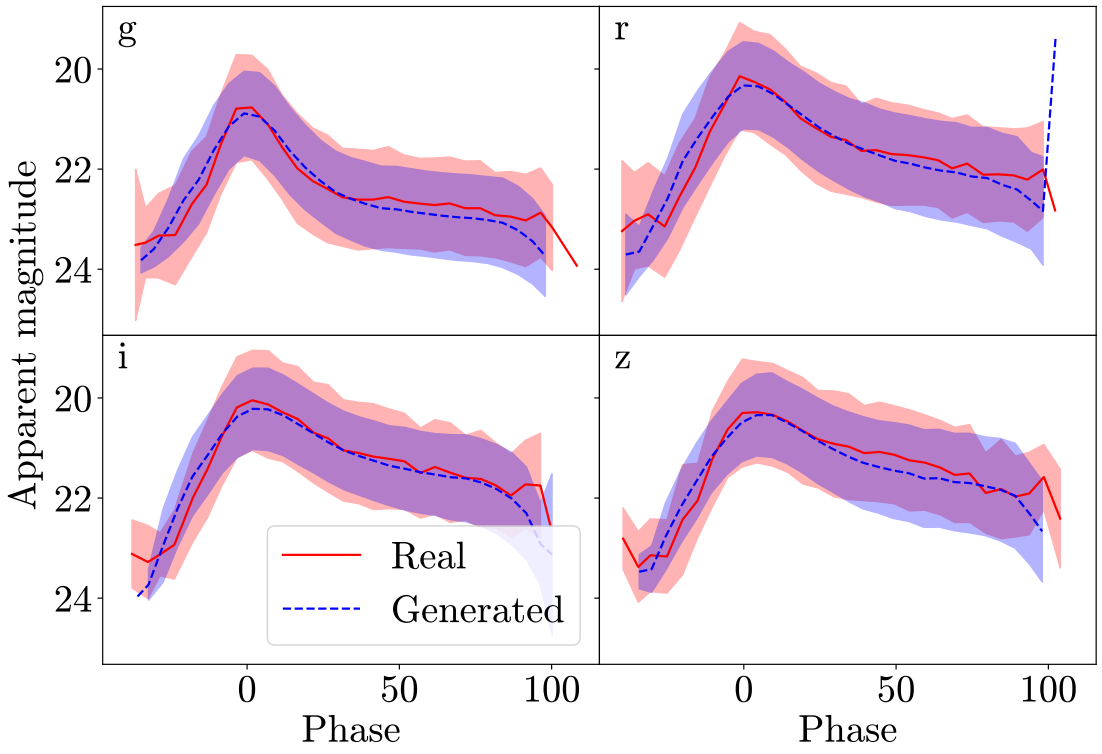

FIGURE A.37: As per Figure 6.6 but for SNe IIb.

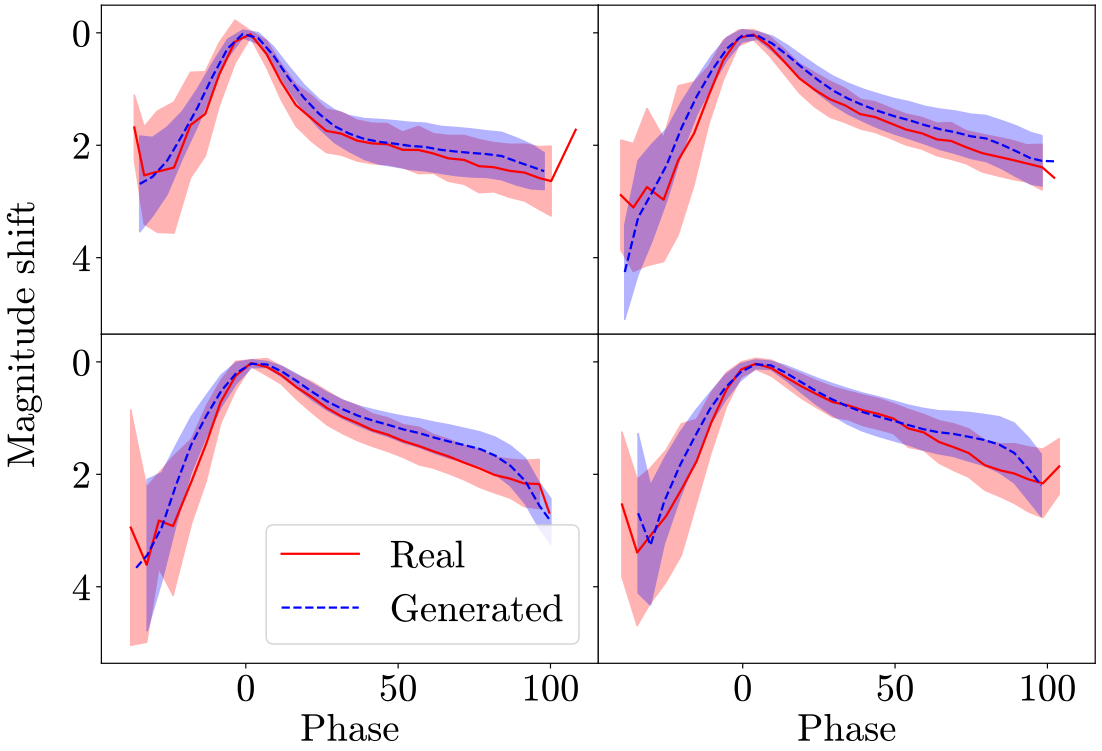

FIGURE A.38: As per Figure 6.7 but for SNe IIb.

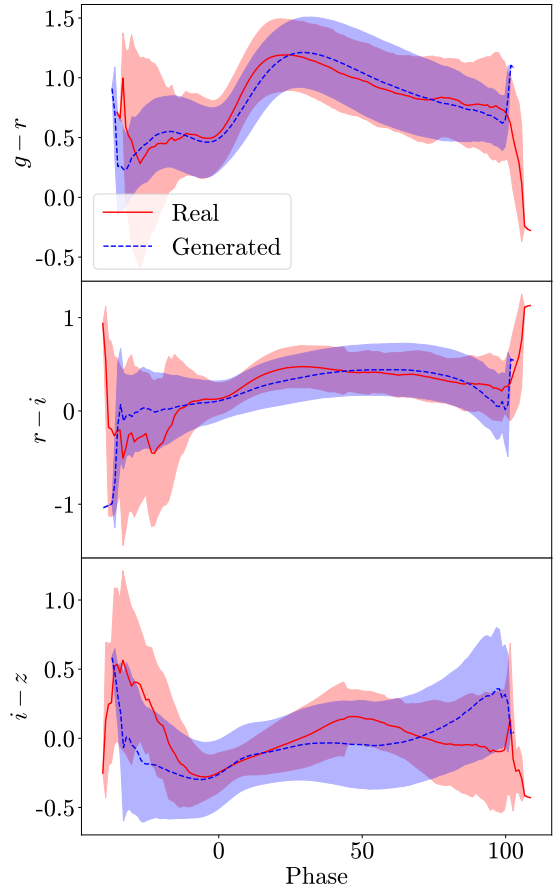

FIGURE A.39: As per Figure 6.8 but for SNe IIb.

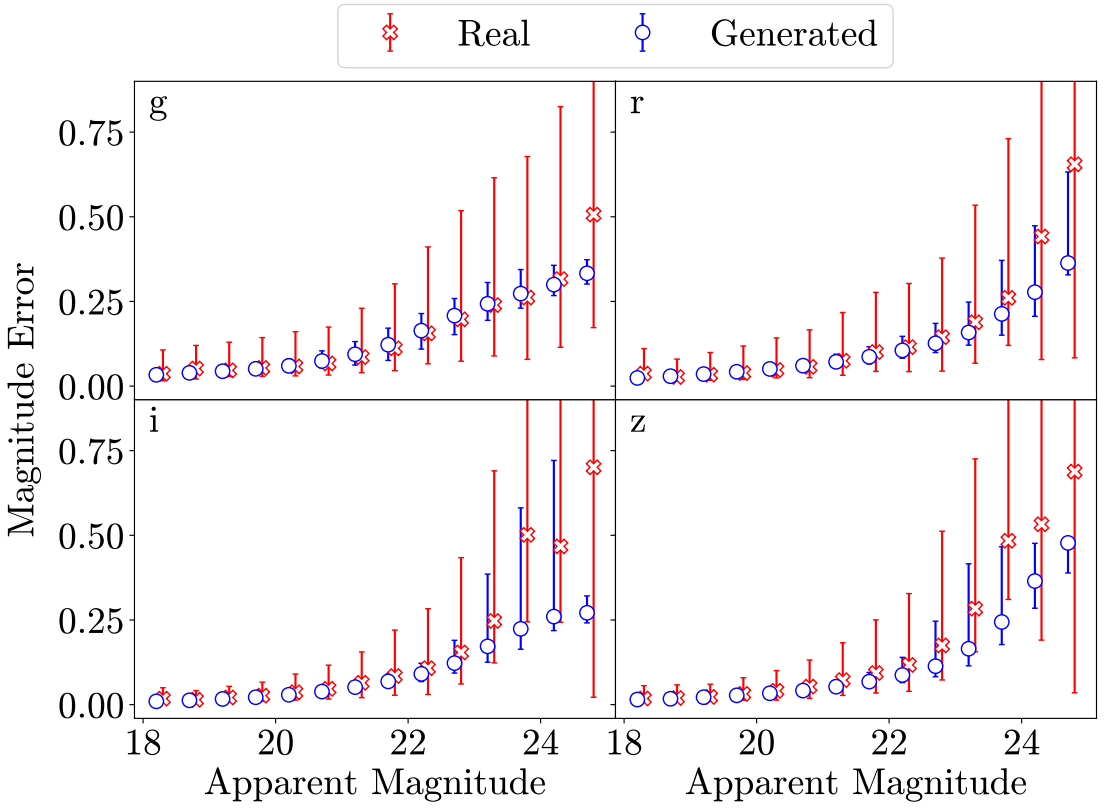

FIGURE A.40: As per Figure 6.9 but for SNe IIb.

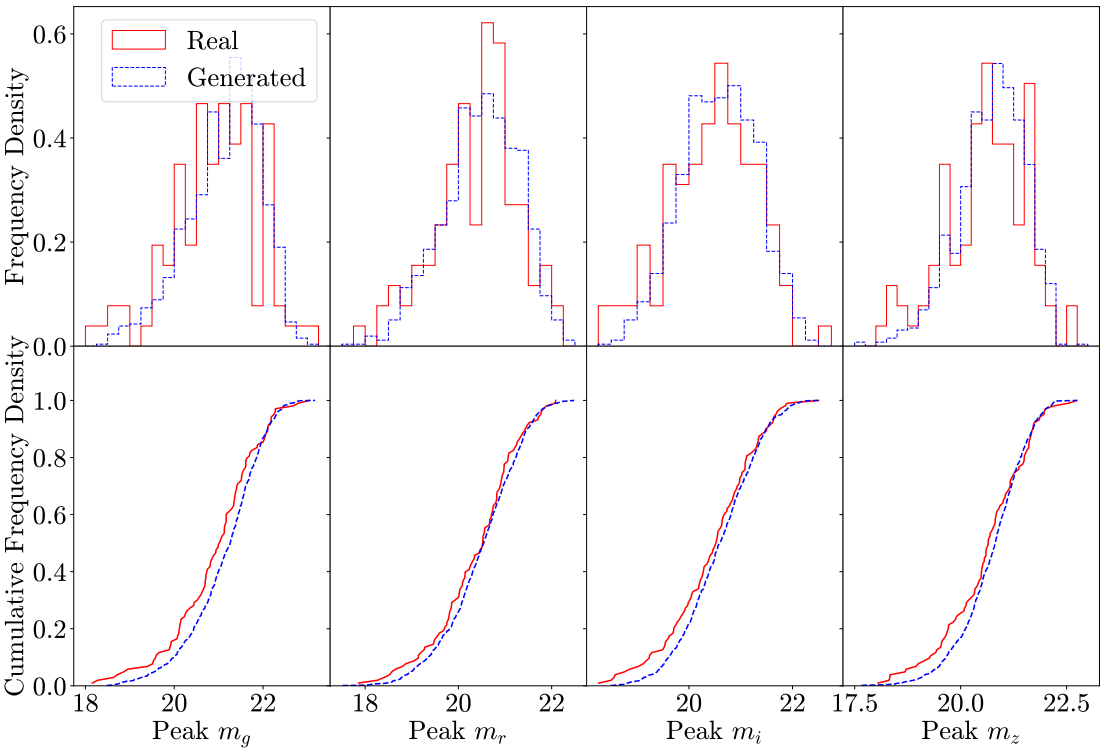

FIGURE A.41: As per Figure 6.2 but for SNe Ic-BL.

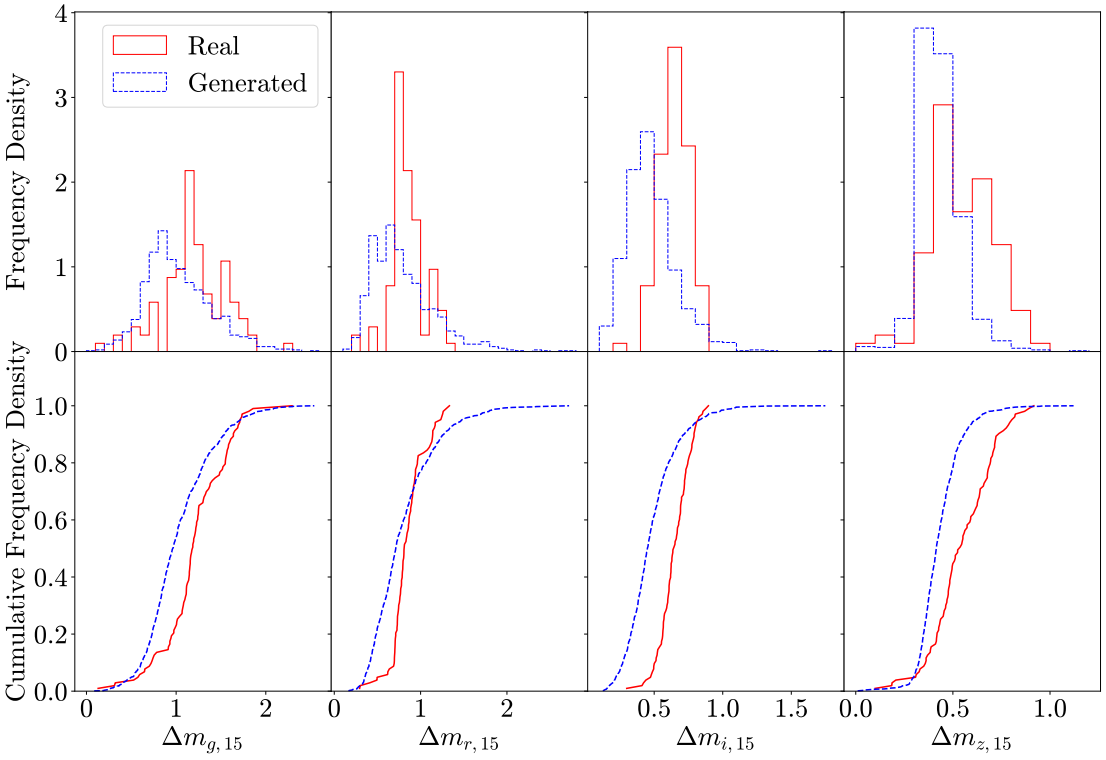

FIGURE A.42: As per Figure 6.3 but for SNe Ic-BL.

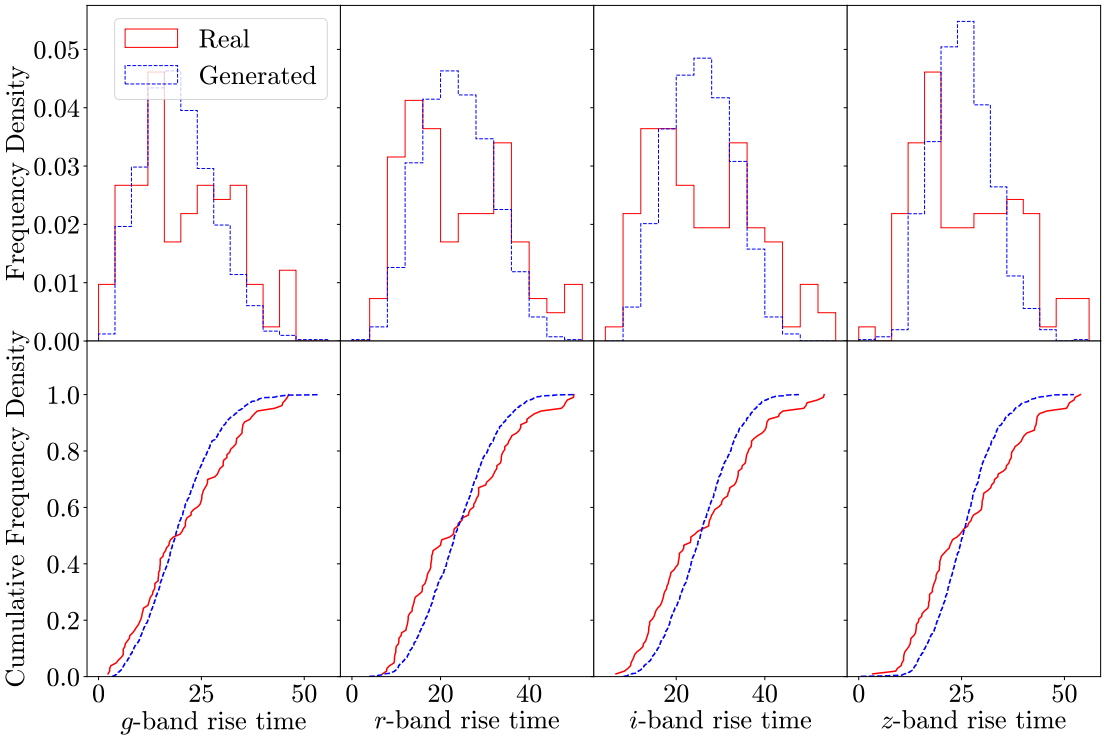

FIGURE A.43: As per Figure 6.4 but for SNe Ic-BL.

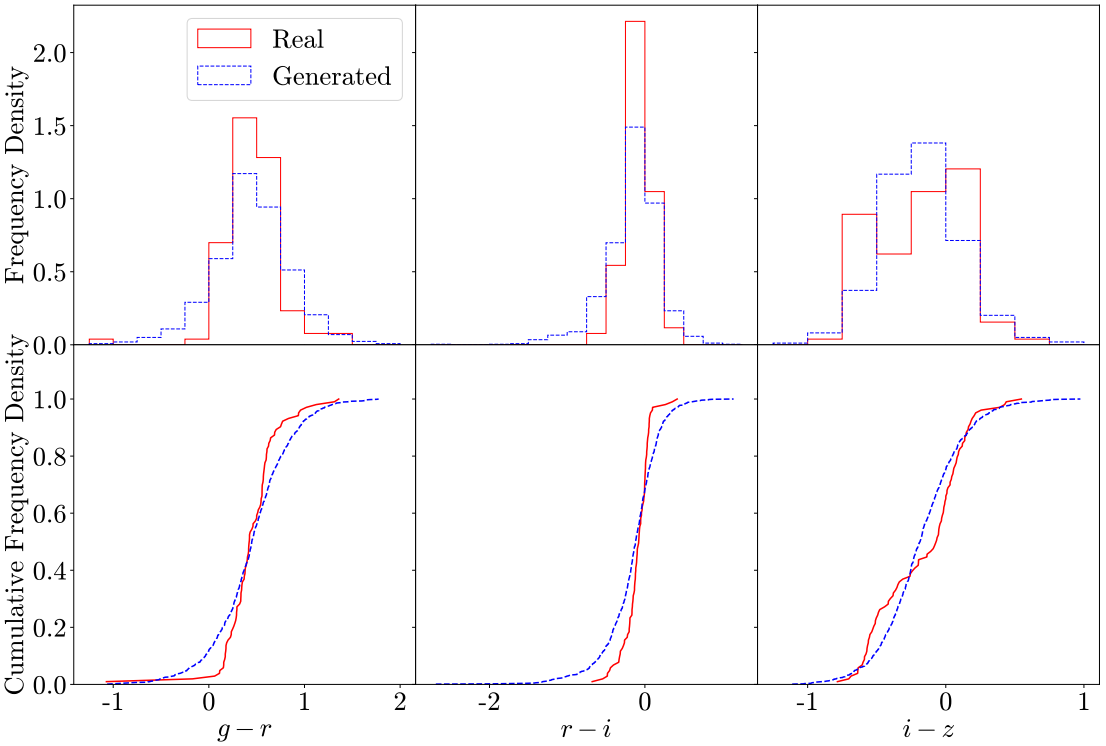

FIGURE A.44: As per Figure 6.5 but for SNe Ic-BL.

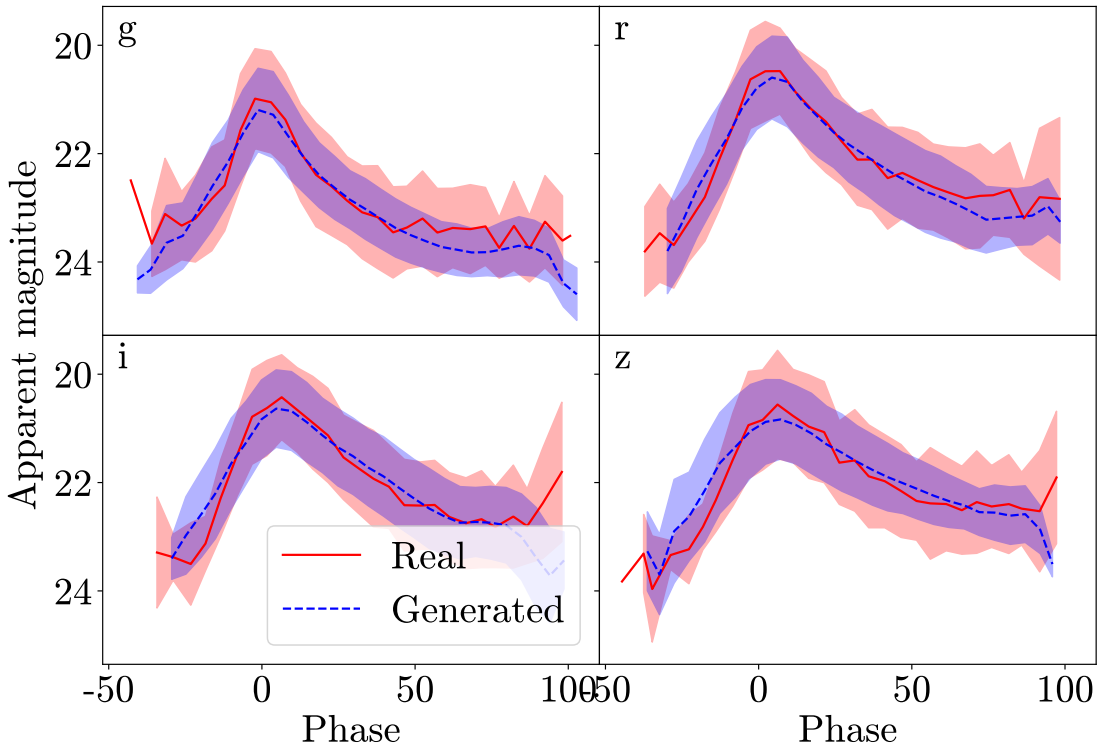

FIGURE A.45: As per Figure 6.6 but for SNe Ic-BL.

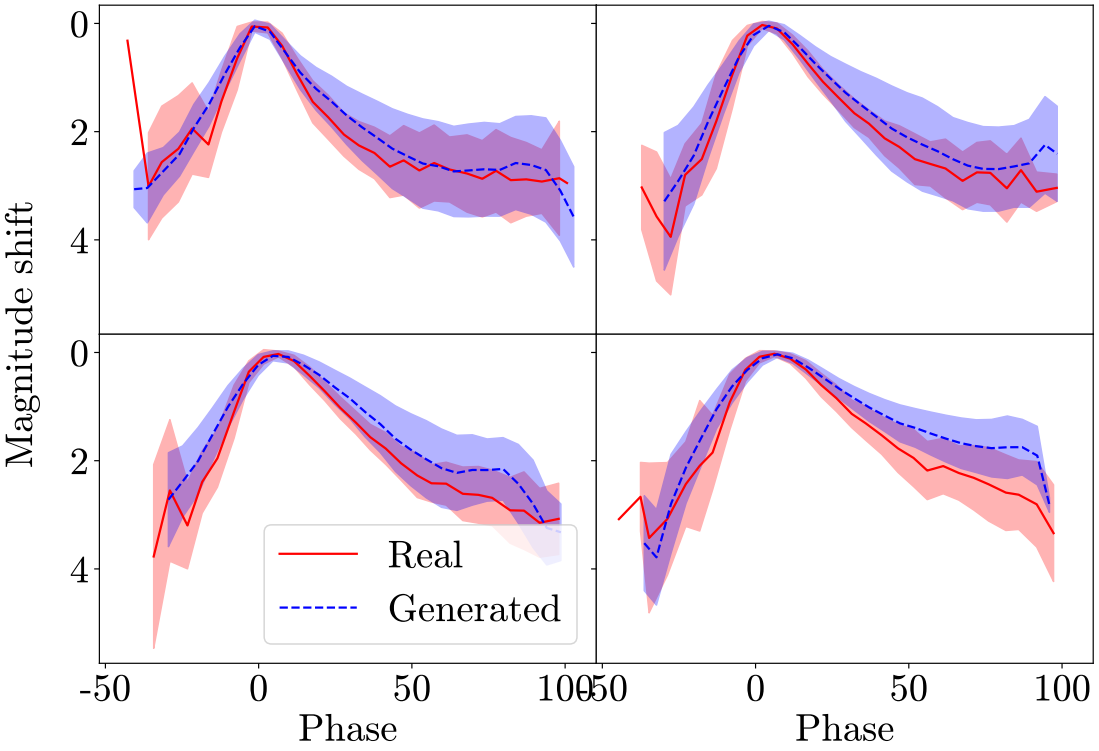

FIGURE A.46: As per Figure 6.7 but for SNe Ic-BL.

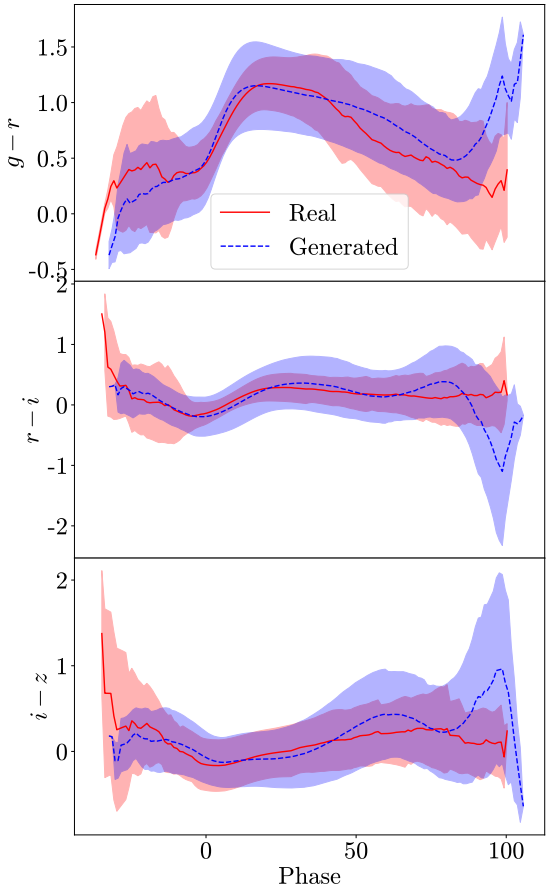

FIGURE A.47: As per Figure 6.8 but for SNe Ic-BL.

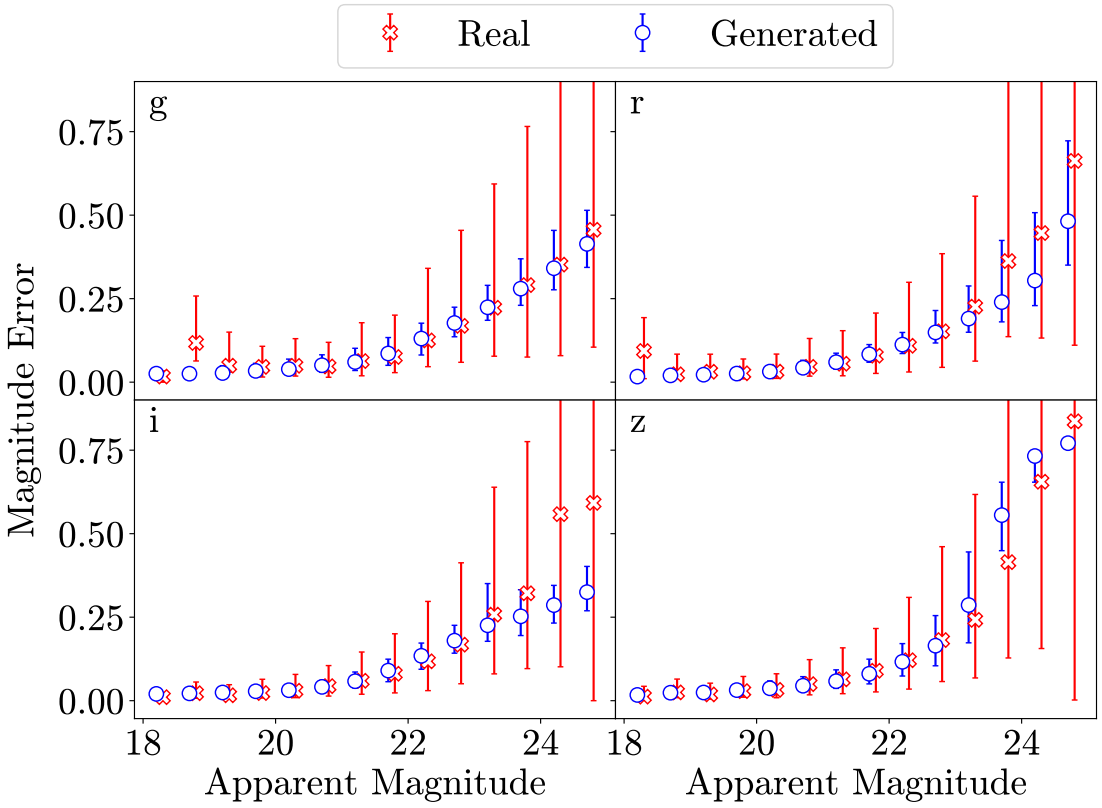

FIGURE A.48: As per Figure 6.9 but for SNe Ic-BL.

References

Abbott T. M. C., et al., 2019, ApJ, 872, L30

Aldering G., Humphreys R. M., Richmond M., 1994, AJ, 107, 662

Anderson J. P., James P. A., 2009, MNRAS, 399, 559

Anderson J. P., Covarrubias R. A., James P. A., Hamuy M., Habergham S. M., 2010, MNRAS, 407, 2660

Anderson J. P., et al., 2014, ApJ, 786, 67

Anderson J. P., et al., 2016, A&A, 589, A110

Angus C. R., Levan A. J., Perley D. A., Tanvir N. R., Lyman J. D., Stanway E. R., Fruchter A. S., 2016, MNRAS, 458, 84

Angus C. R., et al., 2019, MNRAS, 487, 2215

Anupama G. C., Sahu D. K., Gurugubelli U. K., Prabhu T. P., Tominaga N., Tanaka M., Nomoto K., 2008, MNRAS, 392, 894

Arcavi I., et al., 2012, ApJ, 756, L30

Arcavi I., et al., 2017a, Nature, 551, 210

Arcavi I., et al., 2017b, ApJ, 837, L2

Arjovsky M., Bottou L., 2017, arXiv e-prints, p. arXiv:1701.04862

Arjovsky M., Chintala S., Bottou L., 2017, arXiv e-prints, p. arXiv:1701.07875

Arnett W. D., 1982, ApJ, 253, 785

Ayyar V., Knop R., Awbrey A., Andersen A., Nugent P., 2022, PASP, 134, 094501

Baade W., Zwicky F., 1934, Proceedings of the National Academy of Science, 20, 254

Barbon R., Cappellaro E., Turatto M., 1989, A&AS, 81, 421

Barbon R., Benetti S., Cappellaro E., Patat F., Turatto M., Iijima T., 1995, A&AS, 110, 513

Bazin G., et al., 2009, A&A, 499, 653

Bellm E. C., et al., 2019, PASP, 131, 018002

Benson P. J., et al., 1994, AJ, 107, 1453

Bernstein J. P., et al., 2012, ApJ, 753, 152

Bersten M. C., et al., 2012, The Astrophysical Journal, 757, 31

Bersten M. C., et al., 2018, Nature, 554, 497

Bertin E., 2010, SWarp: Resampling and Co-adding FITS Images Together, Astrophysics Source Code Library, record ascl:1010.068 (ascl:1010.068)

Bianco F. B., et al., 2014, ApJS, 213, 19

Blanton M. R., Roweis S., 2007, AJ, 133, 734

Blanton M. R., et al., 2017, AJ, 154, 28

Blondin S., Tonry J. L., 2007, ApJ, 666, 1024

Boone K., 2019, AJ, 158, 257

Boone K., 2021, AJ, 162, 275

Bose S., et al., 2020, ASASSN-18am/SN 2018gk : An overluminous Type IIb supernova from a massive progenitor (arXiv:2007.00008)

Brammer G. B., van Dokkum P. G., Coppi P., 2008, The Astrophysical Journal, 686, 1503

Brout D., et al., 2019a, ApJ, 874, 106

Brout D., et al., 2019b, The Astrophysical Journal, 874, 150

Brown P. J., Breeveld A. A., Holland S., Kuin P., Pritchard T., 2014, Ap&SS, 354, 89

Bruzual G., Charlot S., 2003, MNRAS, 344, 1000

Bufano F., et al., 2014, MNRAS, 439, 1807

Burbidge E. M., Burbidge G. R., Fowler W. A., Hoyle F., 1957, Reviews of Modern Physics, 29, 547

Burns C. R., et al., 2011, AJ, 141, 19

Burrows A., Vartanyan D., 2021, Nature, 589, 29

Cañameras R., et al., 2020, A&A, 644, A163

Cano Z., et al., 2011, ApJ, 740, 41

Cappellari M., 2017, MNRAS, 466, 798

Cappellari M., Emsellem E., 2004, PASP, 116, 138

Cappellari M., et al., 2012, Nature, 484, 485

Chabrier G., 2003, PASP, 115, 763

Chandrasekhar S., 1931, ApJ, 74, 81

Chatzopoulos E., Wheeler J. C., Vinko J., Horvath Z. L., Nagy A., 2013, ApJ, 773, 76

Childress M. J., et al., 2015, MNRAS, 454, 3816

Childress M. J., et al., 2017, MNRAS, 472, 273

Cho K., van Merrienboer B., Bahdanau D., Bengio Y., 2014, arXiv e-prints, p. arXiv:1409.1259

Chu J., Li W., Filippenko A. V., Blondin S., Narayan G., 2008, Central Bureau Electronic Telegrams, 1271, 1

Ciabattari F., Mazzoni E., 2011, Central Bureau Electronic Telegrams, 2827, 1

Clocchiatti A., Wheeler J. C., 1997, ApJ, 491, 375

Curti M., Mannucci F., Cresci G., Maiolino R., 2020, MNRAS, 491, 944

Deng J., Dong W., Socher R., Li L.-J., Li K., Fei-Fei L., 2009, in 2009 IEEE Conference on Computer Vision and Pattern Recognition. pp 248–255, doi:10.1109/CVPR.2009.5206848

Dessart L., Hillier D. J., Waldman R., Livne E., 2013, MNRAS, 433, 1745

Dopita M. A., Kewley L. J., Sutherland R. S., Nicholls D. C., 2016, Ap&SS, 361, 61

Drake A. J., et al., 2009, ApJ, 696, 870

Drout M. R., et al., 2011, ApJ, 741, 97

Eldridge J. J., Tout C. A., 2004, MNRAS, 353, 87

Ergon M., et al., 2015, A&A, 580, A142

Felten J. E., 1976, ApJ, 207, 700

Ferjad Naeem M., Oh S. J., Uh Y., Choi Y., Yoo J., 2020, arXiv e-prints, p. arXiv:2002.09797

Filippenko A. V., 1997, ARA&A, 35, 309

Fioc M., Rocca-Volmerange B., 1997, A&A, 500, 507

Fioc M., Rocca-Volmerange B., 2019, A&A, 623, A143

Fitch F. B., 1944, Journal of Symbolic Logic, 9, 49–50

Fitzpatrick E. L., Massa D., 2007, ApJ, 663, 320

Flaugher B., et al., 2015, The Astronomical Journal, 150, 150

Foglizzo T., 2017, in Alsabti A. W., Murdin P., eds, , Handbook of Supernovae. Springer, p. 1053, doi:10.1007/978-3-319-21846-5_52

Folatelli G., et al., 2014, ApJ, 793, L22

Foley R. J., et al., 2003, PASP, 115, 1220

Fox O. D., et al., 2014, ApJ, 790, 17

Fremling C., et al., 2016, A&A, 593, A68

Friedman J. H., 2001, The Annals of Statistics, 29, 1189

Frohmaier C., et al., 2021, MNRAS, 500, 5142

Gal-Yam A., 2017, Observational and Physical Classification of Supernovae. Springer, p. 195, doi:10.1007/978-3-319-21846-5˙35

Gal-Yam A., 2019, ARA&A, 57, 305

Gal-Yam A., Ofek E. O., Shemmer O., 2002, MNRAS, 332, L73

Gal-Yam A., Yaron O., Pastorello A., Taubenberger S., Fraser M., Perley D., 2021, Transient Name Server AstroNote, 76, 1

Galama T. J., et al., 1998, Nature, 395, 670

Galbany L., et al., 2016, AJ, 151, 33

Galbany L., et al., 2018, ApJ, 855, 107

García-Berro E., Badenes C., Aznar-Siguán G., Lorén-Aguilar P., 2017, MNRAS, 468, 4815

García-Jara G., Protopapas P., Estévez P. A., 2022, ApJ, 935, 23

Gehrels N., 1986, ApJ, 303, 336

Geller M. J., Hwang H. S., Fabricant D. G., Kurtz M. J., Dell'Antonio I. P., Zahid H. J., 2014, ApJS, 213, 35

Goldstein D. A., et al., 2015, AJ, 150, 82

Goodfellow I. J., Pouget-Abadie J., Mirza M., Xu B., Warde-Farley D., Ozair S., Courville A., Bengio Y., 2014, arXiv e-prints, p. arXiv:1406.2661

Graham M. L., Clubb K. I., Mauerhan J., Filippenko A. V., Serduke F. J. D., Nugent P. E., 2014, The Astronomer's Telegram, 6591, 1

Graur O., Bianco F. B., Huang S., Modjaz M., Shivvers I., Filippenko A. V., Li W., Eldridge J. J., 2017a, ApJ, 837, 120

Graur O., Bianco F. B., Modjaz M., Shivvers I., Filippenko A. V., Li W., Smith N., 2017b, ApJ, 837, 121

Grayling M., et al., 2021, MNRAS, 505, 3950

Grayling M., et al., 2022, arXiv e-prints, p. arXiv:2207.08520

Guillochon J., Nicholl M., Villar V. A., Mockler B., Narayan G., Mandel K. S., Berger E., Williams P. K. G., 2018, ApJS, 236, 6

Gulrajani I., Ahmed F., Arjovsky M., Dumoulin V., Courville A., 2017, arXiv e-prints, p. arXiv:1704.00028

Gutiérrez C. P., et al., 2017a, ApJ, 850, 89

Gutiérrez C. P., et al., 2017b, The Astrophysical Journal, 850, 90

Gutiérrez C. P., et al., 2018, MNRAS, 479, 3232

Gutiérrez C. P., et al., 2020, MNRAS, 496, 95

Guy J., et al., 2007, A&A, 466, 11

Hartley W. G., et al., 2022, MNRAS, 509, 3547

Helou G., Kasliwal M. M., Ofek E. O., Arcavi I., Surace J., Gal-Yam A., 2013, ApJ, 778, L19

Hicken M., et al., 2017, ApJS, 233, 6

Hložek R., et al., 2020, arXiv e-prints, p. arXiv:2012.12392

Ho A. Y. Q., et al., 2020, ApJ, 893, 132

Hochreiter S., Schmidhuber J., 1997, Neural Comput., 9, 1735–1780

Iben I. J., Tutukov A. V., 1984, ApJS, 54, 335

Inserra C., 2019, Nature Astronomy, 3, 697

Inserra C., et al., 2013, ApJ, 770, 128

Janka H.-T., 2017, in Alsabti A. W., Murdin P., eds, , Handbook of Supernovae. Springer, p. 1095, doi:10.1007/978-3-319-21846-5_109

Japelj J., Vergani S. D., Salvaterra R., Renzo M., Zapartas E., de Mink S. E., Kaper L., Zibetti S., 2018, A&A, 617, A105

Jerkstrand A., Fransson C., Maguire K., Smartt S., Ergon M., Spyromilio J., 2012, A&A, 546, A28

Jones D. O., et al., 2017, ApJ, 843, 6

Jones D. O., et al., 2021, ApJ, 908, 143

Joung M. K. R., Mac Low M.-M., 2006, ApJ, 653, 1266

Karachentseva V. E., Karachentsev I. D., Kashibadze O. G., 2020, Astrophysics, 63, 151

Karpenka N. V., Feroz F., Hobson M. P., 2013, MNRAS, 429, 1278

Karras T., Aila T., Laine S., Lehtinen J., 2017, arXiv e-prints, p. arXiv:1710.10196

Kasliwal M. M., et al., 2012, ApJ, 755, 161

Kato T., Uemura M., Ishioka R., Nogami D., Kunjaya C., Baba H., Yamaoka H., 2004, Publications of the Astronomical Society of Japan, 56, S1

Kerzendorf W. E., et al., 2019, A&A, 623, A34

Kessler R., et al., 2009, PASP, 121, 1028

Kessler R., Conley A., Jha S., Kuhlmann S., 2010a, arXiv e-prints, p. arXiv:1001.5210

Kessler R., et al., 2010b, PASP, 122, 1415

Kessler R., et al., 2015, AJ, 150, 172

Kewley L. J., Geller M. J., Jansen R. A., 2004, AJ, 127, 2002

Khatami D. K., Kasen D. N., 2019, ApJ, 878, 56

Kiewe M., et al., 2012, ApJ, 744, 10

Kilpatrick C. D., et al., 2016, The Astronomer's Telegram, 9536, 1

Kingma D. P., Ba J., 2014, arXiv e-prints, p. arXiv:1412.6980

Kochanek C. S., 2018, MNRAS, 473, 1633

Kotera K., Phinney E. S., Olinto A. V., 2013, MNRAS, 432, 3228

Kuehn K., Lidman C., Martini P., Mudd D., Zhang B., Yuan F., 2014, The Astronomer's Telegram, 6789, 1

Kumar B., et al., 2013, MNRAS, 431, 308

LSST Science Collaboration et al., 2009, arXiv e-prints, p. arXiv:0912.0201

Larson R. B., 1974, /mnras, 169, 229

Leaman J., Li W., Chornock R., Filippenko A. V., 2011, MNRAS, 412, 1419

Lennarz D., Altmann D., Wiebusch C., 2012, A&A, 538, A120

Leroy A. K., et al., 2019, ApJS, 244, 24

Levan A., et al., 2005, ApJ, 624, 880

Lewis J. R., et al., 1994, MNRAS, 266, L27

Li W. D., 2000, AIP Conference Proceedings

Li W., et al., 2011, MNRAS, 412, 1441

Li S., Frank A., Blackman E. G., 2014, MNRAS, 444, 2884

Lidman C., et al., 2020, MNRAS, 496, 19

Lilly S. J., Le Fevre O., Hammer F., Crampton D., 1996, ApJ, 460, L1

Lintott C. J., et al., 2008, MNRAS, 389, 1179

Lyman J. D., Bersier D., James P. A., 2013, MNRAS, 437, 3848

Lyman J. D., Bersier D., James P. A., Mazzali P. A., Eldridge J. J., Fraser M., Pian E., 2016, MNRAS, 457, 328

Maeda K., Mazzali P. A., Deng J., Nomoto K., Yoshii Y., Tomita H., Kobayashi Y., 2003, The Astrophysical Journal, 593, 931

Maeda K., et al., 2015, ApJ, 807, 35

Maguire K., et al., 2012, MNRAS, 426, 2359

Malmquist K. G., 1922, Meddelanden fran Lunds Astronomiska Observatorium Serie I, 100, 1

Mandel K. S., Thorp S., Narayan G., Friedman A. S., Avelino A., 2022, MNRAS, 510, 3939

Mathews G. J., Boccioli L., Hidaka J., Kajino T., 2020, Modern Physics Letters A, 35, 2030011

Metlova N. V., Tsvetkov D. Y., Shugarov S. Y., Esipov V. F., Pavlyuk N. N., 1995, Astronomy Letters, 21, 598

Meza N., Anderson J. P., 2020, A&A, 641, A177

Mikuz H., Dintinjana B., Zwitter T., 1993, IAU Circ., 5796, 2

Minaee S., Abdolrashidi A., 2018, arXiv e-prints, p. arXiv:1812.10482

Minkowski R., 1941, PASP, 53, 224

Mirza M., Osindero S., 2014, arXiv e-prints, p. arXiv:1411.1784

Modjaz M., Liu Y. Q., Bianco F. B., Graur O., 2016, ApJ, 832, 108

Modjaz M., Gutiérrez C. P., Arcavi I., 2019, Nature Astronomy, 3, 717

Modjaz M., et al., 2020, The Astrophysical Journal, 892, 153

Mogren O., 2016, arXiv e-prints, p. arXiv:1611.09904

Mohd Razali N., Yap B., 2011, J. Stat. Model. Analytics, 2

Möller A., et al., 2022, MNRAS, 514, 5159

Monard L. A. G., 2009, Central Bureau Electronic Telegrams, 2071, 1

Morales-Garoffolo A., et al., 2014, MNRAS, 445, 1647

Morganson E., et al., 2018, PASP, 130, 074501

Motamed S., Rogalla P., Khalvati F., 2021, Informatics in Medicine Unlocked, 27, 100779

Muthukrishna D., Narayan G., Mandel K. S., Biswas R., Hložek R., 2019, PASP, 131, 118002

Möller A., de Boissière T., 2019, MNRAS, 491, 4277–4293

Nadyozhin D. K., 1994, ApJS, 92, 527

Nakar E., Piro A. L., 2014, The Astrophysical Journal, 788, 193

Newman J. A., et al., 2013, ApJS, 208, 5

Nicholl M., 2021, Astronomy and Geophysics, 62, 5.34

Nicholl M., Guillochon J., Berger E., 2017, ApJ, 850, 55

Nicholls B., et al., 2016, The Astronomer's Telegram, 9521, 1

Noeske K. G., et al., 2007, The Astrophysical Journal, 660, L43

Nomoto K. I., Iwamoto K., Suzuki T., 1995, Phys. Rep., 256, 173

Ofek E. O., et al., 2014, ApJ, 789, 104

Okyudo M., Kato T., Ishida T., Tokimasa N., Yamaoka H., 1993, PASJ, 45, L63

Osterbrock D. E., 1989, Astrophysics of gaseous nebulae and active galactic nuclei. University Science Books

Pandey S. B., Anupama G. C., Sagar R., Bhattacharya D., Sahu D. K., Pandey J. C., 2003, MNRAS, 340, 375

Papadopoulos A., et al., 2015, MNRAS, 449, 1215

Parikh T., Thomas D., Maraston C., Westfall K. B., Andrews B. H., Boardman N. F., Drory N., Oyarzun G., 2021, MNRAS, 502, 5508

Pasquet J., Pasquet J., Chaumont M., Fouchez D., 2019, A&A, 627, A21

Pastorello A., et al., 2007, Nature, 447, 829

Pastorello A., et al., 2008, MNRAS, 389, 955

Patat F., et al., 2001, ApJ, 555, 900

Perley D. A., et al., 2016, ApJ, 830, 13

Perley D. A., et al., 2020, The Astrophysical Journal, 904, 35

Perley D. A., et al., 2022, ApJ, 927, 180

Perlmutter S., et al., 1999, ApJ, 517, 565

Pessi P. J., et al., 2019, MNRAS, 488, 4239

Pettini M., Pagel B. E. J., 2004, MNRAS, 348, L59

Phillips M. M., 1993, ApJ, 413, L105

Pignata G., et al., 2009, Central Bureau Electronic Telegrams, 1663, 1

Pignata G., et al., 2011, ApJ, 728, 14

Piro A. L., 2015, The Astrophysical Journal, 808, L51

Prentice S. J., et al., 2016, MNRAS, 458, 2973

Prentice S. J., et al., 2018, MNRAS, 478, 4162

Prentice S. J., et al., 2019, MNRAS, 485, 1559

Prentice S. J., et al., 2020, MNRAS, 499, 1450

Pskovskii I. P., 1977, Soviet Ast., 21, 675

Pugh H., Park S., Li W., 2004, IAU Circ., 8425, 1

Pursiainen M., et al., 2018, MNRAS, 481, 894

Qiu Y., Li W., Qiao Q., Hu J., 1999, AJ, 117, 736

Reynolds T. M., et al., 2020, MNRAS, 493, 1761

Richards J. W., Homrighausen D., Freeman P. E., Schafer C. M., Poznanski D., 2012, MNRAS, 419, 1121

Richardson D., III R. L. J., Wright J., Maddox L., 2014, The Astronomical Journal, 147, 118

Richmond M. W., Treffers R. R., Filippenko A. V., Paik Y., Leibundgut B., Schulman E., Cox C. V., 1994, AJ, 107, 1022

Richmond M. W., Treffers R. R., Filippenko A. V., Paik Y., 1996, AJ, 112, 732

Riess A. G., et al., 1998, AJ, 116, 1009

Riess A. G., et al., 2022, ApJ, 934, L7

Rosenblatt F., 1957, Technical Report 85-460-1, The perceptron - A perceiving and recognizing automaton. Cornell Aeronautical Laboratory, Ithaca, New York

Rubner Y., Tomasi C., Guibas L. J., 2000, International Journal of Computer Vision, 40, 99

Rust B. W., 1974, PhD thesis, Oak Ridge National Laboratory, Tennessee

Ryder S. D., et al., 2018, ApJ, 856, 83

Sahu D. K., Tanaka M., Anupama G. C., Gurugubelli U. K., Nomoto K., 2009, ApJ, 697, 676

Sahu D. K., Anupama G. C., Chakradhari N. K., 2013, MNRAS, 433, 2

Sahu D. K., Anupama G. C., Chakradhari N. K., Srivastav S., Tanaka M., Maeda K., Nomoto K., 2018, MNRAS, 475, 2591

Sako M., et al., 2011, ApJ, 738, 162

Salim S., et al., 2007, ApJS, 173, 267

Sapir N., Waxman E., 2017, The Astrophysical Journal, 838, 130

Schlafly E. F., Finkbeiner D. P., 2011, ApJ, 737, 103

Schlegel E. M., 1990, MNRAS, 244, 269

Schlegel D. J., Finkbeiner D. P., Davis M., 1998, ApJ, 500, 525

Schmidt M., 1968, ApJ, 151, 393

Schulze S., et al., 2021, ApJS, 255, 29

Shappee B. J., et al., 2014, ApJ, 788, 48

Shivvers I., et al., 2017, PASP, 129, 054201

Smith N., 2017, in Alsabti A. W., Murdin P., eds, , Handbook of Supernovae. Springer, p. 403, doi:10.1007/978-3-319-21846-5_38

Smith N., et al., 2015, MNRAS, 449, 1876

Smith M., et al., 2016, ApJ, 818, L8

Smith K. W., et al., 2019, Research Notes of the AAS, 3, 26

Smith M., et al., 2020a, AJ, 160, 267

Smith M., et al., 2020b, MNRAS, 494, 4426

Sollerman J., Kozma C., Fransson C., Leibundgut B., Lundqvist P., Ryde F., Woudt P., 2000, ApJ, 537, L127

Sollerman J., et al., 2002, A&A, 386, 944

Stritzinger M. D., et al., 2018, A&A, 609, A134

Sullivan M., et al., 2006, The Astrophysical Journal, 648, 868

Sullivan M., et al., 2010, MNRAS, 406, 782

Suntzeff N. B., Phillips M. M., Depoy D. L., Elias J. H., Walker A. R., 1991, AJ, 102, 1118

Szalai T., et al., 2016, MNRAS, 460, 1500

Taddia F., et al., 2018, A&A, 609, A136

Taggart K., Perley D. A., 2021, MNRAS, 503, 3931

Tartaglia L., et al., 2017, The Astrophysical Journal, 836, L12

Taubenberger S., et al., 2019, MNRAS, 488, 5473

Terreran G., et al., 2016, MNRAS, 462, 137

Tinyanont S., et al., 2016, ApJ, 833, 231

Tonry J., Denneau L., Stalder B., Heinze A., Sherstyuk A., Rest A., Smith K. W., Smartt S. J., 2016, The Astronomer's Telegram, 9526, 1

Tonry J. L., et al., 2018, PASP, 130, 064505

Trayford J. W., Theuns T., Bower R. G., Crain R. A., Lagos C. d. P., Schaller M., Schaye J., 2016, MNRAS, 460, 3925

Tsvetkov D. Y., Volkov I. M., Baklanov P., Blinnikov S., Tuchin O., 2009, Peremennye Zvezdy, 29, 2

Valenti S., et al., 2016, MNRAS, 459, 3939

Vazdekis A., Sánchez-Blázquez P., Falcón-Barroso J., Cenarro A. J., Beasley M. A., Cardiel N., Gorgas J., Peletier R. F., 2010, MNRAS, 404, 1639

Villar V. A., Nicholl M., Berger E., 2018, ApJ, 869, 166

Vincenzi M., Sullivan M., Firth R. E., Gutiérrez C. P., Frohmaier C., Smith M., Angus C., Nichol R. C., 2019, MNRAS, 489, 5802

Vincenzi M., et al., 2021, MNRAS, 505, 2819

Vincenzi M., et al., 2022, MNRAS,

Wang L. J., et al., 2017, ApJ, 837, 128

Whelan J., Iben Icko J., 1973, ApJ, 186, 1007

Wiseman P., et al., 2020a, MNRAS, 495, 4040

Wiseman P., et al., 2020b, MNRAS, 498, 2575

Wiseman P., et al., 2021, MNRAS, 506, 3330

Woosley S. E., Weaver T. A., 1994, ApJ, 423, 371

Woosley S. E., Pinto P. A., Hartmann D., 1989, ApJ, 346, 395

Woosley S. E., Langer N., Weaver T. A., 1993, ApJ, 411, 823

Yates R. M., Kauffmann G., Guo Q., 2012, MNRAS, 422, 215

Yoshii Y., et al., 2003, ApJ, 592, 467

Yuan F., et al., 2015, MNRAS, 452, 3047

Zahid H. J., Dima G. I., Kewley L. J., Erb D. K., Davé R., 2012, ApJ, 757, 54

Zahid H. J., Geller M. J., Kewley L. J., Hwang H. S., Fabricant D. G., Kurtz M. J., 2013, ApJ, 771, L19

Zhou X., 1993, IAU Circ., 5782, 2

de Jaeger T., et al., 2020a, MNRAS, 495, 4860

de Jaeger T., Stahl B. E., Zheng W., Filippenko A. V., Riess A. G., Galbany L., 2020b, MNRAS, 496, 3402

de Jaeger T., Galbany L., Riess A. G., Stahl B. E., Shappee B. J., Filippenko A. V., Zheng W., 2022, MNRAS, 514, 4620

van Driel W., et al., 1993, PASJ, 45, L59